PROPERTIES AND OBSERVATIONS OF DWARF IRREGULAR GALAXIES

By

CAROLINE ELIZABETH SIMPSON

A DISSERTATION PRESENTED TO THE GRADUATE SCHOOL
OF THE UNIVERSITY OF FLORIDA IN PARTIAL FULFILLMENT
OF THE REQUIREMENTS FOR THE DEGREE OF
DOCTOR OF PHILOSOPHY

UNIVERSITY OF FLORIDA

1995

To my parents
Richard and Emily Simpson,
and my sister
Elizabeth Simpson.

ACKNOWLEDGMENTS

The chairman of my Ph.D. committee, Dr. Stephen Gottesman, must be commended for all of his tutelage and patience during my time as his student. I have learned much from him. I would also like to thank the other members of my committee for their help and advice, especially Dr. Haywood Smith and Dr. Humberto Campins. Financial support for much of this work was provided by the Florida Space Grant Consortium, and travel money for the observations was provided by a Sigma Xi Small Research Grant.

I would also like to acknowledge the support I've received from my former supervisors and coworkers at Space Telescope Science Institute. Drs. Conrad Sturch, Barry Lasker, Brian McLean, and my dear friend Vicki Laidler all played very important roles in my decision to pursue a graduate degree.

There have been many graduate students here at the University of Florida who have made my time here enjoyable as well as productive: Billy Cooke, Dan Durda, Sumita Jayaraman, Dave Kaufmann, Jane Morrison, Jaydeep Mukherjee, and Ricky Smart, among others. Liz Moore and Elaine Mahon provided not only friendship, but also advice on making and reducing my VLA observations. Special thanks go to my officemate and coworker Seppo Laine.

I would like to thank my ex-roommate and very good friend Jamey Bell as well. Without his good humor and support, life would have been much duller! I would also like to thank Eric Johnson, who has occupied a very special place in my life during the last year. He has provided much personal support and understanding during these hectic final months. His caring presence in my life has made a difficult time much easier.

Finally, I would like to thank my family: my mother for the dream, my father for the drive, and my sister for the confidence. Without their love and encouragement, none of this would have been possible.

TABLE OF CONTENTS

ACKNOWLEDGMENTS iii

LIST OF TABLES vii

LIST OF FIGURES viii

ABSTRACT xiv

CHAPTERS

1 INTRODUCTION 1

Star Formation in Dwarf Irregular Galaxies 1

Project Descriptions 3

HI Survey 3

LSBD-BCD Study 5

2 DWARF GALAXIES 7

Type Descriptions 8

Dwarf Elliptical Galaxies 8

Dwarf Irregular Galaxies 9

Blue Compact Dwarf Galaxies 10

Stochastic Self-Propagating Star Formation 10

System Evolution 15

3 OBSERVATIONS 22

21–Centimeter Line Emission 22

Aperture Synthesis Theory 26

Imaging 32

Calibration 32

Imaging 35

4 HI SURVEY PROJECT 38

Introduction 38

Project Description 42

Number Density 42

Spatial Distribution 47

Observations 48
Data Reduction 51
Analysis 55
Noise 55
Detection Criteria 56
Survey Results 61
Void Field 61
Cluster Field 68
Interaction Field 73
Discussion 81

5 BLUE COMPACT AND LOW SURFACE BRIGHTNESS DWARF PROJECT 85
Introduction 85
The Data 87
Sample Description 87
Observations 89
Data Reduction 89
Analysis 91
HI Distribution and Kinematics 93
Observed Parameters and Correlations 102
Discussion 113

6 CONCLUSIONS 163
Summary 163
Future Work 169

APPENDICES

A COMPANION TO DDO 169 172

B VOLUME CALCULATION 177

REFERENCES 180

BIOGRAPHICAL SKETCH 186

LIST OF TABLES

4.1: Physical Properties of target galaxies. 49

4.2: Derived Properties of detected galaxies. 82

5.1: Physical properties of BCD galaxy sample, taken from the RC3. 118

5.2: Physical properties of LSBD galaxy sample, taken from the RC3. 119

5.3: Observational parameters for entire galaxy sample. 120

5.4: Derived parameters for BCD galaxy sample. 121

5.5: Derived parameters for LSBD galaxy sample. 122

5.6: Correlation parameters for BCD galaxy sample. 123

5.7: Correlation parameters for LSBD galaxy sample. 124

LIST OF FIGURES

2.1: Star formation rate (SFR) as a function of time over a 2.6 billion year period for model galaxies having radii between 0.4 and 6 kpc. The SFR is the fraction of cells undergoing star formation per 10 million year time step. Taken from Figure 1 in Gerola et al., 1980. 15

4.1: Radial frequency function determined by Tyson and Scalo (1988). 40

4.2: Gaussian fit (solid line) to the noise in a channel with no signal emission. 56

4.3: Peak signal-to-noise per channel for the low redshift data set for the Void field observations. 62

4.4: Peak signal-to-noise per channel for the low redshift data set for the Void field observations; including the data for UGC 10805. 63

4.5: Flux spectrum of the blanked data cube for UGC 10805. 64

4.6: Integrated HI column density map of UGC 10805. Contour levels are 0.24 (2σ), 0.5, 1, 2, 3, and 4×10^{20} atoms cm^{-2}. 64

4.7: Peak signal-to-noise per channel for the high redshift data set for the Void field observations. 66

4.8: Flux spectrum of blanked cube for possible detection in the high redshift Void field. 67

4.9: Peak signal-to-noise per channel for the low redshift data set for the Cluster field observations. 69

4.10: Peak signal-to-noise per channel for the low redshift data set for the Cluster field observations; including the data for UGC 2014. 70

4.11: Flux spectrum of the blanked data cube for UGC 2014. 71

4.12: Integrated HI column density map of UGC 2014. Contour levels are 0.79 (2σ), 1, 3, 5, and 8 $\times$ 10^{20} atoms cm^{-2}. 71

4.13: Peak signal-to-noise per channel for the high redshift data set for the Cluster field observations. 72

4.14: Peak signal-to-noise per channel for the low redshift data set for the Interaction field observations, excluding M81dB and UGC 5455. 74

4.15: Flux spectrum of blanked cube for possible detection in the Interaction field. 75

4.16: Peak signal-to-noise per channel for the low redshift data set for the Interaction field observations; including the data for M81dB and UGC 5455. 76

4.17: Flux spectrum of the blanked data cube for M81dB. Vertical error bars indicate $\pm 1\sigma$ variation. 76

4.18: Integrated HI column density map of M81dB. Contour levels are 1.2 (2σ), 3, 5, and 9 $\times$ 10^{20} atoms cm^{-2}. 77

4.19: Flux spectrum of the blanked data cube for UGC 5455. 78

4.20: Integrated HI column density map of UGC 5455. Contour levels are 2.5 (2σ), 5, 9, and 11 $\times$ 10^{20} atoms cm^{-2}. 79

4.21: Peak signal-to-noise per channel for the high redshift data set for the Interaction field observations. 80

5.1: Color-Color plot of galaxy sample. Blue is to the lower left. 88

5.2: Integrated HI intensity (0th moment) map of A1116+51. Contour levels are 1.4 (2σ), 2, 2.5, 3, 3.5 $\times$ 10^{20} atom cm^{-2}. 125

5.3: Integrated velocity field (1st moment) map of A1116+51. 125

5.4: Optical greyscale image with HI contours for A1116+51. 126

5.5: Global velocity profile for A1116+51. 126

5.6: Integrated HI intensity (0th moment) map of Haro 33. Contour levels are 4.7 (2σ), 5, 7.5, 10, 12.5, 15, 17.5 $\times$ 10^{20} atom cm^{-2}. 127

5.7: Integrated velocity field (1st moment) map of Haro 33. 127

5.8: Optical greyscale image with HI contours for Haro 33. 128

5.9: Global velocity profile for Haro 33. 128

5.10: Integrated HI intensity (0th moment) map of Haro 4. Contour levels are 1.8 (2σ), 2.5, 5, 7.5 $\times$ 10^{20} atom cm^{-2}. 129

5.11: Integrated velocity field (1st moment) map of Haro 4. 129

5.12: Optical greyscale image with HI contours for Haro 4. 130

5.13: Global velocity profile for Haro 4. 130

5.14: Integrated HI intensity (0th moment) map of Haro 27. Contour levels are 2.2 (2σ), 5, 7.5, 9.0 $\times$ 10^{20} atom cm^{-2}. 131

5.15: Integrated velocity field (1st moment) map of Haro 27. 131

5.16: Optical greyscale image with HI contours for Haro 27. 132

5.17: Global velocity profile for Haro 27. 132

5.18: Integrated HI intensity (0th moment) map of Haro 36. Contour levels are 4.5 (2σ), 5, 10, 15, 20 $\times$ 10^{20} atom cm^{-2}. 133

5.19: Integrated velocity field (1st moment) map of Haro 36. 133

5.20: Optical greyscale image with HI contours for Haro 36. 134

5.21: Global velocity profile for Haro 36. 134

5.22: Integrated HI intensity (0th moment) map of Mrk 328. Contour levels are 1.1 (2σ), 1.5, 2, 2.5, 3, 3.5 $\times$ 10^{20} atom cm^{-2}. 135

5.23: Integrated velocity field (1st moment) map of Mrk 328. 135

5.24: Optical greyscale image with HI contours for Mrk 328. 136

5.25: Global velocity profile for Mrk 328. 136

5.26: Integrated HI intensity (0th moment) map of Mrk 51. Contour levels are 2.1 (2σ), 5, 7.5, 8.5 $\times$ 10^{20} atom cm^{-2}. 137

5.27: Integrated velocity field (1st moment) map of Mrk 51. 137

5.28: Optical greyscale image with HI contours for Mrk 51. 138

5.29: Global velocity profile for Mrk 51 138

5.30: Integrated HI intensity (0th moment) map of Mrk 67. Contour levels are 1.3 (2σ), 2, 3, 4 $\times$ 10^{20} atom cm^{-2}. 139

5.31: Integrated velocity field (1st moment) map of Mrk 67. 139

5.32: Optical greyscale image with HI contours for Mrk 67. 140

5.33: Global velocity profile for Mrk 67. 140

5.34: Integrated HI intensity (0th moment) map of DDO 43. Contour levels are 3.3 (2σ), 5, 7, 9, 11 $\times$ 10^{20} atom cm^{-2}. 141

5.35: Integrated velocity field (1st moment) map of DDO 43. 141

5.36: Optical greyscale image with HI contours for DDO 43. 142

5.37: Global velocity profile for DDO 43. 142

5.38: Integrated HI intensity (0th moment) map of DDO 169. Contour levels are 2.2 (2σ), 5, 7.5, 10 $\times$ 10^{20} atom cm^{-2}. 143

5.39: Integrated velocity field (1st moment) map of DDO 169. 143

5.40: Optical greyscale image with HI contours for DDO 169. 144

5.41: Global velocity profile for DDO 169. 144

5.42: Integrated HI intensity (0th moment) map of DDO 52. Contour levels are 2.5 (2σ), 3, 4, 5, 6, 7 $\times$ 10^{20} atom cm^{-2}. 145

5.43: Integrated velocity field (1st moment) map of DDO 52. 145

5.44: Optical greyscale image with HI contours for DDO 52. 146

5.45: Global velocity profile forDDO 52. 146

5.46: Integrated HI intensity (0th moment) map of NGC 4163. Contour levels are 3.1 (2σ), 5, 7.5, 10, 12.5 $\times$ 10^{20} atom cm^{-2}. 147

5.47: Integrated velocity field (1st moment) map of NGC 4163. 147

5.48: Optical greyscale image with HI contours for NGC 4163. 148

5.49: Global velocity profile for NGC 4163. 148

5.50: Integrated HI intensity (0th moment) map of DDO 131. Contour levels are 2.4 (2σ), 3, 4, 5, 6, 7 $\times$ 10^{20} atom cm^{-2}. 149

5.51: Integrated velocity field (1st moment) map of DDO 131 149

5.52: Optical greyscale image with HI contours for DDO 131. 150

5.53: Global velocity profile for DDO 131. 150

5.54: Integrated HI intensity (0th moment) map of DDO 242. Contour levels are 1.9 (2σ), 3, 4, 5, 6, 7 $\times$ 10^{20} atom cm^{-2}. 151

5.55: Integrated velocity field (1st moment) map of DDO 242. 151

5.56: Optical greyscale image with HI contours for DDO 242. 152

5.57: Global velocity profile for DDO 242. 152

5.58: Integrated HI intensity (0th moment) map of DDO 88. Contour levels are 2.0 (2σ), 3, 4, 5, 6, 7 $\times$ 10^{20} atom cm^{-2}. 153

5.59: Integrated velocity field (1st moment) map of DDO 88. 153

5.60: Optical greyscale image with HI contours for DDO 88. 154

5.61: Global velocity profile for DDO 88. 154

5.62: Integrated HI intensity (0th moment) map of DDO 56. Contour levels are 1.2 (2σ), 1.5, 1.75, 2, 2.25 $\times$ 10^{20} atom cm^{-2}. 155

5.63: Integrated velocity field (1st moment) map of DDO 56. 155

5.64: Optical greyscale image with HI contours for DDO 56. 156

5.65: Global velocity profile for DDO 56. 156

5.66: Velocity width Δv_{50} vs. axial ratio (b/a). 157

5.67: Corrected velocity width (Δv_{50}/sin i) vs. axial ratio (b/a). 157

5.68: HI concentration ($\frac{M(5)_{HI}}{M(2)_{HI}}$) vs. color (U – V). 158

5.69: HI mass $M(2)_{HI}$ vs. HI radius $R(2)_{HI}$. 158

5.70: Average dispersion velocity $\langle \sigma_v \rangle$vs. color (U – V). 159

5.71: Holmberg diameter $R_{26.5}$ vs. .color (U – V) 159

5.72: Optical surface brightness μ_L vs. color (U – V). 160

5.73: HI radius $R(2)_{HI}$ vs. absolute magnitude M_U (log L_U). 160

5.74: HI mass-to-light ($\frac{M_{HI}}{L_U}$) vs. HI surface density $\mu(2)_{HI}$. 161

5.75: HI mass-to-light ($\frac{M_{HI}}{L_U}$) vs. HI mass to total mass ($\frac{M_{HI}}{M_T}$). 161

5.76: Total mass (M_T) vs. luminosity (L_U). 162

A.1: Integrated HI intensity map of DDO 169 Companion. 174

A.2: Velocity field map of DDO 169 Companion. 174

A.3: Global velocity profile of DDO 169 Companion. 175

A.4: Integrated HI intensity map of both DDO 169 and its companion. 175

A.5: Optical image with HI contours of both DDO 169 and its companion. . . 176

A.6: Combined global velocity profiles of DDO 169 and its companion. . . . 176

Abstract of Dissertation Presented to the Graduate School
of the University of Florida in Partial Fulfillment of the
Requirements for the Degree of Doctor of Philosophy.

PROPERTIES AND OBSERVATIONS OF DWARF IRREGULAR GALAXIES

By

CAROLINE ELIZABETH SIMPSON

August, 1995

Chairman: Stephen T. Gottesman
Major Department: Astronomy

Dwarf irregular galaxies, which are small, low mass, asymmetrically shaped systems, are of interest both because of their large numbers and their usefulness as laboratories in which to study large-scale star formation. It is believed that these galaxies form stars through a process known as Stochastic Self-Propagating Star Formation (SSPSF) in which star formation occurs in episodic bursts involving most or all of the galaxy, with the time between starbursts increasing for smaller galaxies. The long quiescent intervals between star-forming episodes ensures that such galaxies spend much of their lives in an optically faint state. In this work, the results of (1) a survey to detect low mass dwarf irregular galaxies, and (2) a study of the atomic hydrogen in eight blue compact dwarfs and eight low surface brightness dwarfs are presented.

To investigate a luminosity function, predicated upon SSPSF, that was postulated to rise steeply at the faint end, we conducted a survey, using the Very Large Array Radio Telescope, that was sensitive to low levels of atomic hydrogen (HI) emission. The survey,

which was sensitive to HI masses as low as $2 \times 10^5\ M_\odot$, detected only four systems: the three catalogued target galaxies and another previously catalogued galaxy. This is in sharp contrast to the large number of systems predicted by the steeply rising luminosity function, and rules out the existence of a large number of low mass galaxies.

The second part of this work examined the HI distributions and kinematics of a sample of 16 dwarf galaxies in varying stages of star-formation. This project investigated the effects of star-formation on the properties of low mass systems. The results of this study indicate that the state of the HI reservoirs in small galaxies is related to the evolutionary stage of the systems with respect to their star-formation histories. Less active galaxies are found to have more diffuse HI distributions, and the ring-like structure associated with some of the systems indicates that the HI has been disrupted. This is in accordance with the SSPSF scenario that predicts an expansion and contraction of the HI in response to the energy produced from a star-formation episode.

CHAPTER 1
INTRODUCTION

Star Formation in Dwarf Irregular Galaxies

Dwarf irregular galaxies are small, low-mass, asymmetrically shaped galaxies. Due to their small sizes and masses, these systems are excellent laboratories for examining star formation and evolution in galaxies as local, rather than global, phenomena. Much work on star formation on a global scale has been done by studying spiral galaxies. These larger, more massive systems have substantial rotation velocities and also undergo differential rotation. It has been shown that only higher rotation velocities support spiral density wave shocks (Strom, 1980), which act as triggers for star formation. As interstellar matter moves through the wave, gas and dust is compressed, causing the collapse of protostellar clouds and initiating a burst of star formation. The differential rotation in spiral galaxies may also spread out regions of star formation, so that the stars are no longer located in the area in which they formed.

In contrast to spiral galaxies, dwarf irregular galaxies (dIrrs) rotate slowly and as rigid bodies (Gallagher and Hunter, 1984, and references therein), and so are not subject to either the spiral density wave shocks or the shearing forces that tend to spread out star-forming regions in larger late-type (spiral) galaxies. The rigid-body nature of the rotation in dIrrs ensures that star-formation regions remain in essentially the same area (in the rotating frame) where they were first triggered; so it is possible to examine star formation in the local environment in which it occurred.

Since dwarf irregular galaxies do not have the rotation velocities necessary to support the gas compression present in larger, spiral galaxies, they must form stars via a mechanism other than density wave compression. It is believed that dIrrs form stars in a process known as stochastic self-propagating star formation (SSPSF) (Searle and Sargent, 1972; Gerola et al., 1980). In this scenario, a galaxy undergoes occasional episodes of very active star formation, interspersed with long quiescent periods of inactivity while the star-formation region "recovers" from the burst. The star-formation bursts occur in "cells"; the size of the cell is independent of the host galaxy (Hunter, 1982), but larger galaxies will have more cells, thus more star-forming regions. Smaller galaxies, with fewer cells, will therefore on average have fewer bursts over a given time, and longer quiescent intervals (Gerola et al., 1980).

In order for star formation to occur, there must be a reservoir of atomic hydrogen (HI) gas present. According to Skillman (1987) and Gallagher and Hunter (1984), the formation of O and B stars will occur only when the surface density of the HI is above a critical minimum column density (number of atoms per unit area), thought to be between 0.5 and 1×10^{21} atoms cm^{-2}. As the stars created during a burst evolve, energy is released into the interstellar medium (ISM), primarily from supernova explosions in the form of supernova winds. This kinetic energy can then cause an expansion in the ISM surrounding the burst as the gas is heated and dispersed, producing a "bubble" in the ISM as the gas is both ionized and pushed outwards (Puche et al., 1992, and references therein). For very low mass systems, such as those we are investigating, the galaxy's mass (i.e. the potential well of the system) may be insufficient to gravitationally bind the expanding gas, and it will escape the system (Dekel and Silk, 1986). For galaxies with enough mass to retain the HI, it is postulated that the gas will expand out, perhaps beyond the edge of the (optically visible) galaxy, and then fall back in, triggering another

star-formation burst once the gas has recollected in the galaxy (e.g. Davies and Phillipps, 1988; Puche and Westpfahl, 1994). The amount and location of HI gas in a galaxy are clues to its past, and possible future, star formation, and therefore to its evolution.

Project Descriptions

In this study, we investigate the large and small scale properties of dwarf irregular galaxies, focussing on the relationship between their HI morphologies and star-formation history. We have completed two observational projects using the National Radio Astronomy Observatory's (NRAO) Very Large Array (VLA) Radio Telescope in New Mexico.[1] The first study is an investigation of the more global properties of dwarf irregular galaxies as a class: we have conducted a search at 21-cm for these gas-rich systems to examine both their overall numbers and their distribution throughout space. The second study investigates the more local process of star formation within these systems, and how star formation can affect the properties and evolution of dwarf galaxies.

HI Survey

The first project involves determining the number and spatial distribution of dwarf galaxies. It has been suggested that a great many of these low-mass systems exist but have not been detected at optical wavelengths due to their intrinsic faintness (Tyson and Scalo, 1988). Only systems undergoing fairly vigorous star formation are easily visible in the optical since it is the luminous, young O and B-type stars that are detected. According to SSPSF, low-mass galaxies will undergo episodes of star formation very rarely, and since the lifetime of the burst ($\sim 10^7$ yr) is short compared to the interval

[1] The National Radio Astronomy Observatory is operated by Associated Universities, Inc., under cooperative agreement with the National Science Foundation.

between bursts predicted for these systems ($\sim 10^9$ yr) (Gerola et al., 1980), there should be many quiescent (and therefore optically hard to detect) dIrrs for each highly visible "active" dIrr. To determine whether this is indeed the case, we have performed a survey for these quiescent dIrrs. Although these objects are faint optically, atomic hydrogen emits at a wavelength of 21-cm, and these galaxies should contain enough HI to make them detectable at this wavelength.

In addition to examining the number density of dIrrs, we have also investigated their spatial distribution. According to the theory of biased galaxy formation (Dekel and Silk, 1986), lower-mass galaxies should be distributed more uniformly through space than high-mass systems. Therefore, dIrrs should be located not only in clusters but also in galactic "voids"; regions where no galaxies are currently observed. We have surveyed three different extragalactic environments in an effort not only to find such galaxies, but also to see whether they are indeed ubiquitous, or if their distribution is as inhomogeneous as that observed for larger, brighter, more massive galaxies.

It has been speculated that dwarf galaxies may be repositories for large amounts of dark matter. Theoretical work by Dekel and Silk (1986) requires dwarf formation within massive envelopes to account for their observed properties. Observational estimates of the mass-to-light ratio (M/L) of dwarf galaxies range from 2 – 10 (Gallagher and Hunter, 1984), with a median value of 5 as reported by Roberts and Haynes (1994). However, a study of binary dwarf systems by Lake and Schommer (1984) results in M/L ratio estimates of 20 – 5000, indicating a large amount of dark or low-luminosity matter. If indeed, dwarf galaxies are reservoirs for dark matter, their spatial density and distribution may provide information not only on galaxy formation and evolution, but also on the existence and location of dark matter. Indeed, Tyson and Scalo (1988) find that if dIrrs with high M/L ratios do follow the steeply-rising radial distribution function they derive

(i.e. the number of galaxies increases as galaxy size decreases), there may be enough of these small systems to provide the mass necessary to close the Universe.

LSBD-BCD Study

Our survey results, and the suggestion that starburst winds can deplete low mass galaxies of their HI gas, led us to initiate a project to investigate more closely the mechanism and evolution of star formation in dwarf galaxies. The bursting nature of the star formation that occurs in dwarf galaxies supports a possible connection between blue-compact dwarfs (BCDs) and low surface brightness dwarfs (LSBDs). LSBD galaxies are rich in HI, optically faint, and undergoing little star formation. BCDs, on the other hand, are distinguished by a small compact region of high surface brightness; they have large amounts of ionized hydrogen (HII) and are undergoing significant star formation. It has been suggested by several authors (Wirth and Gallagher, 1983 and references therein; Davies and Phillipps, 1988) that LSBDs, upon undergoing a burst of star formation, will evolve into BCDs and then back into LSBDs, when the star formation slows or stops as the HI column density falls below the critical threshold necessary to support it.

We have examined the location and kinematics of HI in a variety of dwarf galaxies to investigate this "evolutionary" sequence. We have observed 16 very low mass dwarf galaxies believed to be in varying stages of a star-formation episode to examine the relationship between their HI distributions and their properties. Eight of the galaxies are BCDs, and eight are LSBDs; therefore we are looking at galaxies that are in (or have recently completed) a burst of star formation (the BCDs), and galaxies that are currently quiescent (the LSBDs). In addition, each of the two samples was chosen to cover a range of colors, as indicated by their (B−V) and (U−B) color indices. Since the highly luminous and relatively short-lived O and B-type stars radiate optically in the blue

end of the spectrum primarily, it is believed that bluer galaxies are currently undergoing vigorous star formation, while redder objects are more "quiet." By choosing objects with different color indices within each sample, we are examining galaxies in different stages of star-formation activity. If the properties of dwarf galaxies do indeed evolve as their HI reservoirs contract and expand, we should observe different HI morphologies not only between the two types of dwarf galaxy, but also between those of different color indices. By mapping the location and motion of the HI gas in each of these systems, we are investigating (1) how star-formation episodes affect a galaxy's properties and characteristics; (2) whether the proposed expansion and contraction of the HI gas does indeed occur; and (3) how it affects the star formation and evolution of dwarf galaxies.

In the following study, we present the results from these two projects: an HI survey to detect optically faint dIrrs, and an HI study of a sample of BCDs and LSBDs. A more detailed discussion of the galaxy types, SSPSF, and the properties and evolution of these systems is presented in Chapter 2; and a general discussion of the HI observations is provided in Chapter 3. The HI survey project, including background, observations, data reduction and results, is described in Chapter 4, and Chapter 5 reports in the same way on the BCD-LSBD project. Conclusions and a discussion of the implications from both these projects are presented in Chapter 6.

CHAPTER 2
DWARF GALAXIES

According to Roberts and Haynes (1994), there are three fundamental types of galaxies: elliptical, "classical" spiral, and dwarf. Dwarf galaxies are usually considered to be those galaxies with absolute blue magnitudes (M_B) fainter than approximately –18 or –16. As a class, these systems possess smaller sizes, lower masses, lower luminosities, bluer (B–V) and (U–B) color indices, lower surface brightnesses, lower (total mass) surface densities but higher HI surface densities, and higher ratios of HI to total mass than either elliptical or spiral galaxies (Roberts and Haynes, 1994; Gallagher and Hunter, 1984).

The large number of dwarf galaxies in the Local Group and other nearby galaxy clusters indicate that these small faint systems are probably the most common type of galaxy (Davies and Phillipps, 1988). Estimates of the luminosity function (the number of galaxies per magnitude per cubic megaparsec)[1] for dwarfs both in clusters and in the field indicate that it is rising exponentially (Binggeli et al., 1988 and references therein). Determination of the actual number of dwarf galaxies is difficult due to the severe selection effects imposed by their faint magnitudes (e.g. Tyson and Scalo, 1988). It has been shown that low surface brightness objects are hard to detect optically, and the tight correlation between faint magnitude and low surface brightness ensures that dwarfs tend to be overlooked in optical surveys (Binggeli et al., 1988; Tyson and Scalo,

[1] We use "luminosity function" here in the classical sense; Binggeli (1988) calls this the "luminosity distribution".

1988). Further discussion of the number and space density of dwarf irregular galaxies is presented in Chapter 4.

Type Descriptions

There are three basic types of dwarf galaxy: dwarf ellipticals or spheroidals (dE/dSph), dwarf irregulars (dIrr; these include LSBDs), and blue compact dwarfs (BCD) (Tammann, 1994). Dwarf ellipticals are very low surface brightness systems, containing mostly metal-poor Population II stars and little or no HI gas. Dwarf irregulars are also low-to-intermediate surface brightness systems, but contain Population I stars and possess considerable amounts of HI gas. Blue compact dwarfs, on the other hand, have small areas of high surface brightness and emission lines that indicate the presence of massive (O and B-type) stars. The bright emission regions are therefore identified as HII regions and so these systems are currently undergoing significant star formation.

These three dwarf galaxy types are discussed in further detail below. Although they are not the focus of the present study, a brief description of dEs is included, as it is postulated that these systems may be part of an evolutionary chain linking all dwarf galaxy types (see discussion of system evolution, below).

Dwarf Elliptical Galaxies

The distinction, if any, between dE and dSph is not clear (see Binggeli 1994 and Kormendy 1994 for a recent overview of the controversy), and we will refer here to all such systems as dEs for simplicity. These galaxies possess fairly smooth, elliptical isophotes, and are spheroidal in shape (Davies and Phillipps, 1988; Bothun et al., 1986). Their stellar populations consist mostly of old, Population II stars, and it is thought that most dEs ceased all star formation long ago. However, there is observational evidence of an intermediate-age population for some of the Local Group and Fornax cluster dEs,

indicating that for some of these systems there have been at least two separate episodes of star formation (Davies and Phillipps, 1988; Held and Mould, 1994; Da Costa, 1994; Smecker-Hane et al., 1994). Their metallicities range from 1/3 to 1 times the metallicity of the sun ($Z_{\odot}$), and they contain very little or no HI (Davies and Phillipps, 1988; Hodge 1971).

Dwarf Irregular Galaxies

These systems exhibit irregular, chaotic structure optically. In general they are low surface brightness systems, with both Population II and Population I stars, the latter indicating current star formation activity. Their fractional HI masses are fairly high (about 15% on average according to Roberts and Haynes, 1994), and their metallicities vary from approximately 1/3 to 1/30 $Z_{\odot}$ (Davies and Phillipps, 1988; Bothun et al., 1986). They rotate slowly, with average circular rotational velocities of around 50 – 70 km s^{-1}. Observed rotation curves indicate that these systems often exhibit solid-body rotation over at least the optical part of the galaxy, with little or no differential rotation (Gallagher and Hunter, 1984; Hunter and Gallagher, 1986). This is in sharp contrast to the larger, more luminous spiral galaxies, which have circular velocities of $\geq$ 200 km s^{-1} and exhibit differential rotation over an extensive disk (Gallagher and Hunter, 1984). In general, dIrrs are thought to be essentially pure disk systems (Gallagher and Hunter, 1984; Fisher and Tully, 1981). However, for the smallest, least-luminous dwarf irregulars, the rotation velocity can be equal to or less than the random (turbulent) gas motions ($\sim$10 km s^{-1}), resulting in a fairly disordered velocity field (Lo et al., 1993; Puche and Westpfahl, 1994; Norton and Lo, 1994).

Blue Compact Dwarf Galaxies

Blue compact dwarf galaxies, also known as HII galaxies, are identified by their compact sizes, uv-excesses, and strong emission line spectra, which show strong, narrow, high-excitation lines superposed on a nearly featureless continuum (Kunth, 1989; Thuan and Martin, 1981). Although these systems possess low total luminosities, they contain small regions of high surface brightness from which the emission lines originate. Their spectra strongly resemble those of giant HII regions, and it has been shown that they are undergoing episodes of intense star formation (e.g. Sargent and Searle, 1970; Arp and O'Connell, 1975; French, 1980). They can contain large fractions of HI (Davies and Phillipps, 1988) and often have large HI extents with respect to their optical diameters (Gordon and Gottesman, 1981). They are metal-poor, with metallicities ranging from 1/3 to 1/40 $Z_{\odot}$, although most BCDs have metallicities of about 1/10 $Z_{\odot}$ (Thuan, 1986). II Zw 18, with a measured abundance of 1/40 $Z_{\odot}$, is currently one of the lowest metallicity galaxies known.

Stochastic Self-Propagating Star Formation

In 1970, Sargent and Searle published a study of two blue compact dwarf galaxies, I Zw 18 and II Zw 40, in which they concluded from the observed spectral energy distributions and color indices that either (a) their current star formation rates (SFRs) were much higher than the average rate in the past, or (b) that these galaxies preferentially formed high mass stars. They stated that the former would indicate these systems were young (just beginning to form stars), while the latter implied their initial mass functions (IMFs) differed greatly from that in the solar neighborhood.

In a follow-up paper (Searle and Sargent, 1972), they concluded from the colors and composition of the two galaxies that rather than having a different IMF, the current SFR

greatly exceeds that in the past. If instead the IMF were such that primarily high mass stars were formed at a steady rate over the lifetime of the galaxy, most of the gas would have been converted into elements heavier than helium. This would both exhaust the HI and raise the metallicity of the galaxy. The large amounts of HI and low metallicities of both of these systems precluded this possibility.

Having established the high current SFRs for these galaxies, they then proposed two possible explanations: that the systems are young (as mentioned in the first paper), or alternatively that the star formation had proceeded in extreme bursts separated by long periods of inactivity. These two options were examined by Searle et al. (1973), who used theoretical evolutionary tracks of individual stars to model the UBV colors of model galaxies consisting of aggregations of open clusters. They found that the colors and properties of normal (i.e. non-dwarf) galaxies were consistent with a constant SFR over 10^{10} years. This was not true for the bluest galaxies, which are dwarf systems. If they too had a constant SFR, then they would have to be young in order to produce the very blue colors observed for these systems. However, when they then modelled colors of a population of galaxies of different ages (10^8 to 10^{10} years), the predicted colors did not match the observed colors, and so they determined that essentially all galaxies are of the same approximate age. Therefore, very blue galaxies such as I Zw 18 and II Zw 40 are not young, and so must be forming stars currently at a much greater rate than in the past.

The results from this work led them to propose a method of global star formation in which galaxies undergo periodic "flashes" or bursts of vigorous star formation, followed by long quiescent periods (Searle et al., 1973). They determined that 5 to 10 brief star formation bursts were required to reproduce the very blue colors observed for some dwarf galaxies.

This idea, which became known as stochastic self-propagating star formation (SSPSF), was expanded and refined by several authors, including Mueller and Arnett (1976), who used it to explain the chaotic structure in late-type spirals; Gerola and Seiden (1978) and Seiden and Gerola (1979), who applied it to spiral galaxies; and Seiden et al. (1979), who invoked it to account for the morphological differences between early (elliptical) and late-type (spiral) galaxies. Gerola et al. (1980) discussed SSPSF for dwarf galaxies and found that whereas for larger systems the SFR will be essentially continuous, in dwarf galaxies the global star formation will occur in discrete short-lived bursts.

Mueller and Arnett (1976) formulated a simple model for what they called "self-propagating star formation" (SPSF) and applied it to spiral galaxies. Essentially, they divide a (2–dimensional) galaxy into star-forming boxes; star formation in one box will propagate to neighboring boxes (presumably via expanding gas shells produced by massive stars). After undergoing an episode of star formation, a box is unable to form more stars until after a certain amount of time (known as the regeneration time) has passed. To keep the global star formation from dying out, they also found it necessary to include spontaneous star formation: the chance that a box will form stars without triggering from a neighboring box. A spontaneous level at about 1% of the overall star formation was found to produce the most "typical" spirals. From their models, they determined a regeneration time of about 10^8 years.

In 1978, Gerola and Seiden expanded Mueller and Arnett's model by introducing a finite probability of having a star-forming cell trigger a neighboring cell. This means that star formation will propagate stochastically, and so they called the process "stochastic self-propagating star formation" (SSPSF). For this model, they divide a galaxy into N rings, and each ring into cells of equal area. As they were interested in modeling spiral galaxies, the rings are allowed to rotate differentially. An active (star-forming) cell has a

probability P_{st} of inducing star formation in the next time step in a neighboring cell. After experiencing an episode of star formation, the probability that it will undergo another episode is reduced for a refractory period τ_r, which may be thought of as the time required for the cell to replenish its supply of gas. This probability is not zero but varies over time. The time step used is essentially the time required for some physical process, such as a supernova shock wave, to propagate from one cell to the next, thus (possibly) triggering star formation; it depends on the cell size (i.e. the size of the galaxy and the number of rings) and the propagation velocity of the physical process. In addition to the stimulated probability P_{st}, a probability for spontaneous star formation, P_{sp}, is also included.

In a paper published in 1980, Gerola et al. applied SSPSF explicitly to dwarf galaxies. By modelling SSPSF in galaxies of different sizes, they showed that whereas star formation in larger systems is basically continuous over long times, smaller galaxies undergo a discontinuous, bursting mode of star formation. The reason for this is twofold: (1) the amplitude of the fluctuation in the SFR increases as the size of the galaxy decreases, so that smaller systems are more likely to experience fluctuations large enough to completely halt star formation propagation; and (2) as star formation propagates to neighboring regions, the rate of propagation in a small system can outpace the regeneration of the cells, so that all cells will have undergone star formation too recently to be triggered again.

These are both consequences of the number of cells per galaxy. As the cell size for star formation is chosen to be constant, larger galaxies have more cells, so that at any given time, more cells are both available for star formation and are actually in star formation. Thus a large system will undergo essentially constant star formation over time as the star formation propagates around from cell to cell. Small systems may consist of as few as one or two cells, so that the entire galaxy can be in a state of star formation over

brief periods of time ($\leq 10^8$ years), and such an event can have dramatic consequences on the system as a whole (e.g. Searle et al., 1973). The star formation can then switch off, as mentioned above, and the galaxy will remain in a quiescent state until the cells have a chance to regenerate. Thus under SSPSF, small systems will have short intense episodes of star formation, separated by long inactive periods.

For the models used in their 1980 paper, Gerola et al. found that the star formation mode switched from continuous to bursting for galaxies with radii $\leq$ 10 cells. As they chose galactic radii from 0.4 to 6 kiloparsecs (kpc) and a cell size of 200 parsecs (pc), this translates to galactic radii $\leq$ 2 kpc. Both this and the increase in fluctuation amplitude are illustrated in Figure 2.1, taken from Gerola et al. (1980). Observations of star formation regions in both irregular and spiral galaxies supports the use of a constant cell size. Hunter (1982) finds an average size of 100 pc for all star forming regions, and an average of 180 pc for the three largest HII regions in a galaxy.

Gerola et al. used this bursting mode of SSPSF to explain the large dispersion of properties observed for dwarf irregular galaxies. Small galaxies will experience very large changes in their SFRs over time, which leads to a wide distribution in their physical characteristics. For the small galaxies in their model, Gerola et al. found very large ranges in values of the average SFR, the (B$-$V) and (U$-$B) colors, HI mass to blue luminosity (M_{HI}/L_B), and especially total L_B, which varied by as much as 5 magnitudes over the 2.5 million time period used. These changes come about as a natural consequence of SSPSF.

A refinement to this bursting mode of star formation was proposed by Tosi et al. in 1991 and 1992. By comparing synthetic color-magnitude diagrams and stellar luminosity functions to observations of nearby dwarf irregulars, they found that a "gasping" mode of star formation was required. This consists of long ($\geq$ few $\times$ 10^8 yr) modest star formation interspersed with short ($< 10^8$ yr) quiescent times. As pointed out by Marconi

et al. (1994), this can be viewed as a transition between the continuous SF seen in larger irregulars and the bursting SF predicted for low mass dIrrs in the SSPSF model.

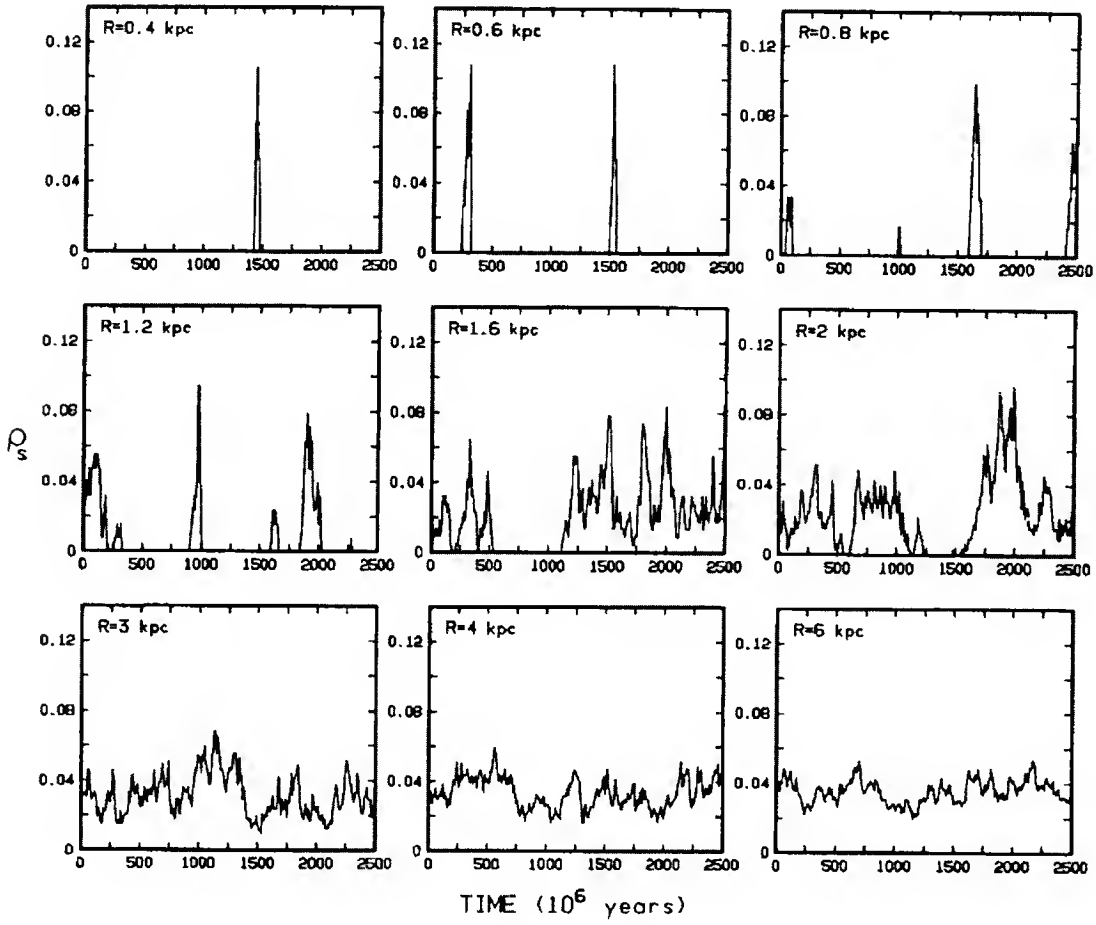

Figure 2.1: Star formation rate (SFR) as a function of time over a 2.6 billion year period for model galaxies having radii between 0.4 and 6 kpc. The SFR is the fraction of cells undergoing star formation per 10 million year time step. Taken from Figure 1 in Gerola et al., 1980.

System Evolution

The relationship, if any, between the three types of dwarf galaxies is not well-understood at the present time, and indeed is one of the motivations for this investigation. One school of thought maintains that these three categories represent different stages in the same evolutionary chain, with dIrrs either evolving through gas loss into dEs (e.g. Lin and Faber, 1983; Dekel and Silk, 1986; Kormendy, 1985), or evolving into BCDs as they undergo a starburst (e.g. Searle et al., 1973; Thuan, 1985), and perhaps then into

dEs (Davies and Phillipps, 1988; Bothun et al., 1986). A second theory claims that the three types are too dissimilar in their properties to ever evolve from one into another, and so we are not seeing the sequential evolution of one galaxy class but parallel evolution of at least two and perhaps three separate classes (e.g. Binggeli, 1994; Bothun et al., 1986; Davies and Phillipps, 1988 and references therein).

Lin and Faber (1983) found that the Local Group dEs had luminosity profiles that could be fit by an exponential, like those for disk systems, and unlike normal (giant) elliptical galaxies, which follow an $R^{1/4}$ law. This led them to propose that dEs were more closely related to dIrrs than ellipticals and that these Local Group dEs may be the remnants of dIrrs that had lost their gas, perhaps through ram-pressure sweeping or tidal stripping. Support for this structural relationship between dEs and dIrrs was offered by Kormendy (1985), whose photometric study showed that the core parameter relations (core radius r_c and central surface brightness μ_0 vs. absolute magnitude M and velocity dispersion σ, and vs. each other) for dEs and dIrrs are essentially the same. In addition to this, it was determined by Skillman et al. (1989) that there is a correlation between oxygen abundance (O/H) and absolute magnitude for dIrrs, and that this correlation is also followed by dEs, consistent with the idea that dEs could be gas-stripped versions of dIrrs. Sandage and Binggeli (1984), in a study of Virgo Cluster dwarf galaxies, also found that dEs have exponential luminosity profiles and that at low surface brightnesses it becomes difficult to distinguish a dE from a dIrr.

Binggeli (1986) examines this stripping hypothesis in some detail. As evidence for it, he quotes the following: (1) the morphology-density relation found in the Virgo Cluster for dwarfs: the number of dEs increases with increasing local density while the number of dIrrs decreases; (2) dEs resemble dIrrs, not Es, in their luminosity profiles and surface brightness-absolute magnitude (μ–M) relations; and (3) small (i.e. low mass

and faint) dIrrs will photometrically resemble dEs if allowed to "fade" over a few billion years. Arguments against this hypothesis include (1) the disparate flattening distributions between dIrrs and dEs (as demonstrated by the different distributions of ellipticities), with the dEs being rounder than dIrrs, and BCDs being in between (Davies and Phillips, 1988 and references therein), (2) that the brighter dEs have higher surface brightnesses than the irregulars (class Sd/Sm) they should be formed from (also Bothun et al., 1986), and (3) the existence of dEs with small bright nuclei (presumably stellar) which are not seen in the class of dIrrs.

Some of these objections can be overcome by invoking different formation mechanisms for bright and faint dEs: few of the faint dEs are nucleated, and since rotation velocities and dispersions decrease with magnitude (i.e. size), extreme dIrrs will not be very flattened (Kormendy, 1985). Hence, as concluded by Binggeli (1986), only the fainter dEs may be candidates for formation from dIrrs via stripping.

In a variation on the gas-loss hypothesis, Dekel and Silk (1986) investigated the possibility that internal mechanisms such as supernova winds could remove mass from these systems. They postulated that dEs lose most or all of their gas as a result of an initial starburst and the subsequent supernovae; and that perhaps the dIrrs are systems which managed to retain some gas (they invoke the presence of dark halos) during this episode. They also mention the possibilities of the dEs passing through a dIrr stage first, undergoing a starburst, and then becoming dEs as they lose their gas; and that perhaps, for the systems with larger potential wells, the initial expansion of the gas after the burst could be followed by infall, thus recollecting in the galaxy and (re)forming a dIrr. They determined that the critical parameter for supernova-driven gas loss is that the virial velocity be less than $\sim$100 km s^{-1}. Since the virial velocity depends on the potential energy of the system, only less-massive galaxies will lose their gas as a result of this process.

In work reported on by Athanassoula (1994), simulations of galaxy formation successfully reproduce dEs with and without nuclei; the difference depends on the mass of the initial gas cloud. More massive clouds are more likely to produce nucleated dEs, in accord with the observations that it is primarily the more luminous (i.e. larger) dEs that are nucleated. The simulations show three scenarios for dE formation and evolution following initial collapse; which case occurs depends only on the mass of the progenitor cloud. Massive clouds become centrally concentrated in both gas and stars (i.e. become nucleated) and then undergo a starburst which uses up most of the gas, leaving a stellar remnant that then undergoes very slow star formation. Intermediate-mass gas clouds follow the same path, but form non-nucleated systems and lose essentially all of their gas; and low-mass gas clouds undergo a re-expansion upon starbursting and can be completely disrupted. It should also be noted that these models do not require dark matter halos.

Another caveat for formation of dEs from dIrrs was pointed out by Thuan (1985). From infrared observations of samples of dEs in the Virgo Cluster and low surface brightness (LSB) dIrrs and BCDs, he found "mutually exclusive" metallicity ranges: 1/3 – 1 $Z_{\odot}$ for the dEs, and 1/30 – 1/3 $Z_{\odot}$ for the LSB dIrrs and the BCDs. He further stated that the difference in the metallicities between the dEs and dIrrs/BCDs precluded the formation of dEs from dIrrs via mass loss unless there was some period of metal-enrichment that occurred either before or during the episode of mass loss.

Bothun et al. (1986) also explored the connection between dEs, dIrrs, and BCDs. Based on 21 cm, infrared photometry, and CCD multicolor surface photometry, they found that dIrrs tend to have bluer colors, lower surface brightnesses, and larger scale lengths than dEs. The BCDs in their sample had intermediate colors and scale lengths closer to those of the dEs. The lower surface brightnesses and larger scale lengths led them to postulate that the dIrrs have much lower surface mass densities than the BCDs

or the dEs. They concluded that letting the dIrrs fade could not produce dEs with the observed properties (especially since the dIrrs already have fainter surface brightnesses than the dEs); but that the BCDs could. Therefore, they proposed that the progenitors of dEs could be BCDs instead of dIrrs; and that dIrrs and dEs evolve in a parallel, not sequential fashion, separated by a difference in surface mass density.

On the other hand, there is quite a bit of evidence that BCDs are dIrrs that are currently bursting, and it is thought that once the burst is over, these systems will appear as lower surface brightness dIrrs. Gordon and Gottesman (1981) showed that the characteristic relations for colors, luminosities, HI masses, and M_{HI}/L ratios for BCDs follow those for normal late-type (Sd, Sdm) systems, with the BCDs extending the relationships at the faint end. Thuan (1985) showed that dIrrs and BCDs have similar underlying older stellar populations and HI contents and offered this as evidence that BCDs are dIrrs in a bursting stage. Tosi (1994) reviewed work that used the SSPSF scenario to construct detailed chemical evolution models of BCDs. The results show that for BCDs, the star formation episodes are short ($\sim 10^6$ yr) and separated by long ($\sim 10^9$ yr) intervals. In order to reproduce the observations that BCDs are more underabundant in oxygen (O) than in some other elements, such as helium (He) and nitrogen (N), they invoked differential galactic winds, which preferentially remove elements from massive stars (such as O) via the explosions of those massive stars. Models with no gas loss result in galaxies that are too metal-rich, and "simple" supernova winds remove all metals equally; therefore differential winds are required to produce BCDs with the appropriate abundances.

However, Staveley-Smith et al. (1992) conclude that some LSBD galaxies (those with high M_{HI}) could become BCDs, but that the two types are probably not related. The evidence for this is that for the same blue luminosity L_B, BCDs have optical diameters that are 2.5 times smaller than dIrrs, and are 2.2 times less massive (in total mass). Both

contain approximately the same HI mass, as found by Thuan (1985), but the LSB galaxies have lower velocity widths. In order to create a BCD from a bursting LSB dwarf, they found that the burst would have to occur preferentially in the high M_{HI} galaxies; that the kinetic energy produced by the supernovae from the burst be transferred very efficiently to the HI gas; and that therefore to retain the gas after the burst, a large dark halo (or some method of increasing the potential well) must be present.

Davies and Phillipps (1988) proposed a sequential evolution involving all three types of dwarf (see also Puche and Westpfahl, 1994; and Westpfahl and Puche, 1994). Their model begins with a very low metallicity dIrr with a large reservoir of HI. Star formation proceeds bimodally, with low mass stars forming essentially continuously over the entire body of the system and high mass stars forming in occasional condensed bursts. During a burst, the galaxy appears as a BCD. The gas is expelled/expanded by the SF burst, but may eventually begin infalling again, which can trigger another burst once the gas has reached the critical surface density (Σ_{crit}) thought to be necessary for star formation (e.g. Skillman, 1987; Kennicut, 1989; further discussion of this will be presented in Chapter 5). This cycle can repeat, with the galaxy appearing alternately as an LSB dwarf and a BCD, until the gas becomes too depleted to support more bursts. The galaxy will then end up as a dE. This sequence explains why dEs are more metal-rich than either dIrrs or BCDs, and they state that since each succeeding burst becomes more centrally concentrated, the stellar population created in the later bursts will be occurring only in the nucleus and so the resultant dE can appear both nucleated and less flattened than the progenitor dIrr.

To conclude, there are indications both for and against the proposition that all three types of dwarf galaxy, dEs, dIrrs, and BCDs, are related. Structural evidence shows similarities between dEs and dIrrs, and BCDs are thought to be dIrrs in a state of vigorous star formation. Whether dEs are formed straight from dIrrs via mass-loss either from

stripping or supernova winds, or whether BCDs represent an intermediate step in this process is not clear. It may be that dEs, dIrrs and BCDs are separate types of systems; or that BCDs are related to either dEs or dIrrs, but not both.

This is the focus of the work that comprises the LSBD-BCD part of this study. We have observed the HI distribution in eight LSBD and eight BCD galaxies. If the proposed evolutionary scheme of dIrr $\rightarrow$ BCD $\rightarrow$ dIrr/dE is correct, then we should see more compact and centralized HI distributions in the (bursting) BCDs than in the (quiescent) LSBDs. This work is presented in Chapter 5.

CHAPTER 3
OBSERVATIONS

The observations of the 21–cm line emission of atomic hydrogen for both the projects that comprise this study were made using the Very Large Array (VLA) Radio Telescope. The VLA, a 27–element interferometer that uses the principle of earth-rotation aperture synthesis, is run by the National Radio Astronomy Observatory, which is operated by Associated Universities, Inc., under cooperative agreement with the National Science Foundation. The nature of 21–cm line emission, a discussion of earth-rotation aperture synthesis, and a general description of the calibration and imaging techniques used to reduce the observations are presented in this chapter.

21–Centimeter Line Emission

The ground state of atomic hydrogen consists of two hyperfine energy levels determined by the orientation of the magnetic dipole moments (or spins) of the electron and the proton that make up the H atom. In the higher energy state, the spins are parallel; they are antiparallel in the lower state. The difference in energy between these two levels is extremely small: 6×10^{-6} eV, which corresponds to a temperature difference (ΔT) of only 0.07 K. A transition between these two states, referred to as a spin-flip transition, will result in the absorption or emission of a photon with a frequency of 1420.405 Megahertz (MHz), or a wavelength of 21.105 cm.

The spin temperature (T_S) of the ISM is $\sim$100 K, and since $\Delta T \ll T_S$, much of the HI is in an excited state. The Einstein probability coefficient, A_{21}, for radiative decay from the upper to the lower energy levels is very low: 2.8689×10^{-15} s^{-1}. Hence the

mean half-life, $t_{\frac{1}{2}} \simeq \frac{1}{A_{21}}$, of the excited state is $\simeq 1.11 \times 10^7$ years (Rohlfs, 1990, p. 225). The rate for collisional excitation or deexcitation is, however, only about 400 years. This means that HI atoms will undergo decay transitions by radiating a photon at 21–cm only once every 1.11×10^7 years; but they will undergo collisional excitation ro deexcitation once every 400 years. Since the collisional rates are so much higher than the radiative decay rate, collisions can establish approximate thermodynamical equilibrium (TDE) populations for the two energy states (Mihalas and Binney, 1981, pp. 484 – 485).

Expressing this in terms of the collisional probability coefficients C_{12} and C_{21}, and the radiative decay probability coefficient A_{21}, we get

$$n_1 C_{12} = n_2(C_{21} + A_{21}) = n_2 C_{21}\left(1 + \frac{A_{21}}{C_{21}}\right). \tag{3-1}$$

As noted above, $A_{21} \ll 1$, and so equation (3-1) reduces to

$$n_1 C_{12} \approx n_2 C_{21}, \tag{3-2}$$

demonstrating that the populations are in approximate equilibrium (England, 1986).

The upper energy level is threefold degenerate since the total spin $\hbar$ can be oriented in three different ways, so that in TDE there will be three H atoms in the upper level for every one in the lower level. This can be shown by the Boltzmann formula:

$$\frac{n_2}{n_1} = \frac{g_2}{g_1} \exp\left(-\frac{h\nu}{kT_S}\right), \tag{3-3}$$

where n_2 and n_1 are the number of atoms in the upper and lower energy states, and g_2 and g_1, representing the degeneracy of each level, are 3 and 1 respectively. The value of $\exp\left(-\frac{h\nu}{kT_S}\right)$ will be close to 1 since T_S in an HI cloud is $\sim$100 K, and so

$$\frac{n_2}{n_1} \simeq \frac{g_2}{g_1} = 3. \tag{3-4}$$

Collisions will provide a population of H atoms in the excited upper-level state and therefore able to produce 21–cm emission upon transition to the ground-level state by

radiative decay. In spite of the infrequency of the radiative decay transition, the large column densities of HI present in galaxies make this "rare" transition detectable, and it is this radiative decay that produces the 21–cm emission observed by radio telescopes.

Emission from a radially moving source (such as a receding galaxy) will be shifted to longer wavelengths due to the Doppler effect, with higher recessional velocities corresponding to longer wavelengths (lower frequencies). In addition to this frequency shift, the width of the emission line will be broadened by any bulk motions (such as turbulence and/or rotation) inherent in the emitting gas, so that the emission from a source with radial motion will be spread across a continuous range of frequencies corresponding to the radial velocities of the emitting gas atoms. This is the essence of spectral line observations: by examining the amount of gas associated with each observed frequency, we can determine the (radial) velocity associated with it and hence examine the kinematics of the gas.

We can calculate the column density N_{HI} of atoms per square centimeter in the lower state along the line of sight for a source by integrating the spin temperature over all frequencies (in units of Hertz):

$$N_{HI} = 3.88 \times 10^{14} \int_0^{+\infty} T_S \tau_\nu \, d\nu, \tag{3-5}$$

where τ_ν is the optical depth. We can recast this equation in terms of the observed brightness temperature T_B by using the transfer equation:

$$T_B = T_S\left(1 - e^{-\tau_\nu}\right). \tag{3-6}$$

As HI regions are usually optically thin (e.g. Mihalas and Binney, 1981, p. 488), $\tau_\nu \ll 1$, and so $T_B \approx T_S \tau_\nu$. Substituting this into equation (3-5) and rewriting in the more usual observational units of velocity rather than frequency, we find the following expression

for the column density associated with a position (α,δ):

$$N_{HI}(\alpha,\delta) = 1.8226 \times 10^{18} \int_{-\infty}^{+\infty} T_B(\alpha,\delta)\, dv, \tag{3-7}$$

with N_{HI} in atoms cm^{-2}, v in km s^{-1}, and T_B in Kelvin. If the material is not optically thin, the calculated column density will be underestimated (England, 1986, p. 22). For an optical depth $\tau_\nu = 1$, equation (3-6) becomes

$$\begin{aligned} T_B &= T_S\left(1 - e^{-1}\right) \\ &= T_S(1 - 0.36788) \\ &= 0.63212\, T_S. \end{aligned} \tag{3-8}$$

Substituting this into equation (3-5), we see that $N_{HI}(\tau_\nu \ll 1) \simeq 0.63212\, N_{HI}(\tau_\nu = 1)$.

The corresponding mass of the HI can be found by integrating this equation over the solid angle subtended by the galaxy and expressing the brightness temperature in terms of the observed flux $S(v)$ (see equation (3-22)) and the distance to the galaxy D:

$$M_{HI} = 2.356 \times 10^5 D^2 \int_{-\infty}^{+\infty} S(v)\, dv. \tag{3-9}$$

For D in megaparsecs (Mpc), S in Janskys (10^{-26}W m^{-2} Hz^{-1}), and v in km s^{-1}, M_{HI} will be in units of solar masses ($1\ M_\odot = 1.989 \times 10^{33}$ gm).

The velocity field of the gas can be determined by calculating the intensity-weighted mean velocity of the gas associated with each position (α,δ). This is done by taking the first moment of equation (3-7) with respect to velocity:

$$\langle v(\alpha,\delta)\rangle = \frac{\int_{-\infty}^{+\infty} T_B(\alpha,\delta)\, v(\alpha,\delta)\, dv}{\int_{-\infty}^{+\infty} T_B(\alpha,\delta)\, dv}. \tag{3-10}$$

The velocity dispersion associated with the gas is then found from the second moment:

$$\sqrt{\langle v^2(\alpha,\delta)\rangle} = \sqrt{\frac{\int_{-\infty}^{+\infty} T_B(\alpha,\delta)\,(v-\langle v\rangle)^2\,dv}{\int_{-\infty}^{+\infty} T_B(\alpha,\delta)\,dv}}\,. \qquad (3\text{-}11)$$

Aperture Synthesis Theory

As the observations for this work were done using the VLA, an earth-rotation aperture synthesis radio interferometer, an overview of aperture synthesis and interferometry are provided in the section below. Good overviews and further references can be found in England (1986), Florkowski (1980), and Christiansen and Högbom (1985), and more thorough discussions in Hjellming and Basart (1982) and Fomalont and Wright (1974). For very detailed information about aperture synthesis with an emphasis on the VLA in particular, the collection of lectures from the Third NRAO Synthesis Imaging Summer School is recommended (1989, *Synthesis Imaging in Radio Astronomy*, eds. R.A. Perley, F.R. Schwab, and A.H. Bridle (ASP Conference Series Vol. 6: PASP)).

The resolving power of a telescope is ideally determined by the diffraction limit $\theta \simeq 1.22\,\frac{\lambda}{D}$, where λ is the wavelength being observed, and D is the aperture diameter of the telescope. For optical wavelength observations, where λ is of the order of a few thousand angstroms (1 angstrom = 10^{-10} meters), this limit is actually set instead by the scintillation of the earth's atmosphere (~0.5 arcseconds) rather than by diffraction. The same is not true for radio astronomy, where the wavelengths observed range from roughly 1 mm to 20 m. In order to achieve the same sort of diffraction-limited resolution as an optical telescope, a radio telescope observing at a wavelength of 1 m would have to have a diameter of 400 km! (Christiansen and Högbom, 1985, p. 7). To overcome this limitation, a method for synthesizing a large

telescope aperture using an array of smaller, discrete antennas has been developed. For thorough discussions of this, good references include Christiansen and Högbom (1985) and Fomalont and Wright (1974). The following brief description follows those given by these authors.

The principle of aperture synthesis can be demonstrated by considering a conventional (filled-aperture) telescope as being divided into N elements. Each of these elements measures the emission from a source, and the signals from all of these elements are then brought together and summed at the antenna focus. In terms of measured voltages, this sum can be expressed as

$$V(t) = \sum_{0}^{N} \Delta V_i(t). \tag{3-12}$$

Since the measured power is proportional to the time-averaged voltages,

$$\langle P \rangle \propto \langle \left(\sum \Delta V_i \right)^2 \rangle = \sum \langle (\Delta V_i \cdot \Delta V_k) \rangle, \tag{3-13}$$

it can be seen that this is just the sum of the products of the individual voltages (ΔV_i and ΔV_k) from all possible pairs of elements. Thus a filled-aperture telescope can be synthesized by only two antennas, placed at all possible positions i and k. In practice, not all positions of i and k need to measured, since combinations of (i, k) that correspond to the same spacing and orientation are redundant. Aligning the baseline between the two antennas along the direction of the earth's rotation allows the aperture to be "filled" over time, as the apparent orientation of the two antennas with respect to the source being observed (i.e. their projected baseline as "seen" by the source) changes due to the earth's rotation. This is known as earth-rotation aperture synthesis.

A two-element interferometer achieves high resolution by correlating the signals of two widely separated antennas observing the same source. The output from an interferometer provides information about both the intensities and positions (relative to

the pointing direction) for all sources in the antennas' beams. The intensity distribution of a radio source can be thought of as the superposition of many components of an electromagnetic field wave, where these components are of different sizes, locations, and orientations. The correlation of the electromagnetic field at two different locations can be described by the spatial coherence function, and the visibility function is a combination of this and the normalized reception pattern of the interferometer elements (the primary beam) (Clark, 1989). It can be shown (e.g. Clark, 1989; Fomalont and Wright, 1974) that these components and the brightness distribution are Fourier transforms of one another, and so by measuring enough of these various components (the visibility function) and applying a Fourier transform, it is possible to recover the intensity distribution of the source being observed. A pair of antennas, acting as an interferometer, samples these different Fourier components as the projected baseline between them (as seen by the source), changes in length and orientation as the earth rotates. More non-redundant baselines mean more components that can be measured and more complete recovery of the intensity distribution. The VLA, with 27 antennas arranged in a Y-shape, is a multiple-interferometer instrument consisting of 351 pairs of antennas (the number of pairs is equal to $\frac{N(N-1)}{2}$, where N is the total number of antennas), and so is able to measure, at any instant, 351 Fourier components (Hjellming and Basart, 1982).

The signal from a two-element interferometer can be written as

$$V_{obs}(u,v) = \int_{-\infty}^{+\infty}\int_{-\infty}^{+\infty} I_{obs}(x,y)e^{-2\pi i(ux+vy)}\,dx\,dy \qquad (3\text{-}14)$$

where V_{obs} is the observed complex visibility function, I_{obs} is the observed brightness distribution, (x, y) are east and north displacements from the pointing center in the tangent plane of the sky, and (u, v) are the east and north components (spacings) of the projected baselines. Thus, the complex visibility corresponding to a particular baseline measures a

single Fourier component of the observed brightness distribution (England, 1986, p. 25). Since V_{obs} and I_{obs} are Fourier transforms of one another, a small extent in the (x, y) plane corresponds to a large extent in the (u, v) plane according to the Similarity Theorem (Bracewell, 1965, p. 101). Thus short baselines will measure large-scale structures, and long baselines will measure small ones (i.e. have high resolutions).

As the visibility function and the brightness distribution are related by a Fourier transform, equation (3-14) can be inverted to obtain I_{obs}:

$$I_{obs}(x,y) = \int_{-\infty}^{+\infty}\int_{-\infty}^{+\infty} V_{obs}(u,v)e^{[+2\pi i(ux+vy)]}\,du\,dv\ . \tag{3-15}$$

It should be noted here that I_{obs}, the observed distribution, is actually the convolution of the true brightness distribution and the synthesized beam (synthesized antenna power pattern):

$$I_{obs}(x,y) = I_{true}(x,y) * B(x,y)\ , \tag{3-16}$$

where $B(x, y)$ is the synthesized beam and the $*$ denotes convolution.

For spectral line observations such as are done to observe the 21–cm emission from hydrogen (H), the observed frequency range (the bandwidth) is divided into a number of independent, contiguous narrow-frequency range channels. This is done by introducing a delay, τ_j, into the signal path which destroys the coherence of the signal except for a specified range centered on a given central frequency, ν_j. The frequency range being observed can then be changed by changing the delay (England, 1986). Adding the delay is equivalent to multiplying the visibility function by a complex exponential:

$$V_{obs}(u,v,\tau) = \int V(u,v,\nu)e^{2\pi i\nu\tau}\,d\nu\ . \tag{3-17}$$

Once again, we have a Fourier transform pair, this time in delay τ and frequency ν (Clark, 1989). The expression for the complex visibility (equation 3-14), integrated over

the bandwidth now becomes:

$$V_{obs}(u,v,\tau) = \int\int\int I_{obs}(x,y,\nu)F(\nu)e^{-i[2\pi\nu\tau+2\pi\nu(ux+vy)]}\,dx\,dy\,d\nu\ , \qquad (3\text{-}18)$$

where $F(\nu)$ is the frequency bandpass function (Hjellming and Basart, 1982; England, 1986). Since the delay is introduced into the signal from first one antenna and then the other, the resultant lags are both positive and negative. This symmetry allows us to ignore the imaginary part of the complex visibility function. Taking the Fourier transform of the real part of equation (3-18) with respect to τ, and integrating with respect to first τ and then ν, we finally get:

$$\int_{-\infty}^{+\infty} Re\{V_{obs}(u,v,\tau)\}e^{i2\pi\nu\tau}d\tau = \int\int I_{obs}(x,y,\nu)\,F(\nu)\,e^{-i2\pi\nu(ux+vy)}\,dx\,dy\ . \qquad (3\text{-}19)$$

This is the visibility function at a frequency determined by the Fourier transform on τ and contains all the information necessary to map the source at frequency ν (Hjellming and Basart, 1982). It is only necessary to calibrate the bandpass function $F(\nu)$ by observing a sufficiently strong continuum source, i.e. one whose intensity doesn't vary appreciably over the (narrow) range of frequencies included in the bandpass.

As a final note in this discussion of interferometry, it should be pointed out that there are two "resolutions" associated with an interferometer array: that set by the diameter of the individual antennas, and that set by the size of the synthesized aperture of the entire array. The first, known as the primary beam, sets the effective field of view for the radio observations, and is usually defined as the half-power beamwidth of the antenna, $\Theta_{\rm HPBW}$. For the VLA antennas, which are 25 m in diameter, this is approximately 1.5 $\lambda_{\rm cm}$, recalling that the resolution $\propto \lambda/D$. For observations at 21-cm, this means that the sensitivity of the antenna response drops to one-half at about 15′ (arcminutes) from the pointing center, resulting in a 30′ field of view.

The synthesized resolution determines the final spatial resolution of the observations and is a function of the lengths of the various baselines of the interferometers making up the array. The VLA's antennas are moveable, and can be arranged in four different-sized configurations, from compact to extended. The most compact, the D-array configuration, has a maximum baseline length of 1.03 km and a synthesized beam of approximately 45″ (arcseconds), while the most extended, the A-array, has a maximum baseline of 36.4 km and a synthesized beam of approximately 1.5″.

Since the surface brightness sensitivity of a radio telescope goes as the inverse of the solid angle of the beam, there is a trade-off between resolution and sensitivity that must be taken into account when planning observations. The flux density detected by a radio telescope can be written as

$$S = \int B P_n \, d\Omega \,, \tag{3-20}$$

where B is the source brightness and P_n is the normalized antenna power pattern. Rewriting B in terms of the brightness temperature

$$B = \frac{2k}{\lambda^2} T_B \tag{3-21}$$

and substituting this into equation (3-20), we find:

$$S = \frac{2k}{\lambda^2} \int T_B P_n \, d\Omega \,. \tag{3-22}$$

The minimum detectable flux density therefore depends on the minimum detectable change in the temperature T:

$$\Delta S_{min} = \frac{2k}{\lambda^2} (\Delta T) \int P_n \, d\Omega \,. \tag{3-23}$$

The minimum detectable change in temperature, ΔT, depends on the system temperature T_{sys}, the observed bandwidth $\Delta\nu$, and the integration time t:

$$\Delta T \propto \frac{T_{sys}}{\sqrt{\Delta\nu t}} \,. \tag{3-24}$$

Integrating equation (3-23) over the beam solid angle Ω_B and rearranging, we find

$$\frac{\Delta S_{min}}{\Omega_B} \propto \frac{\Delta T}{\lambda^2} . \tag{3-25}$$

From this, it can be seen that at a given wavelength, a larger (synthesized) beam can detect smaller changes in T. Therefore, although the largest configuration (the A-array) provides the best resolution, the most compact (the D-array) provides the best sensitivity to low levels of broad emission.

Imaging

As discussed above, a radio interferometer observes the complex visibility function corresponding to a source's brightness distribution. Once these visibilities have been recorded, they must be corrected for instrumental effects (calibrated) and then Fourier transformed to produce images (maps) of the intensity distribution of the source. These images are actually of the convolution of the true brightness distribution and the synthesized beam (cf. equation (3-16)); and thus reproduce the true brightness distribution the beam must be deconvolved from the images. Brief descriptions of each of these steps in the reduction of the data are given below.

Calibration

As in any observations, a method of detecting and correcting for instrumental effects is needed. At the VLA, this is done by observing a primary (or flux) calibrator, as well as secondary (or phase) calibrators and using them to calibrate the amplitude and phase response of the array. The amplitude response of the antennas can vary from antenna to antenna and also over time, resulting in inaccurate flux determinations. The two antennas of an interferometer pair, when pointing in the same direction, should have relative phase offsets (after inclusion of the delay) of zero; any deviation of the phase from

zero is analogous to a slight change in the pointing position of the pair, and a consequent decrease in the amplitude response as the source moves away from the beam center.

The flux calibrator is a very strong source with a known, stable flux, and the phase calibrators are sources with known fluxes and accurately determined positions. These calibrators are used to adjust the system response to correct for any instrumental instabilities that might occur in amplitude or phase over the time of the observations. At 21–cm, the array response should be calibrated every 30 – 40 minutes during the observing run to ensure that the system's phase and amplitude responses are known as a function of time.

In spectral line observations, the signal is divided into n channels of narrow frequency width ($\Delta\nu/n$). One of these channels, called channel zero, is a pseudo-continuum channel consisting of the average signal from the inner three-quarters of the entire bandpass and is therefore a broadband channel. Since the array sensitivity is proportional to the inverse of the observed frequency range (equation (3-24)), the sensitivity in channel zero is much greater than for the individual narrow band channels: $\sim$7x for 64 channels, and $\sim$10x for 128. This increase in sensitivity allows for better calibration, so the amplitude and phase calibrations are determined using channel zero and then applied to the spectral line channels.

As a first step in the calibration, the individual data for both calibrators are examined for any obvious problems such as interference. Each data point, or visibility, corresponds to the signal from one antenna pair over one integration time (usually between 30 and 120 seconds). The redundancy present in the large data sets produced during VLA observations means that discrepant data can safely be discarded without degrading the overall quality of the observations. Once this initial editing is done, the flux of the primary calibrator (which is

assumed to have a known value) is calculated for the center frequency being observed.

Once the flux of the primary calibrator has been established, the antenna gain (amplitude and phase) solutions for the array as a function of time can be determined. We can approximate the baseline-based complex gain $G_{ij}(t)$ by

$$G_{ij}(t) = a_i(t)\, a_j(t)\, e^{i(\phi_i(t)-\phi_j(t))} + \varepsilon_{ij}\,, \tag{3-26}$$

where $a(t)$ is an antenna-based amplitude correction normalized so that $\Sigma a_i(t) = 1$, $\phi(t)$ is an antenna-based phase correction normalized so that $\Sigma\phi_i(t) = 0$, and ϵ_{ij} are the closure errors from the gain solutions (Fomalont and Perley, 1989; Martin, 1986). The smaller the closure errors, the better the approximation of the complex gain $G_{ij}(t)$ is.

In practice, calibrating is an iterative process wherein one tries to minimize the closure errors. The results of a calibration run are examined, baselines producing large closure errors are discarded, and the calibration is repeated. This continues until the closure errors are at or below a level deemed acceptable. For these projects, amplitude errors below about $10 - 15\%$ and phase errors below about $8 - 10$ degrees were usually achieved. These errors correspond to approximately a 5σ level for most of the calibrators used.

After determining a satisfactory gain solution for the array, the fluxes of the phase calibrators are determined using the flux calibrator, and the calibration is applied to the entire dataset, including the source data. This is usually done using a running boxcar average over entire set of the observations, which usually consist of alternating scans of the phase calibrator(s) and the source(s). However, for some sources observed for the BCD-LSBD project, a two-point interpolation was used instead of a boxcar averages. This was done when the observation scans for a source were widely separated in time to increase coverage of the (u, v) plane, thus ensuring projected baselines of many lengths.

In those cases where the data consisted of two sets of observations of the same source done hours apart, the calibration interpolation was done separately for each observation.

Recall that all this calibration has been done using the channel zero data set. The calibration can now be applied to the line data set, which consists of a number of narrow frequency channels. The last step in calibration is to correct for any variation in the instrumental response across the frequency bandwidth observed; i.e. any variations from channel to channel. Since the flux calibrator has been chosen to have a constant flux across the bandwidth, any variations in flux are due only to the response of the instrumental bandpass. A bandpass correction is calculated by dividing the line data set for the flux calibrator by the channel zero data set. The bandpass correction in amplitude and phase is then applied to the line data for the source.

Imaging

Once the data are calibrated, an image, or map, of the source's brightness distribution can be obtained by Fourier transforming the visibility data set (cf. equation (3-15)). As the data sets involved in spectral line interferometry are very large, a Fast Fourier Transform (FFT) is used rather than a Direct Fourier Transform (DFT). The FFT, which performs the transform on data that has been gridded first, requires computational times proportional to $N_x N_y log(N_x N_y)$, where $N_x N_y$ is the size of the image in pixels. The DFT however, which evaluates the transform at each individual data point, requires times proportional to $N_x N_y N_{uv}$, where N_{uv} is the total number of visibilities (data points) in the data set. Since this number can be on the order of hundreds of thousands for VLA data, the computational time for a DFT becomes prohibitive. Therefore, although gridding the data produces undesirable artifacts in the images (aliasing), the FFT is the preferred method of transforming the data (Hjellming and Basart, 1982).

In order to use an FFT, the data must be gridded into an N_x by N_y complex array, where N_x and N_y are powers of two. However, first the data is smoothed (via convolution in the (u, v) plane) to suppress aliasing and so that it can be uniformly sampled at the grid points. Unsampled regions are assigned a value of zero, which introduces extensive sidelobes into the synthesized beam, producing what is known as the "dirty beam". To provide good sampling, the cell size (pixel size) for the images should be chosen so that there are approximately 3 – 4 cells per synthesized beam (Hjellming and Basart, 1982; England, 1986).

The application of the FFT to the gridded complex visibility results in what is known as a "dirty" image: this is the source intensity distribution convolved with the dirty beam (cf. equation (3-16)). The dirty beam is the Fourier transform of the sampling function. For spectral line data, a cube of dirty images with one image for each frequency channel is produced; the three axes are right ascension, declination, and frequency or velocity. These images contain not only the emission from the line being observed (i.e. 21–cm), which is frequency dependent and so varies from channel to channel, but also continuum emission from "background" resolved or unresolved point sources that is continuous across all the channels. The continuum emission is subtracted out, usually by subtracting the average of several channels at each "end" of the cube that are known to contain only continuum emission. This results in a cube containing only the line emission from the source being observed.

Once the continuum emission has been subtracted, the images must be corrected for the distortions introduced by the dirty beam. This is done using a CLEAN algorithm, originally developed by J. Högbom and modified by B. Clark (England 1986, and references therein; see also Florkowski, 1980). In essence, the CLEAN algorithm operates by centering the (dirty) synthesized beam pattern on the peak emission point in an image,

convolving the beam with a point source containing some specified fraction of the peak emission (usually 0.1, or 10%), and subtracting the result from the image. This is repeated iteratively until the peak emission reaches a specified level, usually one or two times the r.m.s. noise on the image. The location and amount of flux subtracted is kept track of, and these components are then convolved with the "clean" beam (usually an elliptical gaussian fitted to the primary response of the dirty beam) and added back into the image. Since the clean beam does not have the extended sidelobes of the dirty beam, this procedure removes such artifacts as well as secondary grating responses from the image.

The calibrated, continuum subtracted, and CLEANed data cube is now ready for any analysis judged necessary and/or useful. Integrating the cube in velocity produces a "zeroth" moment map of the column density (see equation (3-7)); taking the first moment with respect to velocity results in a moment map of the velocity field (equation (3-10)); and taking the second moment results in a moment map of the velocity dispersion (equation (3-11)). These moment maps can be analyzed to determine the location and amount (mass) of HI, as well as its large-scale motions such as rotation.

The data for both projects done for this study were obtained and reduced in accordance with the general methods outlined above. Specifics for the survey project are discussed in Chapter 4, and those for the BCD-LSBD project in Chapter 5.

CHAPTER 4
HI SURVEY PROJECT

Introduction

Although dwarf galaxies are thought to be the most numerous type of galaxy, there are many indications that they are underrepresented in current surveys. Optical surveys tend to miss objects that are of small optical extent and/or of low surface brightness, with this bias increasing at greater distances. Hence, compact but high surface brightness systems as well as large but low surface brightness systems may not be detected (e.g. Binggeli et al., 1988; Davies and Morgan, 1994). Dwarf galaxies, which are both small *and* generally of low surface brightness, tend to suffer strongly from these selection effects.

Observations of dwarf irregular galaxies in the Virgo cluster and in the field indicate that the luminosity function for dIrrs is flat or even possibly decreasing (Sandage et al., 1985; Tammann, 1985; Binggeli et al., 1990). Tyson and Scalo (1988) state that this observed turnover at $M_B \geq -14$ in the magnitude distribution for dIrrs is due not to an inherent decrease in the number of galaxies at fainter magnitudes, but is the result of a combination of selection effects due to limiting apparent surface brightness and angular size. They further state that these effects will be more severe for galaxies that are undergoing sporadic bursts due to SSPSF.

As pointed out by Searle et al. (1973), one of the implications of SSPSF is that a galaxy will spend only a small fraction of its time in a bursting phase, when it will be optically bright due to the large numbers of luminous O and B stars being formed. This means that a galaxy will spend most of its time in a quiescent state, when it will be

optically much less visible due to the lack of luminous (and therefore short-lived) stars. Smaller, less massive galaxies, which burst less frequently, will spend even more time in a quiescent stage, making them even less likely to be detected at optical wavelengths. Therefore, the bursting systems are just a very small part of a much larger, optically faint population of galaxies.

This suggestion that small galaxies spend only a small fraction of their lives in an optically visible state led Tyson and Scalo (1988) to postulate that existing catalogs, based on optical observations, were missing most of this presumed faint parent population. In order to predict the "true" number of dwarf galaxies, they used the SSPSF scenario to model starbursts in a sample of 10^5 dwarf galaxies. They assumed a power law frequency distribution of galaxy sizes (radii) of the form

$$f(r) \propto r^{\gamma} , \qquad (4\text{-}1)$$

so that γ is now the variable of interest to be determined.

By stochastically sampling and then applying optical selection effects (apparent magnitude, surface brightness, and angular size) to their parent population (undergoing SSPSF), they created a simulated catalog that could be compared to a real catalog of dIrrs based on actual observations. They then adjusted the parameters for their model parent population until the simulated catalog most closely matched the real catalog of galaxies, so that they felt confident that their modelled parent population was an accurate reflection of the true (postulated) parent population represented by the observed catalog. They found the best fit for a value of $\gamma = -4.2 \pm 0.2$, so that the "true" frequency distribution of galaxy sizes is

$$f(r) = K_r r^{-4.2} , \qquad (4\text{-}2)$$

where K_r is a normalization constant.

This frequency distribution represents a luminosity function for dwarf irregular galaxies that rises steeply for smaller (i.e. fainter) galaxies. (See Figure 4.1, below).

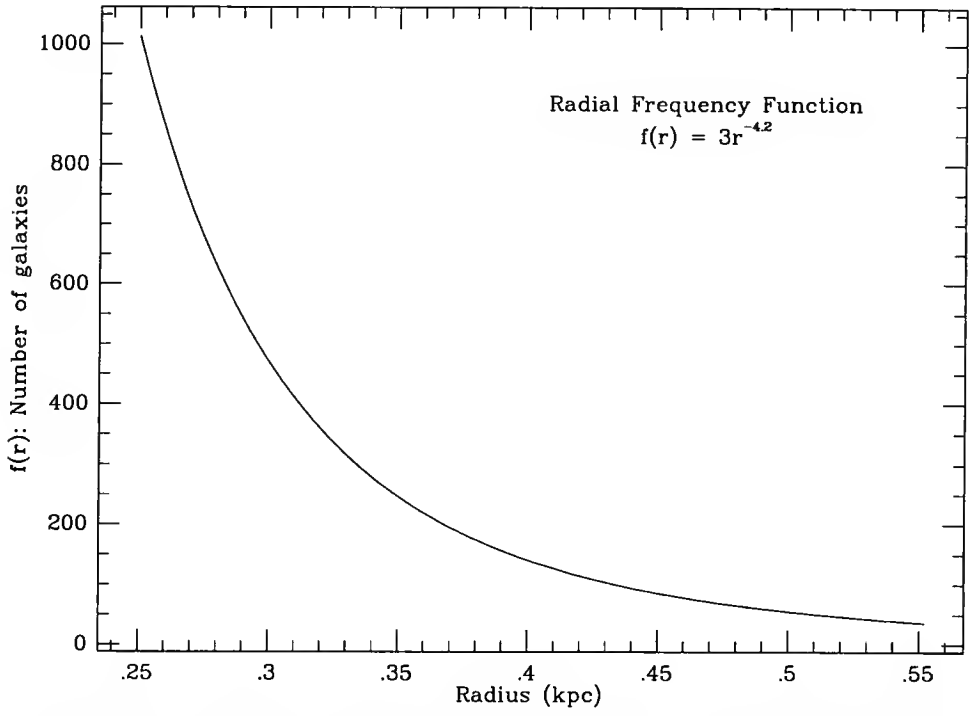

Figure 4.1: Radial frequency function determined by Tyson and Scalo (1988).

By integrating this function over all galaxy sizes,

$$n = \int f(r)\,dr = \int_{r_{min}}^{r_{max}} K_r\, r^{-4.2}\,dr$$

$$= \frac{K_r}{3.2}\,(r_{min})^{-3.2} \quad \text{for } r_{max} \gg r_{min}\,, \tag{4-3}$$

where K_r was determined to be 3 for a space density n in Mpc^{-3}, if r is in kpc. From this, Tyson and Scalo estimated that the space density n of galaxies could range from 10 to 160 galaxies per cubic Mpc for assumed minimum radii of 0.5 and 0.2 kpc, respectively. They further speculated that if dwarf irregular galaxies contain appreciable amounts of dark matter as indicated by some observations (Lake and Schommer, 1984; Sargent and

Lo, 1985), then these galaxies could exist in high enough numbers to provide enough mass to close the universe: $\Omega_{dwarf} = \frac{\rho}{\rho_{crit}} \rightarrow 1$.

In their paper, Tyson and Scalo assumed a constant space density for dIrr galaxies: their simulated sample was distributed evenly throughout space. This uniform distribution is contrary to that observed for brighter galaxies, which exhibit "clumping" on several scales. Normal (non-dwarf) galaxies are clustered on both small and large scales. They tend to occur in groups such as our Local Group; and in clusters such as Virgo. In turn, these groups and clusters form larger and larger groups and clusters (superclusters) as one looks on larger and larger scales. The large scale structure of the universe is a complex network of what appears to be intersecting "bubbles", with galaxies distributed preferentially along the surfaces of bubbles enclosing large voids where few or no galaxies have been found.

In an effort to explain this large-scale structure in the distribution of bright galaxies, the concept of biased galaxy formation was introduced. Biased galaxy formation proposes "large-scale segregation between luminosity (= luminous galaxies) and mass (= dark matter)" (Binggeli et al., 1990, p. 42): mass is postulated to be uniformly distributed throughout space, but luminous matter (bright galaxies) does not follow the mass distribution, being clustered instead.

In 1986, Dekel and Silk, using cold dark matter biasing, developed a model showing that galaxies that form from small amplitude fluctuations ($\sim 1\sigma$) in the mass distribution will become dwarf galaxies, whereas normal (bright) galaxies form preferentially from large ($\sim 2 - 3\sigma$) deviations. Therefore they proposed that dwarf galaxies will trace the underlying mass distribution more closely than the brighter normal galaxies. This lack of clustering for smaller less-massive galaxies implies that they will be found not only in galaxy groups and clusters, but also in the voids.

Project Description

In order to examine the validity of Tyson and Scalo's luminosity function (1988), we initiated and carried out a search for this large population of quiescent dwarf galaxies. Although these objects are optically faint, they contain large amounts of HI gas which make them "bright" at the radio wavelength of 21–cm. We therefore conducted a 21-cm wavelength survey of three separate areas (fields) using the VLA. Although not subject to the strong selection effects that bias optical surveys, HI surveys are sensitive to the amount of flux, and so are subject to a flux bias. Since the "surface density" of the atomic hydrogen (i.e. the column density N_{HI}; see equation (3-7)) and therefore the HI mass (see equation (3-9)) is a function of the flux, HI surveys are subject in essence to a gas mass selection effect. These surveys will miss objects with either low HI contents, such as dEs, and/or objects with low column densities of HI.

Number Density

Using the radial frequency distribution found by Tyson and Scalo (1988) (equation (4-2) above), we were able to predict the number of galaxies we should detect within the volume of space encompassed by the primary beam of the VLA in the following manner.

The total number, N, of galaxies with radii greater than r_{min} within a volume V can be written as

$$N = \int_V \int_{r_{min}}^{r_{max}} f(r)\, dr\, dV, \tag{4-4}$$

where $f(r)\, dr$ is Tyson and Scalo's radial distribution function for galaxies (equation (4-2)). The volume element dV over a distance interval from s to $(s + ds)$, subtending a solid angle ω, is

$$dV = \omega\, s^2\, ds\,. \tag{4-5}$$

(For an instrument such as the VLA, ω is just the solid angle of the primary beam; see the section on Observations, below.) Since the detectable HI mass is a function of the distance (equation (3-9)), the survey volume is also a function of the HI mass. Lower mass galaxies can only be detected in nearby volumes, so that the effective volume searched for lower mass systems is smaller than that for higher mass systems. When predicting the number of galaxies we expected to see, we had to take this dependence of the volume on the HI mass into account. The minimum detectable HI mass, Mh_{min}, is

$$Mh_{min} = k_h \, s^2 \,, \tag{4-6}$$

where

$$k_h = 2.356 \times 10^5 \int F_{min} \, dv \,. \tag{4-7}$$

F_{min} is the minimum acceptable flux for a detection, and dv is the velocity width in km s^{-1} of one channel.

Equation (4-6) can be rewritten in terms of the total mass, M_T, rather than the HI mass by using the empirical relation

$$M_T = 5.36 Mh \tag{4-8}$$

determined by Tyson and Scalo from their catalog of observed dwarf galaxies. Hence, we now have

$$M_{T(min)} = ks^2 \,, \tag{4-9}$$

where the constant k has become $5.36 \times k_h$:

$$k = 5.36 \times \left(2.356 \times 10^5\right) \int F_{min} \, dv \,. \tag{4-10}$$

Rewriting equation (4-6) in terms of s as a function of $M_{T(min)}$,

$$s = \left(\frac{M_{T(min)}}{k} \right)^{\frac{1}{2}} \tag{4-11}$$

and differentiating this with respect to M_T, we find the following expression for ds as a function of $M_{T(min)}$:

$$ds = \frac{1}{2k^{\frac{1}{2}}} \left(M_{T(min)}\right)^{-\left(\frac{1}{2}\right)} dM_{T(min)} \,. \tag{4-12}$$

We can now write the volume element as a function of the minimum detectable (total) mass M by substituting equations (4-11) and (4-12) into the expression for dV (equation (4-5)):

$$\begin{aligned} dV_m &= ws^2 ds \\ &= \frac{\omega}{2k^{\frac{3}{2}}} \left(M_{min}\right)^{\frac{1}{2}} dM_{min} \,, \end{aligned} \tag{4-13}$$

where we have dropped the subscript T for clarity. So the total number N of galaxies with radii between r_{min} and r_{max} within a volume V becomes

$$\begin{aligned} N &= \int_V \int_{r_{min}}^{r_{max}} f(r)\, dr\, dV_m \\ &= \frac{\omega}{2k^{\frac{3}{2}}} \int_{M(s_{min})}^{M(s_{max})} \int_{r_{min}}^{r_{max}} f(r)\, dr\, \left(M_{min}\right)^{\frac{1}{2}} dM_{min} \,. \end{aligned} \tag{4-14}$$

The limits for the volume integration, $M(s_{max})$ and $M(s_{min})$ are the minimum detectable total masses at the maximum and minimum distances surveyed. These quantities are found from equation (4-9) above.

Because there is a relationship between the mass and the radius of a galaxy, we must rewrite the radial distribution $f(r)\, dr$ as a function of mass ($f(M)\, dM$) before evaluating this integral. To do this, we need a relation between the radius and mass of a galaxy. Tyson and Scalo, again based upon their catalog of observed dwarfs, found that

$$M(r) = K_M r^q \,, \tag{4-15}$$

where $\log(K_M) = 8.06 \pm 0.15$ and $q = 1.82 \pm 0.2$ for M in solar masses and r in kpc. Solving for r,

$$r = \left(\frac{M}{K_M}\right)^{\frac{1}{q}}, \tag{4-16}$$

and differentiating with respect to M, we obtain the following expression for dr:

$$dr = \frac{1}{q(K_M)^{\frac{1}{q}}} M^{\left(\frac{1}{q}-1\right)}. \tag{4-17}$$

Substituting these expressions for r and dr into the radial distribution function (equation (4-2)) allows us to transform

$$\int f(r)dr = K_r \int_{r_{min}}^{r_{max}} r^{\gamma}\, dr \tag{4-18}$$

to

$$\int f(M)\, dM = \frac{K_r}{q(K_M)^{\frac{\gamma+1}{q}}} \int_{M_{min}}^{M_{max}} M^{\left(\frac{\gamma+1}{q}-1\right)} dM\,. \tag{4-19}$$

Evaluating the integral for $f(M)\ dM$ in the limit $M_{max} >> M_{min}$ allows us to find $f(M)$ as a function of M_{min}:

$$\int f(M)\, dM = -\frac{K_r(\gamma+1)^{-1}}{(K_M)^{\frac{\gamma+1}{q}}} (M_{min})^{\frac{\gamma+1}{q}}\,; \tag{4-20}$$

which is the number of galaxies per cubic Mpc with masses greater than M_{min}. Using this result, we can now write the integral in equation (4-14) completely as a function of M_{min}:

$$N = -\left(\frac{\omega K_r}{2k^{\frac{3}{2}}}\right) \frac{(\gamma+1)^{-1}}{(K_M)^{\frac{\gamma+1}{q}}} \int_{M(s_{min})}^{M(s_{max})} (M_{min})^{\frac{\gamma+1}{q}+\frac{3}{2}}\, dM_{min}\,. \tag{4-21}$$

The integration limits $M(s_{min})$ and $M(s_{max})$ were determined from

$$\begin{aligned} M &= ks^2 \\ &= \left[5.36 \times \left(2.356 \times 10^5\right) \int F_{min}\, dv\right] s^2, \end{aligned} \tag{4-22}$$

where F_{min} for this project was defined to be 5.12 times the r.m.s. noise (σ) on a single channel map[1]. For the estimated values of the observational parameters σ, the single channel width dv, and s_{min} and s_{max}, we used σ = 0.6 mJy, dv = 41 km/s, and s_{min} and s_{max} are 2.5 and 53 Mpc, respectively. We therefore find that

$$M_T(s_{min}) = 9.95 \times 10^5 \, M_\odot \text{ and}$$

$$M_T(s_{max}) = 4.47 \times 10^8 \, M_\odot \, . \qquad (4\text{-}23)$$

Using the value determined (see Observations section, below) for the VLA's primary beam solid angle, ω = 9.6014 $\times$ 10^{-5} steradians, and recalling that K_r = 3, K_M = $10^{8.06}$, γ = – 4.2, and q = 1.82, we find from evaluating equation (4-21) that the estimated total number of galaxies that are detectable by the VLA in one of our survey fields is 9.1. The uncertainties associated with this number are difficult to assess, as several of the uncertainties in the quantities that go into the determination are correlated, preventing an accurate determination using straightforward propagation of errors. However, a rough estimate obtained in this way results in an uncertainty on the order of -9, $+40$ galaxies per field. The upper limit indicated by this value would be easily detectable and can be ruled out by the results of this and other surveys, as will be shown below. The lower limit would indicate an extremely low space density of dwarf galaxies, and would be of no cosmological interest, as the fraction of dwarf galaxies in the Universe would be insignificant compared to their larger more massive brethren.

Another uncertainty in this numerical estimate is the result of a bias analogous to the well-known Malmquist bias (Mihalas and Binney, 1981, p. 242). The uncertainty in

---

[1] This level corresponds to a 5σ detection in the Hanning smoothed data; see the sections on data analysis and detection criteria, below, for further clarification.

the mass-radius relation means that, for a given radius, some galaxies will actually have masses slightly lower that than dictated by the mass-radius relation. This uncertainty also means that, similarly, there will be galaxies with masses slightly higher than the one predicted by the mass-radius relation. The galaxies with slightly higher masses will be detectable out to a greater distance, and so are visible over a volume that is slightly larger than the nominal one. These systems will be included in a survey of the nominal volume. Conversely, the galaxies with slightly lower masses aren't detectable over the entire nominal volume, and will be excluded. Since the higher mass systems are sampled throughout a larger volume than the lower mass systems, we are including more higher mass systems than we are excluding lower mass systems. This causes a net increase in the total number of galaxies of a given radius that are detectable. This bias will be greater for galaxies with smaller radii, due to the steep increase in the (Tyson and Scalo) radial distribution function. We have not accounted for this bias in the derived numerical estimate, and so in this sense, the 9.1 galaxies per field is a lower limit.

Spatial Distribution

In addition to investigating the number of dwarf galaxies, we were interested in examining their spatial distribution as well, to see whether these small systems are indeed more uniformly distributed than the brighter normal galaxies as predicted by Dekel and Silk's models (1986) for biased galaxy formation. Therefore the survey was designed to encompass three different extragalactic environments. The first region is located within a void, the second in a cluster of galaxies, and the third in the well-known interaction field of M81/M82. This last field was included to test the idea that dwarf galaxies may form as a by-product of galaxy-galaxy interactions. Lo and Sargent (1979) conducted a search for intergalactic HI clouds in nearby groups, including the M81 group, and suggested that the presence of such gas in interacting systems was of a tidal origin. Their

detection of 3 previously uncataloged low surface brightness dwarf galaxies, including one in the M81 group[2], and more recent work on the possible formation of dwarfs in the tidal tails of interacting systems (Duc and Mirabel, 1994; Mirabel et al., 1994; and Hibbard et al., 1994) has provided support for the idea that dwarf galaxies can form through galaxy–galaxy interactions.

If the theory of biased galaxy formation is correct, then our survey should detect essentially the same number of galaxies in the void and in the cluster fields; and if dwarfs do indeed form more readily in interaction fields, then we should find an enhancement in the M81/M82 interaction environment.

Observations

Each of the three fields was chosen to include a known dwarf galaxy; the presence of some signal in the observations provided a means to check that the array was operating correctly and the data were reduced properly. In the void field, the observations were centered on UGC 10805, a dwarf irregular located near the edge of the void. The cluster field was centered on UGC 2014, a dwarf irregular in a nearby cluster; and the interaction field was chosen to include M81 Dwarf B (hereafter M81dB), one of the two dwarf galaxies detected by Lo and Sargent (1979). Table 4.1 presents physical properties of these systems as reported in the Third Reference Catalogue of Bright Galaxies (known as the RC3; de Vaucouleurs et al., 1991). In Table 4.1, α and δ are the right ascension and

---

[2] They actually reported 4 previously uncataloged detections, with 2 in the M81 group, but one of these (M81 Dwarf B) is UGC 5423.

Table 4.1: Physical Properties of target galaxies.

	UGC 10805 (Void Field)	UGC 2014 (Cluster Field)	M81 Dwarf B (Interaction Field)
α (B1950)	$17^h\ 17^m\ 34^s$	$02^h\ 29^m\ 48^s$	$10^h\ 01^m\ 24^s$
δ (B1950)	+14° 26′ 47″	+38° 27′ 00 ″	+70° 37′ 00 ″
Common names	DDO 207	DDO 22	UGC 5423
D_{25}	1.66′	2.04′	0.87′
B_T	15.3	15.65	15.19 [a]
Δv_{20} (km s^{-1})	55 ± 5	67 ± 7	67 ± 7
Δv_{50} (km s^{-1})	37 ± 7	49 ± 12	39 ± 7
$V_\odot$ (km s^{-1})	1554 ± 4	565 ± 6	340 ± 5
d (Mpc)	16.86	6.85	4.54
M_{HI} ($M_\odot$)	4.23×10^8	8.95×10^7	1.87×10^7

[a] m_B rather than B_T.

declination for equinox B1950. D_{25} is the apparent major isophotal diameter measured where the surface brightness level is 25.0 B-magnitudes per square arcsecond. B_T is the total apparent magnitude in the B system. The following two lines, Δv_{20} and Δv_{50}, are the full–widths of the HI line as measured at the 20% and 50% levels of the peak signal, respectively.$V_\odot$ is the mean heliocentric radial velocity derived from HI observations, and d is the distance as determined by the velocity corrected to the galactic standard of rest (V_{GSR}) as defined in the RC3, and using H_0 = 100 km s^{-1} Mpc^{-1}. We have chosen to use this value for H_0 both to be in accord with Tyson and Scalo (1988), and because it provides us with a conservative volume estimate.

In order to provide both reasonable velocity resolution (channel width) and wide velocity coverage (bandwidth), two sets of observations were made for each field. Hardware limitations restricted the VLA observing mode to a 64 channel spectrometer with a channel width of 195 kHz ($\sim$ 41 km s^{-1}); this provided a total bandwidth of

12.5 MHz. This bandwidth corresponds to a velocity range of about 2500 km s^{-1}; which is a distance range of 25 Mpc, using H_0 = 100 km s^{-1} Mpc^{-1}. To extend the volume surveyed, we observed each field at two different center frequencies, separated by 12.5 MHz. Since the two sets of observations covered adjacent frequency ranges of 12.5 MHz (2500 km s^{-1}), the combination of the two sets of observations had a total bandwidth of 25 MHz and thus a total combined velocity range of approximately 5000 km s^{-1}.

The center frequencies chosen for the two sets of observations done for each field were 1401 MHz for the high redshift (4100 km s^{-1}) observations and 1413 MHz for the low redshift (1500 km s^{-1}) observations. The total velocity range actually observed was therefore approximately 230 km s^{-1} to 5371 km s^{-1}, so that the distance range surveyed for each of the three fields was from about 2.3 to about 53.7 Mpc. The total volume[3] surveyed per field was then

$$Vol = \frac{1}{3}\omega\left(D_{max}^3 - D_{min}^3\right), \tag{4-24}$$

where ω is the beam solid angle of the primary beam of the VLA. Approximating the VLA primary beam as a 2-D Gaussian with a FWHM of 31.6′, we find that the beam solid angle is 9.6041 × 10^{-5} steradians. Using the minimum and maximum distances of 2.3 and 53.7 Mpc, the maximum total volume per field is 4.96 Mpc^3. The actual survey volumes vary from this slightly; one or more channels at the end of the bandpass were sometimes discarded due to the loss of sensitivity produced by the bandpass roll-off.

Observations for the cluster and interaction fields were done on Jan. 21/22 1990, and observations for the void field were done on May 15/16, 1991. After preliminary

---

[3] This assumes constant sensitivity across the FWHM of the primary beam. A more correct estimate, which includes the dropoff in sensitivity across the beam as a function of angle from the pointing center, is discussed in Appendix B.

reduction of the cluster and interaction fields, the high redshift observations were found to be contaminated by the presence of an internal interference spike very close to the center frequency of 1401 MHz. Since these (Jan. 1990) observations had been done in auto-correlation mode, it was impossible to isolate and remove the effects of this interference. Subsequently, time to reobserve these data sets was applied for and granted, and the high redshift observations for the cluster and interaction fields were retaken on August 2, 1992.

As this was a detection experiment, high sensitivity to low levels of emission was required. Since the minimum detectable flux is inversely proportional to the array size (see equation (3-25)), the most compact array configuration, the D-array, was used for the observations. Each of the three fields was observed for approximately 8 hours; 4 hours at each center of the two center frequencies. We therefore had 6 data sets: high and low redshift observations for each of the three fields. The expected r.m.s. noise at the one-sigma level in one channel is:

$$\sigma\,(\mathrm{mJy}) = \frac{C}{\sqrt{N(N-1)\,n\,\Delta t\,\Delta\nu}}\,, \tag{4-25}$$

where C is a system constant which was 10 for the January 1990 observations and 9.4 for the May 1991 and August 1992 data. N is the number of antennas used, which was generally 27; n is the number of IF pairs, which was 1/2; Δt is the total observing time in hours, and $\Delta\nu$ is the width of one channel in MHz, which was 0.195. Evaluating this for a 4–hour observation predicts an r.m.s noise of 0.6 mJy for each of the six sets of observations.

Data Reduction

The data reduction was performed using the NRAO Astronomical Image Processing System (AIPS), which is a package of software programs designed to examine, edit, calibrate, and image VLA data. Each data set was edited to remove spurious data points,

and then calibrated and Fourier transformed to produce a set of images, which were then analyzed as described in the following section. The general procedures used are discussed here, with specifics mentioned in the section on survey results.

As discussed in Chapter 3, the data calibration is carried out using the "channel-zero" data, which is the average of the inner three-quarters of the total bandpass observed. This increases the sensitivity of the calibrator data, and therefore provides a better calibration of the source line data.

The channel-zero data for each calibrator and source were examined and any anomalous data points (usually identified by a flux value far from the mean) were removed. Once the calibrator data were edited satisfactorily, the gain, phase, and bandpass calibrations were performed according the precepts in Chapter 3. The calibration was then applied to the line data for each source data set. The channel-zero editing was also applied to the line data sets to remove any problem data identified by the channel-zero data.

After calibration, the line data sets were ready for editing and transforming into images. Examination of some of the data sets revealed the presence of solar interference when the observations were done during daytime. This type of interference is common in D-array data due to the short baselines used, and can be diagnosed by the systematically high flux values of the daytime data from the shortest baselines in the array. Such data was identified and removed from the data sets in question. The amount of data affected was small, since only the very shortest baselines are sensitive to solar emission.

In each of the line data sets, several channels from across the entire bandpass were also examined to locate any frequency-dependent interference that might be present. As mentioned above, the high-redshift data sets for each field were contaminated by the presence of a very strong, narrow-frequency interference spike at approximately 1401 MHz. The presence of the interference spike resulted in data values with anomalously

high (several tens of Janskys) flux values. The narrowness of the feature restricted the worst of the contamination to one or a few channels in the middle of the bandpass. Removal of the affected data was done by using the AIPS task CLIP to remove all data points with flux values greater than a specified level (generally around 0.6 Jy). In the highly affected central channels, this removed approximately half the data for the channel. The effect is to raise the r.m.s. noise level on the channel; effectively reducing the sensitivity in those channels, and thus increasing the lowest signal detectable in the affected channels.

After editing the line data, each data set was reduced in the following way: channels without obvious signal were combined in the (u, v) plane data and then imaged (Fourier-transformed) to produce a map of the continuum emission: the frequency-independent emission from background sources. After imaging the line data, this continuum emission map was subtracted from each of the line channel maps, producing a cube of images containing only line emission. In the case of the interaction field data sets (those centered on M81dB), there was also strong sidelobe emission present from the nearby starburst galaxy M82. This was removed by CLEANing a map centered on M82; since CLEANing produces a model of the emitting source, it was then possible to subtract this model of M82 from the (u, v) data. Since the source flux was no longer present in the (u, v) data, there was no beam response to produce sidelobes during imaging, so that the resulting maps were no longer contaminated.

Before analysis of the data could proceed, one more step in the reduction was necessary. Because of the wide bandpass (12.5 MHz) used for these observations, the channel maps were affected by Gibb's phenomenon. This produces "ringing" in the channels, where emission appears as alternately positive and negative in adjacent channels. To correct this, the continuum-subtracted data cubes were Hanning smoothed

in velocity. Hanning smoothing is a running weighted average over three channels of the form

$$I_{n_H} = \frac{1}{4} I_{n-1} + \frac{1}{2} I_n + \frac{1}{4} I_{n+1} \,, \tag{4-26}$$

where I is the intensity of a particular pixel in channel n, and In_H is the intensity of that pixel in the Hanning smoothed channel at the same velocity as channel n. Besides correcting "ringing", Hanning smoothing also reduces the noise in each channel. Propagation of errors shows that the noise in a Hanning smoothed map will be approximately 0.6124 times the noise in the unsmoothed data. This type of smoothing is often used to reduce noise and enhance signal (as in the second project, discussed in Chapter 5). The price paid for this improvement in the signal to noise is the loss of some velocity resolution. According to Rohlfs (1990, p. 159), the velocity resolution of Hanning smoothed data will be twice the channel separation of the unsmoothed data. As the channel separation of the unsmoothed data for this project is $\sim$ 41 km s^{-1}, the resolution of the Hanning smoothed data is 82 km s^{-1}. It should also be noted that since the first and last channels cannot be smoothed this way, they are blanked in the Hanning smoothed data set, thus reducing the velocity coverage by 41 km s^{-1} at each end.

After continuum-subtraction and smoothing, any apparent signal in the maps was CLEANed to remove the effects of the dirty beam (see Chapter 3). In general, this meant only the target galaxies were CLEANed. Any possible detections that were identified during analysis of the data later were weak enough that they did not produce a strong response from the beam, and so were not contaminated by sidelobes and did not require CLEANing.

Analysis

Noise

In any set of observations, there are errors associated with the data. As described by Fomalont in *Synthesis Imaging in Radio Astronomy* (1989), these errors are of two types: (1) stochastic (random) errors due to the instrumentation limits; and (2) systematic errors due to instrumental imaging defects. Imaging defects, if present, are corrected as well as possible during the calibration, editing, and imaging of the data. The stochastic errors (or "noise") determine the background emission level of the data maps, and for a correlation-type detector, such as is used in the VLA, these errors should follow a Gaussian distribution in the image plane and are quantified by the r.m.s. intensity level associated with each pixel in an image.

A Gaussian distribution is characterized by its mean, μ, and standard deviation, σ:

$$f(x) = \frac{1}{\sigma\sqrt{2\pi}}\, e^{-\frac{1}{2}\left(\frac{x-\mu}{\sigma}\right)^2}. \qquad (4\text{-}27)$$

A pixel with a value far from the mean would not be following a Gaussian distribution, and can be attributed to a signal. A detection is thus defined as a signal that appears at a certain level above the background noise.

In order to use Gaussian statistics to describe the significance of a possible detection and thereby decide whether it is valid, it must first be shown that the background level, or noise, of a channel map does indeed follow a Gaussian distribution. A Gaussian function was fitted to the emission (pixel intensity values) in an "empty" channel: one with no signal, therefore containing only noise. This is shown in Figure 4.2. The filled circles represent the binned intensities of the individual pixels; the solid line is the Gaussian fit. A χ^2 test was applied to the residuals to test the goodness of the fit; the value of the reduced χ^2 was 1.043. The probability of obtaining a number of this magnitude when

comparing a completely random set of data points to the specified function (a Gaussian in this case) is 38%. As a perfect fit should have a reduced χ^2 of 1 and a probability of 50%, the model fit is quite good. Therefore, the noise on a channel map can be considered to be Gaussian in nature, and so a possible detection can evaluated in terms of its significance (i.e. level above the background noise) as determined by Gaussian statistics.

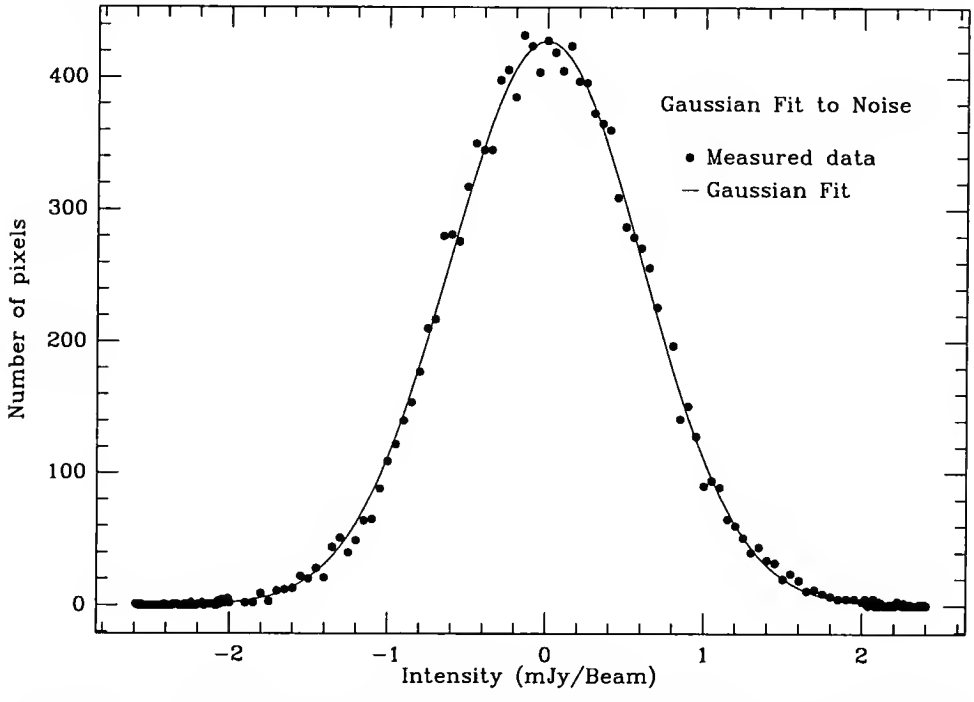

Figure 4.2: Gaussian fit (solid line) to the noise in a channel with no signal emission.

Detection Criteria

In order to minimize spurious detections, several criteria were defined and applied to the data during reduction and analysis. There are two basic characteristics to examine when attempting to distinguish between noise and signal: flux level and velocity (or channel) continuity.

Since the noise follows a Gaussian distribution, establishing an appropriate flux level cut-off between noise and signal can be found using Gaussian statistics. The first step in locating possible signal was to search the data cube for any pixels with an intensity greater than $5\sigma_{ch}$, where σ_{ch} is the r.m.s intensity for an individual channel map. For a

Gaussian distribution, the probability that x will have a value within $\mu \pm \sigma$ is given by

$$P(x) = \int_{\mu-\sigma}^{\mu+\sigma} \frac{1}{\sigma\sqrt{2\pi}} e^{-\frac{1}{2}\left(\frac{x-\mu}{\sigma}\right)^2} dx. \tag{4-28}$$

Evaluating this integral shows that approximately 68% of the values of x will fall within $\mu \pm \sigma$. Letting $t = \frac{x-\mu}{\sigma}$, the probability function can be recast to find the probability that a value of x falls within $\pm t$:

$$P(t) = \frac{1}{\sqrt{2\pi}} \int_{-t}^{+t} e^{-\frac{1}{2}t^2} dt, \tag{4-29}$$

where *P(t)* is the well-known error function. Evaluating the probability function to determine the number of pixels expected to fall outside the $\pm 3\sigma$ interval (i.e. t = 3 for μ = 0), shows that 0.27% of the data should have values greater or less than three times the noise ($3\sigma_{\rm ch}$). The channel maps used for the survey project consist of 256 × 256 pixels, or a total of 65,536 pixels per channel; therefore one expects (65,536 × 0.0027 =) 176.9 pixels to appear with such values for a map containing only noise. At the 5σ level, this probability decreases to 5.734×10^{-5}% for 65,536 pixels. This is equivalent to only 0.04 pixels per channel expected with values greater or less than $5\sigma_{\rm ch}$. Therefore, any pixels with values at or above $5\sigma_{\rm ch}$ can be defined as significant: signal, instead of noise.

The velocity continuity criterion demands that a signal appear in more than one channel. The observed velocity width of a galaxy is a combination of the channel width Δv_{ch} of the observations and the intrinsic velocity width of the HI spectral line of the galaxy (which is a function of both the turbulent and rotational motions of the gas; see Chapter 5 for details)v_c:

$$\Delta v_{obs} = \sqrt{(2v_c)^2 + (\Delta v_{ch})^2}\,. \tag{4-30}$$

The rotational component of the intrinsic velocity is a function of galaxy mass and radius, and is larger for more massive systems. For a galaxy to appear in two channels

($\Delta v_{obs} \sim 2 \times 41 = 82$ km s^{-1}) requires an intrinsic velocity greater than ~ 35 km s^{-1}, which is quite low (cf. Gallagher and Hunter, 1984). It is therefore reasonable to expect all but the most extreme dwarfs to appear in more than one channel of the unsmoothed data.

In general, noise spikes, or anomalous high-flux pixels, can be identified and eliminated based on their appearance in only one channel. However, the identification of noise spikes in the survey data was complicated by the Hanning smoothing of the data. As this is a running average of every three channels, a one-channel noise spike will show up in the two adjacent channels as well after Hanning smoothing.

A $5\sigma_{ch}$ noise spike in a channel of the Hanning smoothed data would appear at $5.1240\sigma'$ signal in the unsmoothed data, where σ' is the noise in one channel of the unsmoothed data. Hanning smoothing a one-channel spike of this level will result in the appearance of "signal" at the levels of $3.3\sigma_{ch}$, $5\sigma_{ch}$, and $3.3\sigma_{ch}$ in three consecutive channels of the Hanning smoothed data. Therefore, the Hanning-smoothed data cube was examined for pixels with intensities greater than $5\sigma_{ch}$; when such a pixel was found, pixels at the same location in the two adjacent channels were examined. If these were found to be at a level greater than $3.5\sigma_{ch}$, it was considered to be a possible detection.

Once the entire data cube was examined, channels with possible signal were blanked and then integrated. The blanking is done to avoid integrating up the noise as well as the signal, and was performed using a conditional blanking technique. In this method, a blanking mask is created by convolving each map in the data cube with a Gaussian with a FWHM twice that of the beam. The blanking is then performed by testing each pixel on the mask; for those with intensities $|F| \geq 2\sigma_m$ (σ_m is the noise on the convolved mask channel), the *corresponding* pixel in the *unconvolved* map is retained. The pixels corresponding to those that fail this test on the mask are blanked. The result is a blanked

version of the unconvolved cube, containing only pixels whose absolute values on the mask were $\geq 2\sigma_m$.

After blanking, any channels suspected to contain signal were integrated using the AIPS task XMOM. A flux limit was used, so that only pixels with intensities $|F| \geq 2.5\sigma_{ch}$ were included in the integration. Negative values were included to avoid introducing a positive bias in the final moment map. XMOM produces zeroth, first, and second moment maps; the zeroth moment is an image of the integrated flux, or column density; the first moment is an image of the velocities; and the second moment is an image of the velocity dispersions associated with each pixel (see equations (3-7), (3-10), and (3-11)).

Once the moment maps were created, two further criteria were applied to any possible detections: the object had to have a peak integrated intensity greater than five times the r.m.s. noise on the zeroth moment map (σ_{xmom}); and the HI mass of the object had to be greater than five times that expected from the integrated flux due to the noise in one beam (σ_{HI}).

The 5σ limit was determined as follows: a point source (i.e. 1 beam) signal of 3.5σ, 5σ, 3.5σ appearing in three consecutive channels will add coherently: $3.5\sigma + 5\sigma + 3.5\sigma = 12\sigma$. The noise will add approximately as $\sqrt{N}$; where N = number of channels = 3. Thus the signal-to-noise = $12\sigma \div \sqrt{3}\sigma = 6.9$. This assumes a point source where the signal overlaps exactly. For a source with single-channel peaks that do not overlap exactly, the signal will add as $(\frac{3.5}{2})\sigma + 5\sigma + (\frac{3.5}{2})\sigma = 8.5\sigma$ assuming the overlap is at the half-power point. The noise adds as before, and so the signal-to-noise = $8.5\sigma \div \sqrt{3}\sigma = 4.9$. Therefore, to be classified as a valid detection, the peak integrated flux value on the moment map had to be greater than five times the r.m.s. measured on the noise map (i.e. greater than $5\sigma_x$).

It should be mentioned that since the data was Hanning smoothed, the data in consecutive channels is correlated, not independent, and so the noise during the integration doesn't add exactly as the square-root of the number of channels. To determine the noise level on the integrated moment map more accurately, the unblanked signal channels were integrated without using any flux limits, so that all pixels in the relevant maps were included in the integration. The AIPS task TVSTAT was then used to determine the r.m.s level ($\sigma_{\rm xmom}$) of this "noise" map. This measured level was higher than that calculated using $\sqrt{\rm N}$; so the $5\sigma_{\rm xmom}$ criterion is somewhat conservative.

Finally, the HI mass of the object under investigation had to be greater than five times that expected from the flux due to the noise in one beam ($\sigma_{\rm HI}$). This was determined by the HI mass corresponding to the flux at the one-sigma level in one beam. The general equation for the HI mass is (cf. equation (3-9))

$$M_{HI} = 2.356 \times 10^5 \, D^2 \int S \, dv \quad M_\odot \tag{4-31}$$

where D is the distance to the galaxy in Mpc, S is the signal flux in Janskys, and dv is the velocity width of the signal in km s^{-1}. The expected r.m.s. associated with this integral can then be found from:

$$\sigma_{HI} = 2.356 \times 10^5 \, D^2 \sigma_{xmom} \, , \tag{4-32}$$

where $\sigma_{\rm xmom}$ is the noise on the integrated zeroth moment map.

To summarize, the detection of a signal required:

(1) the appearance of a signal at levels greater than $3.5\sigma_{\rm ch}$, $5\sigma_{\rm ch}$, and $3.5\ \sigma_{\rm ch}$ in three consecutive channels,

(2) that the peak integrated signal on the zeroth moment map be greater than $5\sigma_{\rm xmom}$,

(3) that the integrated HI mass be greater than $5\sigma_{HI}$, where σ_{HI} is the HI mass expected from a $1\sigma_{xmom}$ signal in one beam.

Survey Results

The results of the analysis of the three observed fields are discussed in the following section. The data for each of the six sets of observations was edited, calibrated, and reduced as described above. The velocity resolution of the Hanning smoothed data is $\sim$ 82 km s^{-1}; the spatial resolutions varied for each set of observations and are discussed individually below. Velocities were converted to the galactic standard of rest (GSR) using the precepts set forth in the RC3 (de Vaucouleurs et al., 1991), and distances were then calculated from the velocities using H_0 = 100 km s^{-1} Mpc^{-1}. All volume calculations were done using equation (4-24).

Void Field

Observations in this field were centered on a catalogued dwarf irregular located at the edge of the Local Void. UGC 10805 (also known as DDO 207) has a position of α (B1950) = 17^h 17^m 34.4^s, δ (B1950) = +14° 26′ 47.0″ , and a heliocentric velocity of 1554 km s^{-1} (see Table 4.1). Observations of both the low and high-redshift data sets were done on May 15/16, 1991, and the data were calibrated, edited, and reduced as described above. After Hanning smoothing, the single-channel r.m.s. for the low redshift data set was 0.428 mJy per beam (B), and 0.383 mJy B^{-1} for the high redshift data set.

Low redshift Void field data set. The spatial resolution of this data set is 91.5″ × 87.4″; the position angle of the beam is −46.6° (measured from the north through the east). The channel separation is 41.6 km s^{-1}; the Hanning smoothed resolution is twice this: 83.2 km s^{-1}. The heliocentric velocity range covered for the low redshift data is from 380.0 to 2754.3 km s^{-1}; these are distances of 5.12 to 28.86 Mpc. One channel from

each "end" of the bandpass was discarded during Hanning smoothing (see discussion on Hanning smoothing, above), and an additional 3 channels at the edge of the bandpass were discarded due to the poor quality of the data resulting from the roll-off of the bandpass response. The total volume observed is 0.76532 Mpc^3.

To locate possible signal (other than UGC 10805 itself, which appears in this data set and is discussed below), the AIPS routine IMEAN was used to find the statistics for each channel, including the peak pixel intensity and r.m.s. (σ_{ch}) for the entire channel. A plot of the peak signal-to-noise as represented by the peak pixel intensity divided by the r.m.s. for each channel (σ_{ch}) is presented in Figure 4.3. The data for the galaxy has been excluded from this plot. It can be seen that there are no points with values greater $5\sigma_{ch}$ in this data set; therefore, the only detection for this set of observations was UGC 10805 itself.

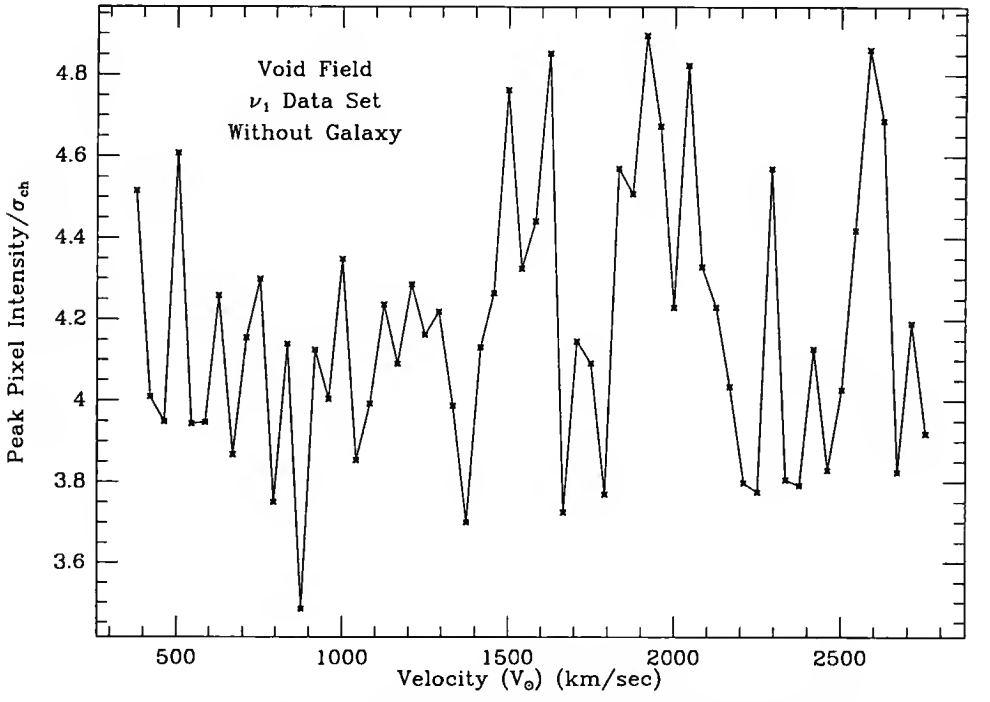

Figure 4.3: Peak signal-to-noise per channel for
the low redshift data set for the Void field observations.

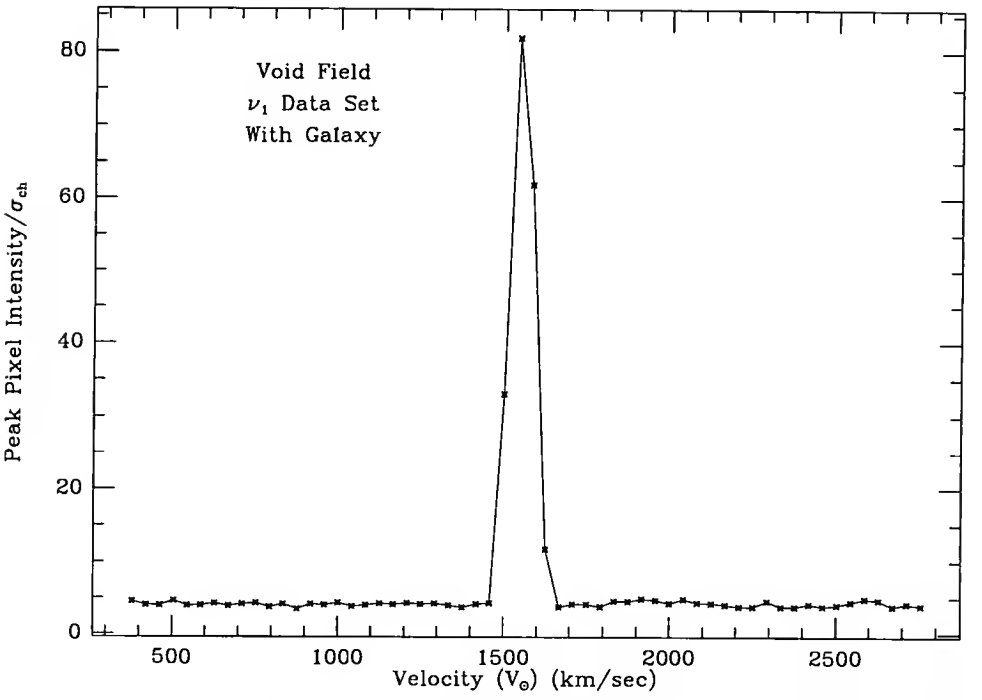

Figure 4.4: Peak signal-to-noise per channel for the low redshift data set for the Void field observations; including the data for UGC 10805.

UGC 10805. UGC 10805 was located in the center of the observed bandpass, as is shown in Figure 4.4: the plot of peak pixel intensity divided by the r.m.s. noise in each channel. This figure shows the same data as that in Figure 4.3, but this time, with the data for the galaxy included. Signal from the galaxy was observed over 4 channels; figure 4.5 shows the flux spectrum of the galaxy signal from the blanked data cube. The horizontal error bar shows the velocity resolution (83 km s^{-1}); the vertical error bar indicates the one-sigma variation (± 0.0018 Jy) in the summed flux in each channel.

The channels containing signal were integrated in velocity to produce moment maps of the galaxy. Figure 4.6 shows the zeroth moment map, which is the integrated intensity (column density; see equation (3-7)) in units of H atoms cm^{-2}. The synthesized beam is shown in the lower right corner.

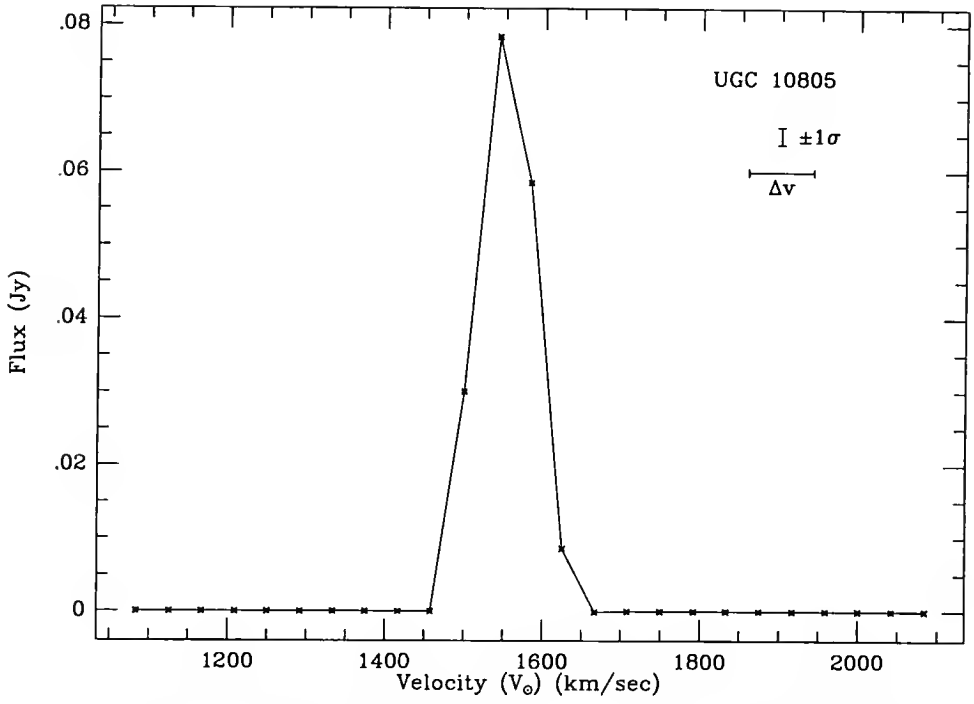

Figure 4.5: Flux spectrum of the blanked data cube for UGC 10805.

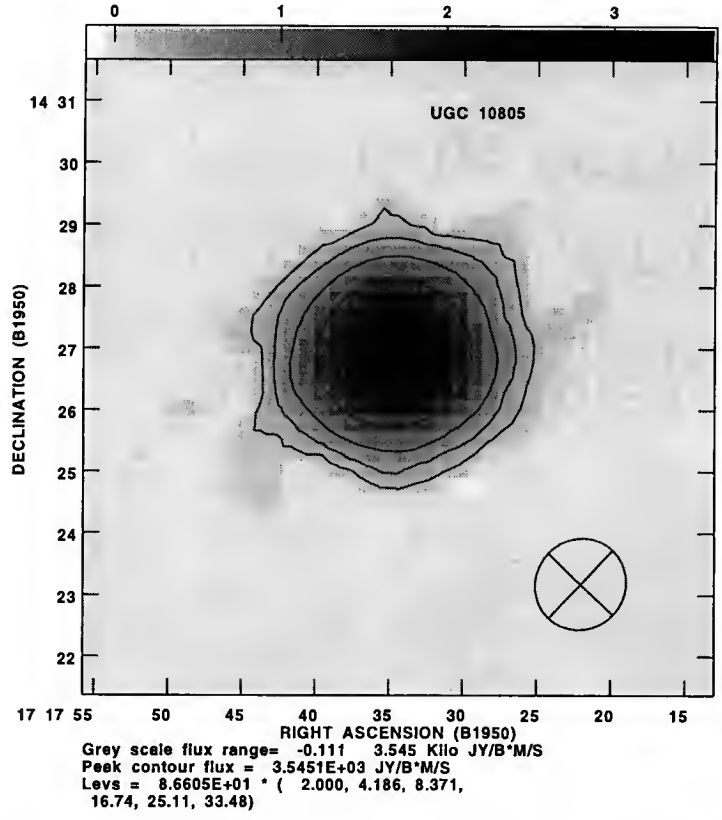

Figure 4.6: Integrated HI column density map of UGC 10805. Contour levels are 0.24 (2σ), 0.5, 1, 2, 3, and 4 $\times$ 10^{20} atoms cm^{-2}.

The derived properties for UGC 10805 are as follows:

Peak column density $N_{HI} = 4.89 \pm 0.12 \times 10^{20}$ atoms cm^{-2}

Peak signal-to-noise (N_{HI}/σ_{xmom}) = 40.9

Systemic (flux-weighted) heliocentric velocity $V_{\odot} = 1552.5 \pm 0.8$ km s^{-1}

Distance D = 16.85 Mpc

HI mass $M_{HI} = 4.86 \pm 0.17 \times 10^8$ $M_{\odot}$

HI mass signal-to-noise (M_{HI}/σ_{HI}) = 83.9

$\Delta v_{50} = 36.0 \pm 1.4$ km s^{-1}

The velocity width Δv_{50} has been corrected for the velocity resolution (cf. equation (4-30) above). The poor velocity resolution prevents us from making an accurate determination of the velocity width at the 20% of peak flux level. The velocity uncertainties are conservative statistical errors which reflect the uncertainties in the pixel intensity values due to the noise on the maps. Systematic effects such as those from errors in measurement of the spectrum width are not included. The major and minor axes of the HI distribution dimensions (after deconvolution of the beam from the image) are 97.1″ and 84.7″ respectively, and are oriented at a position angle of −83°. All of these properties are also listed in Table 4.2 in the Discussion section, along with those for the other detected galaxies.

Comparison with the quantities from the RC3 listed in Table 4.1 shows close agreement with the results presented here: the HI mass we derive is slightly higher than the 4.23×10^8 $M_{\odot}$ in the RC3.

High redshift Void field data set. The spatial resolution of this data set is 61.7″ × 60.4″; the position angle of the beam is 16.19° (measured from the north through the east). The channel separation is 42.4 km s^{-1}, and so the velocity resolution of the Hanning smoothed data is 84.8 km s^{-1}. The heliocentric velocity range covered for this data set

is from 2960.7 to 5376.0 km s^{-1}; these are distances of 30.93 and 55.08 Mpc. As for the low redshift data for this field, one channel from each end of the bandpass was discarded during Hanning smoothing, and an additional 3 channels were discarded due to the poor quality of the data resulting from the roll-off of the bandpass response. The total volume observed for this data set is 4.402 Mpc^3.

Using the same method as for the low redshift data set, the map cube was searched for any signal greater than $5\sigma_{ch}$; the plot of the peak pixel intensity per channel in terms of the r.m.s. in each channel is shown in Figure 4.7. There is a possible detection at the high velocity end of the bandpass, where there is signal with values greater than 3.5, 5, and $3.5\sigma_{ch}$ in three consecutive channels.

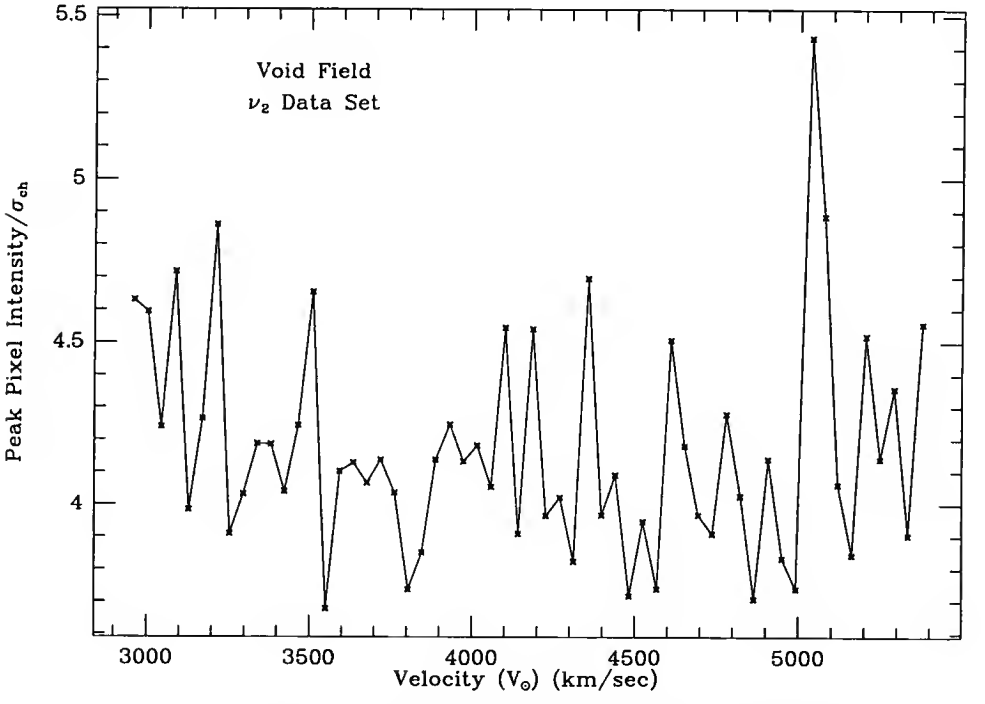

Figure 4.7: Peak signal-to-noise per channel for the high redshift data set for the Void field observations.

Examination of the data cube revealed that this possible signal extended for 8 channels. These channels were CLEANed, and then blanked and integrated. Although

the signal passed the initial detection criterion, it failed the last two: the signal on the integrated map was below $5\sigma_{\mathrm{xmom}}$ in terms of both the peak column density (N_{HI} = 8.6 $\times$ 10^{19} atoms cm^{-2} = $3.5\sigma_{xmom}$) and in terms of the HI mass ($M_{HI} = 2.1 \times 10^8\, M_\odot = 4.1\sigma_{HI}$, at a distance of 51.8 Mpc). A search of the NED database[4] revealed no catalogued objects within a 5′ radius. The object's spectrum is included below (see Figure 4.8), for completeness.

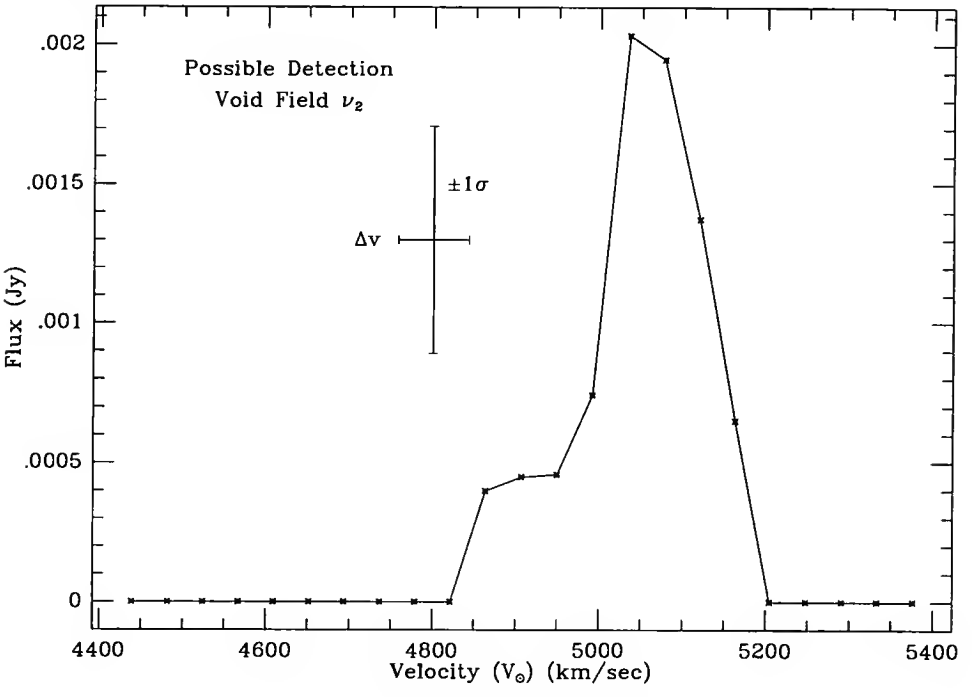

Figure 4.8: Flux spectrum of blanked cube for possible detection in the high redshift Void field.

Results for the Void field. Owing to the loss of the end channels in both the high and low redshift data sets, there is a slight gap in velocity coverage between them: the maximum distance for the low redshift data set is 28.86 Mpc; the minimum for the high redshift set is 30.93. Adding the volumes from both data sets results in a total observed

[4] The NASA/IPAC Extragalactic Database (NED) is operated by the Jet Propulsion Laboratory, California Institute of Technology, under contract with the National Aeronautics and Space Administration.

volume for this field of 5.17 Mpc^3. Only the target galaxy, UGC 10805, was detected. There is the possibility of another object in the data set, but it did not integrate up to levels above 5σ in either HI mass or column density. However, since this possible detection is at the end of the observed bandpass where the sensitivity is beginning to drop off, there is a remote possibility that this object really does exist. Follow-up observations centered at its heliocentric velocity would settle the question. For the purposes of this study, however, it cannot be regarded as a detection.

Cluster Field

The observations of this field were centered on at α (B1950) = $02^h\ 29^m\ 48^s$, δ (B1950) = +38° 28′ 00″, to target a catalogued dwarf irregular located in a cluster of galaxies. UGC 2014 (also known as DDO 22) has a heliocentric velocity of 565 km s^{-1} (see Table 4.1). Observation of the low data set was done on Jan. 21/22, 1990; the high redshift data set was taken on August 2/3, 1992. The data were calibrated, edited, and reduced as described above. After Hanning smoothing, the single-channel r.m.s. for the low redshift data set was 0.597 mJy per beam (B), and 0.450 mJy B^{-1} for the high redshift data set.

Low redshift Cluster field data set. The spatial resolution for this set of observations is 59.00″ × 52.00″; the beam position angle is 60.50°. The channel separation is 41.6 km s^{-1} and so the resolution of the Hanning smoothed data is 83.2 km s^{-1}. Only one channel at each end of the bandpass was discarded (as a result of the Hanning smoothing) and so the heliocentric velocities range from 256.0 to 2754.3 km s^{-1}. The corresponding distance range, calculated from the GSR velocities, is from 3.76 to 28.74 Mpc. This is a volume of 0.758 Mpc^3.

The data were analyzed for possible detections in the same fashion as the Void data; a plot of the peak signal-to-noise in each channel is shown in Figure 4.9. The signal

from UGC 2014, which appears in this data set, has been excluded from this plot. The points above $5\sigma_{ch}$ at the high velocity end of the bandpass were investigated, and proved to be residual emission from a continuum source that was incompletely removed during continuum subtraction. The peak emission producing the high signal-to-noise in the line data set coincided with the position of a strong source visible in the continuum map; a search of the NED database identified it as the radio source B3 0231+385. As a check, the channels with the residual emission were blanked and integrated, and the column density and HI mass signal-to-noise levels were checked. These both proved to be below 5 (N_{HI} = $4.4\sigma_{xmom}$; M_{HI} = $1.5\sigma_{HI}$). Therefore the only detection for this data set was UGC 2014.

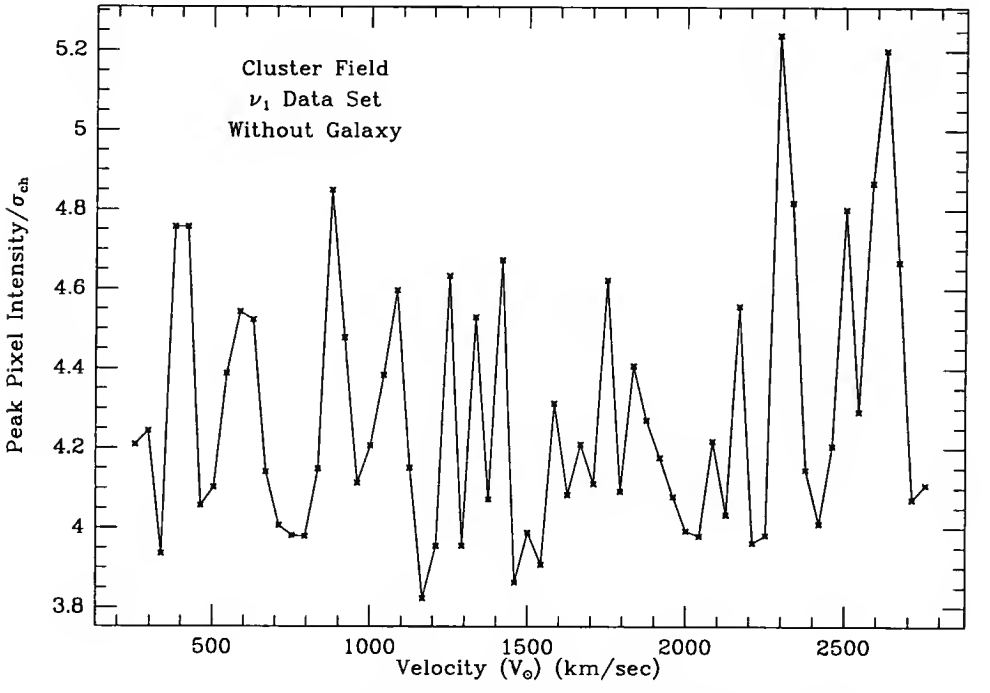

Figure 4.9: Peak signal-to-noise per channel for the low redshift data set for the Cluster field observations.

UGC 2014. Figure 4.10 shows the peak pixel signal-to-noise per channel of the Hanning smoothed data, including the emission from UGC 2014. The channels containing this emission were blanked and integrated to produce a moment map of the integrated intensity. The flux spectrum of the blanked cube is shown in Figure 4.11, and the moment

map is presented in Figure 4.12. Derived properties for UGC 2014 are:

Peak column density N_{HI} = 8.82 ± 0.40 × 10^{20} atoms cm^{-2}

Peak signal-to-noise (N_{HI}/σ_{xmom}) = 22.3

Systemic (flux-weighted) heliocentric velocity $V_{\odot}$ = 565.3 ± 0.1 km s^{-1}

Distance D = 6.85 Mpc

HI mass M_{HI} = 6.13 ± 0.33 × 10^7 $M_{\odot}$

HI mass signal-to-noise (M_{HI}/σ_{HI}) = 50.4

Δv_{50} = 47.6 ± 1.9 km s^{-1}

The major and minor axes of the HI distribution are 97.2″ and 34.8″, oriented at a position angle of 179.8°. These data are also shown in Table 4.2. Velocity uncertainties are as for UGC 10805: conservative statistical estimates only.

Comparison with Table 4.1, the data listed for this system in the RC3, shows that we are detecting about 68% of the listed flux. However, our value is within the range of fluxes listed in Huchtmeier and Richter's HI Catalog (1989). Our value for Δv_{50} agrees very well with the one in the RC3, as do the heliocentric velocity and distance.

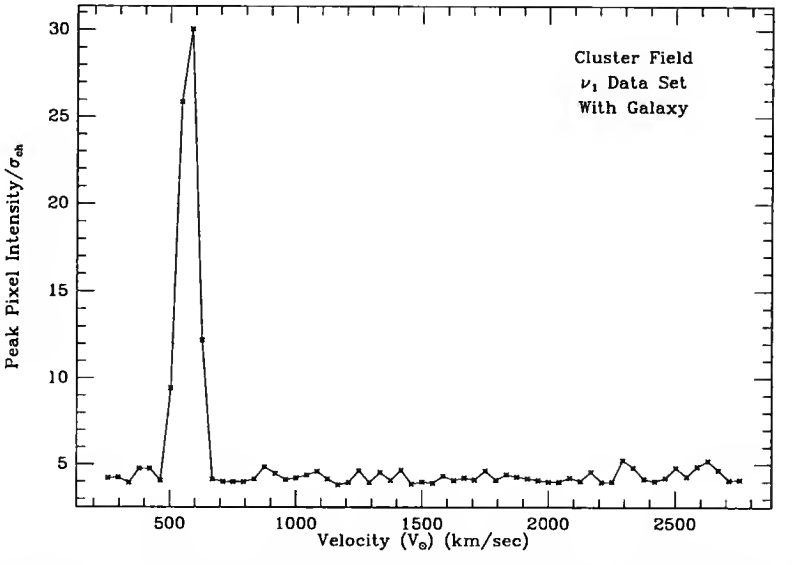

Figure 4.10: Peak signal-to-noise per channel for the low redshift data set for the Cluster field observations; including the data for UGC 2014.

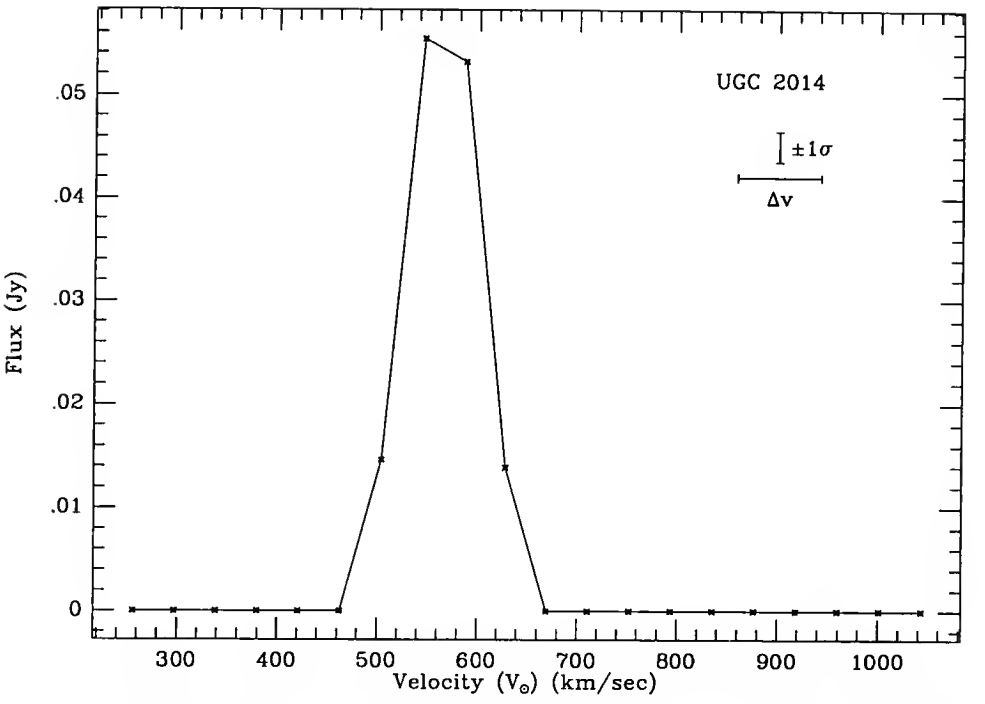

Figure 4.11: Flux spectrum of the blanked data cube for UGC 2014.

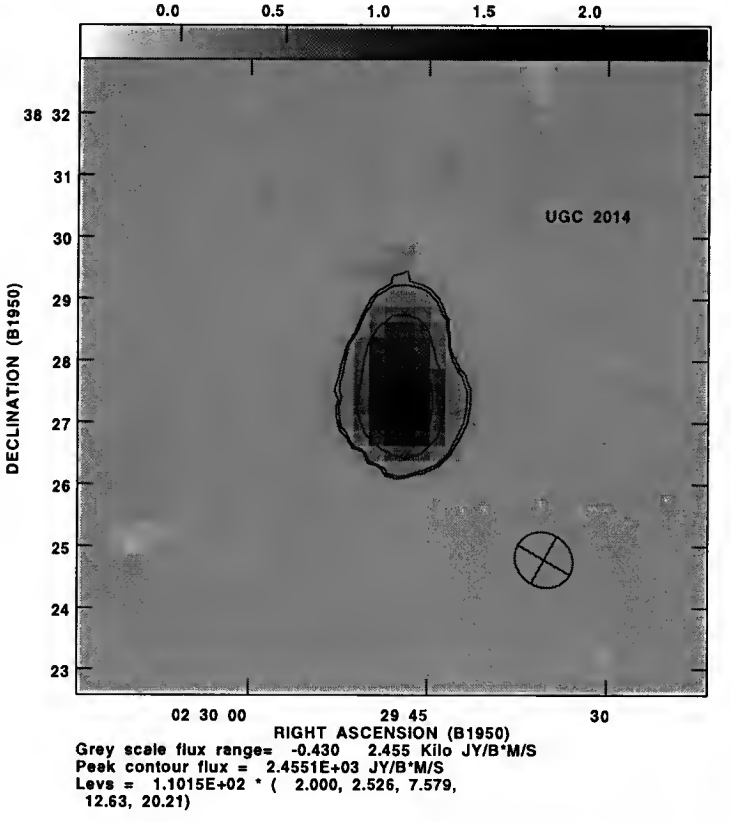

Figure 4.12: Integrated HI column density map of UGC 2014. Contour levels are 0.79 (2σ), 1, 3, 5, and 8 $\times$ 10^{20} atoms cm^{-2}.

High redshift Cluster field data set. The spatial resolution of this data set is 70.2″ × 55.9″; the position angle of the beam is −88.5° (measured from the north through the east). The channel separation is 42.3 km s^{-1}, and so the velocity resolution of the Hanning smoothed data is 84.6 km s^{-1}. One channel from each end of the bandpass was discarded during Hanning smoothing. The heliocentric velocity range covered for this data set is from 2954.2 to 5495.5 km s^{-1}; corresponding to distances of 30.74 and 56.15 Mpc, respectively. The total volume observed for this data set is 4.738 Mpc^3.

The plot of the peak pixel intensity per channel in terms of the r.m.s. in each channel was searched for any data points with values greater than $5\sigma_{ch}$; none were found. This plot is shown in Figure 4.13.

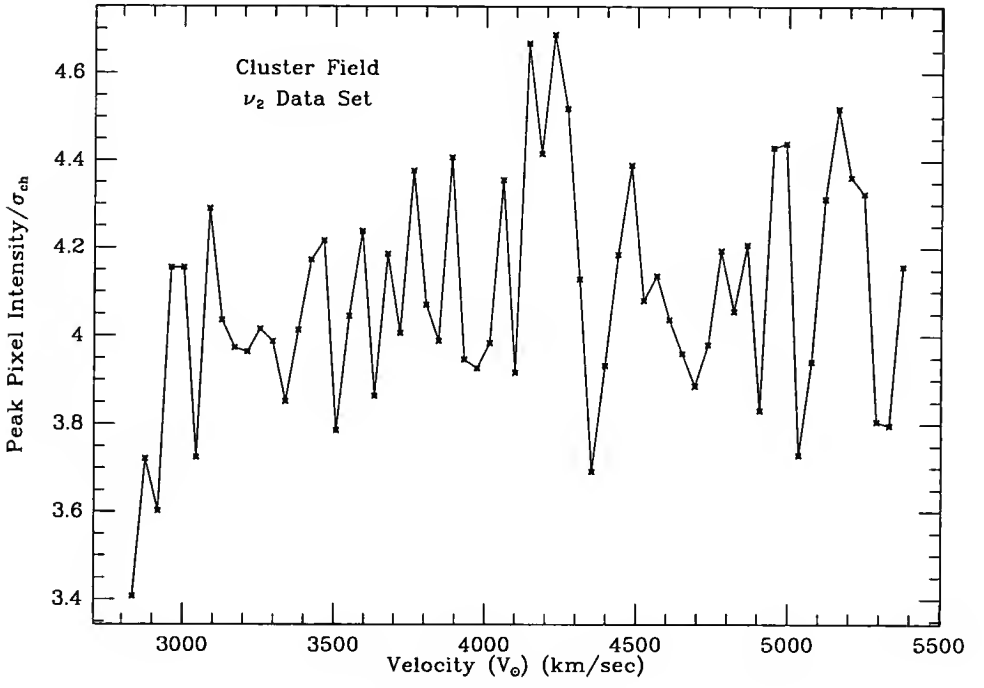

Figure 4.13: Peak signal-to-noise per channel for the high redshift data set for the Cluster field observations.

Results for the Cluster field. As for the Void data set, the loss of channels has resulted in a slight gap in velocity coverage between the low and high redshift data

sets. The combination of the two data set volumes results in a total volume surveyed for this field of 5.25 Mpc^3. Again, only the target galaxy, UGC 2014, was detected. A possible detection in the low redshift data set was proved to be an incompletely subtracted continuum source.

Interaction Field

The observations of this field were centered on at α (B1950) = $10^h\ 02^m\ 00^s$, δ (B1950) = +70° 37′ 00″, to target the catalogued dwarf irregular M81dB (UGC 5423). This galaxy is located near M81 and M82, which make up an interacting system that also includes NGC 3077. M81dB has a listed heliocentric velocity of 340 km s^{-1} (see Table 4.1). Observation of the low data set was done on Jan. 21/22, 1990; the high redshift data set was taken on August 2/3, 1992. The data were calibrated, edited, and reduced as described above. After Hanning smoothing, the single-channel r.m.s. for the low and high redshift data sets were 0.595 and 0.568 mJy B^{-1}, respectively.

Low redshift Interaction field data set. The spatial resolution for this set of observations is 54.11″ × 53.81″; the beam position angle is 44.28°. The channel separation is 41.6 km s^{-1} and so the resolution of the Hanning smoothed data is 83.2 km s^{-1}. Only one channel at each end of the bandpass was discarded (as a result of the Hanning smoothing) and so the heliocentric velocities range from 256.1 to 2754.3 km s^{-1}. The corresponding distance range, calculated from the GSR velocities, is from 3.68 to 28.67 Mpc. This corresponds to a volume of 0.753 Mpc^3.

Initial visual inspection of the data cube revealed the presence of definite signal apart from that associated with M81dB. A search of the NED database at the position of the signal identified it as the previously cataloged dwarf irregular UGC 5455, which is discussed in detail below. The rest of the data were analyzed for other possible detections;

a plot of the peak signal-to-noise in each channel, excluding the signal from both M81dB and UGC 5455, is shown in Figure 4.14. There is one data point greater than $5\sigma_{ch}$, located near the very end of the bandpass.

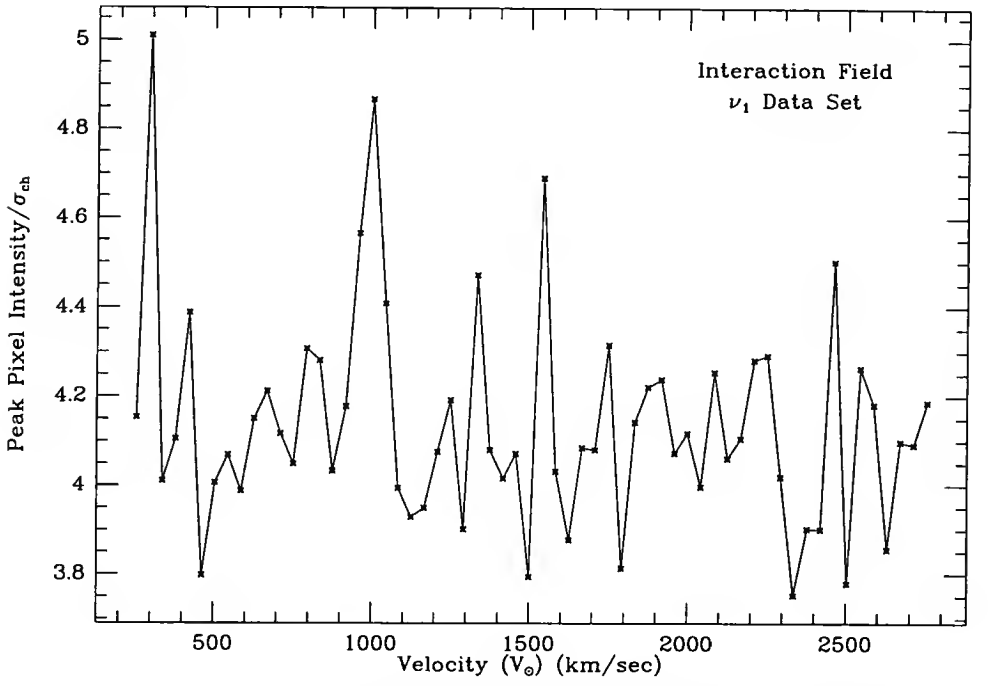

Figure 4.14: Peak signal-to-noise per channel for the low redshift data set for the Interaction field observations, excluding M81dB and UGC 5455.

The end channels were blanked and inspected, and the last three channels were integrated. The spectrum of the blanked cube is presented below in Figure 4.15; the vertical error bars represent $\pm 1\sigma$ variation. They are plotted separately as the noise in these end channels rises steeply towards the end of the bandpass and so an average value is not truly representative for the three channels.

The integrated signal did not pass the final two detection criteria, and no catalogued object was found in the NED database within a 5′ radius of its position. Although the peak column density was at a significance level of $4.3\sigma_{xmom}$; the HI mass was only at the level of $3.6\sigma_{HI}$. Its location at the very end of the bandpass makes it difficult to determine whether this possible detection is from an object just at the edge of our

bandpass, or whether it is an artifact of the high noise prevalent in the end channels. The poor quality of the data would tend to indicate the latter. As for the possible detection in the Cluster field, this object fails two of the detection criteria and so is not considered a valid detection for this experiment.

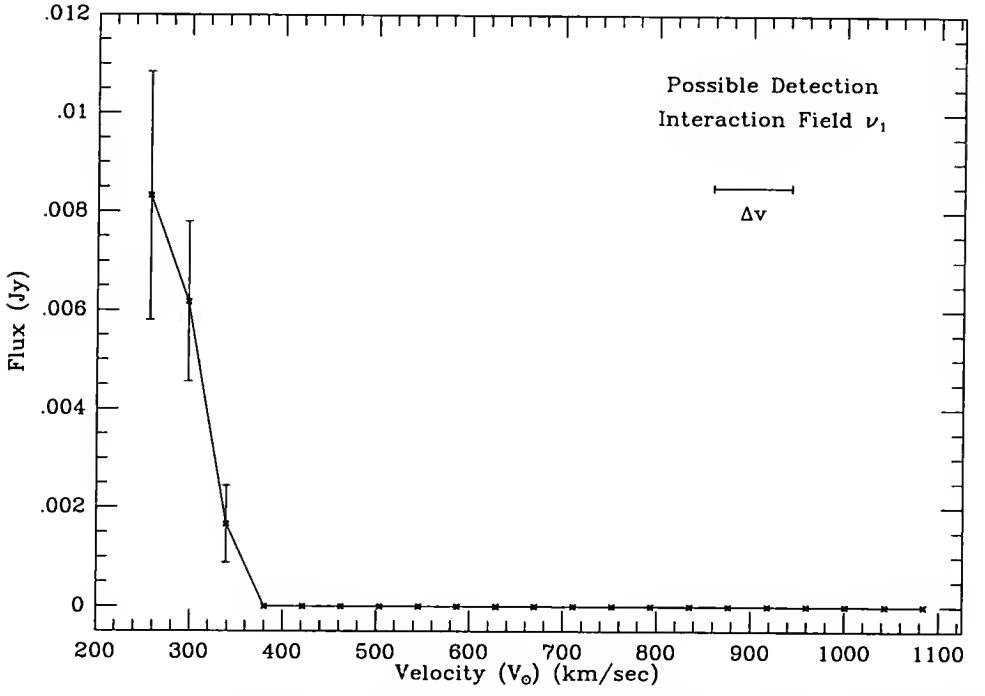

Figure 4.15: Flux spectrum of blanked cube for possible detection in the Interaction field.

M81dB. Figure 4.16 shows the peak pixel signal-to-noise per channel of the Hanning smoothed data, including the emission from M81dB (high velocity end) and UGC 5455 (center of bandpass). The channels containing the emission from M81dB were blanked and integrated to produce a moment map of the integrated intensity. The flux spectrum of the blanked cube is shown in Figure 4.17, and the moment map is presented in Figure 4.18. Individual error bars are plotted on the spectrum since the signal is in the end channels, where the noise varies from channel-to-channel.

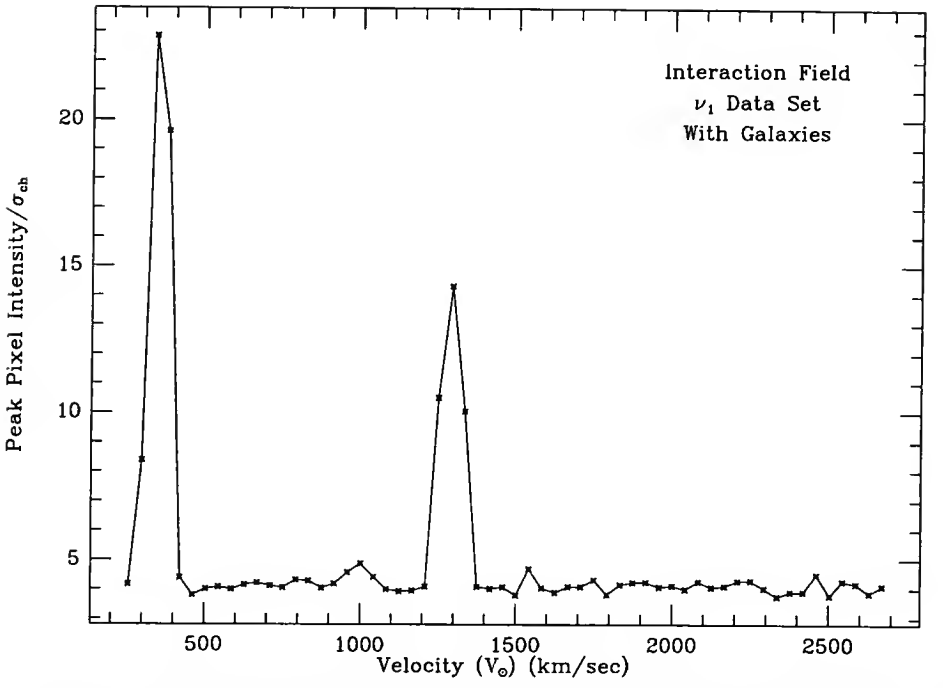

Figure 4.16: Peak signal-to-noise per channel for the low redshift data set for the Interaction field observations; including the data for M81dB and UGC 5455.

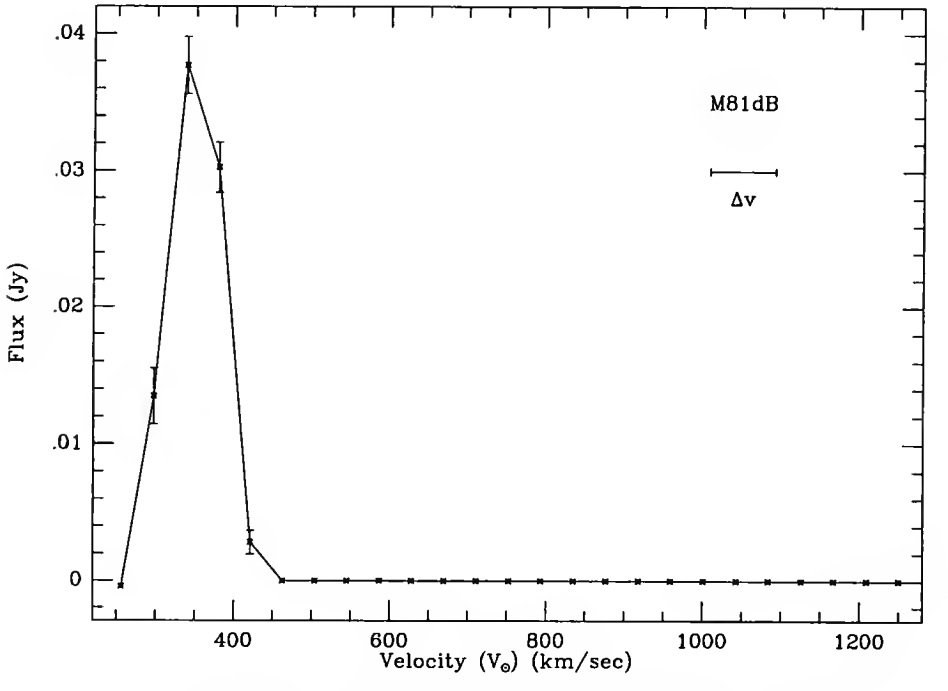

Figure 4.17: Flux spectrum of the blanked data cube for M81dB. Vertical error bars indicate $\pm 1\sigma$ variation.

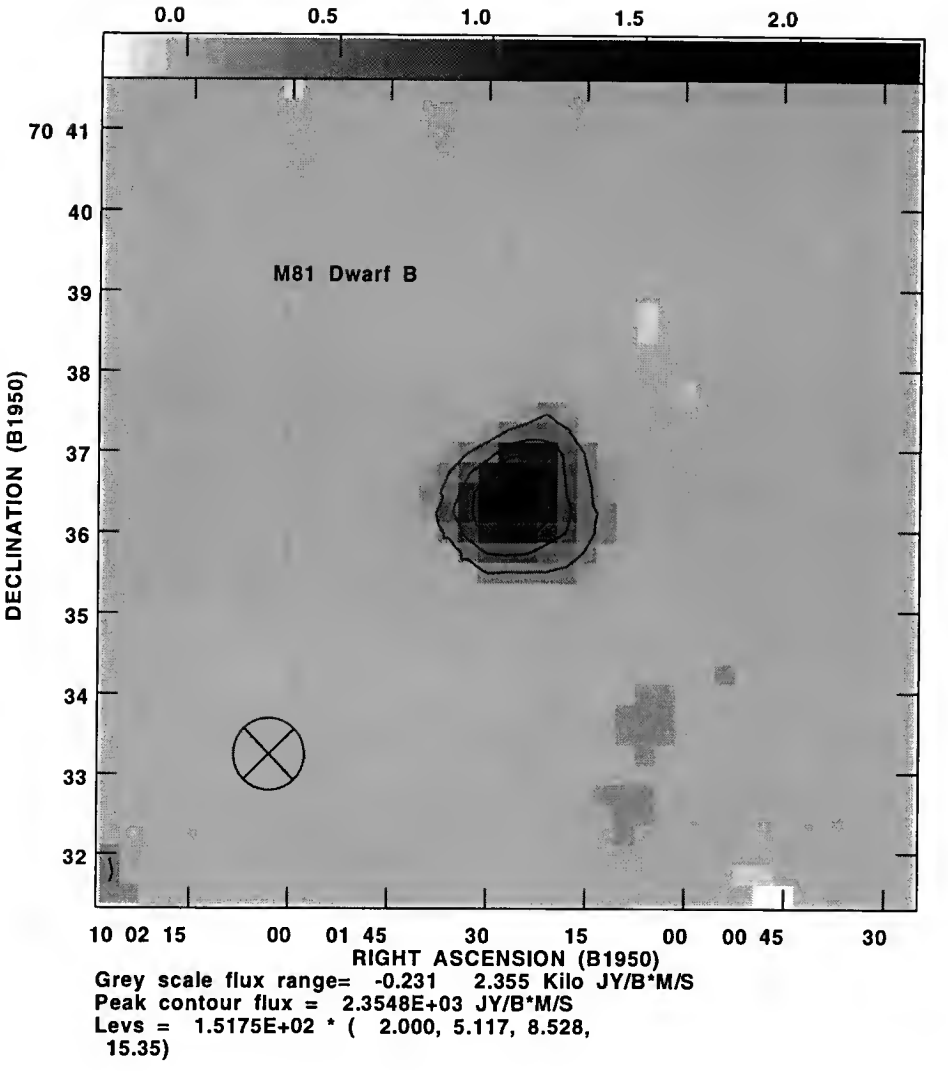

Figure 4.18: Integrated HI column density map of M81dB. Contour levels are 1.2 (2σ), 3, 5, and 9 $\times$ 10^{20} atoms cm^{-2}.

Derived properties for M81dB are:

Peak column density N_{HI} = 8.92 $\pm$ 0.57 $\times$ 10^{20} atoms cm^{-2}

Peak signal-to-noise (N_{HI}/σ_{xmom}) = 15.5

Systemic (flux-weighted) heliocentric velocity $V_{\odot}$ = 349.7 $\pm$ 2.7 km s^{-1}

Distance D = 4.62 Mpc

HI mass M_{HI} = 1.76 $\pm$ 0.08 $\times$ 10^7 $M_{\odot}$

HI mass signal-to-noise (M_{HI}/σ_{HI}) = 23.1

Δv_{50} = 46.4 $\pm$ 5.4 km s^{-1}

The major and minor axes of the HI distribution are 48.5″ and 31.8″, oriented at a position angle of 131.6°. These data are also shown in Table 4.2. Velocity uncertainties are, again, conservative statistical estimates only.

Comparison with Table 4.1 shows that we are detecting about 94% of the flux listed in the RC3, and our value for Δv_{50} agrees fairly well with the one in the RC3. The heliocentric velocity and distance are slightly different than the published ones; this may be due to the poorer quality of the data since the signal appears at the end of the bandpass.

UGC 5455. Figure 4.16 shows not only the signal from M81dB, but also strong emission from UGC 5455; another dwarf irregular galaxy whose presence in this field was not realized until the data were reduced. The channels containing emission were blanked and integrated, and the spectrum and integrated intensity maps are presented in Figures 4.19 and 4.20.

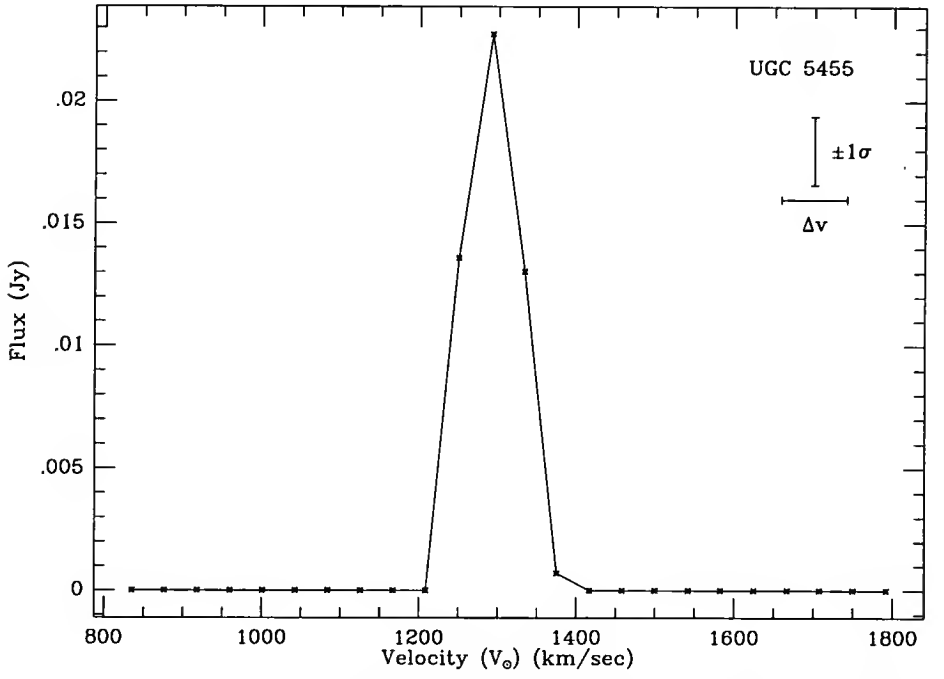

Figure 4.19: Flux spectrum of the blanked data cube for UGC 5455.

Derived properties for UGC 5455 are listed below and in Table 4.2; the column density and HI mass have been corrected for primary beam attenuation. Since UGC 5455 lies approximately 21′ from the pointing center of the field, the sensitivity of the primary beam is reduced by roughly a factor of 3.5, and so the measured values were corrected by this amount.

Peak column density $N_{HI} = 12.19 \pm 1.23 \times 10^{20}$ atoms cm^{-2}

Peak signal-to-noise (N_{HI}/σ_{xmom}) = 9.9

Systemic (flux-weighted) heliocentric velocity $V_{\odot} = 1293.2 \pm 6.6$ km s^{-1}

Distance D = 14.06 Mpc

HI mass $M_{HI} = 3.69 \pm 0.15 \times 10^{8}$ $M_{\odot}$

HI mass signal-to-noise (M_{HI}/σ_{HI}) = 24.9

$\Delta v_{50} = 46.9 \pm 8.0$ km s^{-1}

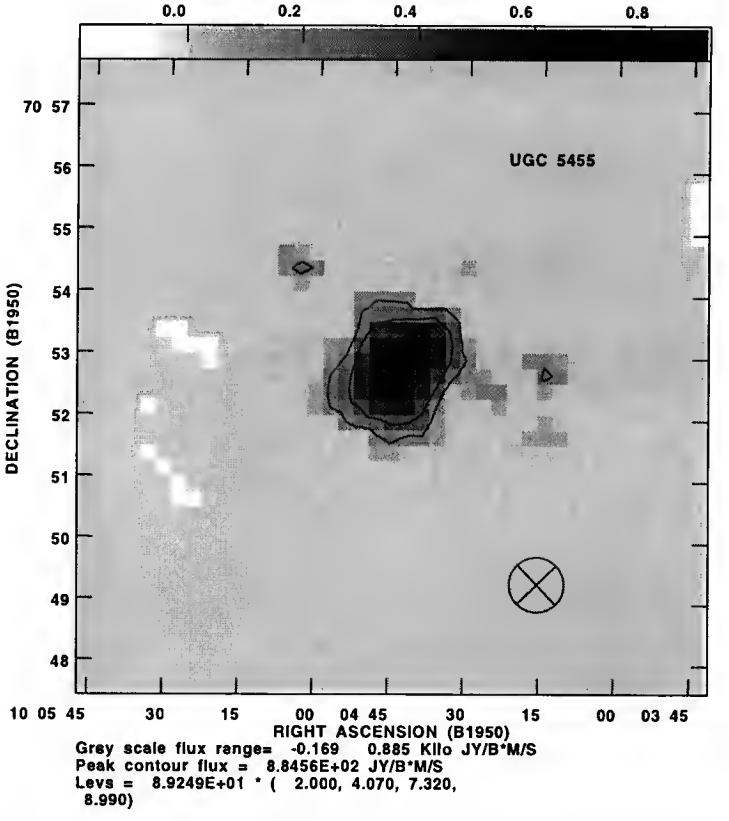

Figure 4.20: Integrated HI column density map of UGC 5455. Contour levels are 2.5 (2σ), 5, 9, and 11 $\times$ 10^{20} atoms cm^{-2}.

The major and minor axes of the HI distribution are 85.0″ and 52.9″, oriented at a position angle of 144.1°. These data are also shown in Table 4.2. Velocity uncertainties are conservative statistical estimates only.

The HI mass listed in the RC3 for this system is $3.69 \times 10^8\ M_\odot$, which is in exact agreement with the HI mass reported above. The listed 50% velocity width of 57 ± 12 is also in reasonable agreement.

High redshift Interaction field data set. The spatial resolution of this data set is 118.3″ × 48.4″; the position angle of the beam is −44.1° (measured from the north through the east). The channel separation is 42.4 km s^{-1}, and so the velocity resolution of the Hanning smoothed data is 84.8 km s^{-1}. One channel from each end of the bandpass was discarded during Hanning smoothing. The heliocentric velocity range covered for this data set is from 2834.6 to 5376.1 km s^{-1}; corresponding to distances from 29.47 to 54.88 Mpc. The volume observed for this data set is 4.473 Mpc^3.

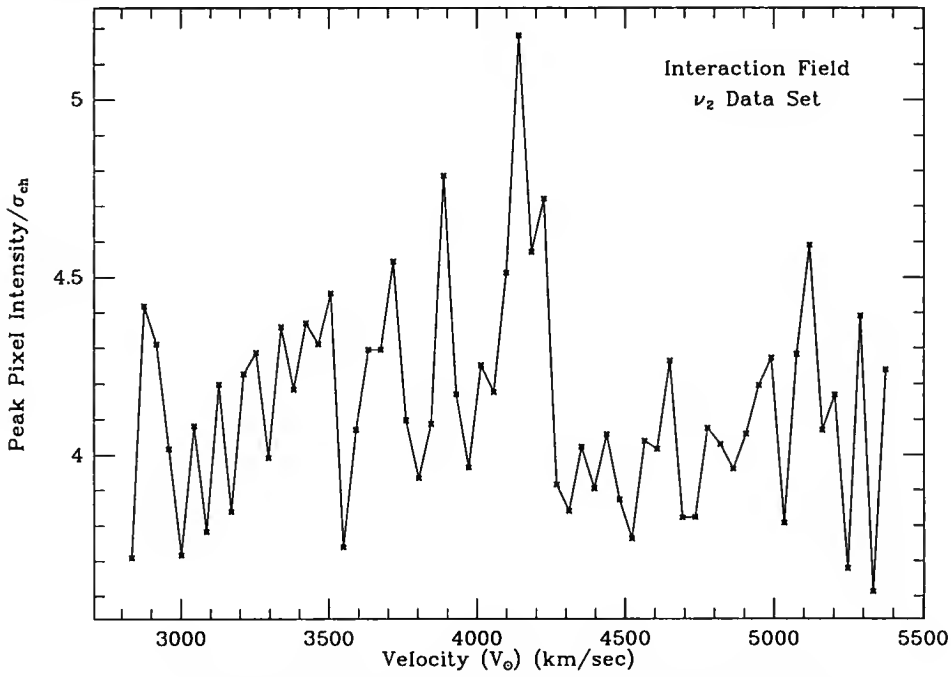

Figure 4.21: Peak signal-to-noise per channel for the high redshift data set for the Interaction field observations.

The plot of the peak pixel intensity per channel in terms of the r.m.s. in each channel was searched for any data points with values greater than $5\sigma_{ch}$; the plot is shown in Figure 4.21. As can be seen, there is one such point, in the center of the bandpass. The data were blanked and integrated; but the integrated signal was not above 5σ in either column density or HI mass. The signal-to-noise levels were 3.4 in column density and 1.3 in HI mass; therefore this does not constitute a valid detection. In addition, the spectrum of the blanked cube showed that signal from only two channels was being included in the integration; and a NED search turned up no catalogued objects within a 10′ radius of its position.

Results for the Interaction field. As for the other two fields, the loss of channels from each end of the bandpass due to Hanning smoothing has resulted in a slight gap in velocity coverage between the low and high redshift data sets. The combination of the two data set volumes results in a total volume surveyed for this field of 5.23 Mpc^3. Unlike the other two fields, however, we detected a galaxy other than the target, M81dB. UGC 5455 was observed in the low redshift data set along with M81dB. A possible detection in the high redshift data set did not integrate up to a significant level and is probably a noise spike.

Discussion

In this project, we have attempted to place limits on the luminosity function proposed by Tyson and Scalo in their 1988 paper. Using the radial distribution function they determined combined with the sensitivity limits inherent in our VLA observations, we predicted we should find approximately 9 galaxies in each of our three fields. However, we detected only one galaxy (our target systems) in each of the Void and Cluster fields; and two galaxies (including the target galaxy) in the Interaction field. The properties of

these systems as derived from the observations are presented in Table 4.2. Each field encompassed approximately 5 Mpc^3, and so the actual total volume surveyed was 15.65 Mpc^3. This gives us an observed number density of 0.26 galaxies Mpc^{-3}.

Table 4.2: Derived Properties of detected galaxies.

	UGC 10805	UGC 2014	M81dB	UGC 5455
Δv_{50} (km s^{-1})	36.0 ± 1.4	47.6 ± 1.9	46.4 ± 5.4	20.3 ± 8.0
$V_\odot$ (km s^{-1})	1552 ± 0.8	565.3 ± 0.1	349.7 ± 2.7	1293.2 ± 6.6
N_{HI} (atoms cm^{-2})	4.89 ± 0.12 × 10^{20}	8.82 ± 0.40 × 10^{20}	8.92 ± 0.57 × 10^{20}	12.19 ± 1.23 × 10^{20}
N_{HI}/σ_{xmom}	40.9	22.3	15.5	9.9
d (Mpc)	16.85	6.85	4.62	14.06
M_{HI} (10^7 $M_\odot$)	48.6 ± 1.7	6.13 ± 0.33	1.76 ± 0.08	36.9 ± 1.5
M_{HI}/σ^{HI}	83.9	50.4	23.1	24.9

There were four possible detections investigated: one in the high redshift data set for the Void field, one in the low redshift Cluster data set, and one each in the low and high redshift data sets of the Interaction field. The possible detection in the Cluster field was shown to be the remnants of a poorly subtracted-out continuum source; and the one in the high redshift Interaction data set was at such a low level that it showed up in only two channels of the blanked data cube and is most likely a noise spike. The other two possible detections, in the high redshift Void data and the low redshift Interaction data, are near or at the end of the bandpass, where the sensitivity falls off and the data quality is poor. This makes it difficult to determine the validity of the detections, and follow-up observations would be necessary to settle the question. However, for the purposes of this project and according to the detection criteria established for it, neither of these two "objects" integrated up to levels significant enough to count as a valid detection.

It should be stressed that the survey presented here is sensitive to very low HI masses, and so examines the faint end of the luminosity function. This is the area in which Tyson and Scalo's radial distribution function is steepest. Therefore, our essentially null results, while not definitive, place a limit on Tyson and Scalo's radial distribution function: it would seem to predict too many small galaxies. Other surveys have reached the same conclusion: that although there are many dwarf galaxies, which are often overlooked in traditional surveys, there is not the large number indicated by the steep function suggested by Tyson and Scalo. Reviews of searches for both low-mass HI-rich galaxies and "intergalactic HI clouds" (concentrations of HI with no discernible optical component) are given by Brinks (1994), Briggs (1990), and Roberts (1988). Briggs, in particular, concentrates on searches for dwarf irregulars, and concludes that present HI surveys are sensitive enough to have detected a large population, if such exists. However, these searches, while occasionally detecting objects, do not support Tyson and Scalo's luminosity function (see, for example, Weinberg et al., 1991).

Several authors have investigated the faint end of the luminosity function using the form proposed by Schechter (1976):

$$\Phi(L) = \Phi^*(L/L^*)^{\alpha} \exp(-L/L^*) d(L/L^*) . \qquad (4\text{-}33)$$

In this expression, $\Phi(L)dL$ is the number of galaxies per unit volume in the luminosity interval from L to $L+dL$, Φ^* is the number of galaxies per unit volume, L^* is the luminosity at which the function changes slope (in the (logΦ, log L) plane), and α is the slope of the luminosity function when $L << L^*$. The parameters Φ^*, L^* (or, more commonly, M^*, the corresponding characteristic absolute magnitude), and α are determined by fitting the data. Schechter determined that for both cluster and bright nearby field galaxies, $\alpha \simeq -1.25$, and $M^* \simeq -21$. According the review by Binggeli et

al. (1988), the faint end of the luminosity function for clusters is well-fit by $\alpha \sim -1.25$ and $M^* \sim -21$; while that for field galaxies has a flatter slope, with $\alpha \sim -1.0$. According to Fisher and Tully (1981) and Staveley-Smith et al. (1992) however, the very faint end of the luminosity function is represented by a steeper slope of $\alpha \sim -1.5$. Staveley-Smith et al. use this to derive a (conservative) space density of 3 Mpc^{-3}, assuming a lower absolute magnitude cut-off of -10.

The number of systems detected in this experiment, one each in the Void and Cluster fields, and two in the Interaction field, is too low to draw conclusions about the spatial distribution of dwarf irregular galaxies. Several studies of the clustering of both low surface brightness galaxies and blue compact dwarfs have been undertaken by various authors (e.g. Salzer and Rosenberg, 1994; Pustil'nik et al., 1994; Alimi, 1994; and Roukema, 1994); and a good overview of current research is given by Hopp (1994). The consensus is that although dwarf galaxies, both low surface brightness and blue compact, appear to be slightly less clustered than brighter, more massive galaxies, they do not "fill the voids." This rules out any strong biasing, such as is suggested by Dekel and Silk (1986) in their Cold Dark Matter models.

There are two possible explanations for the lack of detections in this and other HI surveys: either there is no large population of small galaxies, or these small systems are not gas-rich, and therefore are not detectable at 21–cm. As discussed in Chapter 2, it may be that small, low-mass galaxies lose their HI as a result of a vigorous star-formation episode. If such an event caused the HI reservoir associated with the system to expand, it could fade into "invisibility" at radio wavelengths once the column density became too low to detect. In an effort to examine the plausibility of this second idea, we undertook a study of 16 dwarf galaxies at 21–cm; this work is presented and discussed in Chapter 5.

CHAPTER 5
BLUE COMPACT AND LOW SURFACE BRIGHTNESS DWARF PROJECT

Introduction

The possibility that low mass dwarf galaxies suffer expansion and perhaps loss of their HI gas as a result of an episode of vigorous star formation prompted us to undertake an investigation of the distribution and kinematics of the HI associated with such systems. To examine the effects of star formation on the HI properties of low-mass dwarf galaxies, we present here the results of VLA observations of the HI associated with 16 dwarf galaxies, of which 8 are believed to be undergoing significant amounts of star formation and 8 are thought to have low star formation rates currently.

As mentioned in Chapter 2, it has been proposed that dwarf galaxies undergo a bursting mode of star formation (SSPSF), followed by a long quiescent period. Under SSPSF, star formation occurs in regions known as cells; a cell that is currently forming stars can trigger star formation in a neighboring cell; there is also a stochastic probability that a cell will be begin forming stars spontaneously. The star formation within a cell will cease once the HI gas (out of which the stars form) is either exhausted or dispersed as a result of energy injected into the ISM as a result of the starburst (e.g. from the evolution of massive stars). Once the star formation has stopped, the cell, depleted of HI, cannot undergo any more star formation until the HI is replenished somehow, perhaps through gravitational recollection (infall).

For small systems, consisting of only one or a few such cells, a star formation episode can involve the entire galaxy. Since the potential wells of these low mass systems are

not very deep, the HI may be disrupted by the starburst and pushed out perhaps beyond the edge of the optical galaxy. The star formation will then stop, and the galaxy will not be able to form more stars until the HI has recollected.

This scenario for star formation has prompted the idea that the three different types of dwarf galaxies, dIrrs, BCDs, and dEs, are related, and simply represent different stages in the evolution of a low mass system. It has been proposed that BCDs are dIrrs that are currently in a starburst, and that dEs may be galaxies that have either used up or completely lost their HI gas as a result of one or more star forming episodes. This was discussed in more detail in Chapter 2.

Observations to support this idea include the detection of holes and possibly expanding bubbles in the HI distribution of both large and dwarf irregulars (Puche et al., 1992; Puche and Westpfahl, 1994; Westpfahl and Puche, 1994). Expanding shells, or bubbles of HI gas have been observed in the Local Group irregular Holmberg II (Puche et al., 1992). Some of these shells surround "cavities" in the ISM which contain Hα emission indicative of massive star formation, and clusters of massive stars have been observed in some of the largest holes. Although the holes and shells of expanding gas in Ho II resemble those seen in the arms of larger, spiral galaxies, the sizes of the expanding cavities have greater dimensions. The authors attribute this to the lower gas density in Ho II, which is a result of its greater scale height: the lower mass of Ho II means that the gas distribution is not as tightly confined to the plane of the system. Consequences of this lower gas density are that the bubbles can expand to larger sizes before suffering "blow-out", or disruption.

In a follow-up study, Puche and Westpfahl (1994) present HI images of several dwarf irregulars; structures similar to those observed in Ho II can also be seen in these lower mass systems. Their lowest mass objects, which have the lowest rotation velocities

(from about 5 to 30 km s^{-1}), show the HI distributed in a ring, with a large central hole. They state this as evidence for the expansion of the HI reservoirs associated with these galaxies and propose that this expansion will either eventually halt and the HI will begin a gravitational contraction and condense back into the galaxy, or that the HI will continue to expand and will be lost if the potential energy (binding energy of the gas) of the system is less than the kinetic energy of the expanding gas.

In an effort to examine more closely the idea that dIrrs and BCDs are the same class of object at different stages of star formation and that the HI reservoir associated with these systems undergoes expansion and contraction in response to the star formation, we have observed the HI in a sample of low surface brightness dwarfs (LSBDs) and blue compact dwarfs (BCDs). The sample is described in the following section, and then the observations and data reduction are discussed. Analysis of the data and a discussion of the results are presented in the last two sections.

The Data

Sample Description

As the intent of this project is to examine the differences due to star formation in HI properties of low mass galaxies, we have chosen to observe 8 LSBDs and 8 BCDs. The LSBDs are thought to be dIrrs that are currently quiescent, and the BCDs are thought to be currently undergoing vigorous star formation. As massive stars radiate primarily at bluer wavelengths, galaxies containing such stars have bluer (U-B) and (B-V) color indices. And since massive stars, formed during star bursts, have short life spans (10^6 – 10^7 yr), galaxies with bluer color indices are currently or were very recently forming stars. In order to try to observe galaxies in varying stages of star formation, we have chosen galaxies across a range of color indices. The idea is that the bluer BCDs are

in the earlier stages of a star formation episode than the redder ones, and that the bluer LSBDs were more recently forming stars than the redder ones. A plot of the color-index distribution of the 16 galaxy sample is shown in Figure 5.1.

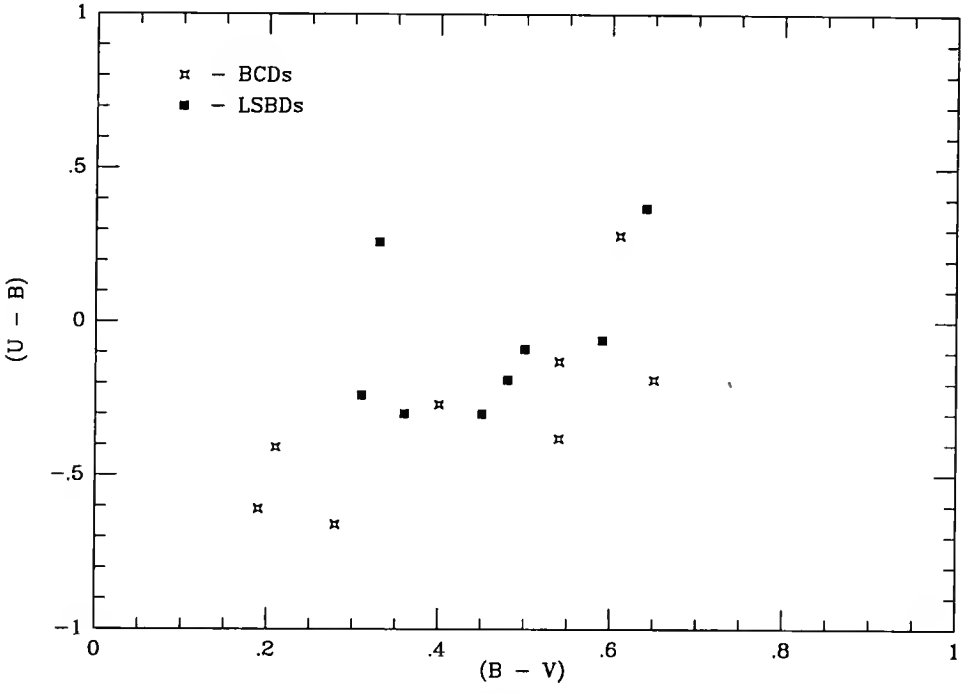

Figure 5.1: Color-Color plot of galaxy sample. Blue is to the lower left.

Another consideration in selection was the HI content of the galaxies. In order to have a sample that was essentially similar in most respects except star formation, all of our galaxies have HI masses on the order of 10^7 to 10^8 $M_\odot$. We chose this mass range in order to examine the very low mass galaxies, which would be most affected globally by a star-formation burst. In addition to the mass restriction, we also chose only field galaxies that appeared to be relatively isolated, to avoid systems that may be interacting or within the "special environment" of a group or cluster. The final sample of 16 galaxies and their catalogued properties as listed in the RC3 (except where otherwise noted), are presented in Tables 5.1 and 5.2. For ease of comparison, this and all subsequent tables and figures are presented at the end of this chapter.

Observations

In order to obtain both good spatial resolution and reasonable signal-to-noise, the C-array configuration of the VLA was used to make the observations. Observations were made on July 5 and 6, 1993, with the time spent on each source varying from about 10 minutes for the "brighter" galaxies, up to about 2 hours for the weakest sources (Mrk 67 and Mrk 51). The resulting resolution was about 25″ on average, and the single-channel signal-to-noise varied from about 5 to 10 for the different data sets.

Most of the galaxies have fairly narrow velocity widths ($\Delta v_{50} \leq 100$ km s^{-1}) and were observed using a 128 channel spectrometer with a bandwidth of 1.5625 MHz; this is a channel width of 12.207 kHz, or $\sim$2.5 km s^{-1}. For those systems with velocity widths ≥ 100 km s^{-1}, the 64 channel mode was used, resulting in a channel width of 48.828 kHz, or $\sim$10 km s^{-1}. In all cases, on-line Hanning smoothing was used to increase the signal-to-noise. The observational parameters, including beam sizes, channel width, time spent on source, noise, and signal-to-noise for a single channel are listed in Table 5.3.

Data Reduction

The data reduction was performed using the AIPS software package and followed the general procedures discussed in Chapters 3 and 4. The channel zero data for the calibrators were examined and edited to remove any obviously anomalous data; once the data were deemed sufficiently edited, each data set was calibrated in both gain and phase. As mentioned in Chapter 3, most of the sources for this project were observed twice, at widely separated intervals (usually several hours apart). In these cases, each set of observations for a given source was calibrated separately, to avoid interpolating the gain and phase responses of the antennas across the long time between observations. Once

a satisfactory calibration of the channel zero data was achieved, it was then applied to the corresponding line data set.

After calibration, the source data were examined and any discrepant points were discarded. There was no overt interference present in any of the data sets, and for those observed during the daytime, only a minimal amount of solar interference was detected (the C-array, with longer baselines than the D-array, is less susceptible to solar interference). Such problems were easily identified and removed from the data.

A Fast Fourier Transform (FFT) was then applied to each (u, v) line data set, creating a cube of image maps, one map for each frequency (velocity) observed. The cube was examined and line-free channels at each end of the cube were identified. These channels were then averaged together in the (u, v)-plane (using the AIPS task AVSPC) and mapped. This map of the line-free continuum emission was then subtracted from the data cube, resulting in a cube containing only HI-line signal. The channels containing line emission were then CLEANed to remove the effects of the dirty beam (as discussed in Chapter 3).

The galaxies that were observed with a channel separation of 2.5 km s^{-1} were then Hanning smoothed to increase the signal-to-noise. This lowers the velocity resolution to twice the channel separation (Rohlfs, 1990, p. 159), but also reduces the r.m.s. noise by a factor of approximately 0.6 (40%). The loss of velocity resolution was deemed acceptable since turbulent motions (i.e. dispersion velocities) in these systems are on the order of 10 km s^{-1} (Gallagher and Hunter, 1984).

In a few cases, the signal-to-noise was so low that less than 30% of the reported single-dish flux was being recovered; this indicated that low-level signal was being lost in the noise. To further reduce the noise and therefore increase the amount of detected flux, these data sets were smoothed again; this time spatially. This was done by convolving the cubes in RA and DEC using a Gaussian function with the same FWHM as the synthesized

beam. This smoothing lowers the noise by roughly another 40% but reduces the spatial resolution by effectively increasing the FWHM of the beam in each dimension by $\sqrt{2}$.

Once each data cube was CLEANed (and smoothed, if necessary), it was blanked and integrated using the same procedure discussed for the survey data in Chapter 4. In brief, a conditional blanking was applied using a mask created by Hanning smoothing the cube in velocity, and then convolving it in RA and DEC using a Gaussian function with twice the FWHM of the synthesized beam. This is done both to suppress the noise and enhance the signal. After blanking, each data cube was integrated along the velocity axis, using the AIPS task XMOM, to produce moment maps. The flux limits used for the blanking and integrating were the same as those used for the survey project data: $\pm 2\sigma_{\rm m}$ for the blanking and $\pm 2.5\sigma_{\rm ch}$ for the integrating. A more detailed discussion of both the blanking and integrating procedures was presented in Chapter 4.

Analysis

The reduced data set for each galaxy consists of moment maps of the intensity (or column density) distribution, the velocity distribution, and the velocity dispersion associated with each point (pixel) in the moment maps. These zeroth (intensity) and first (velocity) moment maps are presented in figures located at the end of the chapter. Optical images, extracted[1] from the Digitized Sky Survey[2] (Lasker et al., 1990), are also

---

[1] Images obtained using SkyView (http://skyview.gsfc.nasa.gov/skyview.html). SkyView was developed under NASA ADP Grant NAS5–32068 by Thomas A. McGlynn under the auspices of the High Energy Astrophysics Science Archive Research Center at the Goddard Space Flight Center Laboratory for High Energy Astrophysics.

[2] Based on photographic data obtained using the Oschin Schmidt Telescope on Palomar Mountain. The Palomar Observatory Sky Survey was funded by the National Geographic Society. The Oschin Schmidt Telescope is operated by the California Institute of Technology and Palomar Observatory. The plates were processed into the present compressed digital format with their

presented with contour overlays of the HI distribution in the figures. Global velocity profiles, representing the sum of the flux in each channel (i.e. at each velocity) are shown as well. A table of the observed parameters for each galaxy, including the linear and velocity resolutions, heliocentric velocity, distance (assuming H_0 = 100 km s^{-1} Mpc^{-1}), velocity width at the 50% level of peak intensity, peak column density, and total HI mass detected are presented in Tables 5.4 and 5.5. Also included in these two tables is γ, the percentage of the single-dish HI flux (as reported in the RC3) that we have detected (i.e. the HI mass reported here compared to that listed in Tables 5.1 and 5.2).

It can be seen that we have only detected between 11% – 60% of the reported single-dish fluxes, there are two possible reasons for this. The amount of broad, low-level emission detectable by the C-array configuration of the VLA interferometer is limited by both the lengths of the baselines available (see Chapter 3) and the signal-to-noise. The C-array configuration, with a minimum baseline length of 0.073 km, is only sensitive to structures on scales smaller than about 7′ (Perley, 1994, p. 8). Structures larger than this are "invisible" to the array; therefore any extended emission will not be detected. However, none of the systems we observed is larger in any dimension than approximately 4′, so the baseline length coverage offered by the C-array configuration was more than adequate. The other, and more important, limitation is therefore the fairly low signal-to-noise for these observations ($\sim$ 5 – 10). Low-level emission will be "lost" in the noise and therefore will not be integrated up into the final moment maps. The variation in the amount of detected flux as denoted by γ is therefore due to the particular signal-to-noise for each data set, and to the amount and extent of low-level emission that may be associated with a given system.

---

permission. The Digitized Sky Survey was produced at the Space Telescope Science Institute (ST ScI) under U.S. Government grant NAG W-2166.

HI Distribution and Kinematics

The HI intensity distributions are shown in greyscale images (see figures located at the end of this chapter). The images for all 16 galaxies are shown at the same angular size: each image is $4' \times 4'$. The linear scale, calculated using the distance listed in Table 5.3, is indicated by a bar 1 kpc long, printed in the image. The angular resolution is indicated by the ellipse drawn in each image; the ellipse represents the size and position angle of the beam (convolved up by $\sqrt{2}$ for those data sets which were convolved spatially).

Unfortunately, the range in linear resolutions across the galaxy sample prevents us from being able to make a quantitative comparison of the nature of the HI distributions. The more distant and/or smaller systems are not as well resolved by the synthesized beam, and so it is difficult to make definitive statements about the true nature of the HI distributions in these cases. It can be seen in the moment maps that several of the BCD galaxies are just barely resolved by the beam, particularly A1116+51, Haro 27, Mrk 328, and Mrk 67. The LSBDs, which are for the most part at closer distances than the BCDs in this sample, are better resolved and exhibit a variety of structures. For instance, DDO 43, DDO 242, and DDO 88 resemble incomplete rings surrounding central depressions, and DDO 131, DDO 52, and DDO 56 apparently consist of several concentrations, or "clumps", of HI.

Information about the kinematics of the HI gas in these galaxies is available by examining the global profiles and velocity distribution maps as well as the velocity dispersion (second moment) maps. The global profiles are an indication of the distribution and motion of the HI gas in the galaxy; the intrinsic velocity width (i.e. after correction for the velocity resolution of the observations; see equation (4-30)) is produced by both the random motions, known as the dispersion velocity, and the ordered motions, or

rotation, of the gas. The shape of the global profile can be used to estimate the type and amount of rotation present in the system. A rotating disk with a turn-over in the velocity field (i.e. a flattening or decrease in the rotation curve) will have a "double-horned" profile with a central depression; this depression will be less pronounced for systems with greater central concentrations of HI (Gordon, 1979). For the case of a very centrally concentrated system, or one with a rotation velocity of the same magnitude as the dispersion velocity, the profile will appear almost Gaussian. This type of profile is frequently seen for dwarf irregular galaxies. Four of the eight BCDs in our sample (A1116+51, Haro 33, Haro 4, and Haro 36) and three of the LSBDs (DDO 169, NGC 4163, and DDO 242) have approximately Gaussian profiles.

Information about the motion of the HI gas in a system is available not only from the shape of its velocity profile, but also from its width. Since the intrinsic width is due to the combination of the random and rotational velocities of the gas, a broader profile indicates either an increased dispersion or greater rotation velocity. As mentioned earlier, it is thought that the dispersion velocity in most galaxies is on the order of $\sim$ 10 km s^{-1}, and so a broader profile usually is taken as evidence of greater rotation.

The first moment maps of the velocity distributions provide information about the ordered motions in the galaxies. The gradient in velocity across the system, as indicated in these maps by the greyscale shading from light to dark, is a result of the radial motion of the gas towards and away from the observer. Direction of the rotation can be deduced from the isovelocity contours, or "isovels", which are aligned with the axis of rotation and so are perpendicular to the plane of rotation. The magnitude of the velocity gradient can provide an estimate of the amount of rotation present as well. In our sample, Haro 27 is a good example of a system undergoing rotation: it has a wide profile ($\sim$ 156 km s^{-1}) with steep sides and a fairly flat, slightly sloping top, and the first

moment map shows a steady gradient across the galaxy, with crowded, parallel isovels. In contrast, DDO 242 has a narrow, essentially Gaussian profile of approximately 19 km s^{-1} (all velocity widths reported here have been corrected for the channel resolution) and shallow velocity gradient, with widely separated isovels that are suggestive of a somewhat disordered velocity field.

The HI distribution and kinematics of each galaxy are described below, along with a brief description of the stellar distribution as compared to the HI as demonstrated by the HI overlays on the optical images. The HI distribution and velocity maps, as well as the profiles are in the figures following the body of this chapter. The dispersion velocity information was obtained by taking the average value off the second moment map, within the 2σ contours; these values are listed in Tables 5.6 and 5.7.

A1116+51. This galaxy is just barely resolved by the (convolved) beam, and so detailed information on the HI structure is not available, although the column density map does show a central concentration. The velocity map shows a somewhat shallow gradient, and this combined with the narrow Gaussian global profile would indicate that this system has a low rotation velocity. However, it should be pointed out that we have only recovered approximately 11% of the listed single-dish flux for this system, and our measured velocity width (Δv_{50}) is only about 1/3 of the one catalogued in the RC3. The average dispersion velocity from the second moment map (not shown) is about 14 km s^{-1}, indicating that the velocity field is somewhat disordered. The optical image (Figure 5.4) with the HI column density contours shows an offset between the stellar and HI distributions of about 3 arcsec in RA and 2 arcsec in DEC. Whether this offset is real, or produced by a difference in the coordinate reference frames used for the two type of data, is unclear. In any case, the HI and stellar distributions appear to be centrally concentrated to some degree.

Haro 33. This system is somewhat better resolved, and the HI distribution appears to be fairly symmetric and centrally condensed. The velocity distribution map shows somewhat ordered motion, but again, the gradient is fairly shallow and the velocity width and Gaussian profile are indicative of a fairly low, essentially solid-body type of rotation. The dispersion velocity for this galaxy is about 16 km s^{-1}, which is indicative of a fairly significant turbulent component to the HI gas. As with A1116+51, there appears to be a slight offset between the optical and gaseous distributions; the same caveat about the validity of this offset applies. The HI shows a small "blob" to the east, with the nearby HI contours of the galaxy apparently stretched in this direction as well. It is not currently known whether this HI feature is related to the small optical knot apparently located in the southeast of the system; optical spectroscopy of the knot would be necessary to establish its association with Haro 33.

Haro 4. Haro 4, also known as Mrk 36, is another galaxy that is barely resolved, and so not much more can be said about its HI distribution other than that it appears here to be somewhat centrally concentrated. It too possesses a narrow Gaussian global profile; the small "bump" in the profile about 680 km s^{-1} is associated with the very small (and just barely significant) HI feature located to the northwest of the body of the galaxy. The optical image shows slight elongation along this direction which is also seen in HI. The velocity map shows an almost nonexistent gradient across the galaxy, reinforcing that the rotation rate of the system is fairly low.

Haro 27. This galaxy is slightly more resolved than Haro 4, and shows less central condensation as well. The HI is slightly elongated as is the optical; again, it is not known whether the slight offset between the two is real. This system has a very broad, non-Gaussian global profile (156 km s^{-1}), and the velocity map shows both a steep gradient and very crowded parallel isovels. Clearly Haro 27 is undergoing significant (for a dIrr)

rotation. The average dispersion velocity from the second moment map is also on the high side, with a value of 28 km s^{-1}.

Haro 36. Haro 36 is even more resolved than Haro 27, and the HI distribution in the center gives a hint of the existence (perhaps) of two peaks, or one elongated one. The profile is of moderate width, and resembles a sightly asymmetric Gaussian. The velocity field shows a moderate gradient, and the isovels show that some ordered rotation is taking place. The average dispersion velocity is about 14 km s^{-1}. Again, we have a system with a small HI feature, located to the northeast and slightly separated from the main body of the galaxy, aligned along the major axis of what appears to be both an optical and HI elongation.

Mrk 328. This galaxy is just barely or not quite resolved, and we have detected only about 17% of the single-dish flux. Although it appears quite compact optically and in HI, the velocity map and global profile indicate that this galaxy, like Haro 27, is undergoing significant rotation. There appears to be an offset of the HI with the optical distribution of a few arcseconds in each direction, but as with the other systems showing this, we cannot state whether this is a coordinate problem, or is truly the case.

Mrk 51. Mrk 51, with the broadest global profile (158 km s^{-1}), is undergoing significant rotation; there may even be a hint in the curvature of the outermost isovels that the rotation curve turns over, which is not seen in any of the other galaxies in this sample. The dispersion velocity, with an average value of 22 km s^{-1}, is also fairly significant, indicating that there are fairly large turbulent motions in the gas in addition to the ordered rotational ones. The galaxy is resolved, and there appears to be a significant concentration of HI in the center. The optical image and HI overlay show that the two distributions are slightly elongated along the same direction, but again, there appears to be an offset that may or may not be real.

Mrk 67. Mrk 67 is not spatially resolved, and so the HI distribution simply appears essentially beam-shaped and centrally concentrated. The velocity map and double-horned global profile both indicate that the system is rotating; the lack of an apparent turn-over in the velocity field (which would be seen in a closing of the isovels) would indicate that the central depression of the profile is the result of an HI distribution which is NOT centrally concentrated. This is in contrast to the apparent distribution on the column density map; however the poor spatial resolution we have for this system may be masking the true state of affairs. Another possibility is that the poor signal-to-noise is preventing us from observing far enough out in the galaxy to observe a turn-over in the velocity field. The velocity width is moderate (49 km s^{-1}), and the isovels reflect this and also show what appears to be solid-body rotation although the poor spatial resolution makes this difficult to determine. The optical and HI distributions appear to be well-aligned, with the HI peak falling very near the center of the optical body of this compact system; but recall that the poor resolution of the HI data provides very limited information.

DDO 43. This is the first of our LSBD sample and is the first system where we have good resolution. The HI shows a ring-shape surrounding a central hole, with the majority of the HI located in a "clump" in the north side of the ring. The global profile, of moderate width, and the velocity map indicate that the entire ring is rotating; the differing angle of the isovels within each of the 4 or so major concentrations of HI hint that each "clump" may be rotating as a somewhat independent entity as well, although this is far from conclusive. The average dispersion velocity across the entire system is very low, about 6 km s^{-1}; examination of the second moment map shows that the highest dispersions (about 13 km s^{-1}) are associated with the large concentration in the north part of the ring. Comparison of the optical and HI distributions show that, even given the uncertainty in the alignment of the two coordinate frames, the HI is located

almost entirely on the outskirts of the optical body of the galaxy, and in fact appears to be essentially surrounding it. Since we have detected only about 20% of the single-dish flux, there may be HI located within our central hole, but it is low level and/or broad enough that we have not "seen" it with the VLA.

DDO 169. This system is also fairly well resolved but exhibits a much more regular HI distribution than the ring of DDO 43. The HI for DDO 169 is smoothly distributed, with a central concentration and a slight "tail" trailing off to the south east. During the reduction of the data for this system, an HI companion was detected, located about 2 kpc to the northwest of DDO 169. This companion appears to have a very faint optical counterpart on the POSS survey plate (see footnote 3, this chapter) and is discussed in more detail in Appendix A. It should be noted that the single-dish flux listed for DDO 169 in the RC3 includes the HI mass of the companion as well. We have included only the emission from DDO 169 itself in our calculations.

The velocity information for this galaxy, including the moderately wide, slightly asymmetrical, Gaussian profile as well as the separated isovels and shallow gradient of the first moment map, show that it is undergoing some modest rotation. The average dispersion velocity is also moderate, at about 12 km s^{-1}. The optical and HI images, however, show that the optical emission extends farther to the northwest, in the direction of the companion, than the HI distribution does. There are two bright knots in the center of the optical image as well, one of which appears to coincide with the peak in the HI distribution. The extension of the HI to the southeast and the lack of HI to the northwest are intriguing in light of the presence of the companion along the same major axis. Further optical and HI observations of this system are required for a more detailed study.

DDO 52. This is another well-resolved system in which we can see some of the structure in the HI. Most of the gas is located to the south and appears to have two

areas of concentration. The optical image with the HI overlay shows that this southern concentration is also south of the center of the optical emission from the galaxy. There appears to be an enhancement of optical emission in the center of the optical body, with an HI complex located to the west of it. The velocity gradient across the HI emission is evidence of the rotation of the system as a whole; the shape of the global profile is slightly "double-horned" as well. As for DDO 43, the dispersion velocity calculated from the second moment map is quite low: about 6 km s^{-1}.

NGC 4163. NGC 4163 has a well-resolved HI distribution with two areas of concentration and a slight, hooked "tail" exending from the southwest part of the distribution up to the west and slightly north. The narrow Gaussian profile indicates a low rotation velocity, and the dispersion velocity is low as well (about 7 km s^{-1}). The velocity map shows shallow gradients across both of the HI concentrations, each of which has a slightly different average velocity; they may be rotating about each other in some sense. The optical distribution appears to be essentially round in shape, with two optical knots located in the north part of the optical emission. The HI distribution overlies the optical, but the HI concentrations do not appear to coincide with any noteworthy optical features. The HI tail in the southwest does not appear to have any optical counterpart in this image.

DDO 131. This galaxy has a very striking HI distribution consisting of at least three major concentrations of HI that appear to be arranged side-by-side. The global profile is broad, and the velocity gradient on the first moment map reflects this. The isovels run parallel to the major axes of the clumps, and to each other; the entire system seems to be rotating as an entity, however the slightly different distribution of the isovels among the three concentrations would seem to indicate that each clump possesses a different amount of rotation. Unfortunately, the very low optical surface brightness of this system

makes it difficult to compare the stellar distribution with the HI. The majority of the optical body seems to be more-or-less aligned with the largest, central concentration of HI however. It is impossible to tell from the optical image whether there is an optical counterpart to the two side clumps.

DDO 242. Although not quite as well resolved as the previous galaxy, DDO 242 also shows interesting structure in its HI gas. The majority of emission is from a large concentration to the east, with a smaller concentration located to the southwest. This system has the slight appearance of an incomplete ring, or perhaps two elongated neighboring associations. The Gaussian profile is relatively narrow, and the velocity field exhibits a shallow gradient. The dispersion velocity for DDO 242 is also quite low, about 5 km s^{-1}. The optical distribution is quite different than that seen in the HI map; the galaxy has an almost rectangular appearance, with many small optical knots scattered throughout.

DDO 88. The HI distribution for DDO 88 strongly suggests a ring-shaped distribution, and the hint of a central depression in the global profile, combined with a lack of turn-over in the velocity field, would seem to confirm this. The ring consists of several concentrations of HI, with the largest in the north part of the ring. This is another low dispersion velocity system, and the velocity field has a shallow gradient that indicates rotation of the entire ring-shaped distribution. The two most concentrated HI clumps do not appear to have any rotation apart from that of the system as a whole. As for DDO 43, the HI ring appears to encircle the optical distribution, with the central hole coinciding with the bulk of the optical body.

DDO 56. DDO 56, like A1116+51, is a system in which we have detected only about 12% of the single-dish flux. From the appearance of the column density map and the global profile, it would seem that we have detected only the high-density peaks of

the distribution. The signal-to-noise of this set of observations was only $\sim$ 4.6, so we have lost much of what must be a lower-intensity distribution of HI. The velocity map shows system-wide rotation, with perhaps a clump in the southwest undergoing some independant rotation. From the channel maps, it would appear that the northeast and southwest parts of the HI are revolving about each other, but since we are missing so much of the flux in the system, it is hard to draw any conclusions. The optical image, like that of many of the LSBDs in our sample, is essentially round in shape. The HI peaks that we have picked up do not appear to be associated with any optical features apparent in the digitized image.

Observed Parameters and Correlations

In this section, the methods used to derive some of the properties and characteristics of the galaxy sample are discussed, as well as the results from a series of linear regressions performed to examine the relationships between these properties. The observed and derived parameters are listed in Tables 5.4 through 5.7.

Optical parameters. The optical information for our sample was obtained from the RC3; several of these are listed in Tables 5.1 and 5.2. We are interested in examining how the HI properties of these galaxies may differ with respect to the color indices, which we are using as a rough guide to the stage of star formation occurring in these systems. In order to arrive at a single parameter that would be descriptive of this, we have calculated the (U – V) color index from the (B – V) and (U – B) color indices (total indices, corrected for galactic and internal extinction) listed in the RC3. The U band is sensitive to the amount of higher energy flux put out by young, hot, O and B type stars, while the V band is more indicative of the flux from cooler, more evolved stars. The (U – V) color index therefore is a measure of the amount of emission from hot younger stars (formed relatively recently) to that from an older, longer-lived population.

From the listed value of the apparent B magnitude (B_T^0) and the (U – B) color index, we then calculated the apparent U magnitude, and from that and the distance (determined from our HI observations, listed in Tables 5.4 and 5.5), we were able to calculate the absolute U magnitude, M_U, and therefore the U luminosity of each galaxy using the following relation:

$$log\left(\frac{L_U}{L_{B_\odot}}\right) = \frac{M_{B_\odot} - M_U}{2.5}\,. \qquad (5\text{-}1)$$

Note that this is expressed, however, in units of blue solar luminosity, where we have used $M_{B_\odot} = 5.39$ (Staveley-Smith et al., 1992).

As we are also interested in the optical size of these galaxies, we have calculated the Holmberg diameters based upon the information listed in the RC3 (see the notes to Tables 5.1 and 5.2 for details). The Holmberg diameter extends out to the 26.5th isophote and is often used as a good indication of the size of the stellar distribution. The angular Holmberg diameters are listed in Table 5.1 and 5.2; the corresponding linear sizes were calculated using the distances determined from our HI observations. The rest of the derived optical information is listed in Tables 5.6 and 5.7.

HI parameters. Some of the HI parameters determined from our observations are listed in Tables 5.4 and 5.5, such as the total HI mass detected and the 50% velocity widths. The rest, described below, are in Tables 5.6 and 5.7.

In order to have a consistent set of HI properties for comparison with both the optical (isophotal) parameters and for comparison of the HI parameters between the galaxies in our sample, we have established two sets of HI masses and radii. The first, defined as the area and HI mass within the 2×10^{20} atom cm^{-2} contour, is intended as a measure of the majority of the detected flux and is representative of the amount of low density gas in the system. The second, the HI mass and area defined within

the 5×10^{20} atom cm^{-2} contour, is a measure of the high density gas. This contour level was chosen as it is mentioned as a rough empirical estimate of the minimum column density required for the formation of O and B type stars (Gallagher and Hunter, 1984). The HI dimension, R_{HI}, for each of these levels was determined by taking the square root of the area as indicated by the number of pixels contained within the given contour level. These dimensions, defined by a specific column density, are analogous to the optical, isophotally defined Holmberg diameter. In addition to being consistent with the optical parameters, these "isophotal" HI measures also provide a common system of measurements for comparison of the HI properties of our sample. Recall that we have not been able to recover all of the HI flux in these observations and that the fraction of the total flux that we have detected varies widely from galaxy to galaxy. This makes comparisons of, for instance, the total HI masses somewhat uncertain. This problem is mitigated by using masses and dimensions out to a common density level.

For the 2×10^{20} atom cm^{-2} parameters, we only have data for 15 of our 16 galaxies; the LSBD galaxy DDO 56 has a peak density of just over 2×10^{20} atom cm^{-2} and so has no measurable mass or radius at that contour. The 5×10^{20} atom cm^{-2} parameters exclude an additional three systems: the BCDs A1116+51, Mrk 328, and Mrk 67 do not reach peak densities greater than 3 or 4×10^{20} atom cm^{-2} and so cannot be included.

In examining the kinematics of our sample of galaxies, we have estimated the dispersion velocities using a method similar to that used by Lo et al. (1993). The average dispersion, $\langle \sigma_v \rangle$, associated with a galaxy was determined by using the AIPS task TVSTAT to find the average value of the second moment map produced by the AIPS task XMOM (see Chapters 3 and 4). In order to reduce the inclusion of spurious values in this calculation, we restricted the estimation to those pixels with flux values on the

zeroth moment map greater than twice the r.m.s. on the zeroth moment map ($\sigma_{\rm xmom}$; see Chapter 4.) These values are listed in Tables 5.6 and 5.7.

As we do not have the spatial resolution necessary to produce rotation curves for these systems, an alternative method of evaluating the rotation velocity had to be found. Following Staveley-Smith et al. (1992), we have calculated the ratio of the rotation to the dispersion velocity (V_{rot}/σ) and then calculated the rotation velocity by multiplying this ratio by the average dispersion $\langle\sigma_v\rangle$ taken from the second moment maps. The (V_{rot}/σ) ratio is found from their equation (3), which is reproduced here:

$$\left(\frac{V_{rot}}{\sigma}\right)^2 = \frac{\left(1+2q^2\right)\cos^{-1}q - 3q\sqrt{1-q^2}}{q\sqrt{1-q^2} - q^2\cos^{-1}q}\,, \tag{5-2}$$

where q is the intrinsic axial ratio of the system, and requires some explanation. As stated by Staveley-Smith et al. in their 1992 paper, low-mass galaxies, with relatively low rotation rates as a rule, are "fat, not flat objects." When calculating inclinations from observed axial ratios (p), the usual method is to assume an intrinsic flattening; this is often taken as 0.2, the typical value observed for spirals, which are known to be rotating disk systems. Such an intrinsic value is not appropriate for the type of systems under study here, as pointed out by Staveley-Smith et al. (1992) and Lo et al. (1993). In an appendix to that paper, Staveley-Smith et al. show that the intrinsic axial ratio distribution for three different samples of dIrrs, BCDs, and LSB galaxies is well-fit by a power-law distribution and they derive a mean intrinsic axial ratio of $\langle q\rangle = 0.58$. They also find an expression to find the most likely intrinsic axial ratio, q, for a given observed axial ratio, p:

$$q = 0.65p - 0.072p^{3.9}\,. \tag{5-3}$$

We have used the axial ratios (b/a) listed in Tables 5.1 and 5.2 to find values for q and thus for (V_{rot}/σ). The values for (V_{rot}/σ) are listed in Tables 5.6 and 5.7. V_{rot} was found by multiplying (V_{rot}/σ) by $\langle\sigma_v\rangle$.

Estimating the total (dynamical) masses for dwarf galaxies is quite uncertain and somewhat model-dependent. Again, we follow the methods used by Staveley-Smith et al. (1992) and Lo et al. (1993). Essentially, instead of modeling the galaxy as a rotationally dominated, inclined disk system, they both use a virial mass estimate. Starting from the virial theorem, and assuming the system is in equilibrium, we have

$$2K + |U| = 0\,, \tag{5-4}$$

where K is the kinetic energy contained in the system, and $|U|$ is the potential energy. The potential energy can be written as

$$|U| = \frac{GM_T M_{HI}}{\beta r}\,, \tag{5-5}$$

where r is defined as the gravitational radius, M_T is the total (virial) mass, and β is a shape parameter which is 5/3 for a uniform sphere of constant density. (For a more detailed derivation and explanation, see Lo et al., 1993). The kinetic energy, K, is the sum of the kinetic energy of the rotational motions, T, and the kinetic energy of the random motions, Π. Assuming solid body rotation, we then find that

$$\begin{aligned} K &= T + \Pi \\ &= M_{HI}V_{rot}^2 + \alpha\frac{\sigma^2 M_{HI}}{2} \\ &= M_{HI}\left(V_{rot}^2 + \alpha\frac{\sigma^2}{2}\right)\,. \end{aligned} \tag{5-6}$$

Here, α is a parameter that characterizes the random motions, and is 3 for an isotropic velocity dispersion (Staveley-Smith et al., 1992). Combining this result with the equation for the potential energy, above, and solving for the total mass, we find

$$M_T = 2.32 \times 10^5 \beta r\left(2V_{rot}^2 + \alpha\sigma^2\right)\,, \tag{5-7}$$

where M_T will be in solar masses for r in kpc and V_{rot} and σ in km s^{-1}. When calculating the total masses listed in Tables 5.6 and 5.7, we have used $\alpha = 3$ and $\beta = 1.35$, which is a spherical distribution that follows a power-law density distribution (Lo et al., 1993). We have used V_{rot} as described above, and $\sigma = \langle \sigma_v \rangle$ from the second moment maps; and r is the Holmberg radius listed in Tables 5.1 and 5.2 (since these were usually larger than the HI radius as measured by the 2×10^{20} atom cm^{-2} contour).

Several other parameters have also been calculated, and are tabulated in Tables 5.6 and 5.7. These include the optical surface brightness,

$$\mu_L \equiv \frac{L_U}{R_{26.5}}, \tag{5-8}$$

and the HI surface density,

$$\mu_{HI} \equiv \frac{M(2)_{HI}}{R(2)_{HI}}, \tag{5-9}$$

where the *(2)* denotes the "isophotal" values at the 2×10^{20} atom cm^{-2} contour. R_{HI} is the linear dimension calculated from the distance and the angular size of the distribution.

Using the optical and HI parameters described above, we have also calculated some "hybrid" parameters, such the HI mass-to-light ratio, (M_{HI}/L_U). In this instance, we did use the total HI mass detected, rather than an "isophotal" value such as $M(2)_{HI}$. The total HI mass was used since the quantity L_U is calculated from the *total* U absolute magnitude (extrapolated from an isophotal to an asymptotic value; see Vol. I of the RC3 for further explanation and references).

Correlations Using the parameters listed in Tables 5.4 through 5.7, we have run a series of linear regressions and evaluated the correlation coefficients to see whether any of them are related. A linear regression attempts to fit a line of the form $y = ax + b$ to a set of data (x_i, y_i). The correlation coefficient, r, is a measure of the scatter of the

data around this fitted relation. However, the distribution of r is not Gaussian; therefore to evaluate the significance of a given value of r it is necessary to first transform its somewhat complex distribution into a more easily evaluated one, such as a Gaussian. This can be done using the z transform (Hoel, 1954):

$$z = \frac{1}{2} ln \left(\frac{1+r}{1-r} \right) . \tag{5-10}$$

z is normally distributed, with a standard deviation

$$\sigma_z = \frac{1}{\sqrt{N-3}} , \tag{5-11}$$

where N is the number of samples in the data set. As 95% of the data in a Gaussian distribution will fall within $\pm 2\sigma$ of the mean, we have defined as significant any correlation with $(z/\sigma_z) \geq 2$.

To investigate whether or not dIrrs are rotating disk systems, we have checked the correlation between the observed (optical) axial ratio, (*b/a*), and the FWHM velocity width, Δv_{50}. Since our observations represent only part of the total HI flux, we have used the velocity widths listed in the RC3 rather than those found from our observations (see Tables 5.1 and 5.2). Rotating inclined disks should show a correlation between the axial ratio and the velocity width, with Δv_{50} increasing as (*b/a*) decreases. In Figure 5.66, a plot of the observed Δv_{50} vs. the axial ratio, it can be seen that the BCDs do indeed show this sort of relationship. The regression line is indicated, and the fit has a significance of z/σ_z = 1.9. The LSBDs, on the other hand, do not show a similar correlation; the correlation coefficient for the LSBDs is only $0.71\sigma_z$.

If the BCDs are indeed rotating inclined disks, then the Δv_{50} vs. (*b/a*) correlation should decrease once the observed velocity widths are corrected for inclination (Gordon, 1979). This is done by dividing Δv_{50} by the sine of the inclination, which is calculated

from the observed axial ratio:

$$cos^2(i) = \frac{\left(\frac{b}{a}\right)^2 - q^2}{1 - q^2}\,; \tag{5-12}$$

where q is the intrinsic axial ratio. (We have used $q = 0.58$, as discussed in the section on rotation velocities, above). In Figure 5.67, we have plotted Δv_{50}, corrected for inclination, vs. the axial ratio, and it can be seen that the correlation for the BCDs has decreased. This is reflected in the value of the correlation parameter as well; it decreases from $1.9\sigma_z$ to $1.1\sigma_z$. We have also plotted the corrected velocity widths for the LSBD sample as well, and they show an *increase* in correlation: from $0.71\sigma_z$ to $1.3\sigma_z$. We have indicated this by drawing in the regression line for the LSBD sample. Hence, it would appear that the BCDs are in some sense rotating inclined disks, but the LSBDs are not. Gordon (1979) also found a correlation for his sample of BCDs, with the faintest objects having the strongest correlation.

The next correlations we tested for involved the color of the systems, as indicated by their (U – V) color indices, and various HI distribution and kinematical parameters. No correlation was found for (the logs of) $R(2)_{HI}$, $\mu(2)_{HI}$, or (M_{HI}/M_T) vs. (U – V); the significance levels were 0.47, 0.62, and $0.81\sigma_z$, respectively.

A correlation was found, however, for the log of $(M(5)_{HI}/M_{HI}(2))$ vs. (U – V), when the BCD galaxy Haro 36 is not included. We have used the ratio of the HI mass within the 5×10^{20} atom cm^{-2} contour to that within the 2×10^{20} atom cm^{-2} contour as an indication of HI concentration; galaxies with higher ratios contain more concentrated HI. Figure 5.68 shows all the available data plotted; Haro 36 is the point lying off to the upper right. This indicates that relative to the rest of the sample, this galaxy has "too much" high density gas for its (red) color. The regression line is plotted in the figure and is

$$log\left(\frac{M(5)_{HI}}{M(2)_{HI}}\right) = -0.377\,(\pm 0.045)(U - V) - 0.246\,(\pm 0.016)\,; \tag{5-13}$$

the correlation coefficient significance is $1.97\sigma_z$. This indicates that bluer galaxies have greater concentrations of HI, which is in accord with the concept of a critical threshold gas density for massive star formation.

We have also looked at the HI mass-radius relation for our galaxies; this is shown in Figure 5.69 where we have plotted log $(M(2)_{HI})$ vs. $R(2)_{HI}$. As this is a well-known relation in general, it is not surprising to see that relationship is quite tight, with a correlation significance of $5.74\sigma_z$. The fitted regression line is

$$log(M(2)_{HI}) = 0.513\,(\pm 0.014)\,R(2)_{HI} + 6.072\,(\pm 0.027)\,. \qquad (5\text{-}14)$$

This is in fair agreement with the results from Gordon (1979) for his sample of BCDs. He finds a slope (a) of 1.51 and an intercept (b) of 7.68 for his $\log(M_{HI}) - \log(R_{26.5})$ plot; in log-log space, we find a slope and intercept of 2.15 and 6.53, respectively, and a significance of 5.67. Note however, that while Gordon has used an optical dimension, $R_{26.5}$ (the only one available to him), we have used the HI dimension instead.

The next correlations checked involved the HI kinematic parameters. While there was no correlation found for the log of (V_{rot}/σ), as determined from equation (5-2), vs. (U – V), there is a correlation between the log of the average velocity dispersion $\langle\sigma\rangle$ and (U – V), but only for the LSBD galaxies. This is shown in Figure 5.70, where the regression line for the LSBDs has been plotted. This line,

$$log\langle\sigma\rangle = -0.296\,(\pm 0.038)\,(U - V) + 0.906\,(\pm 0.019), \qquad (5\text{-}15)$$

for the LSBDs only, has a correlation significance of $1.94\sigma_z$ and demonstrates that the bluer LSBDs have higher dispersion velocities. Another feature evident from this plot is that, as a group, the BCDs have higher velocity dispersions than do the LSBDs, even when they have similar colors. This was also suggested by Staveley-Smith et al. (1992), when discussing the higher velocity widths they observed for their BCDs as compared

to LSB galaxies of the same luminosity. They suggested that the broadening could be a result of increased dispersions in the ISM of the BCDs due to the kinetic energy deposited there by the starburst, in the form of supernovae explosions and stellar winds from young, massive stars. This would also be in accord with our LSBD correlation, since the bluer systems, thought to be more active, have higher velocity dispersions. We also checked for correlations between the log of (V_{rot}/σ) and the logs of (M_{HI}/L_U) and (L_U), but none were found.

The next relationships examined involve the optical parameters as well as those for the HI. The log of the Holmberg diameter, $R_{26.5}$, is correlated with the (U – V) color index, with a correlation significance of $2.08\sigma_z$. The relation is

$$log(R_{26.5}) = 0.268\,(\pm 0.027)\,(U-V) + 0.408\,(\pm 0.013)\,; \qquad (5\text{-}16)$$

and is shown in Figure 5.71. There is no apparent difference in the distribution of the BCD and LSBD samples; for both, the bluer systems are more optically compact.

A correlation was also found for the log of the optical surface brightness, μ_L vs. (U – V). This is of the form

$$log(\mu_L) = -0.671\,(\pm 0.065)\,(U-V) + 7.161\,(\pm 0.031)\,, \qquad (5\text{-}17)$$

and has a correlation significance of $2.18\sigma_z$. Examination of Figure 5.72 shows that with one exception, DDO 242, all the LSBDs lie below this regression line; while all the BCDs, with one exception, A1116+51, lie above it. This is a reflection of the distinguishing characteristic of these two different types of systems: the BCDs have high surface brightnesses as they are both luminous and compact, and the LSBDs, as their name implies, have low surface brightnesses. Note that Haro 36, which is located in the lower right of the plot, and which was previously identified as having a large high-to-

low-density HI gas ratio for its color, also has a low surface brightness. In this case, however, its low surface brightness fits right in with its red color.

Figure 5.73 shows the next relationship found; that between the absolute magnitude M_U (i.e. the log of the luminosity) and the log of $R(2)_{HI}$. This correlation has a significance of $2.31\sigma_z$, and is represented by

$$log(R(2)_{HI}) = -0.094\,(\pm 0.009)\,(M_U) - 1.142\,(\pm 0.128)\,. \qquad (5\text{-}18)$$

The distribution of the BCDs and LSBDs is similar, with systems of greater luminosity (absolute magnitude) having larger HI dimensions, as measured at the 2×10^{20} atom cm^{-2} contour.

The final set of correlations investigated involved the ratio of the total HI mass to the optical luminosity, (M_{HI}/L_U). Although there was no correlation of this quantity with either (U – V) and only a weak correlation ($1.43\sigma_z$) with M_{HI}, there is a $2.10\sigma_z$ correlation with the log of the HI surface density, $\mu(2)_{HI}$, but only for the BCDs. Figure 5.74 shows this result, with the BCD regression line,

$$log\left(\frac{M_{HI}}{L_U}\right) = 1.166\,(\pm 0.134)\; log(\mu(2)_{HI}) \; - 1.674\,(\pm 0.081)\,, \qquad (5\text{-}19)$$

plotted. From this, it can be seen that the BCDs with higher HI surface densities are those with higher HI mass-to-light ratios, while this is not true for the LSBDs.

In addition to the previous correlation, a relationship between the ratio of the HI mass to the optical luminosity and the ratio of the HI mass to the total mass was also found. The linear regression is

$$log\left(\frac{M_{HI}}{L_U}\right) = 0.460\,(\pm 0.045)\; log\left(\frac{M_{HI}}{M_T}\right) \; - 0.042\,(\pm 0.080)\,, \qquad (5\text{-}20)$$

with a correlation significance of $2.19\sigma_z$. Unlike the correlation with the HI surface density, this relation is true for both the LSBDs and the BCDs, and there does not appear

to be much difference between their distributions, as seen in Figure 5.75. This plot shows that galaxies with higher proportions of HI to total mass also have higher HI mass-to-light ratios.

Since M_{HI} is common to both parameters in the preceding relation, this is, in essence, also a relation between the total HI mass and the luminosity, which is known as the Tully-Fisher relation. The classic Tully-Fisher relation is one between the luminosity and the rotational velocity (of a spiral system): $L \propto V^4$, and since the total mass is a function of the velocity squared, this relation can be written as $L \propto (M_T)^2$. A linear regression between the log of these two parameters (Figure 5.76) has a correlation significance of $3.13\sigma_z$, and shows that

$$log\,(M_T) = 0.894(\pm 0.057)\, log\,(L_U) + 1.737(\pm 0.454)\,, \qquad (5\text{-}21)$$

which is equivalent to $L_U \propto (M_T)^{1.12}$. This is a slightly flatter relation than the one given by the classic Tully-Fisher, but shows that dwarf systems also have a correlation between their luminosities and total masses that is similar to that for larger galaxies: more massive galaxies are more luminous.

Discussion

In summary, linear regression analysis of our galaxy sample has revealed the following correlations:

log ($M(5)_{HI}/M(2)_{HI}$) vs. (U – V): $1.97\sigma_z$

log ($M(2)_{HI}$) vs. $R(2)_{HI}$: $5.74\sigma_z$

log ($\langle\sigma_v\rangle$) vs. (U – V): $1.94\sigma_z$; LSBDs only

log ($R_{26.5}$) vs. (U – V): $2.08\sigma_z$

log (μ_L) vs. (U – V): $2.18\sigma_z$

log $(R(2)_{HI})$ vs. M_U[3]: $2.31\sigma_z$

log (M_{HI}/L_U) vs. log $(\mu(2)_{HI})$: $2.10\sigma_z$; BCDs only

log (M_{HI}/L_U) vs. log (M_{HI}/M_T): $2.19\sigma_z$

log(M_T) vs. log(L_U): $3.13\sigma_z$.

In addition to these relationships, discussed further below, we have also presented moment maps of the HI intensity and velocity distributions, as well as a global velocity profile for each system. Although limited by the poor spatial resolution obtained for the BCD galaxies, the intensity maps seem to indicate that the HI for the two different galaxy types appears to be differently distributed. Certainly, we have detected significant structure in several of the LSBD systems, which is not apparent even in the best resolved of our BCD sample: Haro 33, Haro 36, and Mrk 51, with the highest spatial resolution, all have centrally concentrated, essentially smooth HI distributions. This is in sharp contrast to the ring-shaped distributions of DDO 43, DDO 242, and DDO 88, as well as the "lumpiness" of DDO 131 and DDO 56.

More evidence for the association between star-formation and central concentration of HI is given by the correlation we have found between the (U – V) color index and our concentration parameter, $\left(\frac{M(5)_{HI}}{M(2)_{HI}}\right)$. This correlation shows that those systems with greater concentrations of high density gas are bluer and presumably are forming stars more actively and recently than those with lower HI concentrations. The poor signal-to-noise of our observations unfortunately precludes our being able to make the rotation curve analysis necessary to derive a likely value for a critical gas density threshold. This was done for a sample of low surface-brightness galaxies by van der Hulst et al. (1993), who used Kennicutt's formulation (1989) based upon a Jean's criterion for the collapse

---

[3] Absolute U magnitude

of a cloud to estimate a critical density for each of their galaxies. Comparison of this threshold density (which is a function of radius) with the radially averaged HI surface density revealed that their measured values fell below the critical threshold in these low surface brightness systems. Their result lends support to the idea that a certain density of HI gas is necessary to support significant star formation.

Perhaps the most significant difference in the HI distributions is the location of the HI with respect to the optical emission in these systems. Although there may be some slight offset of the HI and optical for a few of the BCDs, in general there is good agreement between the two types of emission. For each of three LSBD galaxies with "ring-shaped" HI distributions, however, there is very little coincidence with the optical structure of the systems. The rings instead appear to encircle the visible regions. For several of the other LSBD systems, too, there are regions of stellar emission with no associated HI emission detected; this is particularly true for DDO 52 and DDO 56.

These results would tend to lend credence to the picture formulated under SSPSF, wherein a star-formation burst occurs when the HI reservoir of the system is centrally concentrated, as in the BCDs. The HI reservoir then undergoes central depletion and expansion, and the starburst turns off. We would then expect to see low surface-brightness systems with most of their HI located on the outskirts of the optical galaxy, which is exactly what we have detected in several of our LSBD systems.

The correlation of the average dispersion velocities with (U – V) color for the LSBDs also provides some evidence that this scenario is correct. The bluer (presumably more active) LSBD galaxies have higher dispersions, which could be a result of increased turbulence in the ISM due to recently ended star-formation. Although this relationship is not seen in the BCDs, they do, on average, have higher dispersion velocities than the LSBDs; again this could be due to the injection of kinetic energy

into the system from the evolution of the high mass stars that are produced in a starburst.

We also find that fainter galaxies have smaller HI dimensions as defined by the 2 $\times$ 10^{20} atom cm^{-2} contour and that bluer systems are more compact optically. This second feature could indicate that star formation is more likely to occur and/or occurs more frequently in the dense cores of dwarf systems. This is in accord with proposed expansion/contraction of the HI reservoir.

The different distributions of the BCD and LSBD sub-samples in the (log μ_L, (U – V)) plane, as well as the correlation between these two parameters, are evidence of the difference in star-formation between the two types of systems. Although the trend for both types is for bluer galaxies to have higher optical surface brightnesses (thus justifying our use of the (U – V) color index as a star-formation indicator), it is clear from the plot that BCDs and LSBDs of the same color index have different optical surface brightnesses. The BCDs are emitting much more light per unit area than are the LSBDs, and so, regardless of color, have higher densities of luminous (i.e. young, hot, O and B-type) stars than their LSBD counterparts.

There is a correlation between the HI mass-to-light ratio and the HI mass to total mass ratio, which shows that systems with greater fractional HI masses also have a higher gas-to-stellar mass ratio. This indicates that galaxies with larger relative amounts of HI have not formed stars as efficiently, or perhaps just not as recently, as those with lower fractional amounts of HI. Conversely, systems which are currently forming or have recently formed stars could be expected to have a greater stellar component and a lesser gaseous component, since the HI would have been processed into stars.

This trend is also consistent with the correlation for the BCD sample between HI surface density and HI mass-to-light ratio. The BCDs, which are known to be actively

forming stars, have higher HI surface densities in conjunction with greater HI mass-to-light ratios. Again, this is expected if the HI is being turned into stars, so that the reservoir is being depleted and/or the stellar content (as measured by the luminosity) is increasing.

In addition to the information specific to star-formation revealed in this analysis, we have also produced an HI version of the well-known mass-radius relationship, which is tighter for the LSBDs than the BCDs. We also showed, based upon an examination of the observed velocity widths and axial ratios, that the BCDs can be represented as rotating disk systems; but it should be emphasized that we have assumed an intrinsic axial ratio (0.58) that is much less flattened that those traditionally invoked (0.2 – 0.3). This means that rotation should be less significant than for flatter disks; these "puffier" systems require more turbulence to support them. And finally, when comparing the total mass and the luminosity of our dwarf galaxies, we found a relation very similar but not identical to the classic Tully-Fisher relation for spiral galaxies. The relation for our sample is less steep than that for these more massive systems.

Table 5.1: Physical properties of BCD galaxy sample, taken from the RC3.

Object	α[a]	$r_{26.5}$[b] (arcmin)	$(B-V)_T^0$	B_T^0	Δv_{50}	D (Mpc)[d]
	δ (B1950)	b/a	$(U-B)_T^0$	$V_\odot$ (km s^{-1})	Δv_{20} (km s^{-1})	M_{HI} ($10^6 M_\odot$)[e]
A1116+51[c]	$11^h\ 16^m\ 46.2^s$	0.55	0.19	16.77	72	14.07
	51° 46′ 36″	0.84	− 0.61	1341	148	118.8
Haro 33	$12^h\ 42^m\ 11.5^s$	1.17	0.21	14.60	60	9.58
	28° 44′ 43″	0.54	− 0.41	947	123	120.3
Haro 4	$11^h\ 02^m\ 15.6^s$	0.60	0.28	15.70	44	6.15
	29° 24′ 28″	0.74	− 0.66	646	92	13.89
Haro 27	$11^h\ 37^m\ 47.9^s$	1.14	0.40	14.59	—	18.16
	28° 39′ 06″	0.51	− 0.27	1836	164	134.5
Haro 36	$12^h\ 44^m\ 39.3^s$	2.32	0.61	14.20	59	5.84
	51° 53′ 11″	0.78	0.28	502	111	61.05
Mrk 328	$23^h\ 35^m\ 09.4^s$	0.63	0.54	15.35	105	15.67
	29° 51′ 10″	0.85	− 0.13	1379	141	55.51
Mrk 51	$12^h\ 21^m\ 41.1^s$	0.78	0.65	15.35	170	10.92
	04° 30′ 00″	0.35	− 0.19	1175	204	36.81
Mrk 67	$13^h\ 39^m\ 39.5^s$	0.50	0.54	15.75	63	10.05
	30° 46′ 16″	0.93	− 0.38	958	85	14.25

[a] Position listed is that used as the field pointing center for the HI observations.

[b] $r_{26.5} = \sqrt{a_{26.5} b_{265.5}}$; where $a_{26.5}$ and $b_{26.5}$ are the major and minor axes at the 26.5th isophote (mag arcsec^{-2}). These were obtained from the 25th isophotal diameters and axial ratios listed in the RC3, using the precepts set forward on pp. 23 and 24 of the RC3, Volume I; and from Table 6 on page 24.

[c] Information for this system is taken from Thuan and Martin (1981).

[d] Distances calculated from V_{GSR}, assuming H_0 = 100 km s^{-1} Mpc^{-1}.

[e] Calculated from the HI line magnitude, m_{21}, listed in the RC3, using the conversions listed on page 51 of Vol. I.

Table 5.2: Physical properties of LSBD galaxy sample, taken from the RC3.

Object Name	α[a]	$r_{26.5}$[b] (arcmin)	$(B-V)^0_T$	B^0_T	Δv_{50}	D (Mpc)[c]
	δ (B1950)	b/a	$(U-B)^0_T$	$V_\odot$ (km s^{-1})	Δv_{20} (km s^{-1})	M_{HI} ($10^6 M_\odot$)[d]
DDO 43	$07^h\ 24^m\ 49.9^s$	2.32	0.36	14.71	38	3.56
	40° 52′ 22″	0.68	– 0.3	354	51	35.60
DDO 169	$13^h\ 13^m\ 20.3^s$	3.13	0.31	14.31	50	3.42
	47° 45′ 37″	0.35	– 0.24	260	65	40.60
DDO 52	$08^h\ 25^m\ 07^s$	2.91	0.33	14.63	83	3.93
	42° 01′ 13″	0.51	0.26	393	101	37.79
NGC 4163	$12^h\ 09^m\ 37.7^s$	3.37	0.45	13.93	30	1.83
	36° 26′ 50″	0.89	– 0.30	164	47	6.63
DDO 131	$12^h\ 29^m\ 29^s$	2.68	0.48	15.20	55	6.48
	29° 59′ 06″	0.89	– 0.19	642	82	92.92
DDO 242	$13^h\ 38^m\ 47.0^s$	3.93	0.50	12.23	41	3.49
	–29° 39′ 42″	0.60	– 0.09	477	52	35.82
DDO 88	$10^h\ 44^m\ 44.0^s$	4.18	0.59	14.08	44	4.81
	14° 19′ 53″	0.95	– 0.06	572	55	34.12
DDO 56	$09^h\ 07^m\ 32.0^s$	2.68	0.64	14.59	76	5.13
	–22° 48′ 18″	0.74	0.37	724	77	24.92

[a] Position listed is that used as the field pointing center for the HI observations.

[b] $r_{26.5} = \sqrt{a_{26.5} b_{265.5}}$; where $a_{26.5}$ and $b_{26.5}$ are the major and minor axes at the 26.5th isophote (mag arcsec^{-2}). These were obtained from the 25th isophotal diameters and axial ratios listed in the RC3, using the precepts set forward on pp. 23 and 24 of the RC3, Volume I; and from Table 6 on page 24.

[c] Distances calculated from V_{GSR}, assuming H_0 = 100 km s^{-1} Mpc^{-1}.

[d] Calculated from the HI line magnitude, m_{21}, listed in the RC3, using the conversions listed on page 51 of Vol. I.

Table 5.3: Observational parameters for entire galaxy sample.

Object	θ''[a]	Δv_{ch}[b] (km s^{-1})	time on source (minutes)	r.m.s.[c] (mJy)	Peak S/N	Notes[d]
A1116+51	55.1 × 26.5	12.6	46	1.16	5.4	C
Haro 33	29.6 × 17.9	12.6	10	2.74	8.2	
Haro 4	30.5 × 16.9	12.4	42	1.54	10.1	
Haro 27	29.6 × 17.1	12.6	62	1.19	6.6	
Haro 36	29.6 × 21.0	12.5	10	3.53	8.3	
Mrk 328	25.1 × 22.8	12.6	84	0.38	4.8	C
Mrk 51	19.5 × 16.0	12.5	134	0.57	6.8	
Mrk 67	29.0 × 16.6	12.6	115	0.89	5.3	
DDO 43	31.5 × 15.5	5.2	10	2.81	5.1	H, C
DDO 169	41.9 × 26.5	5.2	10	2.58	8.6	H, C
DDO 52	35.1 × 24.1	12.4	10	1.77	6.9	C
NGC 4163	29.6 × 18.7	5.2	10	4.73	7.3	H
DDO 131	39.7 × 24.3	5.2	10	2.55	6.6	H, C
DDO 242	51.4 × 22.4	5.2	10	2.83	7.4	H, C
DDO 88	24.7 × 22.3	5.2	10	1.84	6.0	H, C
DDO 56	47.1 × 25.3	5.2	12	2.50	4.6	H, C

[a]FWHM of synthesized beam; convolved up for spatially smoothed data sets.

[b]Velocity resolution, including the effects of Hanning smoothing for velocity smoothed data sets.

[c]Noise in a single channel.

[d]C indicates the data was spatially convolved; H indicates Hanning smoothing in velocity was performed.

Table 5.4: Derived parameters for BCD galaxy sample.

Object	Linear Resolution (kpc)	$V_{\odot}$[a] (km s^{-1})	D[b] (Mpc)	Δv_{50} (km s^{-1})	N_{HI}[c] (10^{20} atm cm^{-2})	M_{HI} (10^6 $M_{\odot}$)	γ[d]
A1116+51	2.74	1333 ± 2.7	13.9	26.5 ± 4.6	3.73 ± 0.72	13.51 ± 3.89	0.114
Haro 33	1.13	942 ± 2.7	9.5	39.7 ± 6.6	20.68 ± 2.36	64.21 ± 7.23	0.534
Haro 4	0.75	670 ± 5.4	6.4	18.19 ± 5.2	8.64 ± 0.91	4.62 ± 0.78	0.333
Haro 27	2.11	1838 ± 26.9	18.2	155.8 ± 21.7	9.12 ± 1.11	54.28 ± 9.26	0.404
Haro 36	0.75	500 ± 4.9	5.8	44.6 ± 7.6	22.45 ± 2.27	23.92 ± 2.64	0.392
Mrk 328	1.95	1384 ± 10.9	15.8	97.7 ± 5.6	3.50 ± 0.55	9.35 ± 1.81	0.168
Mrk 51	1.01	1198 ± 12.3	11.2	158.0 ± 6.0	8.85 ± 1.07	17.92 ± 2.63	0.487
Mrk 67	1.15	970.5 ± 2.0	10.2	48.7 ± 1.6	4.45 ± 0.65	4.3 ±1.21	0.302

[a]All velocity uncertainties are conservative statistical estimates only.

[b]Based on GSR velocity; H_0 = 100 km s^{-1} Mpc^{-1}.

[c]Peak column density.

[d]Percentage of single-dish flux (from the RC3) detected by the VLA.

Table 5.5: Derived parameters for LSBD galaxy sample.

Object	Linear Resolution (kpc)	$V_{\odot}$[a] (km s^{-1})	D[b] (Mpc)	Δv_{50} (km s^{-1})	N_{HI}[c] (10^{20} atm cm^{-2})	M_{HI} (10^6 $M_{\odot}$)	γ[d]
DDO 43	0.41	356 ± 0.4	3.6	38.4 ± 1.2	11.36 ± 1.65	7.53 ± 0.88	0.212
DDO 169	0.59	262 ± 0.7	3.5	52.3 ± 3.2	10.40 ± 1.09	8.38 ± 0.75	0.206
DDO 52	0.58	385 ± 2.5	3.8	22.2 ± 1.1	8.01 ± 1.26	13.21 ± 1.01	0.350
NGC 4163	0.22	162 ± 0.4	1.8	21.7 ± 3.3	14.43 ± 1.55	3.25 ± 0.27	0.491
DDO 131	1.04	646 ± 2.5	6.5	62.1 ± 3.4	7.77 ± 1.20	53.31 ± 3.49	0.574
DDO 242	0.62	480 ± 0.8	3.5	19.4 ± 4.2	7.79 ± 0.97	14.53 ± 0.92	0.406
DDO 88	0.58	574 ± 0.7	4.8	28.2 ± 2.8	7.20 ± 1.00	16.09 ± 1.00	0.472
DDO 56	0.92	726 ± 6.0	5.2	69.7 ± 7.4	2.56 ± 0.59	3.03 ± 0.58	0.122

[a]All velocity uncertainties are conservative statistical estimates only.

[b]Based on GSR velocity; H_0 = 100 km s^{-1} Mpc^{-1}.

[c]Peak column density.

[d]Percentage of single-dish flux (from the RC3) detected by the VLA.

Table 5.6: Correlation parameters for BCD galaxy sample.

Object	$M(2)_{HI}$[a] ($10^6 M_\odot$)	$M(5)_{HI}$[b] ($10^6 M_\odot$)	$\langle\sigma_v\rangle$ (km s^{-1})	(U − V)	M_T ($10^6 M_\odot$)	μ_{HI}[a] ($\frac{M_\odot}{pc}$)
	$R(2)_{HI}$[a] (kpc)	$R(5)_{HI}$[b] (kpc)	$\left(\frac{V_{rot}}{\sigma}\right)$	L_U ($10^6 L_\odot$)	$\frac{M_{HI}}{L_U}$	μ_L ($\frac{L_\odot}{pc}$)
A1116+51	6.95	—	13.94	− 0.42	819	2.13
	1.81	—	1.24	95.0	0.142	19.37
Haro 33	60.86	52.58	15.59	− 0.20	2234	6.87
	2.98	2.44	1.74	272.5	0.236	26.15
Haro 4	3.66	2.00	8.84	− 0.38	185	3.54
	1.02	0.62	1.37	56.3	0.082	45.08
Haro 27	41.59	29.25	28.34	0.13	14470	4.51
	3.04	2.24	1.80	884.2	0.061	24.18
Haro 36	22.66	20.09	13.72	0.89	1503	7.94
	1.69	1.38	1.32	78.7	0.304	5.09
Mrk 328	5.05	—	15.94	0.41	1378	2.17
	1.52	—	1.22	291.9	0.032	35.14
Mrk 51	13.47	6.94	21.69	0.46	5204	3.56
	1.95	1.08	2.34	152.3	0.118	23.81
Mrk 67	2.31	—	14.37	0.16	534	2.41
	0.98	—	1.14	105.1	0.041	48.37

[a]Taken at the 2×10^{20} atom cm^{-2} contour.

[b]Taken at the 5×10^{20} atom cm^{-2} contour.

Table 5.7: Correlation parameters for LSBD galaxy sample.

Object	$M(2)_{HI}$[a] ($10^6 M_\odot$)	$M(5)_{HI}$[b] ($10^6 M_\odot$)	$\langle\sigma_v\rangle$ (km s^{-1})	(U − V)	M_T ($10^6 M_\odot$)	μ_{HI}[a] ($\frac{M_\odot}{pc}$)
	$R(2)_{HI}$[a] (kpc)	$R(5)_{HI}$[b] (kpc)	$\left(\frac{V_{rot}}{\sigma}\right)$	L_U ($10^6 L_\odot$)	$\frac{M_{HI}}{L_U}$	μ_L ($\frac{L_\odot}{pc}$)
DDO 43	5.83	1.86	5.98	0.06	198	3.21
	1.35	0.55	1.47	31.7	0.237	5.43
DDO 169	6.53	3.76	11.64	0.07	1861	4.24
	1.24	0.78	2.34	40.1	0.209	4.07
DDO 52	9.47	2.89	6.00	0.59	349	3.28
	1.70	0.78	1.80	23.4	0.564	2.21
NGC 4163	2.87	2.16	7.38	0.15	175	5.07
	0.75	0.54	1.18	16.6	0.196	5.28
DDO 131	43.92	24.13	6.70	0.29	413	3.69
	3.45	2.19	1.18	60.3	0.884	2.34
DDO 242	11.79	4.51	5.14	0.41	271	3.12
	1.94	0.96	1.60	246.0	0.059	15.25
DDO 88	11.67	2.40	4.41	0.53	196	2.80
	2.04	0.71	1.12	82.0	0.196	2.38
DDO 56	—	—	4.52	1.01	174	—
	—	—	1.37	39.5	0.077	2.45

[a]Taken at the 2×10^{20} atom cm^{-2} contour.

[b]Taken at the 5×10^{20} atom cm^{-2} contour.

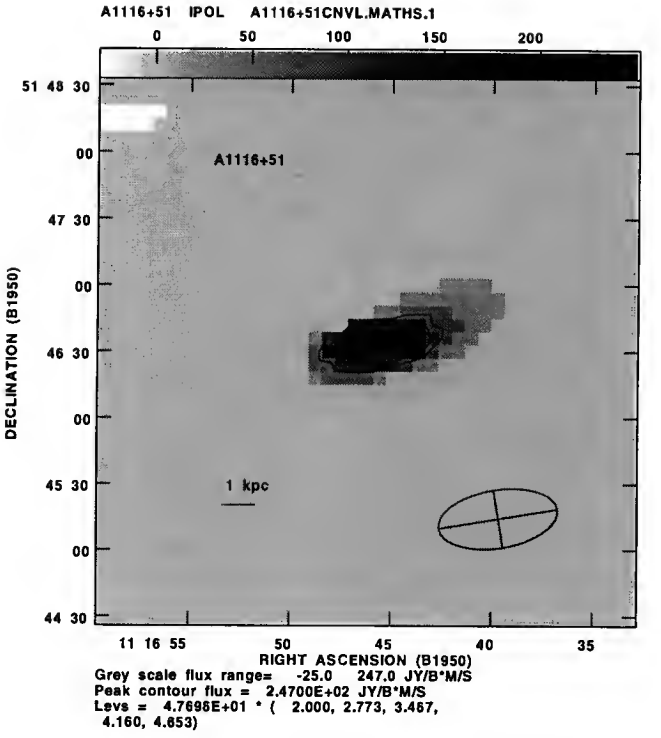

Figure 5.2: Integrated HI intensity (0th moment) map of A1116+51. Contour levels are 1.4 (2σ), 2, 2.5, 3, 3.5 $\times$ 10^{20} atom cm^{-2}.

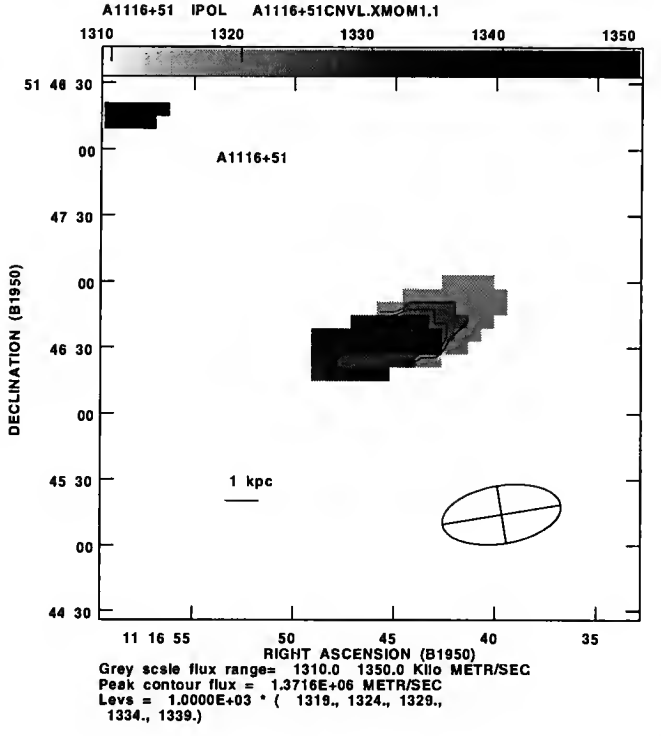

Figure 5.3: Integrated velocity field (1st moment) map of A1116+51.

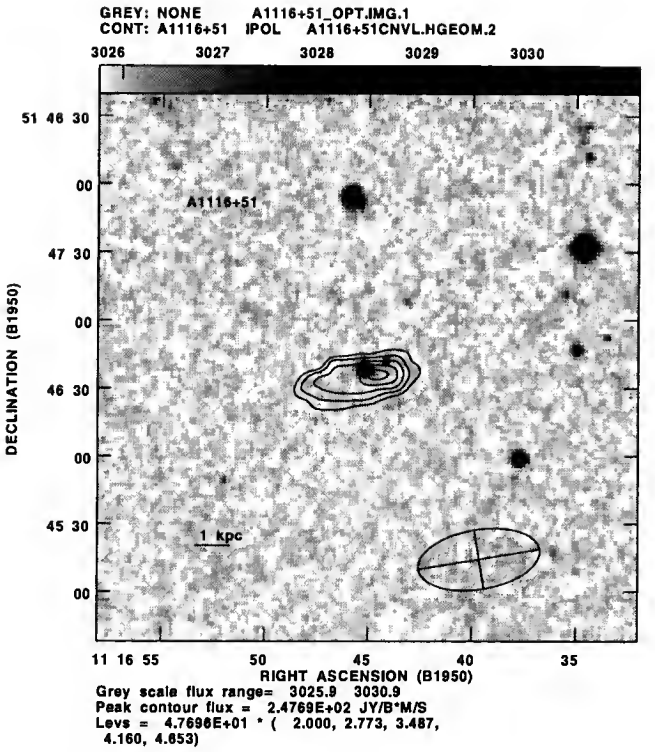

Figure 5.4: Optical greyscale image with HI contours for A1116+51.

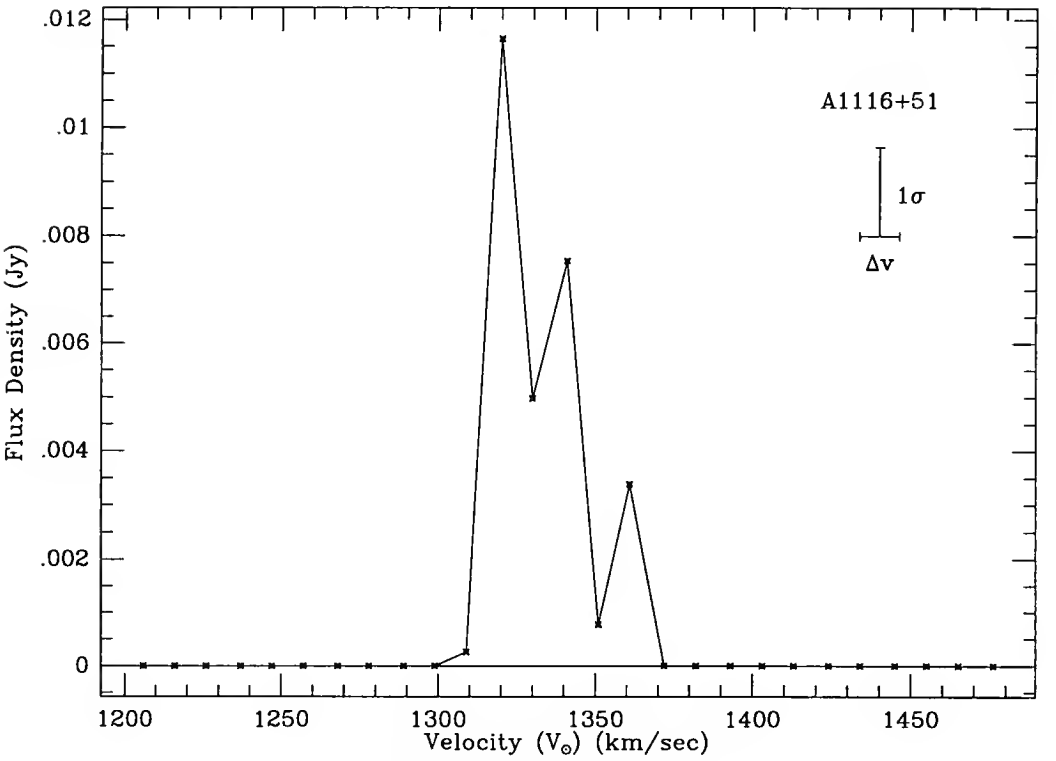

Figure 5.5: Global velocity profile for A1116+51.

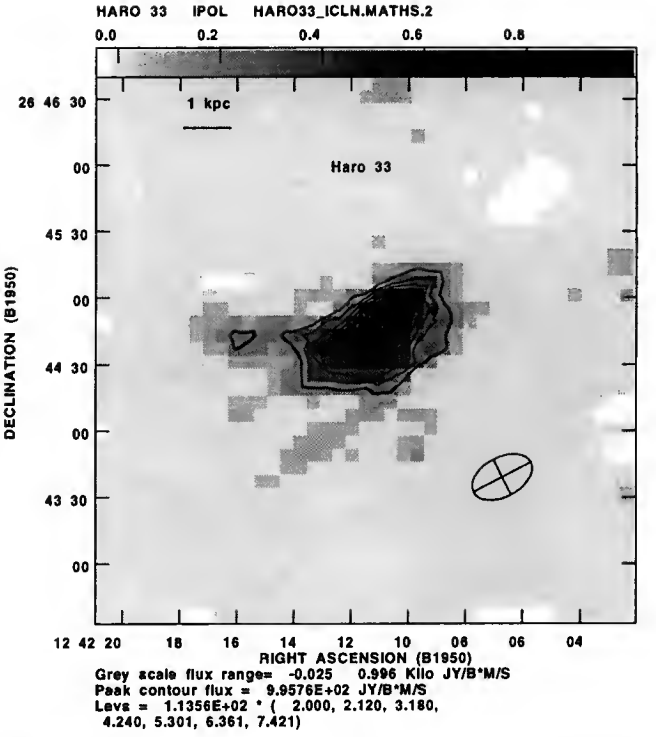

Figure 5.6: Integrated HI intensity (0th moment) map of Haro 33. Contour levels are 4.7 (2σ), 5, 7.5, 10, 12.5, 15, 17.5 $\times$ 10^{20} atom cm^{-2}.

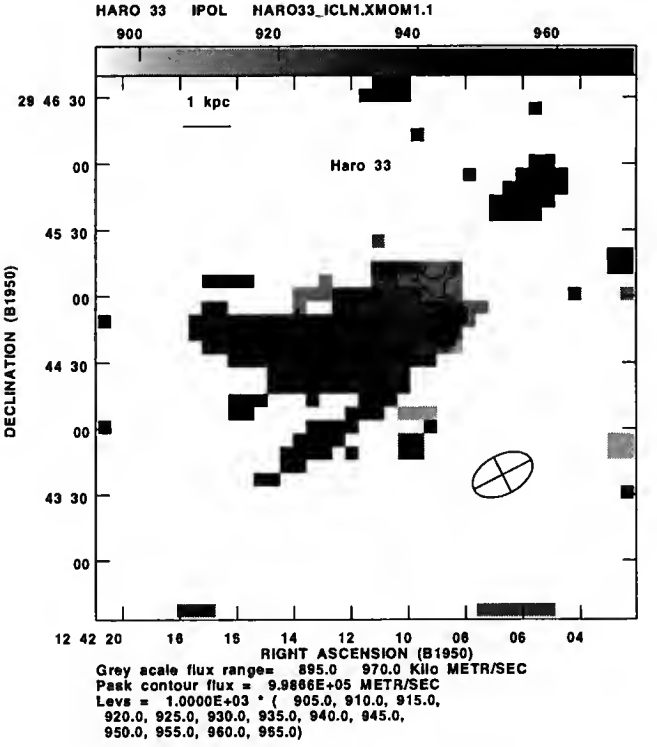

Figure 5.7: Integrated velocity field (1st moment) map of Haro 33.

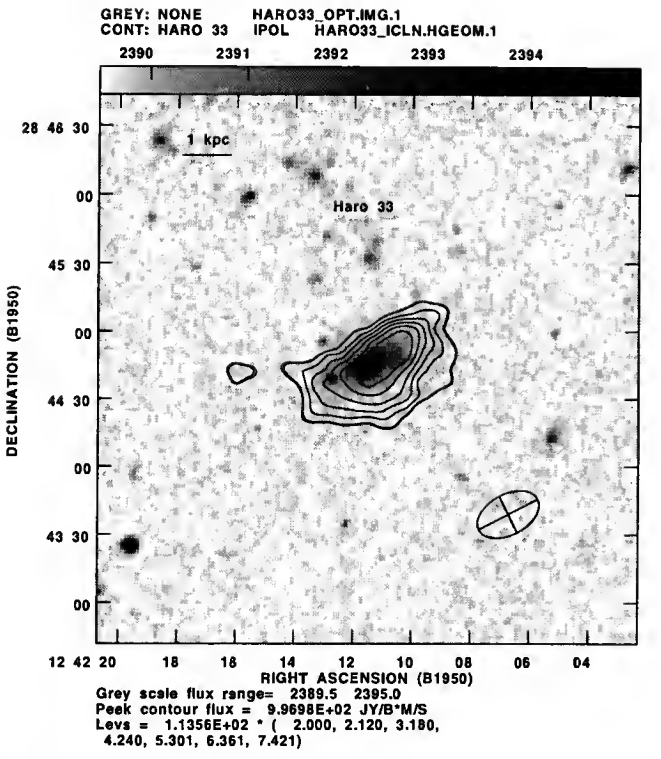

Figure 5.8: Optical greyscale image with HI contours for Haro 33.

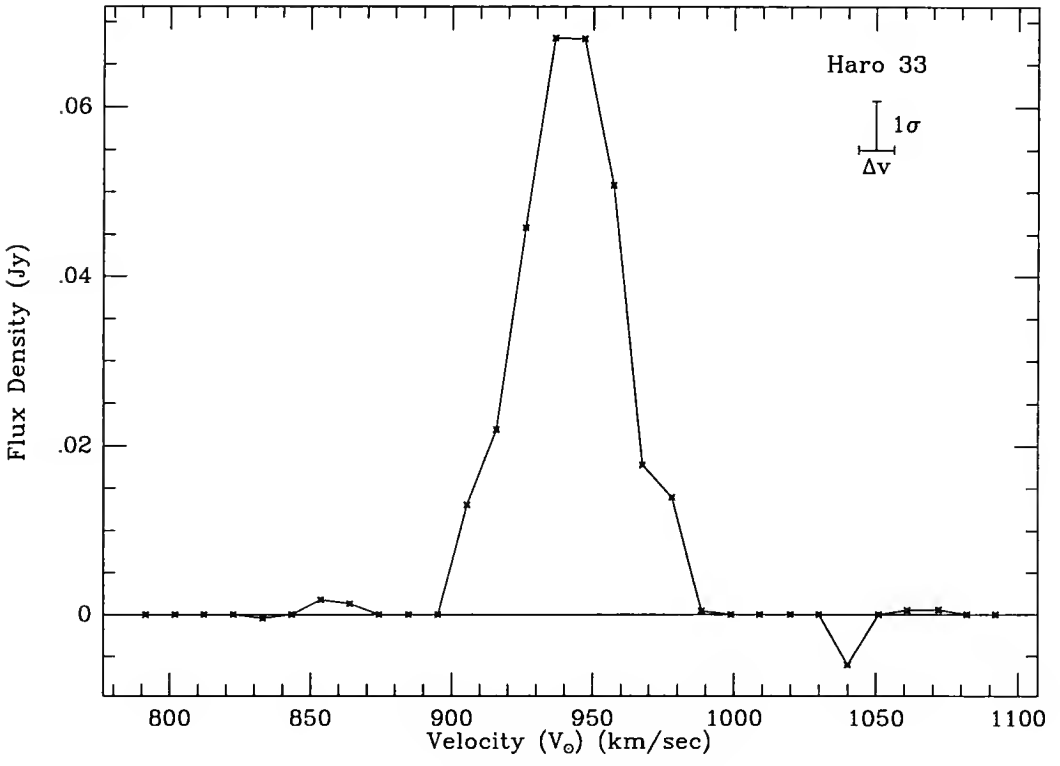

Figure 5.9: Global velocity profile for Haro 33.

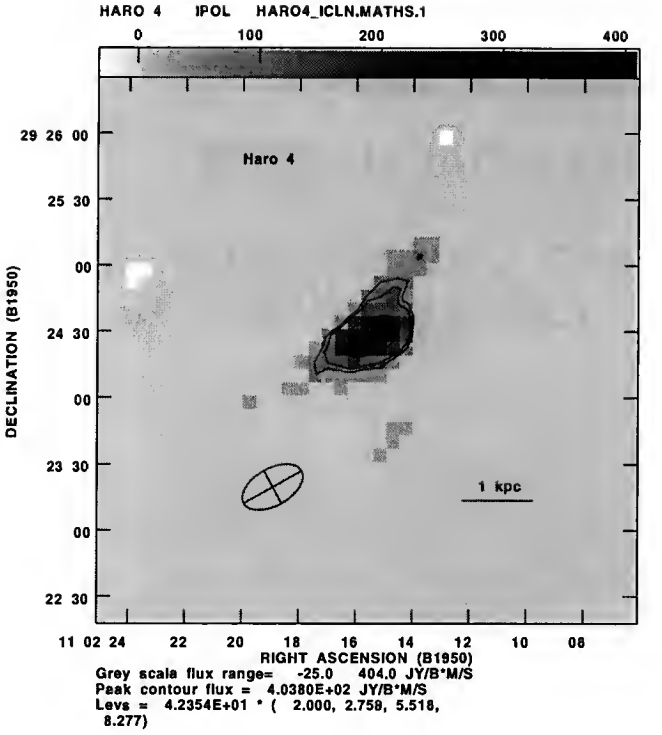

Figure 5.10: Integrated HI intensity (0th moment) map of Haro 4. Contour levels are 1.8 (2σ), 2.5, 5, 7.5 $\times$ 10^{20} atom cm^{-2}.

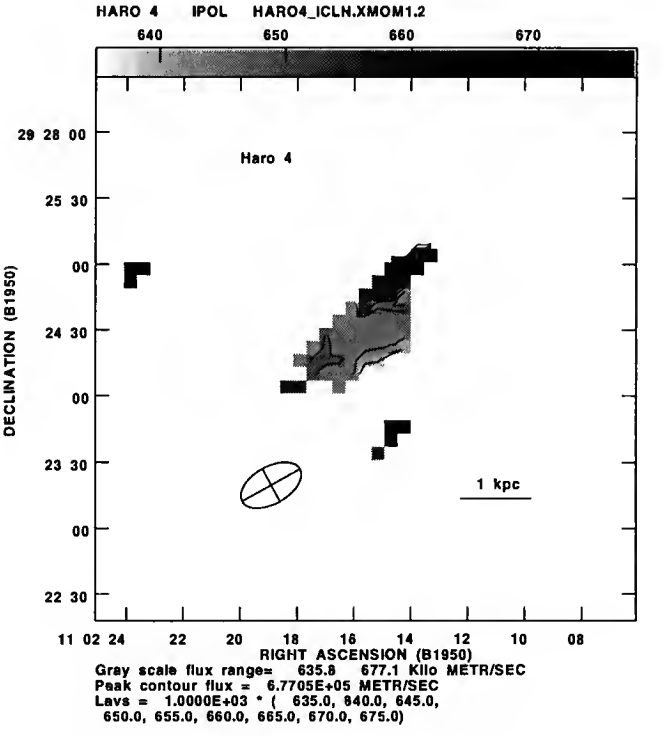

Figure 5.11: Integrated velocity field (1st moment) map of Haro 4.

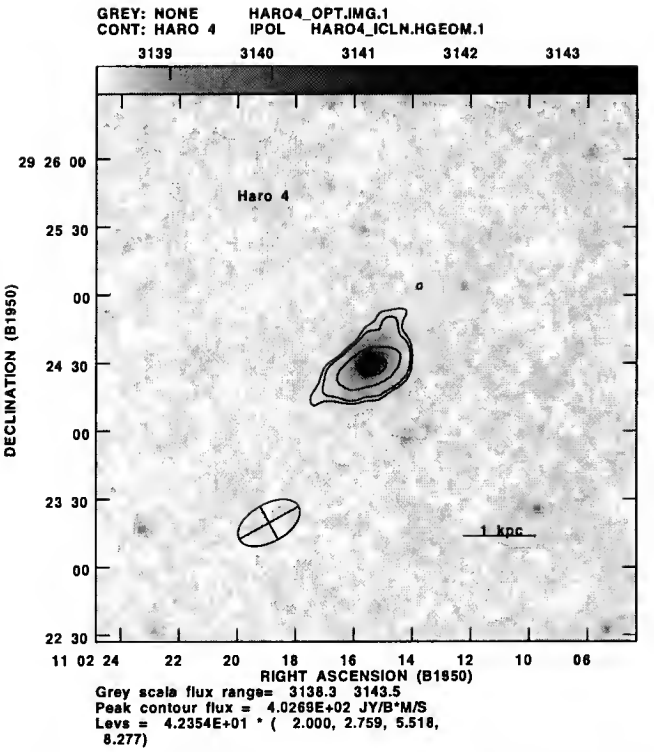

Figure 5.12: Optical greyscale image with HI contours for Haro 4.

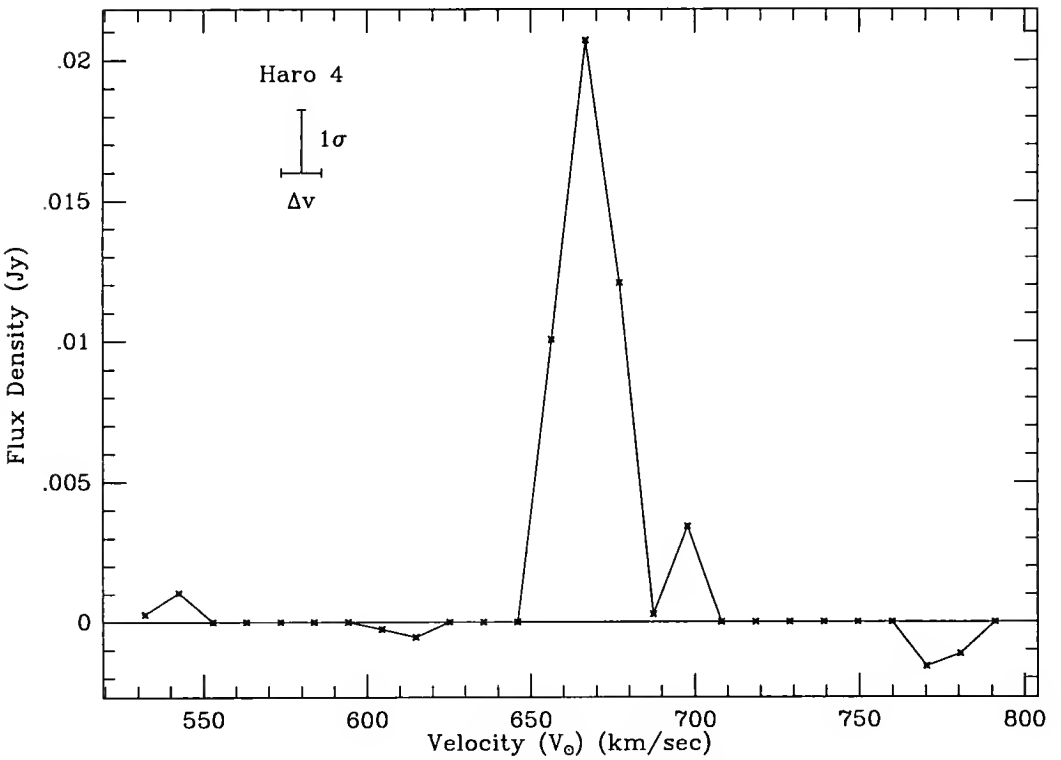

Figure 5.13: Global velocity profile for Haro 4.

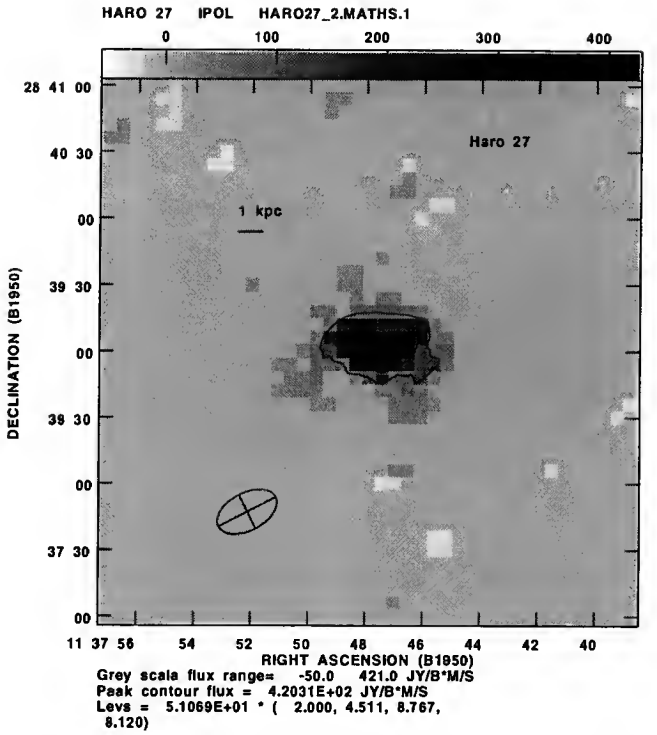

Figure 5.14: Integrated HI intensity (0th moment) map of Haro 27. Contour levels are 2.2 (2σ), 5, 7.5, 9.0 $\times$ 10^{20} atom cm^{-2}.

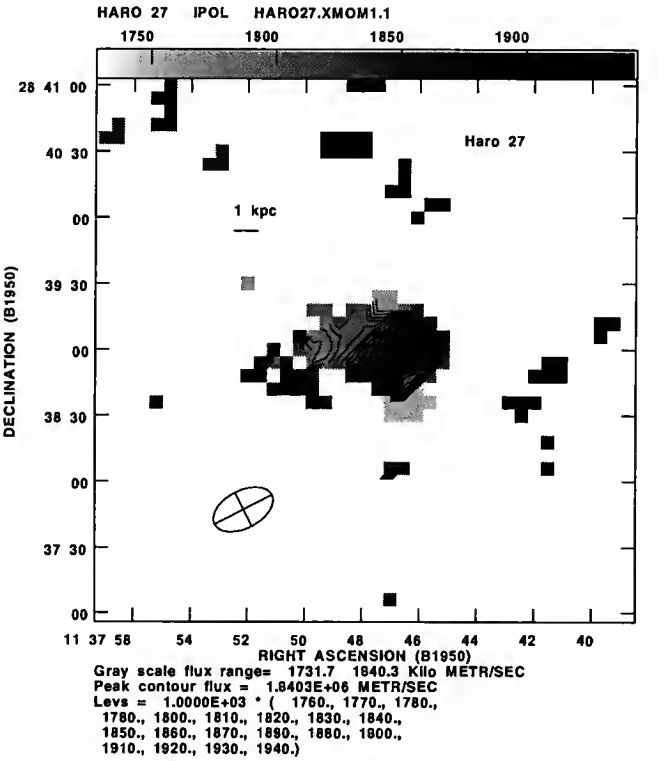

Figure 5.15: Integrated velocity field (1st moment) map of Haro 27.

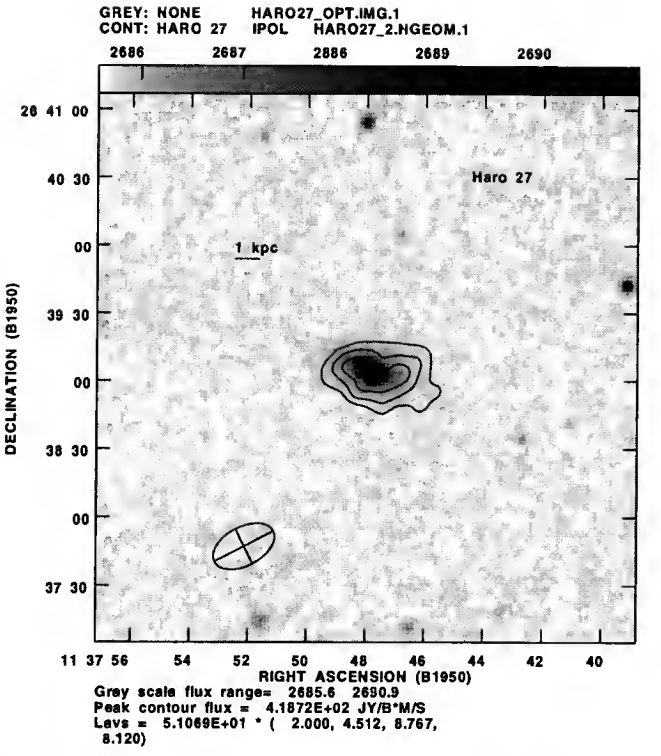

Figure 5.16: Optical greyscale image with HI contours for Haro 27.

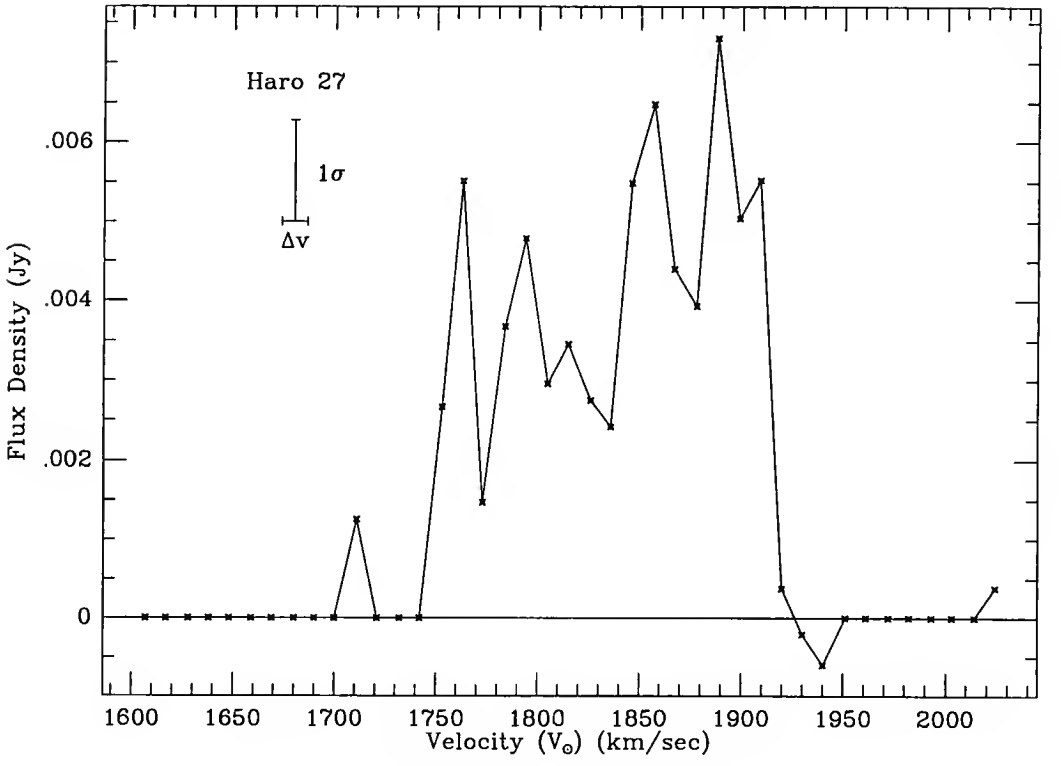

Figure 5.17: Global velocity profile for Haro 27.

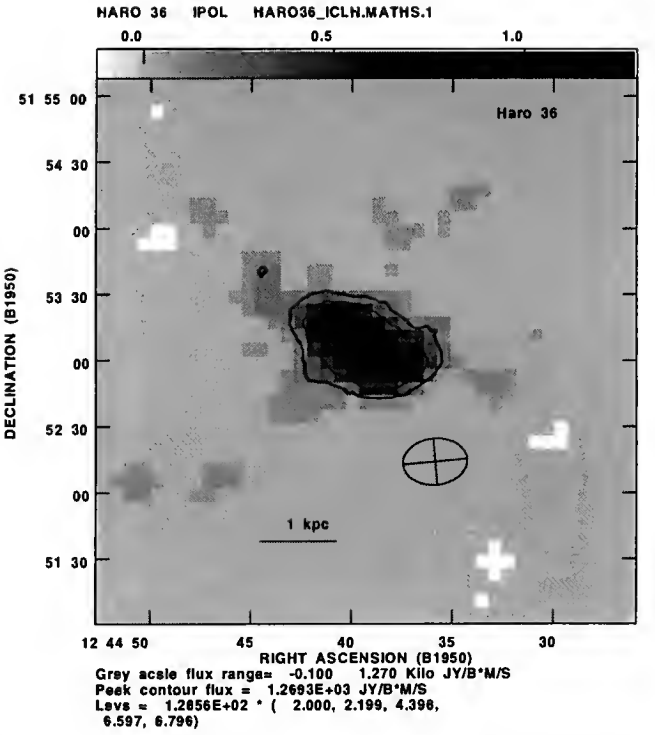

Figure 5.18: Integrated HI intensity (0th moment) map of Haro 36. Contour levels are 4.5 (2σ), 5, 10, 15, 20 $\times$ 10^{20} atom cm^{-2}.

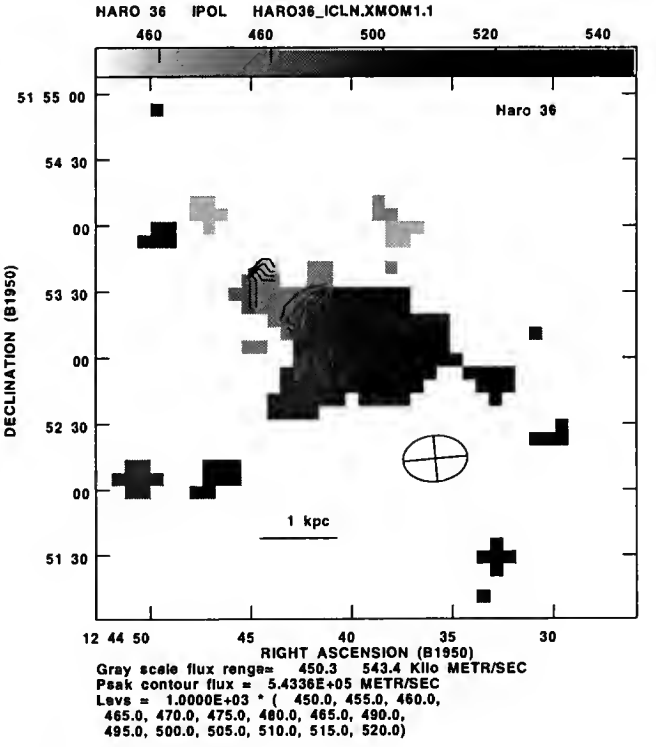

Figure 5.19: Integrated velocity field (1st moment) map of Haro 36.

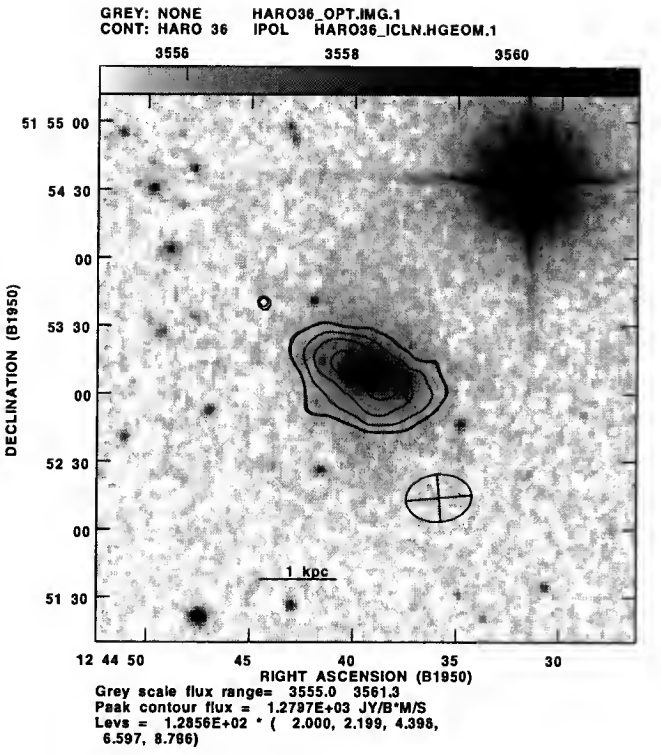

Figure 5.20: Optical greyscale image with HI contours for Haro 36.

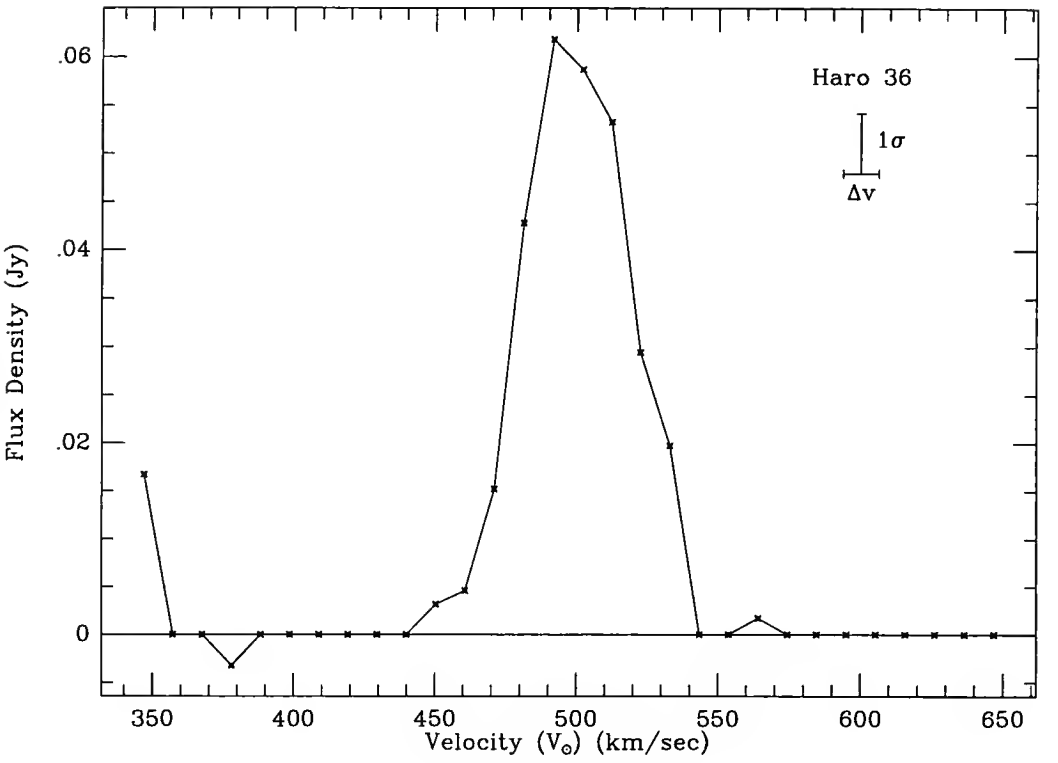

Figure 5.21: Global velocity profile for Haro 36.

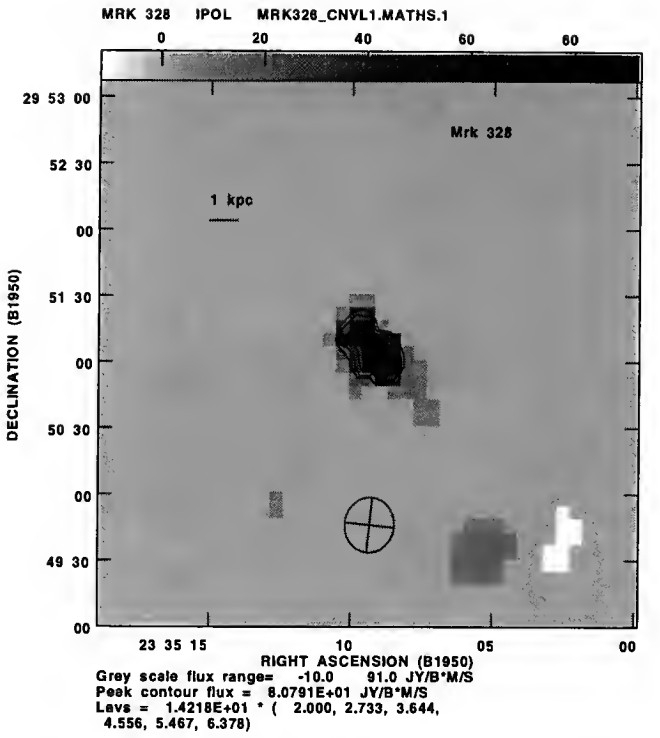

Figure 5.22: Integrated HI intensity (0th moment) map of Mrk 328. Contour levels are 1.1 (2σ), 1.5, 2, 2.5, 3, 3.5 $\times$ 10^{20} atom cm^{-2}.

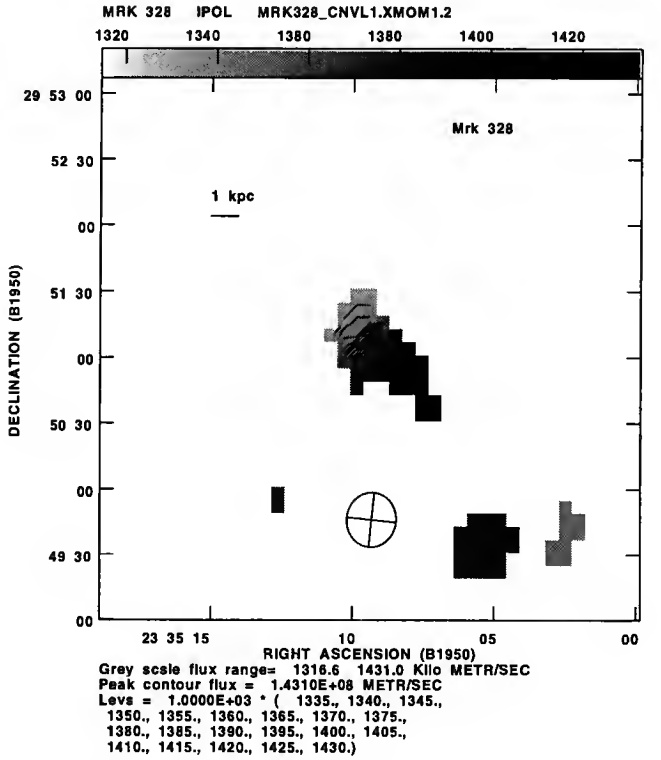

Figure 5.23: Integrated velocity field (1st moment) map of Mrk 328.

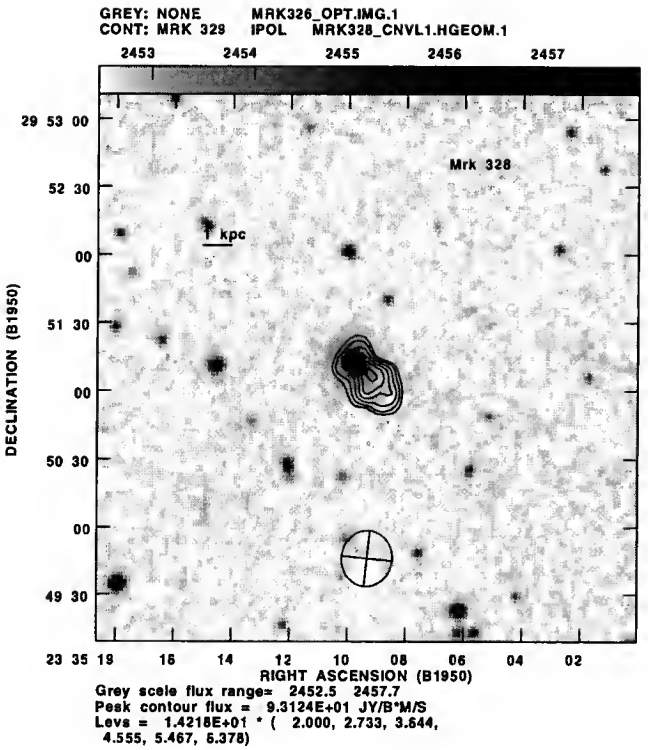

Figure 5.24: Optical greyscale image with HI contours for Mrk 328.

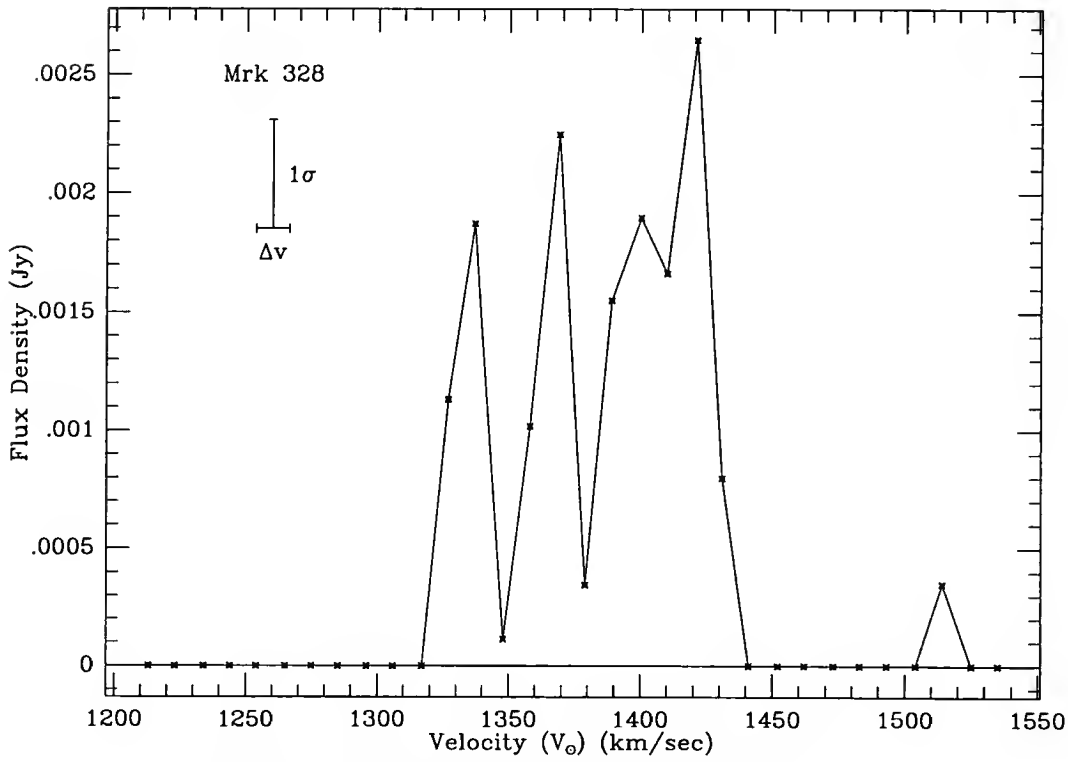

Figure 5.25: Global velocity profile for Mrk 328.

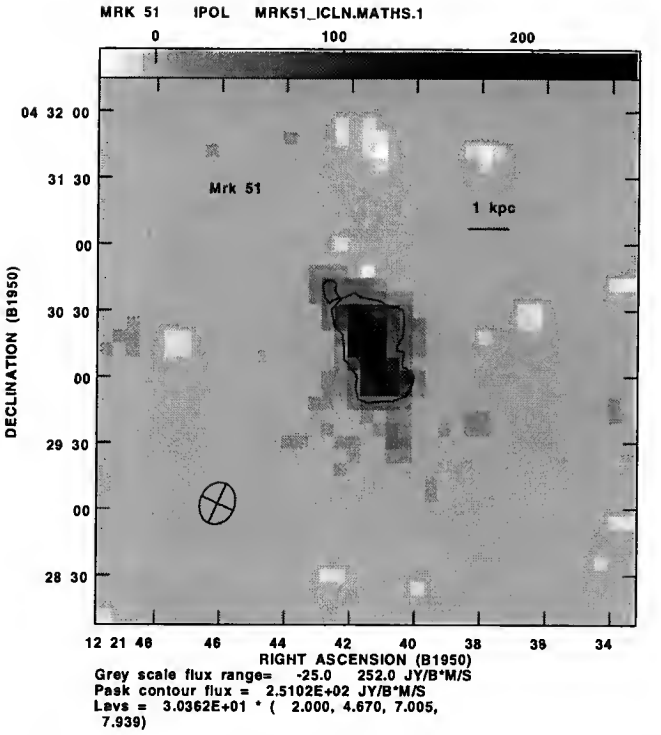

Figure 5.26: Integrated HI intensity (0th moment) map of Mrk 51. Contour levels are 2.1 (2σ), 5, 7.5, 8.5 $\times$ 10^{20} atom cm^{-2}.

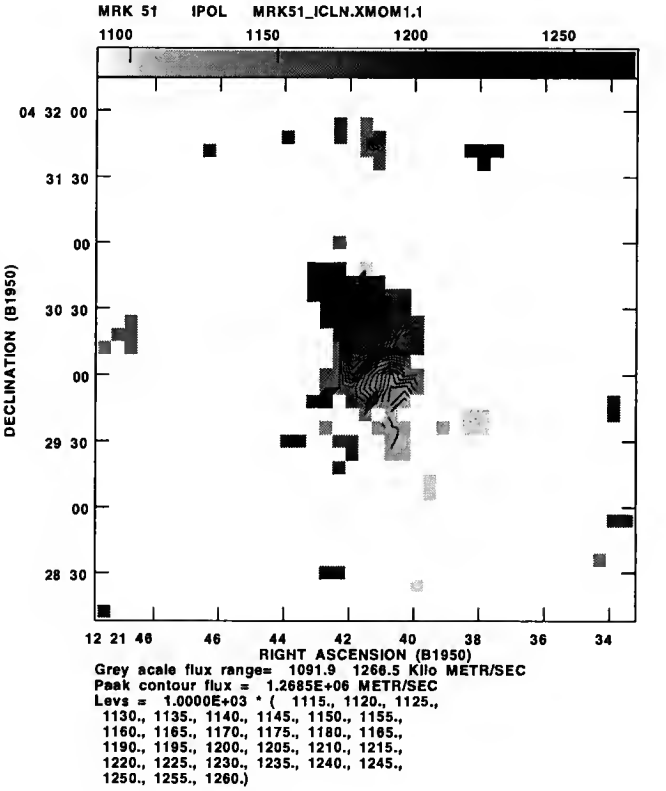

Figure 5.27: Integrated velocity field (1st moment) map of Mrk 51.

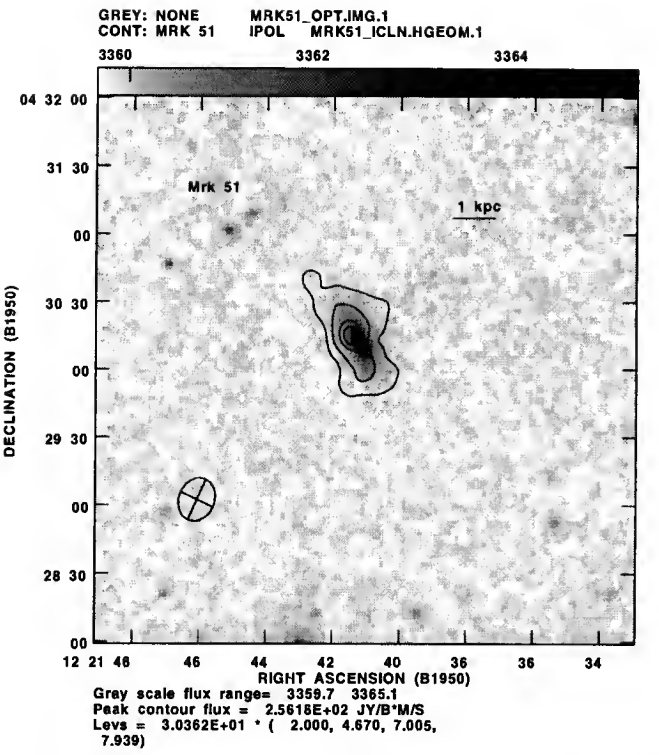

Figure 5.28: Optical greyscale image with HI contours for Mrk 51.

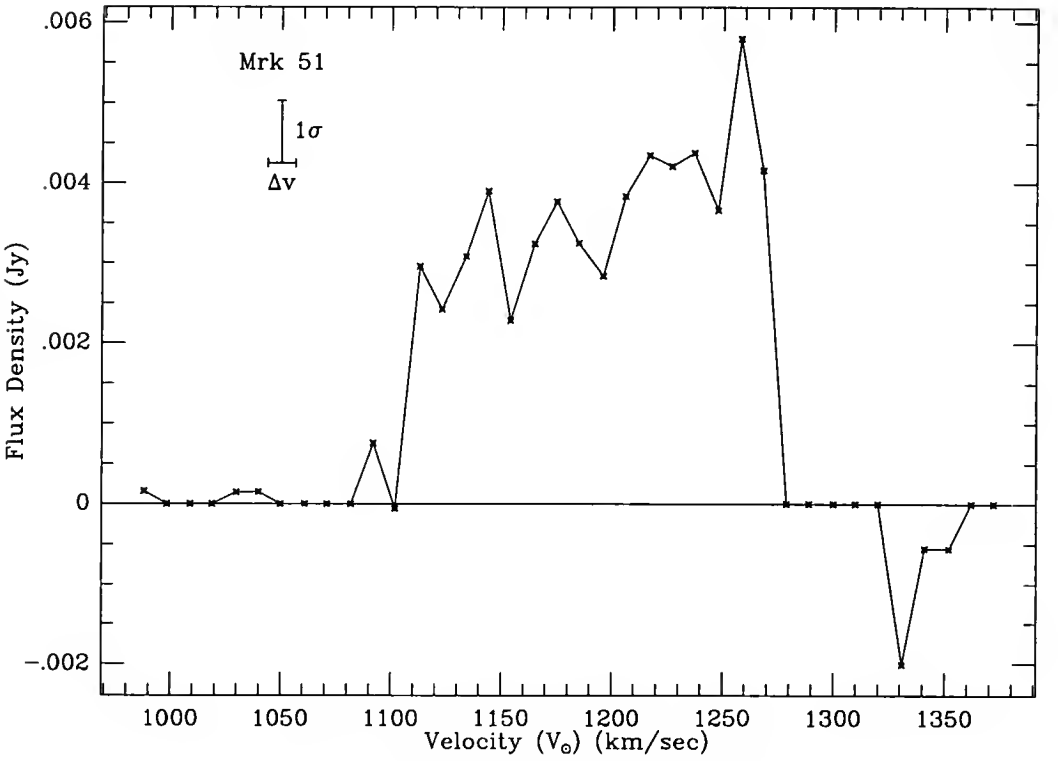

Figure 5.29: Global velocity profile for Mrk 51

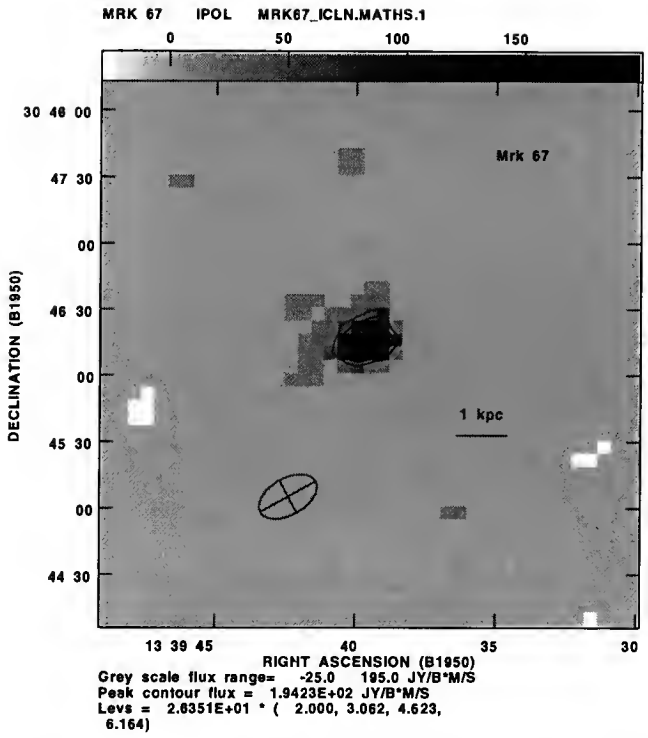

Figure 5.30: Integrated HI intensity (0th moment) map of Mrk 67. Contour levels are 1.3 (2σ), 2, 3, 4 $\times$ 10^{20} atom cm^{-2}.

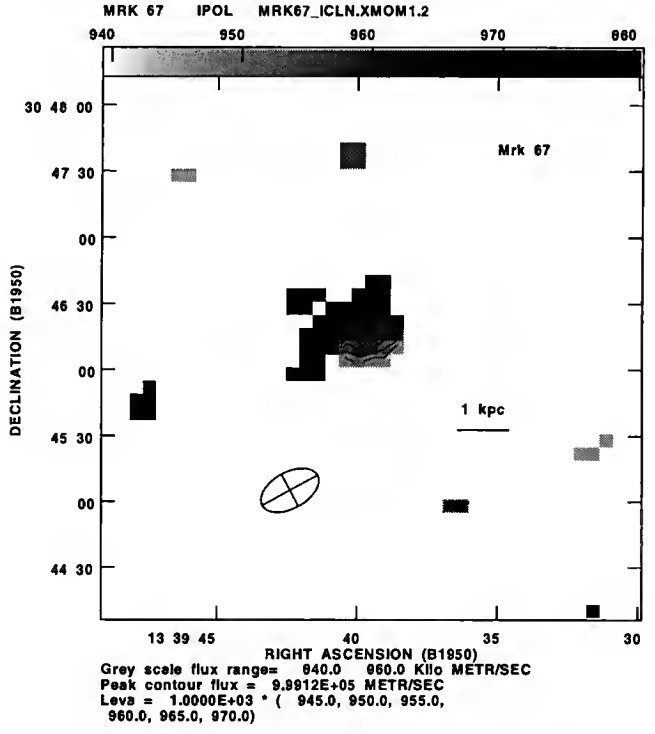

Figure 5.31: Integrated velocity field (1st moment) map of Mrk 67.

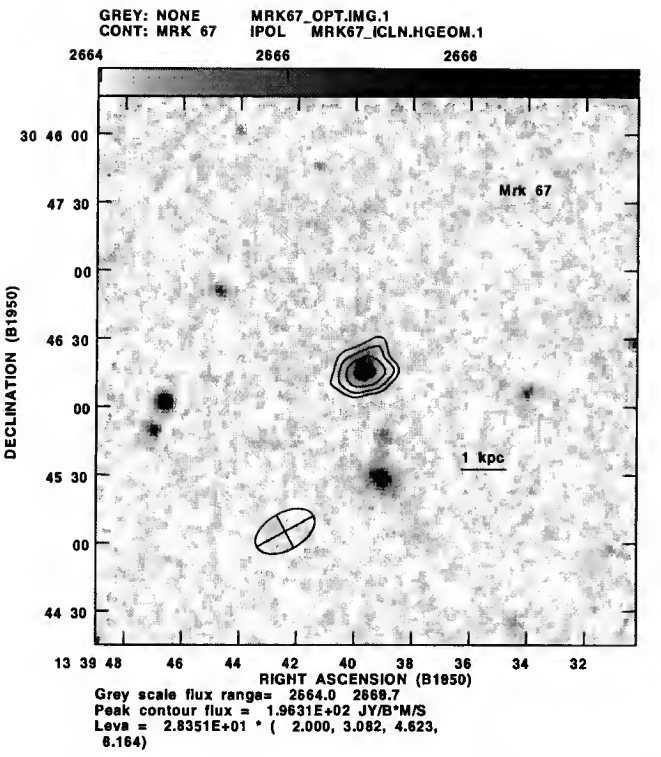

Figure 5.32: Optical greyscale image with HI contours for Mrk 67.

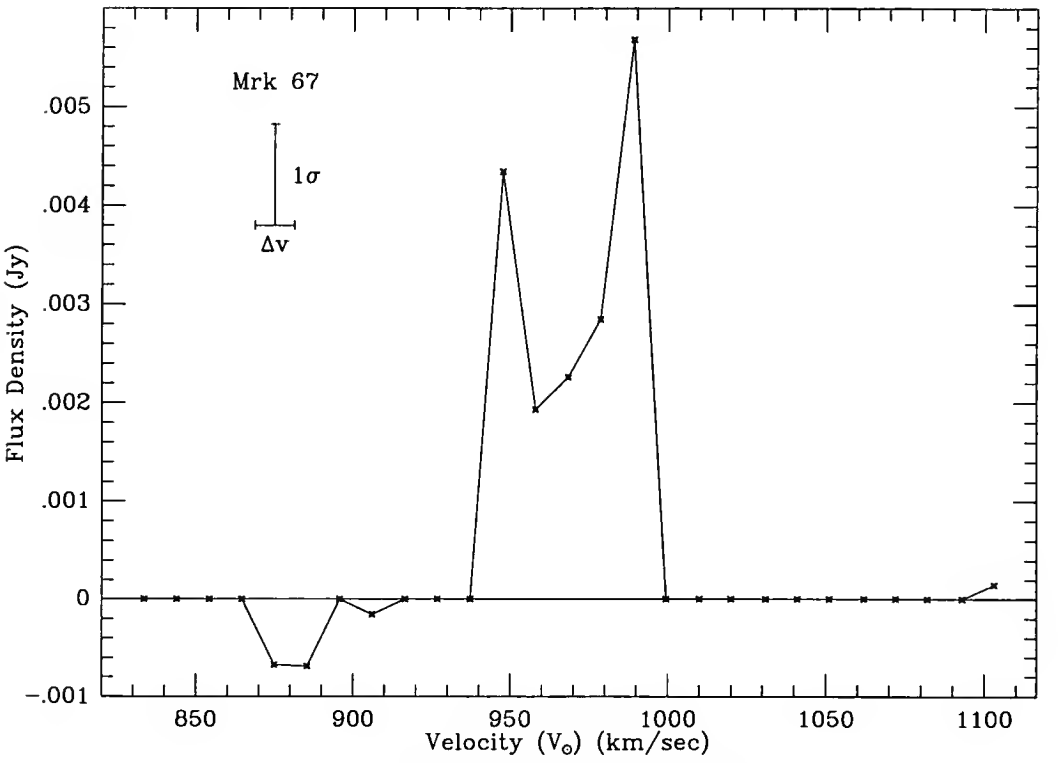

Figure 5.33: Global velocity profile for Mrk 67.

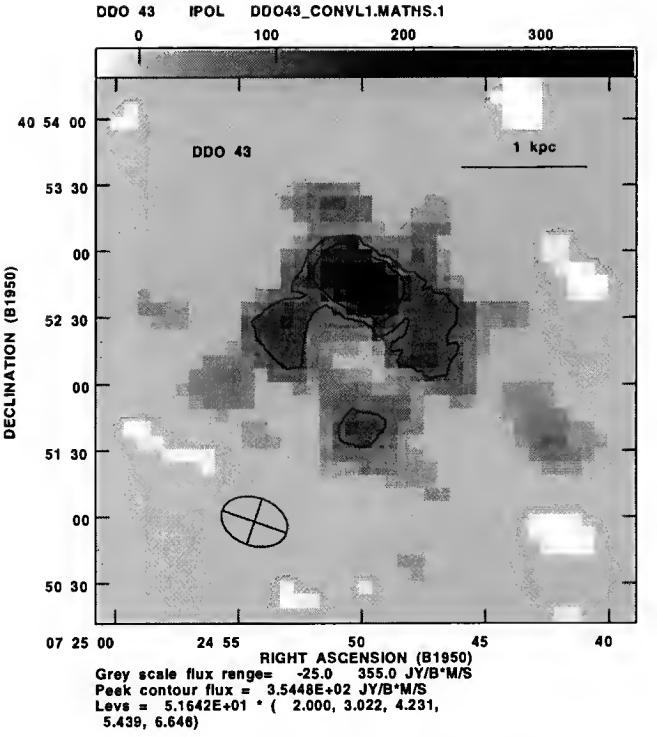

Figure 5.34: Integrated HI intensity (0th moment) map of DDO 43. Contour levels are 3.3 (2σ), 5, 7, 9, 11 $\times$ 10^{20} atom cm^{-2}.

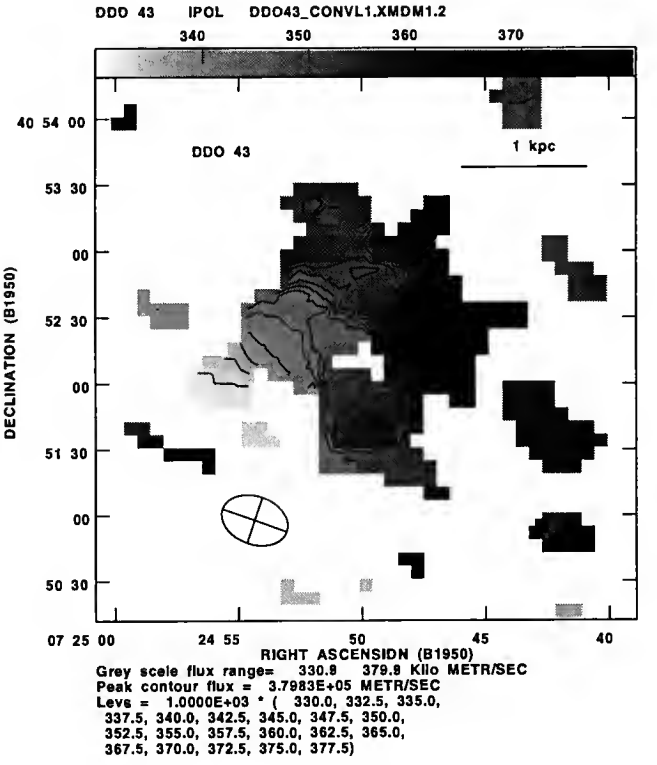

Figure 5.35: Integrated velocity field (1st moment) map of DDO 43.

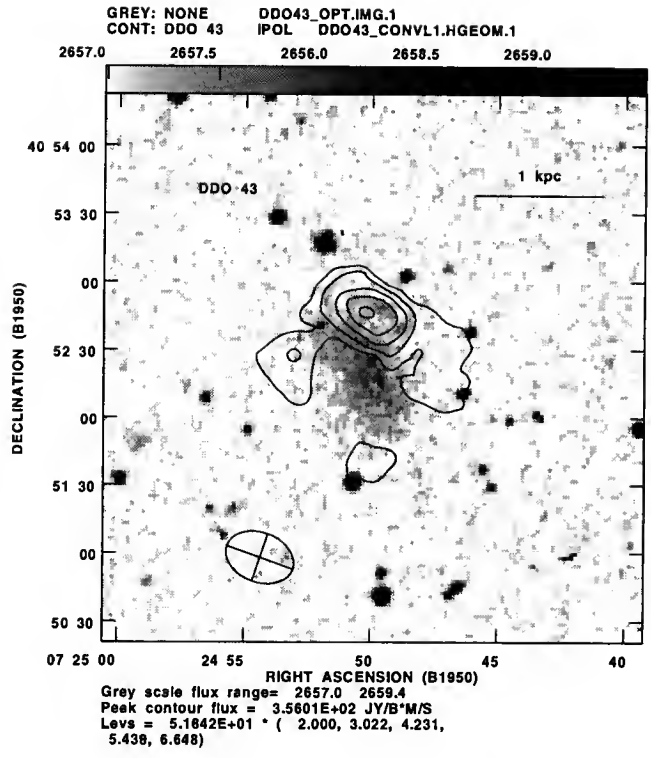

Figure 5.36: Optical greyscale image with HI contours for DDO 43.

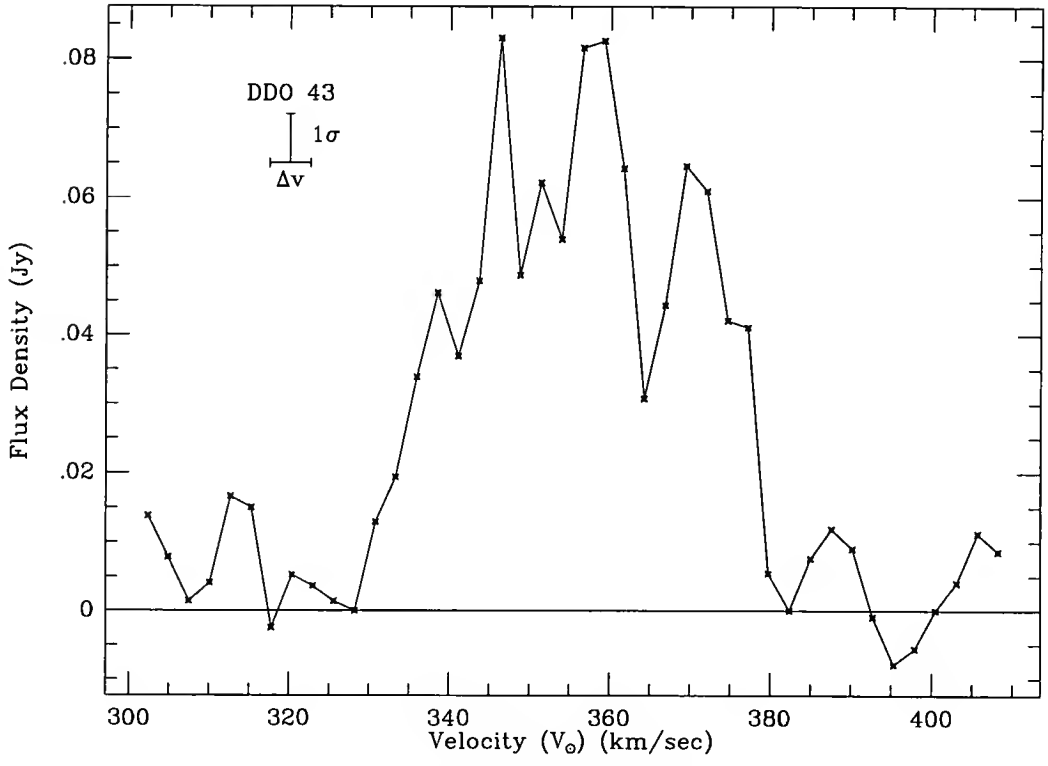

Figure 5.37: Global velocity profile for DDO 43.

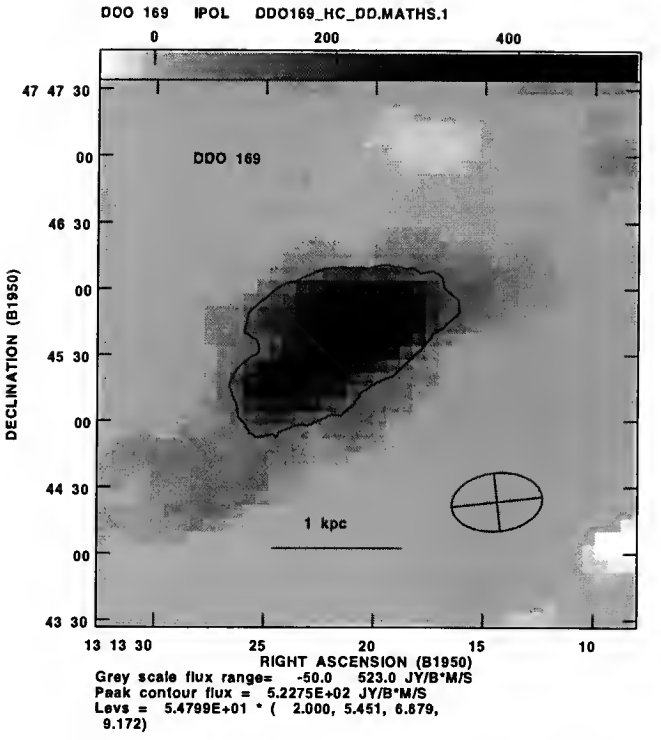

Figure 5.38: Integrated HI intensity (0th moment) map of DDO 169. Contour levels are 2.2 (2σ), 5, 7.5, 10 $\times$ 10^{20} atom cm^{-2}.

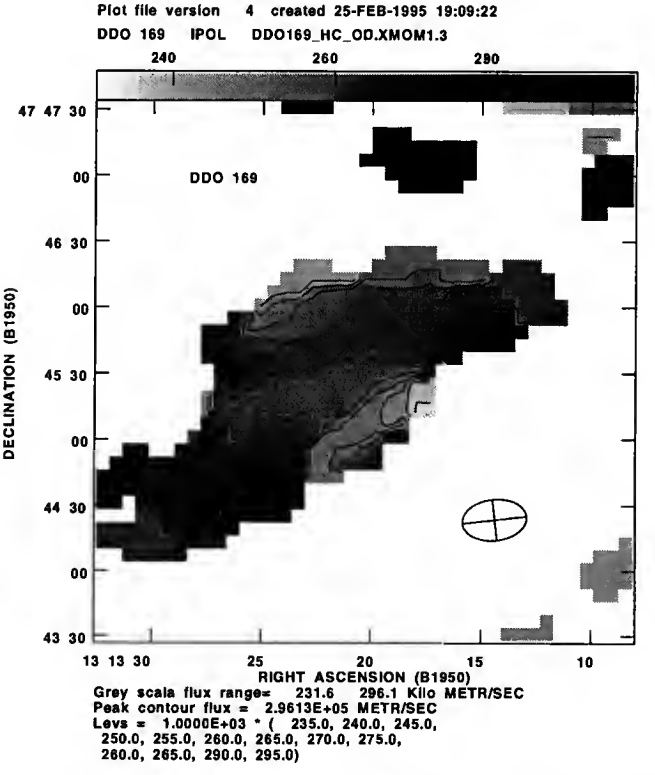

Figure 5.39: Integrated velocity field (1st moment) map of DDO 169.

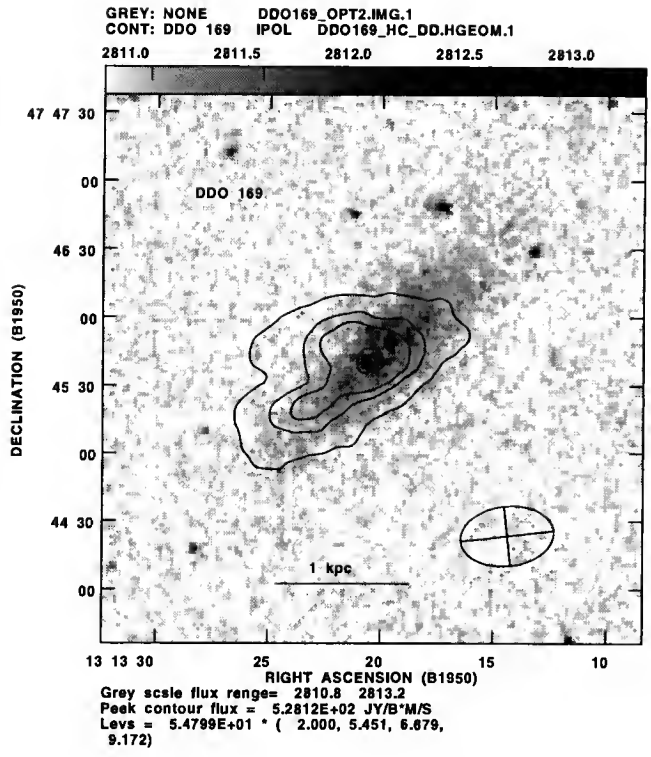

Figure 5.40: Optical greyscale image with HI contours for DDO 169.

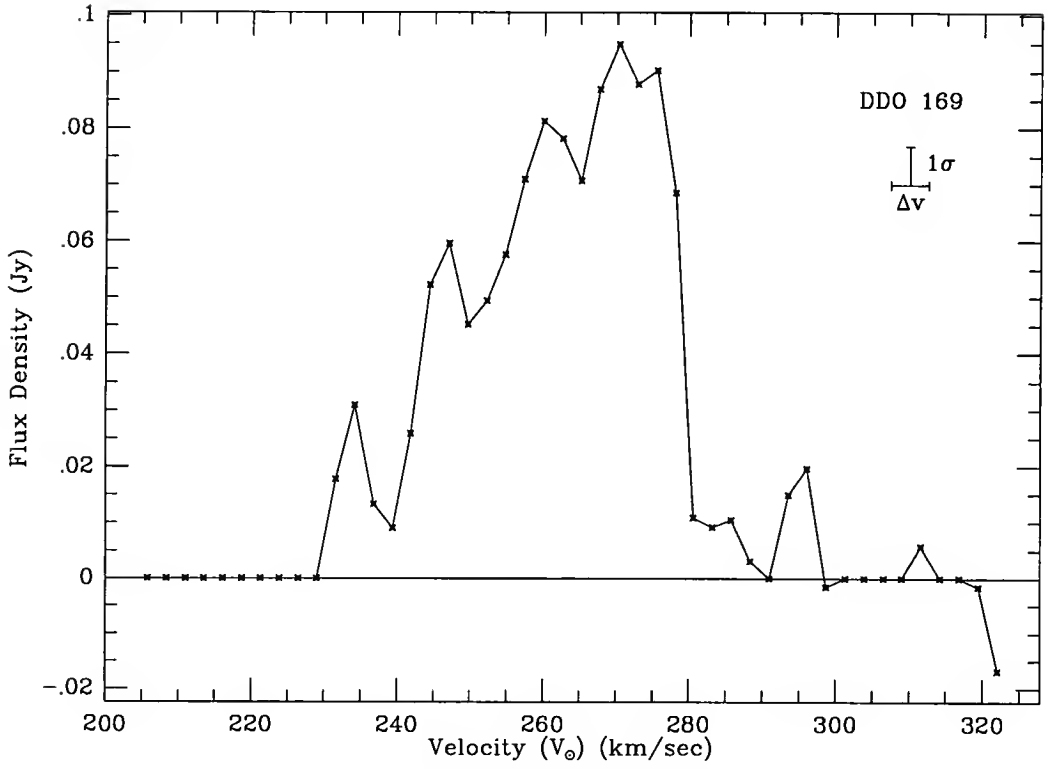

Figure 5.41: Global velocity profile for DDO 169.

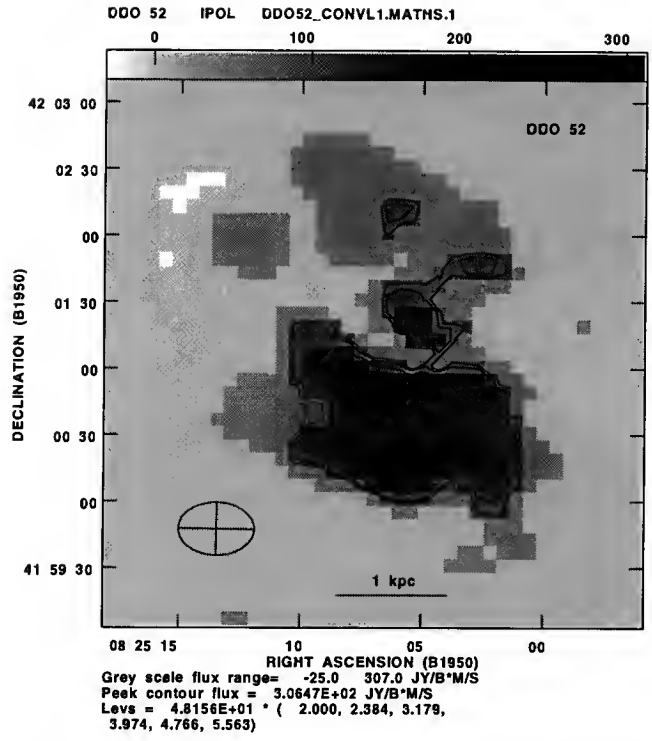

Figure 5.42: Integrated HI intensity (0th moment) map of DDO 52. Contour levels are 2.5 (2σ), 3, 4, 5, 6, 7 $\times$ 10^{20} atom cm^{-2}.

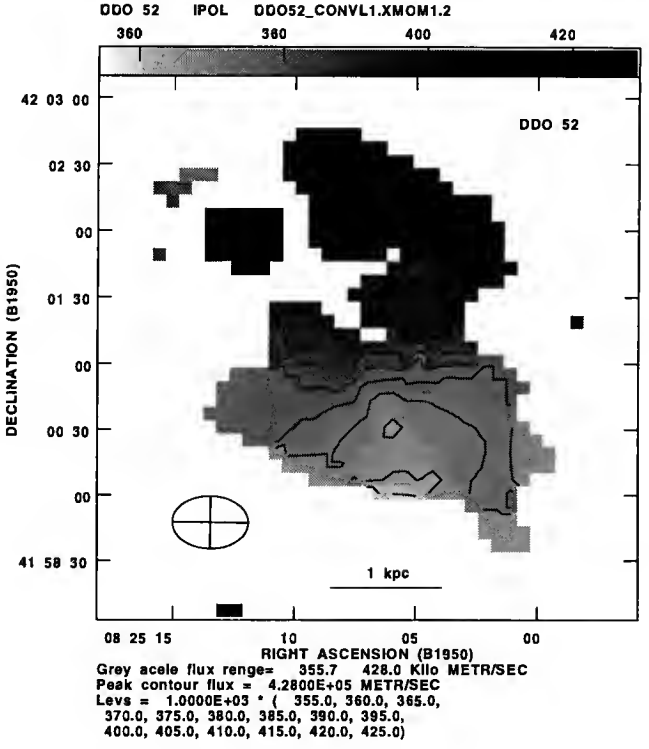

Figure 5.43: Integrated velocity field (1st moment) map of DDO 52.

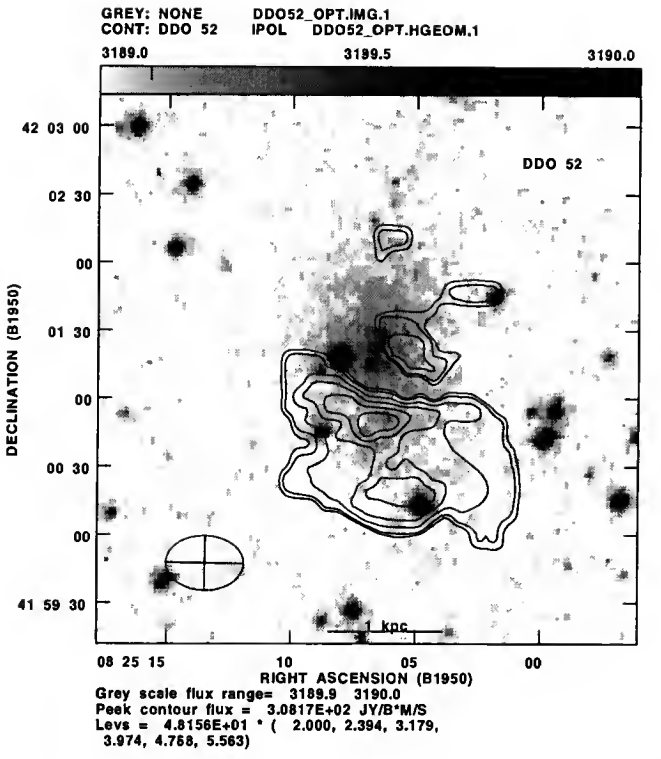

Figure 5.44: Optical greyscale image with HI contours for DDO 52.

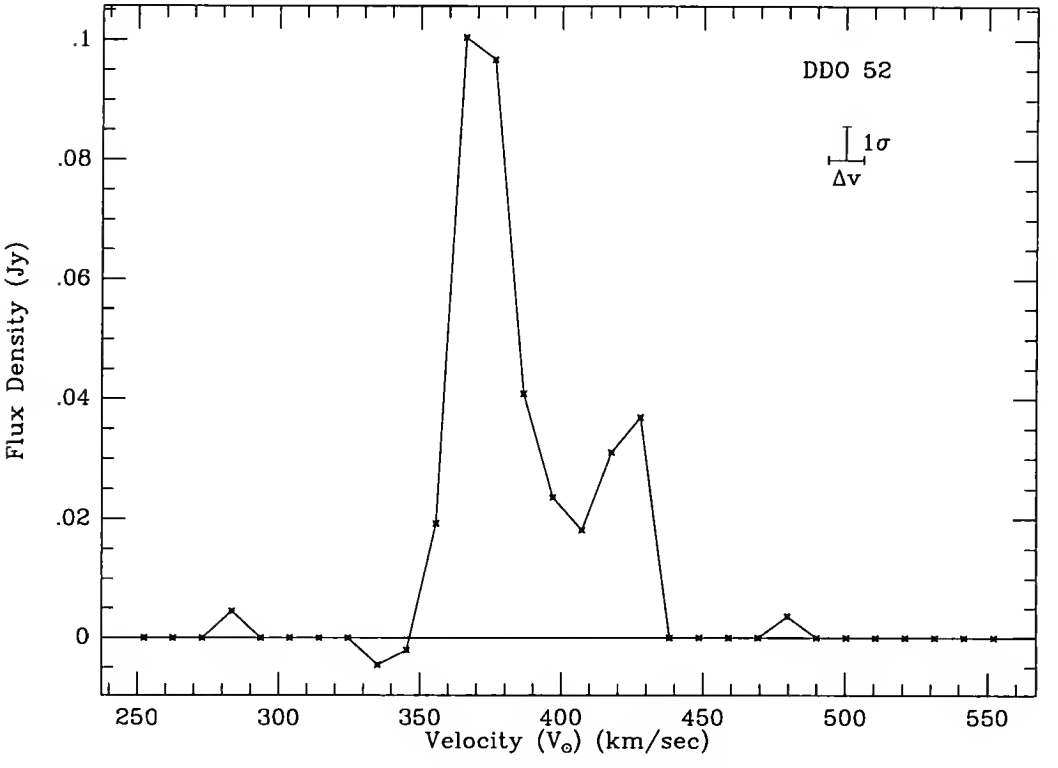

Figure 5.45: Global velocity profile forDDO 52.

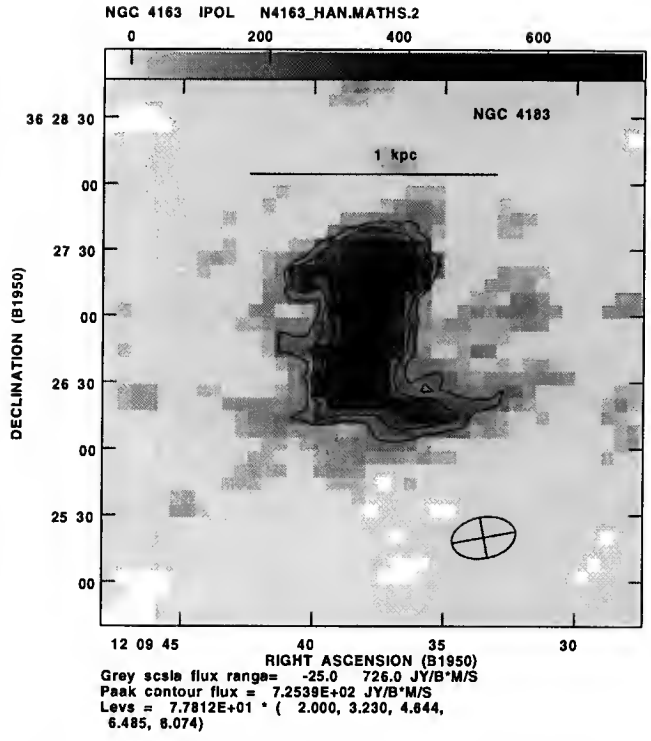

Figure 5.46: Integrated HI intensity (0th moment) map of NGC 4163. Contour levels are 3.1 (2σ), 5, 7.5, 10, 12.5 $\times$ 10^{20} atom cm^{-2}.

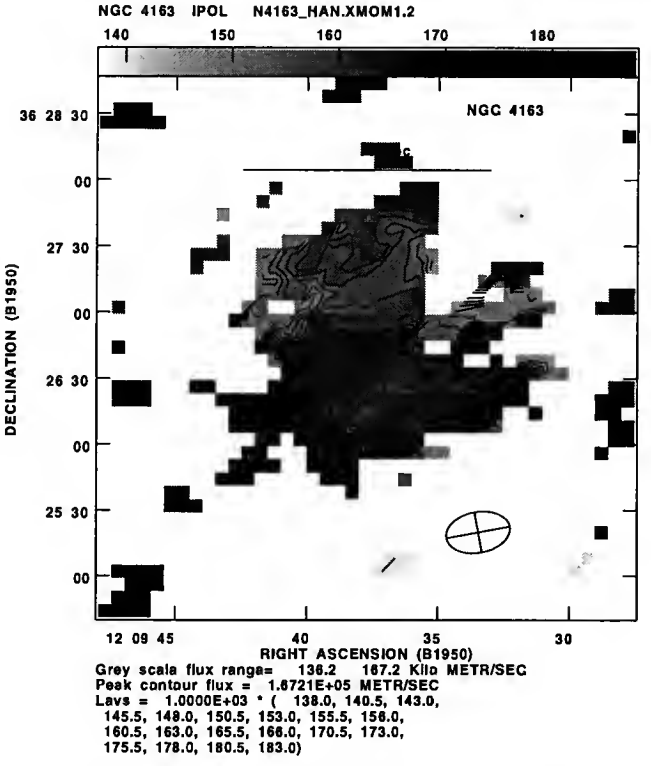

Figure 5.47: Integrated velocity field (1st moment) map of NGC 4163.

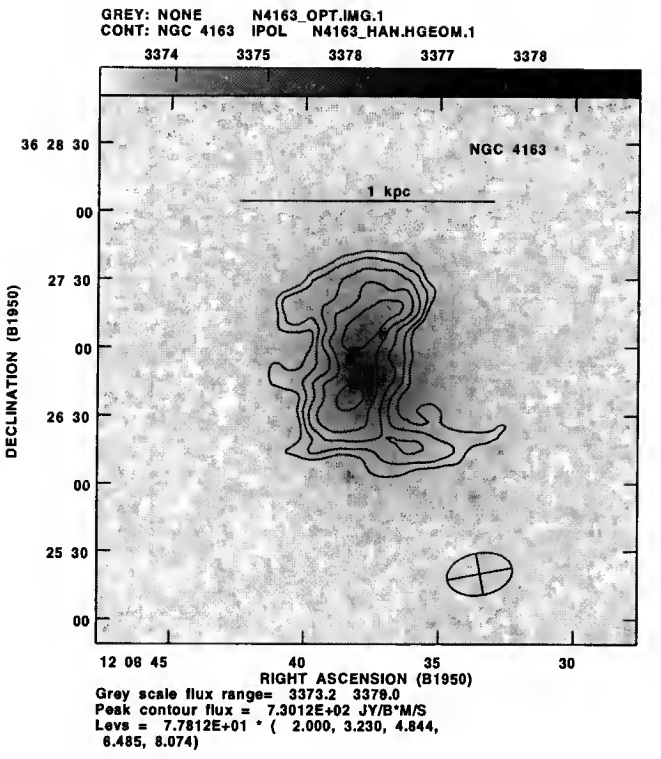

Figure 5.48: Optical greyscale image with HI contours for NGC 4163.

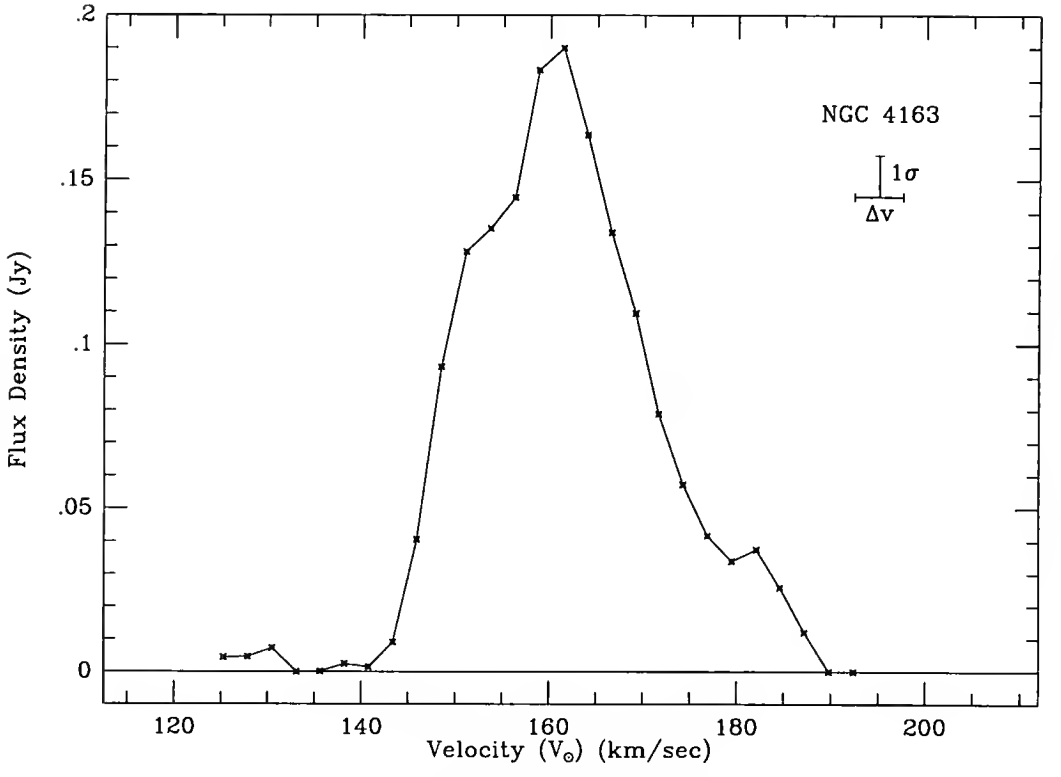

Figure 5.49: Global velocity profile for NGC 4163.

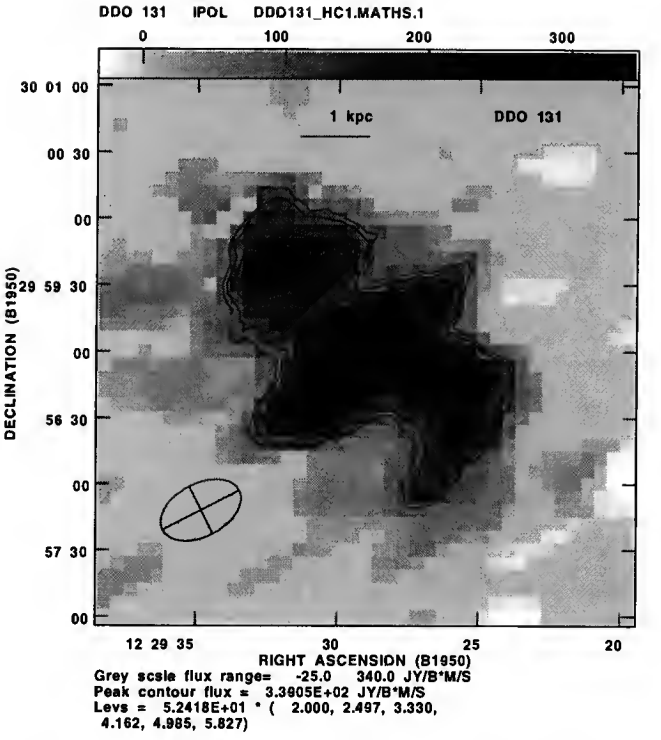

Figure 5.50: Integrated HI intensity (0th moment) map of DDO 131. Contour levels are 2.4 (2σ), 3, 4, 5, 6, 7 $\times$ 10^{20} atom cm^{-2}.

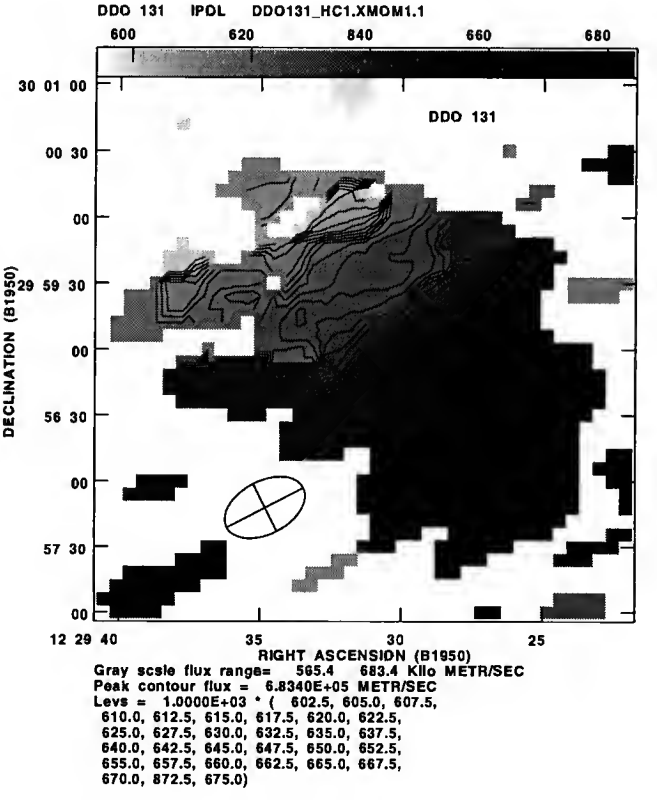

Figure 5.51: Integrated velocity field (1st moment) map of DDO 131 .

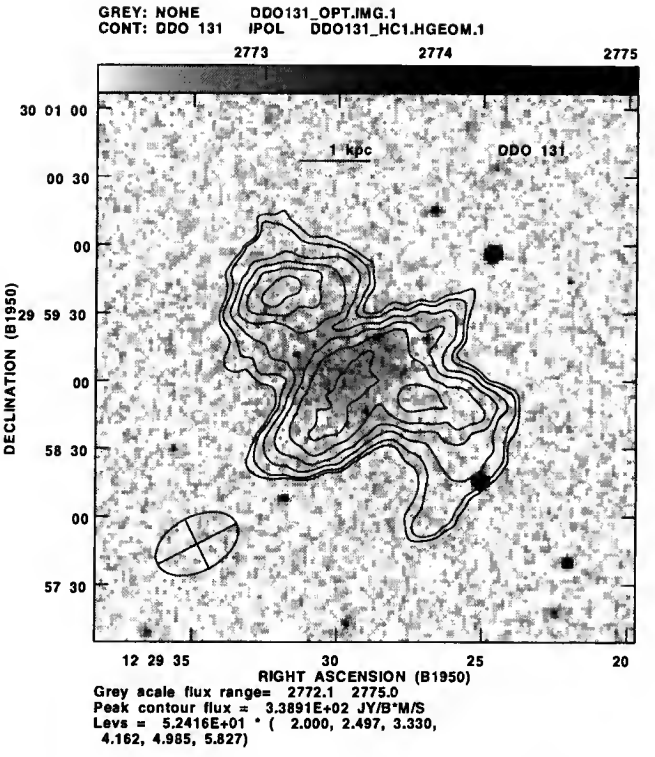

Figure 5.52: Optical greyscale image with HI contours for DDO 131.

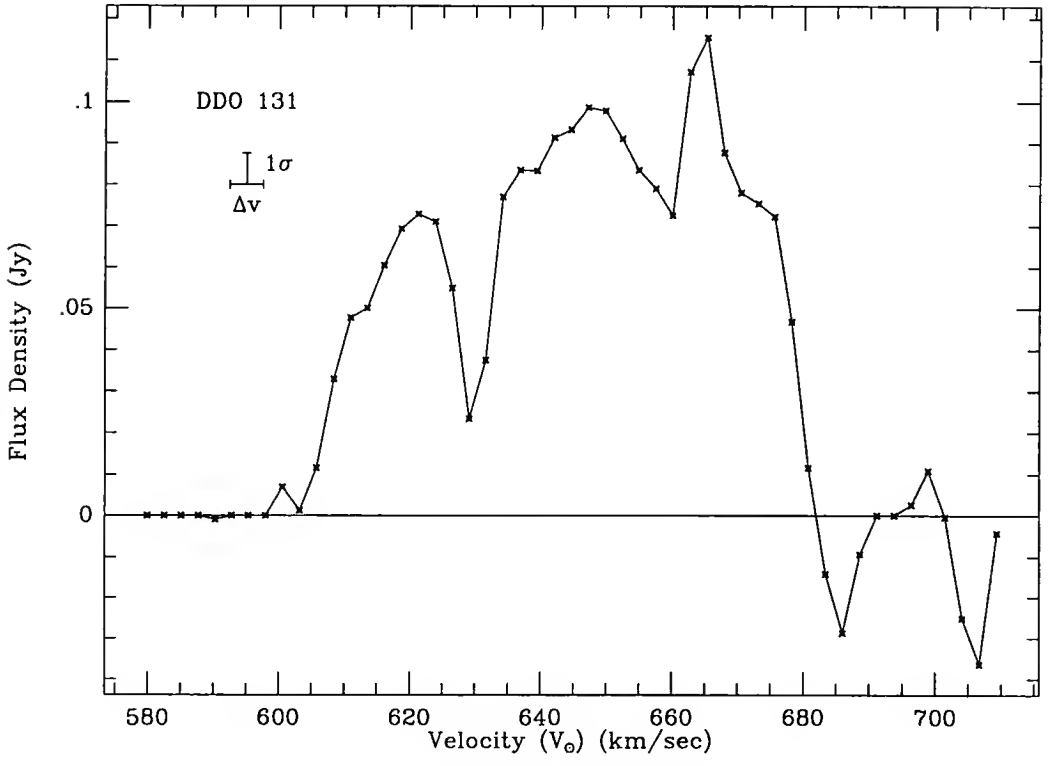

Figure 5.53: Global velocity profile for DDO 131.

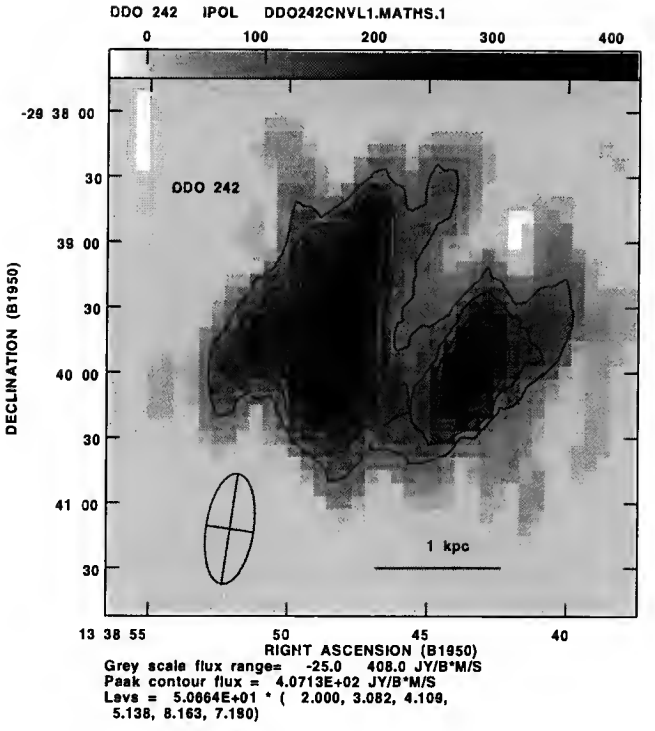

Figure 5.54: Integrated HI intensity (0th moment) map of DDO 242. Contour levels are 1.9 (2σ), 3, 4, 5, 6, 7 $\times$ 10^{20} atom cm^{-2}.

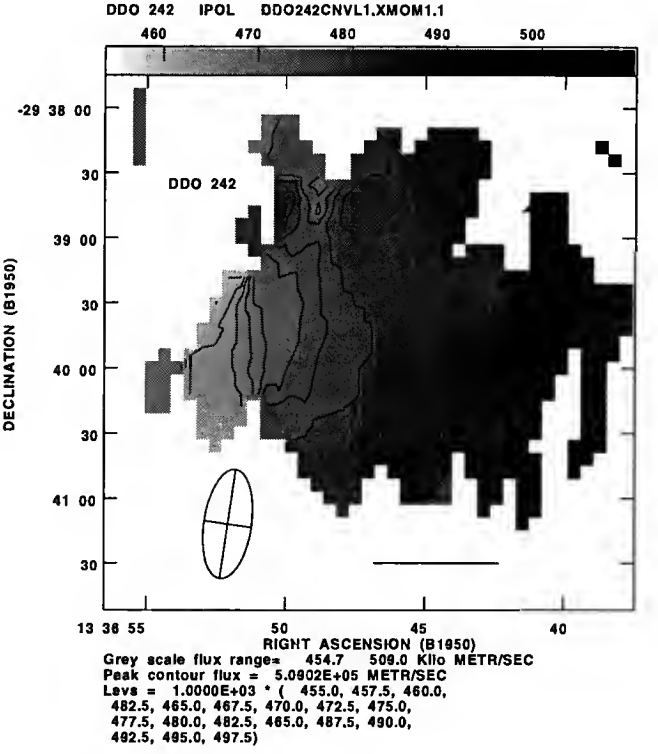

Figure 5.55: Integrated velocity field (1st moment) map of DDO 242.

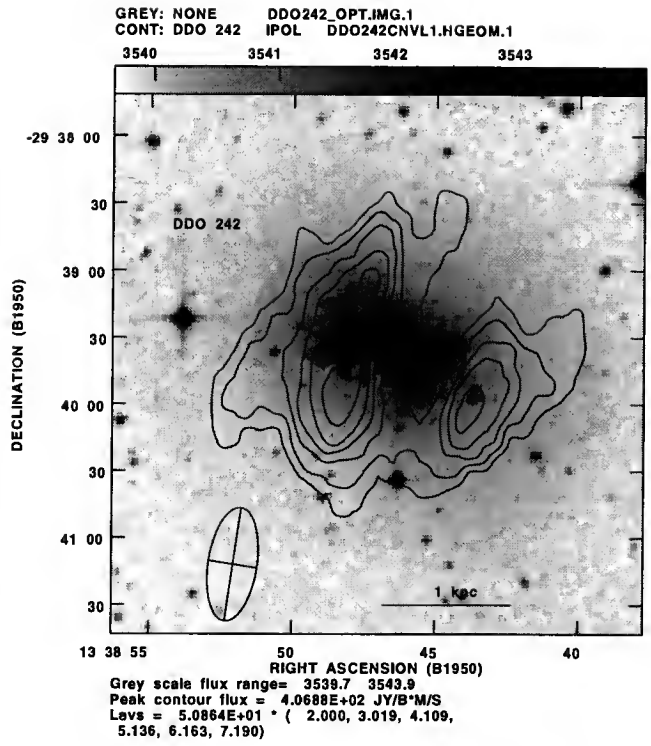

Figure 5.56: Optical greyscale image with HI contours for DDO 242.

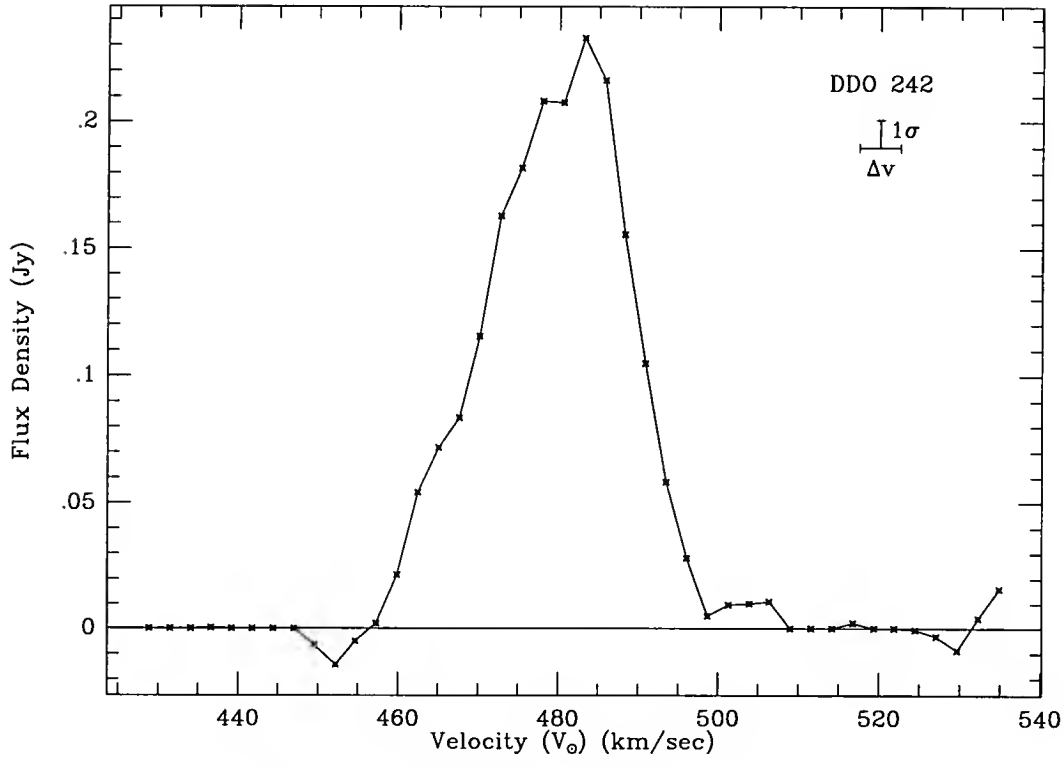

Figure 5.57: Global velocity profile for DDO 242.

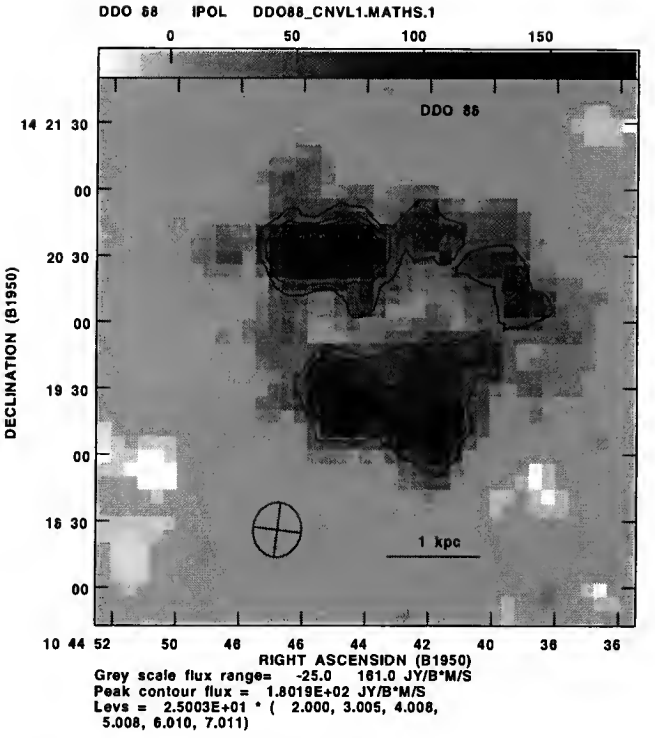

Figure 5.58: Integrated HI intensity (0th moment) map of DDO 88. Contour levels are 2.0 (2σ), 3, 4, 5, 6, 7 $\times$ 10^{20} atom cm^{-2}.

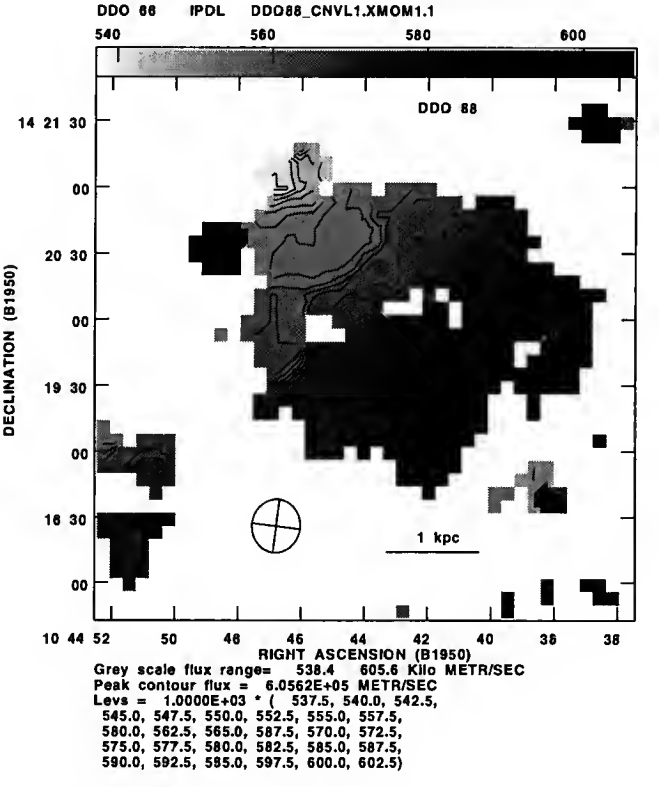

Figure 5.59: Integrated velocity field (1st moment) map of DDO 88.

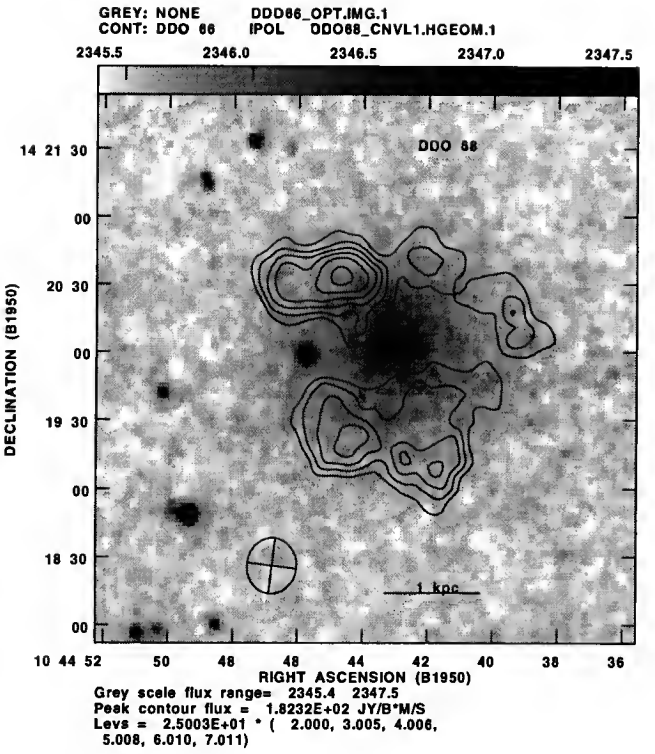

Figure 5.60: Optical greyscale image with HI contours for DDO 88.

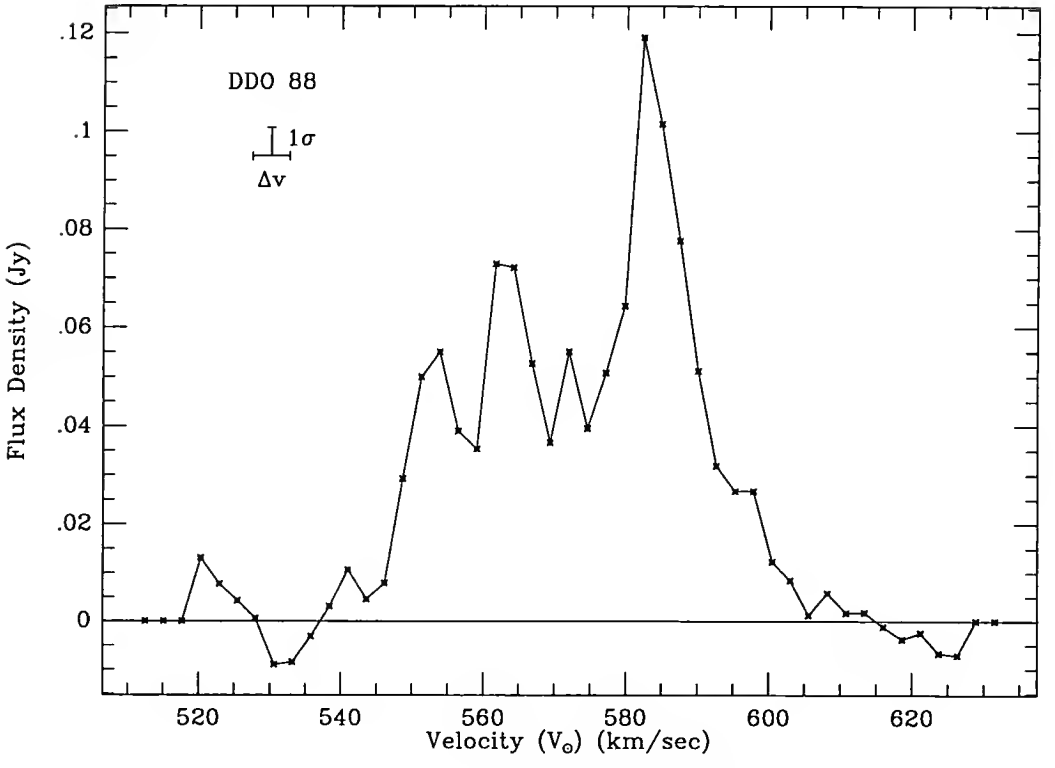

Figure 5.61: Global velocity profile for DDO 88.

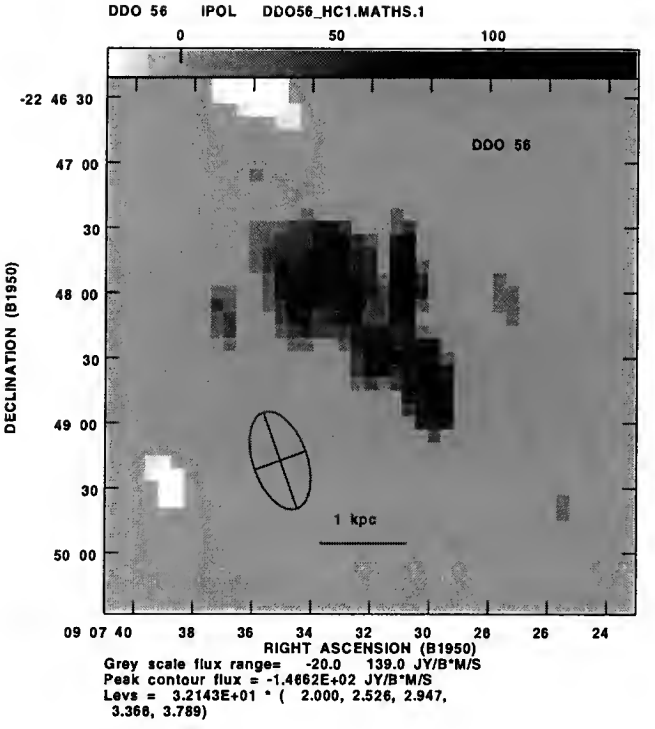

Figure 5.62: Integrated HI intensity (0th moment) map of DDO 56. Contour levels are 1.2 (2σ), 1.5, 1.75, 2, 2.25 $\times$ 10^{20} atom cm^{-2}.

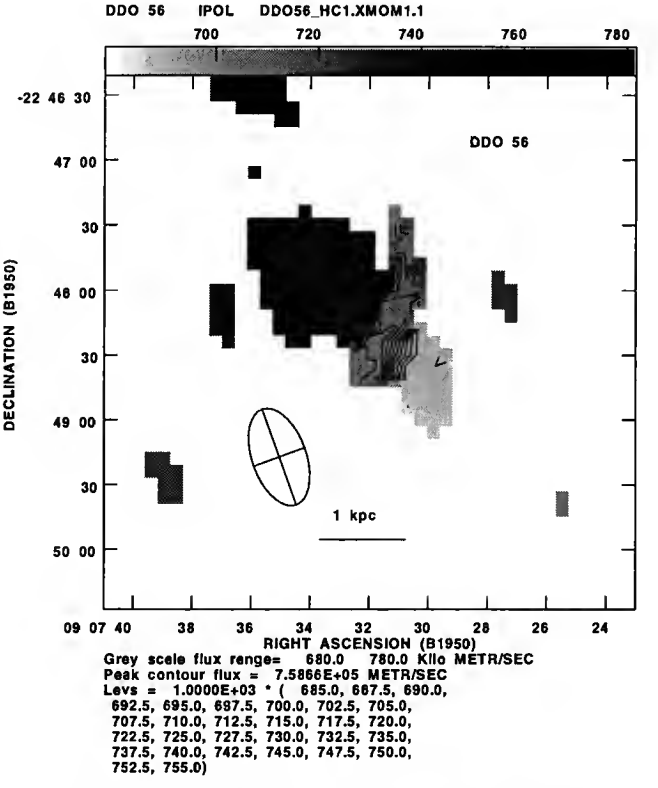

Figure 5.63: Integrated velocity field (1st moment) map of DDO 56.

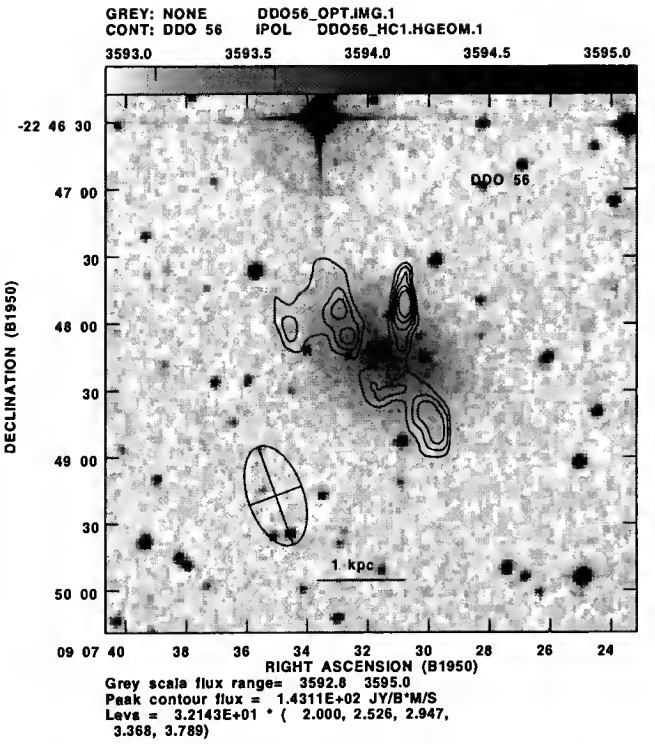

Figure 5.64: Optical greyscale image with HI contours for DDO 56.

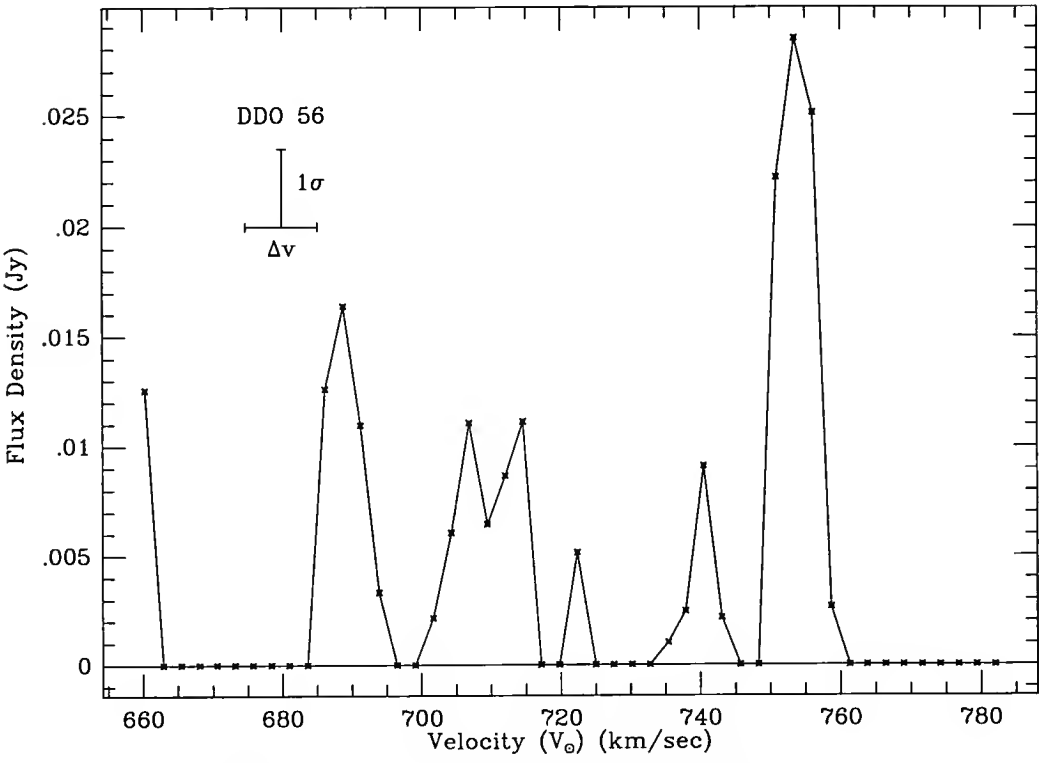

Figure 5.65: Global velocity profile for DDO 56.

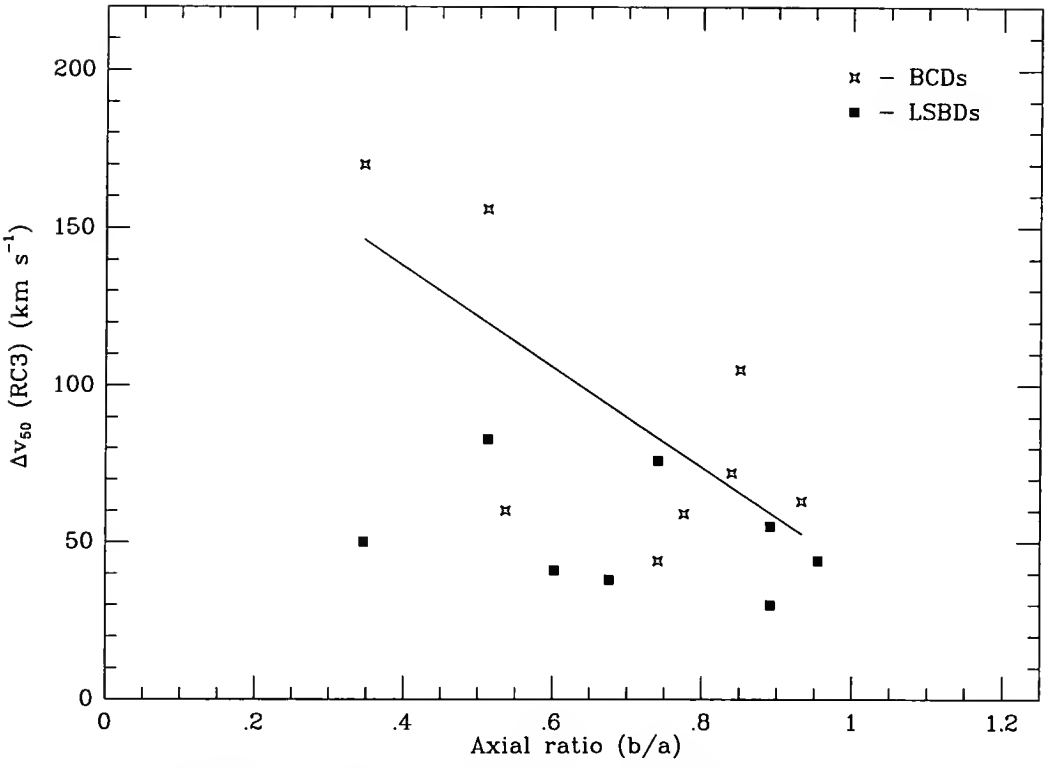

Figure 5.66: Velocity width Δv_{50} vs. axial ratio (b/a).

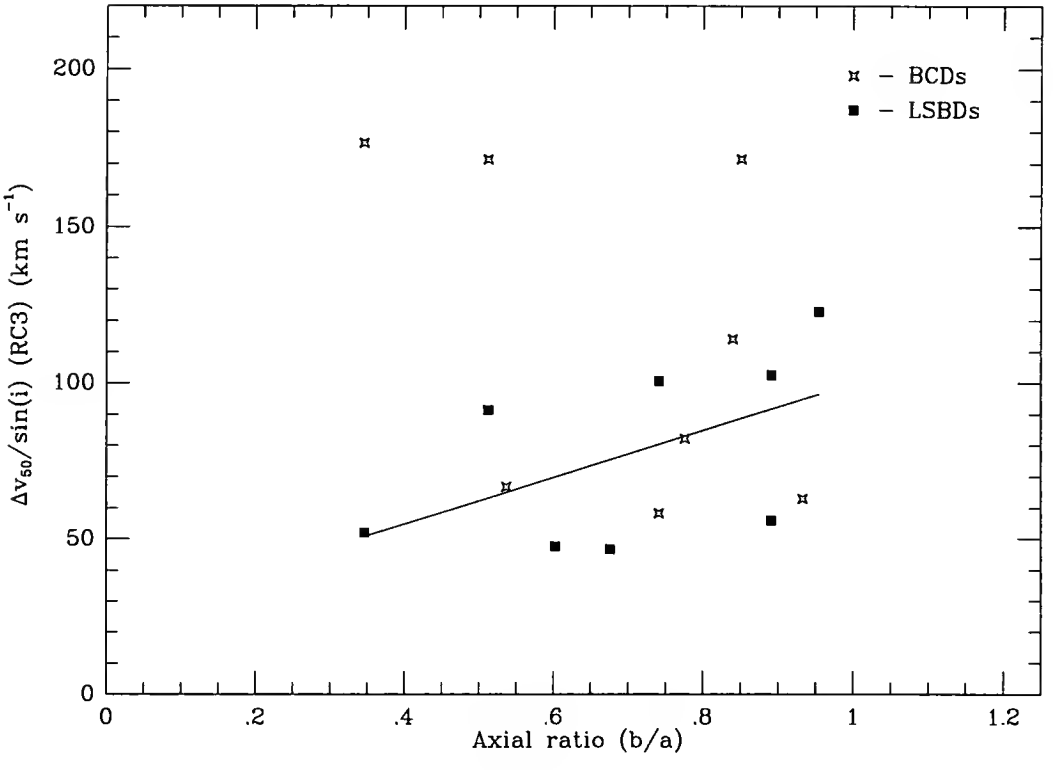

Figure 5.67: Corrected velocity width (Δv_{50}/sin i) vs. axial ratio (b/a).

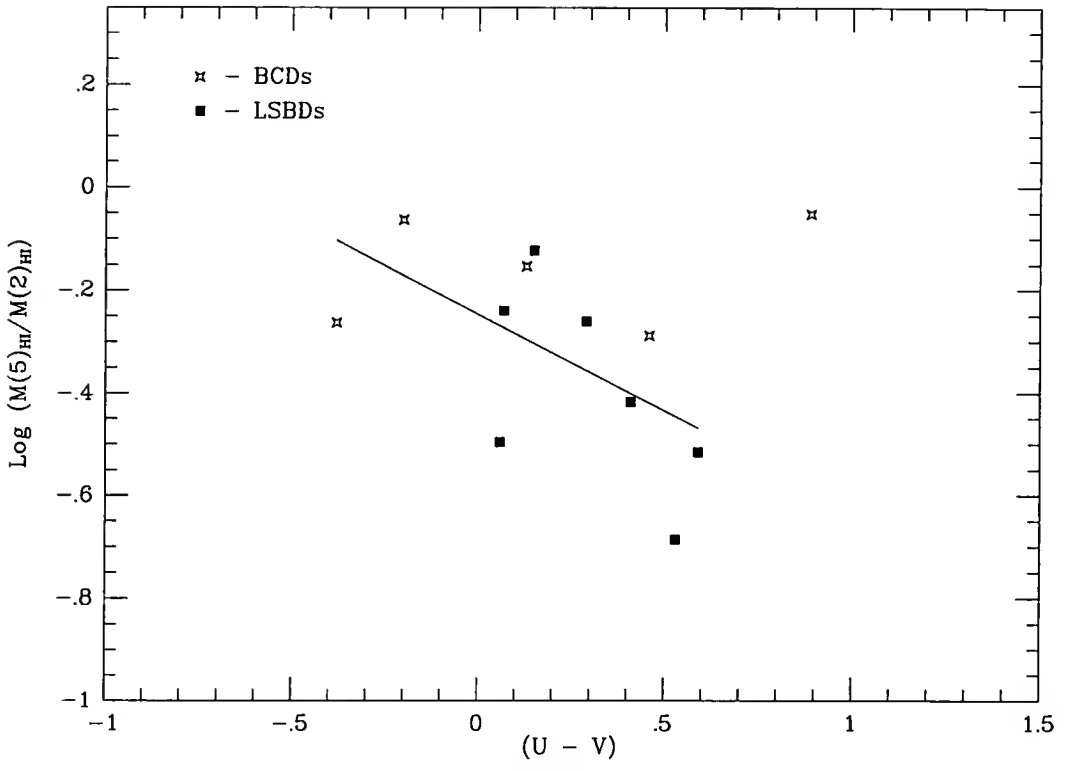

Figure 5.68: HI concentration $(\frac{M(5)_{HI}}{M(2)_{HI}})$ vs. color (U – V).

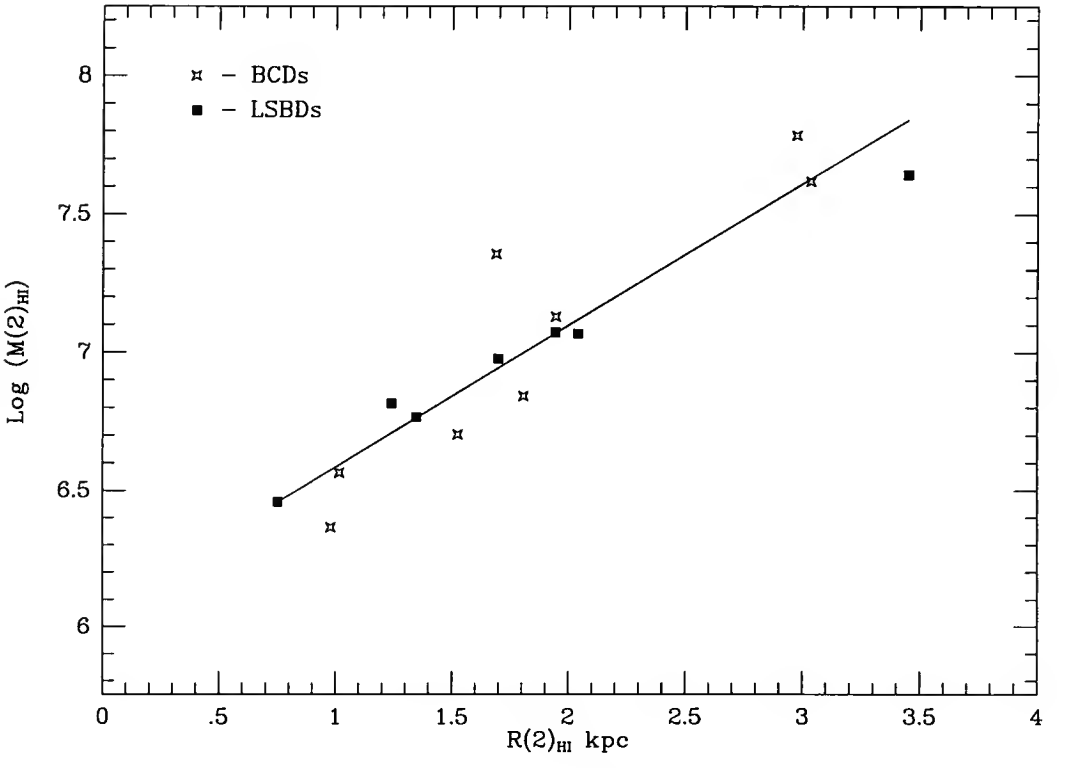

Figure 5.69: HI mass $M(2)_{HI}$ vs. HI radius $R(2)_{HI}$.

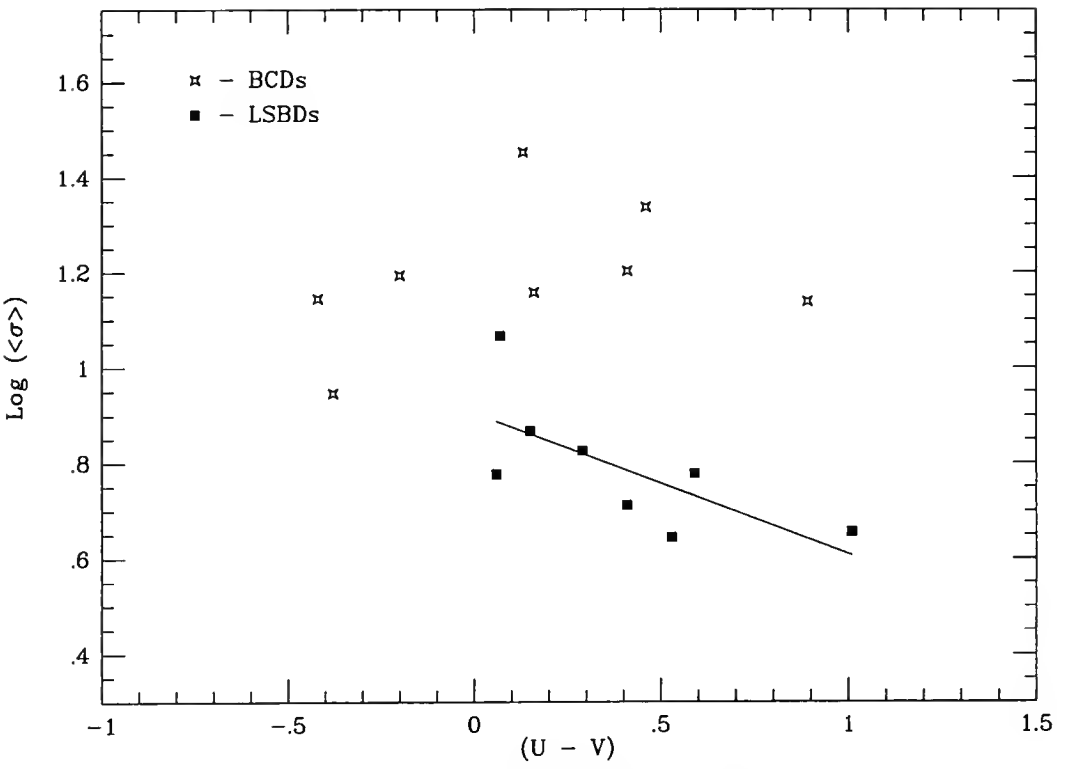

Figure 5.70: Average dispersion velocity $\langle\sigma_v\rangle$vs. color (U – V).

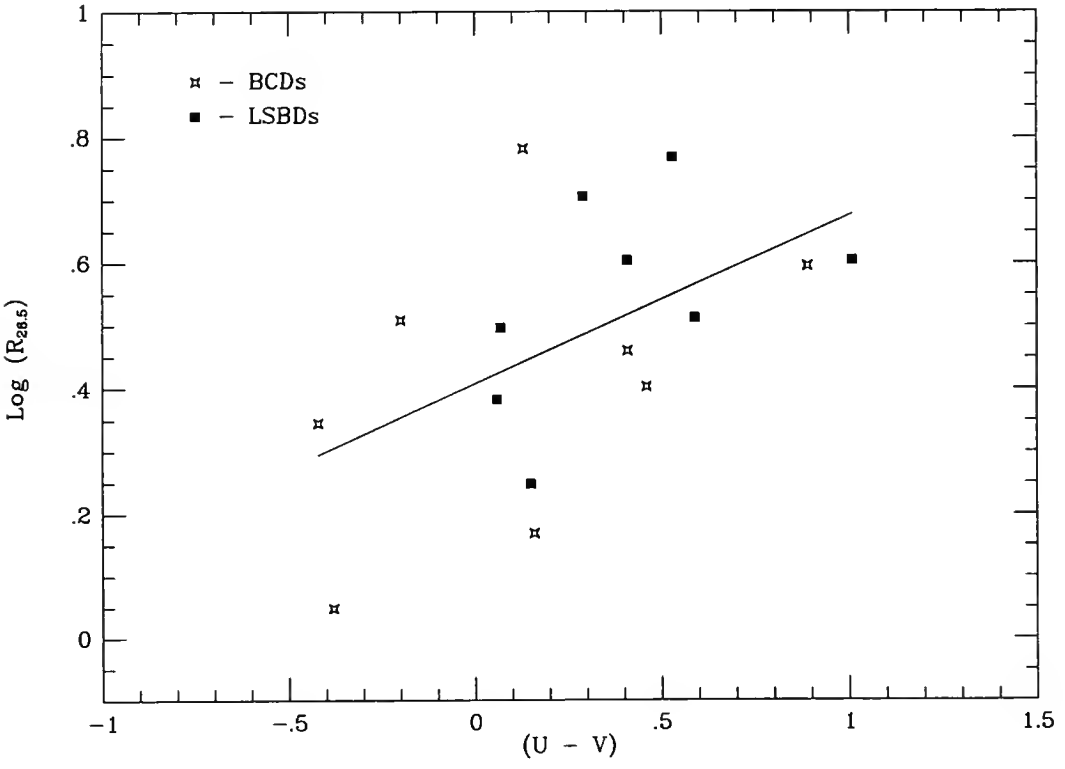

Figure 5.71: Holmberg diameter $R_{26.5}$ vs. .color (U – V)

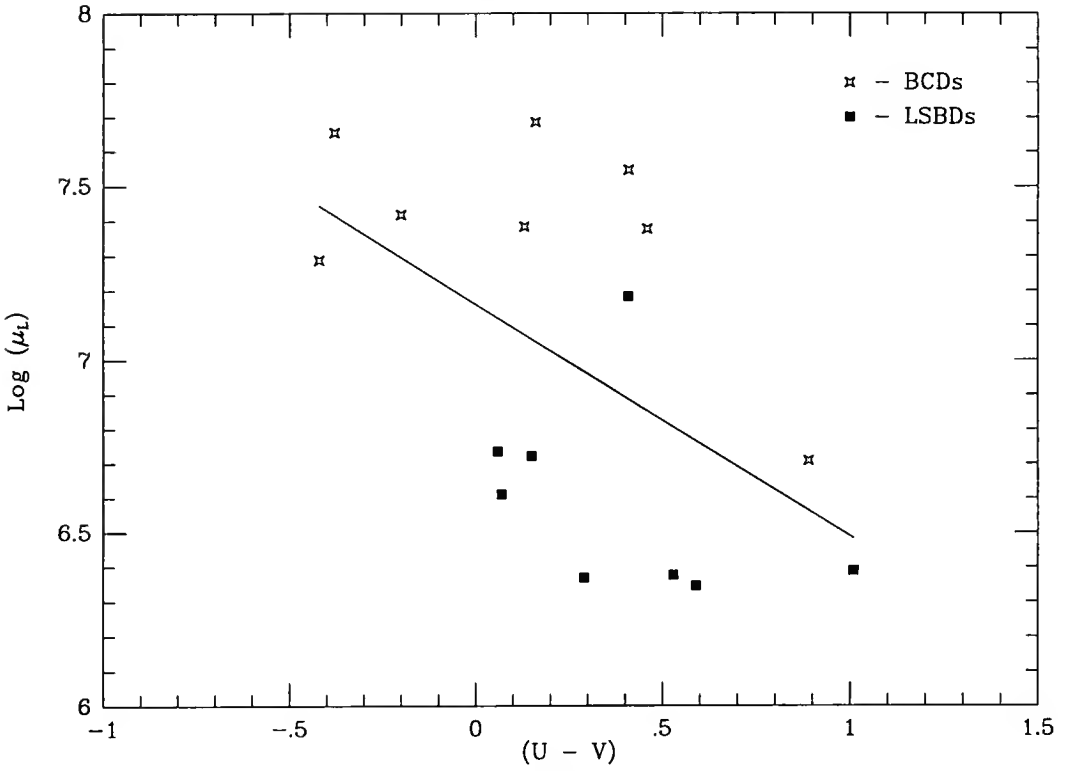

Figure 5.72: Optical surface brightness μ_L vs. color (U – V).

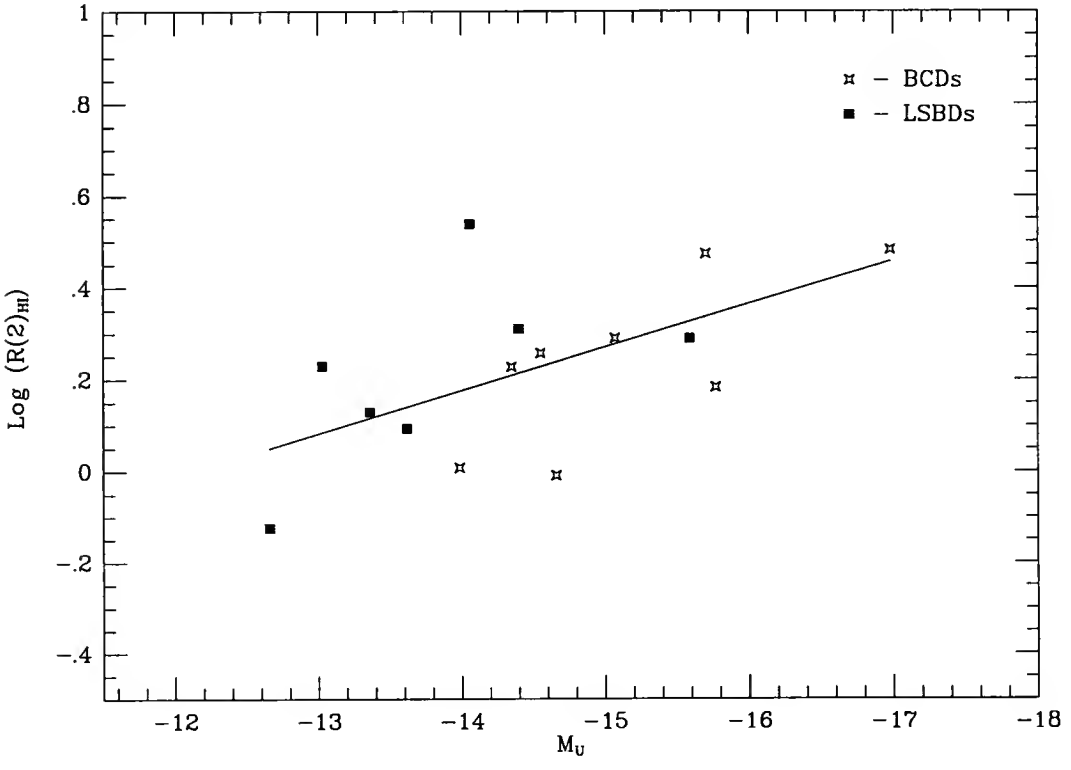

Figure 5.73: HI radius $R(2)_{HI}$ vs. absolute magnitude M_U (log L_U).

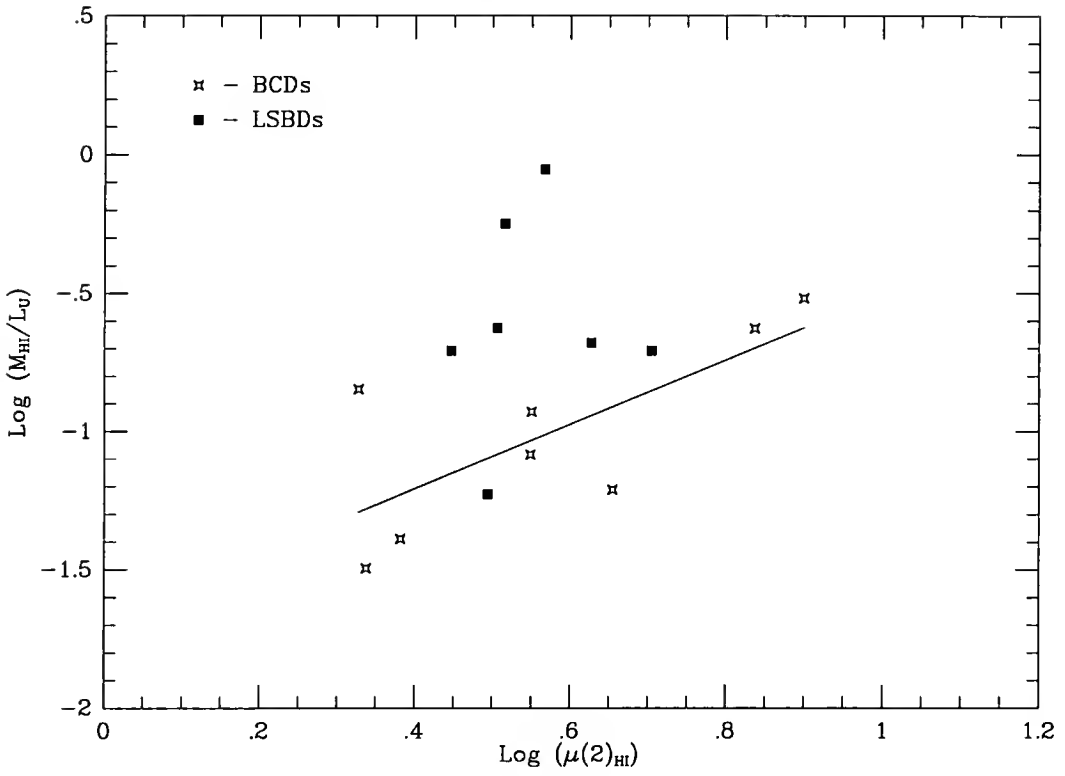

Figure 5.74: HI mass-to-light ($\frac{M_{HI}}{L_U}$) vs. HI surface density $\mu(2)_{\rm HI}$.

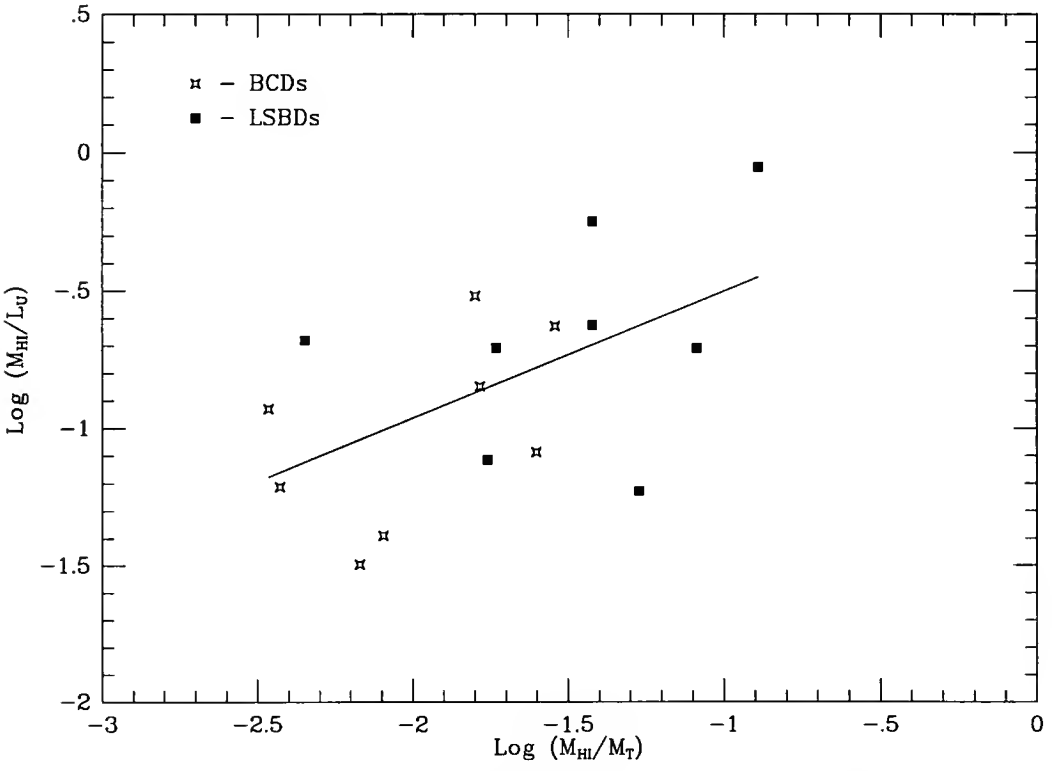

Figure 5.75: HI mass-to-light ($\frac{M_{HI}}{L_U}$) vs. HI mass to total mass ($\frac{M_{HI}}{M_T}$).

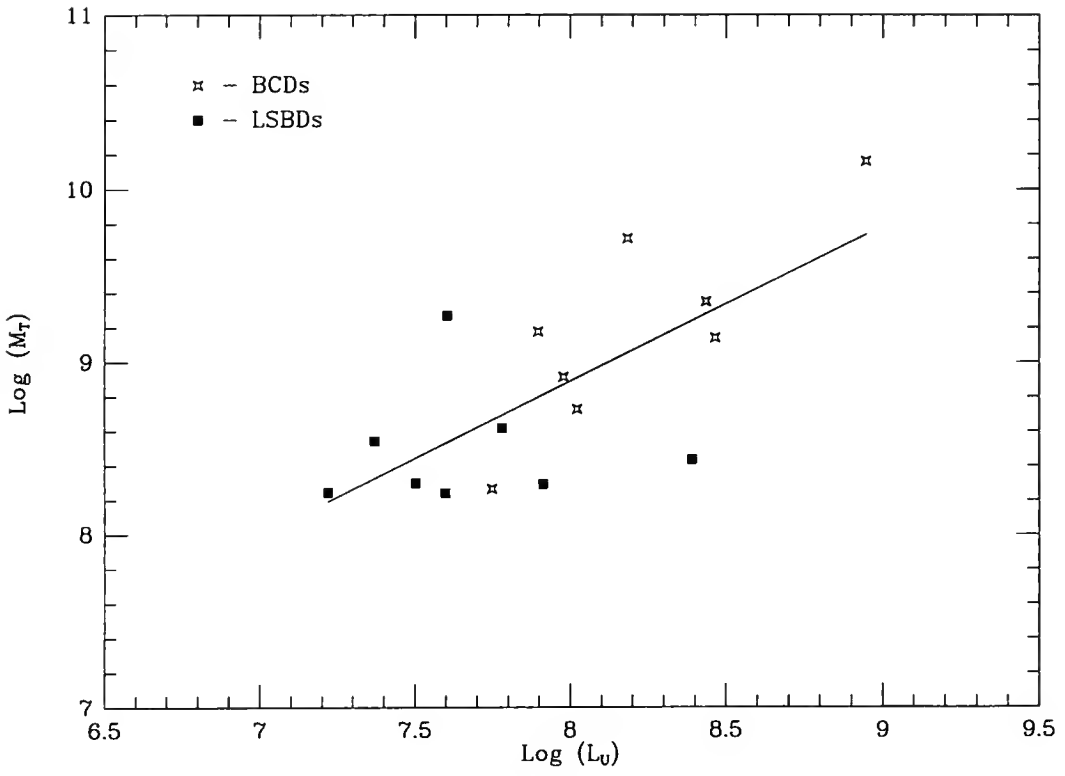

Figure 5.76: Total mass (M_T) vs. luminosity (L_U).

CHAPTER 6
CONCLUSIONS

Summary

In this work, the results of (1) a survey to detect low mass dwarf irregular galaxies, and (2) a study of the atomic hydrogen in eight blue compact dwarfs and eight low surface brightness dwarfs have been presented. Dwarf systems, the small, low mass, and faint end of the morphological spectrum of galaxies, are of interest both because they are the most numerous type of galaxy (Davies and Phillipps, 1988; Binggeli et al., 1988), and because they offer an opportunity to examine star formation on a global scale.

The survey project was motivated by the prediction (Tyson and Scalo, 1988) of a radial distribution function that rises steeply for smaller galactic radii (i.e. fainter systems). To investigate the faint end of this predicted luminosity function, we conducted a survey, using the Very Large Array Radio Telescope, that was sensitive to low levels of HI emission. As dwarf irregular galaxies tend to have high fractional HI masses (Roberts and Haynes, 1994), this radio-wavelength survey was able to detect small but gas-rich systems which tend to be overlooked at optical wavelengths due to their intrinsic faintness (Tyson and Scalo, 1988; Binggeli et al., 1988).

Using the radial distribution function,

$$f(r) = K_r r^{-4.2}\,, \tag{6-1}$$

and empirical relations found by Tyson and Scalo in their 1988 paper, we were able to estimate the number of galaxies expected to be detected by the VLA in our survey.

Assuming a constant space density (but see below), and including the drop-off in sensitivity with distance, we predicted that there should be approximately 9 galaxies[1] detected within each of the three fields (each field composed of observations taken at two different frequencies) we observed. Each field covered approximately 5 Mpc^3; the total volume surveyed was 15.7 Mpc^3.

Although Tyson and Scalo assumed a constant space density in order to calculate an average number density, this type of distribution is clearly not the case for the more-luminous (and therefore better-studied) systems. Non-dwarf (i.e. more massive) galaxies are observed to have a "clumpy" distribution throughout space; they tend to cluster together into groups, and groups of groups. The theory of biased galaxy formation (Binggeli et al., 1990; Dekel and Silk, 1986) explains this clustering by only allowing more massive galaxies to form on high density peaks in the background mass distribution. However, a consequence of this is that smaller (dwarf) systems, formed on lower density peaks, will have a smoother, more ubiquitous spatial distribution: they will be less clustered than more luminous systems.

To investigate not only the number density but also the spatial distribution of dwarf irregular galaxies, we therefore chose to conduct our survey in areas with differing environments. One field was located in the Local Void, the second in a cluster of galaxies, and the last was located in an interaction field where dwarfs may be more abundant as the result of the tidal rearrangement of material that occurs when two or more galaxies interact. In order to ensure that the VLA was operating properly and to check that our observational data were calibrated and reduced prop-

---

[1] But see Appendix B, which takes the dropoff in sensitivity across the primary into account.

erly, we included a catalogued dwarf galaxy in the observations of each of our three fields.

The results of our survey, which was sensitive to HI masses as low as 1.86×10^5 $M_\odot$, indicate that Tyson and Scalo's luminosity function is too steep at the faint end. Although the prediction was for 27 galaxies in our survey volume, we detected only 4: the three targeted systems and one other catalogued dIrr, located in the M81/M82 interaction field (UGC 5455). Other surveys, such as those conducted by Weinberg et al. (1991) and reviewed by Briggs (1990) and Brinks (1994), have also reached the same conclusion: these faint, HI-rich systems do exist, but not in the large numbers suggested by Tyson and Scalo. Our work, while reinforcing that of these previous surveys, has added to the body of knowledge by concentrating on the poorly-studied, very low-mass end of the luminosity function. Our results rule out the existence of a large population of very low mass gas-rich dwarf galaxies.

Although our paucity of detections has important ramifications for the number density distribution of galaxies, it unfortunately precludes our being able to make a definitive statement about the spatial distribution (clustering) of dIrrs. An overview of the recent literature (see Chapter 4 for references) reveals that current observations indicate that dIrrs do not follow a smooth spatial distribution, although they are not clustered quite as strongly as their brighter counterparts. It is clear that biasing in which dwarfs "fill the voids" is not compatible with the observations.

The next question addressed in this body of work was raised as a result of the negative results of our survey. Another possibility to explain the lack of detectable low mass dIrr systems is that perhaps they are not gas-rich and so are not visible at radio (21–cm) wavelengths. It has been postulated (Davies and Phillipps, 1988; Puche and Westpfahl, 1994) that low mass galaxies could lose their HI gas as a

natural result of the episodic star-formation that is thought to occur in these systems.

This type of episodic star-formation, known as Stochastic Self-Propagating Star Formation (SSPSF), was first put forth by Searle et al. (1973), and was further developed and applied specifically to dwarf systems by Gerola et al. in 1980. They found that low mass galaxies will undergo bursts of star formation separated by long quiet intervals, and that the starburst will involve much, if not all, of the smallest systems.

Such a global event will have a dramatic effect on a low mass galaxy, and this idea has led various researchers to propose a "unification" scheme for the three different types of dwarf galaxy (e.g. Davies and Phillipps, 1988; see discussion of system evolution in Chapter 2 for further references). The general idea is that a significant amount of star formation taking place in a dwarf galaxy can pump enough energy into the ISM (via stellar evolutionary processes such as supernovae explosions and stellar winds from massive stars) to either disperse, or even eject, the HI reservoir that provided the initial fuel for the starburst. The dissipation and/or consumption of the neutral gas, out of which stars form, would provide a mechanism for shutting off the star-formation episode.

In very low mass systems, the injection of energy from an episode of star formation could even push the remaining HI beyond the boundaries of the galaxy, where it would be lost (e.g. Puche and Westpfahl, 1994). From this idea, several evolutionary chains linking dEs, dIrrs, and BCDs have been proposed. It has been postulated that dIrrs evolve directly into dEs as a result of gas-loss (Lin and Faber, 1983; Dekel and Silk, 1986; Kormendy, 1985), or into BCDs (Searle et al., 1973; Thuan, 1985), or first into BCDs and then eventually into dEs (Davies and Phillipps, 1988; Bothun et al., 1986).

It is the repercussions of SSPSF on low mass systems that we have investigated in the second part of this study. Chapter 5 presents the results of our VLA HI observations of 8

BCDs and 8 LSBDs. In an effort to identify systems in different stages of the proposed evolutionary chain(s) mentioned above, we chose our sample to encompass a range of (U – B) and (B – V) color indices. We then calculated the (U – V) color index, and have used that as an indicator of star-formation activity. The use of this parameter would seem to be justified as we have found a correlation between optical surface brightness and (U – V) color for our galaxies, with bluer galaxies having higher surface brightnesses.

The other correlations that we have found, as well as the HI distributions and kinematics revealed in the moment maps produced from our observations, tend to indicate that the state of the HI reservoirs in small galaxies is indeed related to the evolutionary stage of the systems with respect to their star-formation histories. We have shown that bluer (more actively star-forming) galaxies have more concentrated HI as indicated by $(\frac{M(5)_{HI}}{M(2)_{HI}})$ and that the bluer LSBDs have higher velocity dispersions, indicating more disturbed HI reservoirs. In addition, we found that the BCDs, on average, also possess higher dispersion velocities than the LSBD sub-sample as a whole; both this and the dispersion-color correlation for the LSBDs indicate that more energy has, indeed, been pumped into the ISM of the more actively star-forming galaxies.

Although limited by the poor spatial resolution for our BCD sub-sample, and the poor signal-to-noise for the entire galaxy sample, it is clear from the moment maps presented in Chapter 5 that the LSBDs, at least, do show a great deal of structure in their HI distributions. The moment maps for the best-resolved of our BCDs, as well as the global profiles, which have very good velocity resolution (5 – 12 km s^{-1}), are not incompatible with a centrally condensed HI distribution, although this is not conclusive by any means.

The lumpy HI structure seen in the LSBDs, and especially the ring-like distributions evident in DDO 43, DDO 242, and DDO 88, are what one would expect to see given the evolutionary scenario outlined above. These systems, DDO 88 in particular, strongly

resemble the smallest systems studied in detail by Puche and Westpfahl (1994). These galaxies are shown to consist of expanding (or contracting) shells, or bubbles, of HI; with the innermost edges of the shells coinciding with the outermost boundaries of the stellar distribution. This is very similar to what we see in our data.

The results from this investigation of our 16 galaxies provides support for the overall theory of SSPSF, and that such episodes of vigorous star formation do seem to affect the global properties of low-mass systems. The HI structure and kinematics seen in several of our LSBDs show that there has been a disruption, and that this is consistent with that seen in systems known to have expanding (or contracting) shells. Although this provides support for the idea of an evolutionary connection between dIrrs and BCDs, the apparently different rotation rates of the two types of systems does not. There is also evidence that suggests the existence of a critical surface density to support star formation: the correlation between the HI "concentration index" and the (U – V) color index shows that galaxies with more concentrated HI are more actively (or recently) forming stars.

In summary, the work presented here shows that (1) the luminosity function for low mass, gas-rich dwarf irregular galaxies is not as steep as predicted by Tyson and Scalo (1988); and (2) that the HI kinematics and structure of blue compact and low surface brightness dwarf irregular systems are consistent with an evolutionary scheme wherein the HI reservoirs in these galaxies take on different characteristics depending upon their star-formation histories. It would be possible, given these results, that dIrrs could indeed lose much of their HI gas as a result of a significant star-formation episode. This work does not therefore rule out an evolutionary chain from dIrr $\rightarrow$ BCD $\rightarrow$ dE; and in fact, lends credence to this theory.

Future Work

The projects reported on here, while suggestive, are not definitive and the possibilities for more in-depth investigations are many. Further kinematical analysis of the existing HI data for the LSBD galaxies exhibiting ring structure could provide preliminary information about whether these systems are indeed expanding/contracting bubbles. If this is the case, an estimate of the expansion velocity, combined with the size of the shell, can provide an estimate of the time when the gas was/will be collected in the center of the system.

As in any observational study, new observations with greater spatial resolution and higher signal-to-noise could greatly clarify the intriguing possibilities suggested by the existing observations. Assembling a set of observations with consistent (similar) spatial resolutions would be of great interest. In particular, higher resolution observations of the current sample of BCDs would provide a means for a true comparison of the HI distributions in these systems and the LSBDs. Conducting observations taken with the high-resolution B-array configuration of the VLA, when combined with the more sensitive C-array data, is one possibility; although the lower sensitivity of the B-array would require very long total integration times. Very little work on the detailed structure of the HI in BCDs has been done to date, and such an investigation holds great promise.

Better signal-to-noise would allow us to examine the HI out to greater extents, and perhaps allow us to fit rotation curves to these systems. Once a rotation curve has been derived, it would be possible to further investigate the proposal that the gas in a galaxy must reach a critical density in order to support star formation. Further investigation of the HI clumps in several of the LSBD observations would allow us to examine the stability of these sub-structures, and perhaps shed light on this issue.

Optical observations of these galaxies would allow us to better compare the HI and stellar distributions. CCD observations (V, R, and I) of most of these systems have already been taken using the 36–inch reflector at the University of Florida's Rosemary Hill Observatory. Once these data are reduced, we would like to use these images to further investigate the coincidence (or lack thereof) between the location of the stars and gas relative to each other in these galaxies.

In addition to the information obtained by comparison of the HI and stellar distributions, the images at different wavelengths can also be subtracted from each other, providing information about the color-gradients across the galaxies. This type of investigation can allow us to estimate the locations and extent of different components of the underlying stellar populations. If, for instance, these systems are bluer in the center and redder towards the outskirts, that would indicate that there was widespread star-formation in the past (a broad, red (and therefore old) stellar population) with more recent activity (younger, bluer stars) confined to the innermost parts of the galaxies. Differences in the color-gradients between the BCD and LSBD sub-samples could provide evidence that they undergo large-scale star formation differently, and this could help clarify whether the two types of dIrrs are related or not.

High spatial resolution optical images at near-infrared wavelengths such as J, H, and K would provide another, more sensitive, means of probing the stellar population components of these galaxies as well. Such observations could be used to study the mass function of the stars in these systems, therefore examining in greater detail the mechanism of star formation for such galaxies and allowing better comparisons to be made with more massive (spiral) galaxies.

Another type of useful observation would be Hα images, which indicate the location of current star-formation activity. Such emission coming from the centers of the HI

"holes" seen in some of our LSBDs would provide evidence that, indeed, a starburst had recently taken place there.

The field of dwarf galaxy research has expanded greatly in the past 20 years, as technological advances have improved the resolution and sensitivity of astronomical observations. These small systems, once considered oddities peculiar to the Local Group, are now recognized as common systems whose dynamical simplicity provides us with an unprecedented opportunity to investigate processes such as star formation on a manageable scale.

APPENDIX A
COMPANION TO DDO 169

During the data reduction and analysis of the low surface brightness irregular dwarf galaxy DDO 169, a nearby ($\sim 2'$) small galaxy was found. A search of the NED database failed to turn up any known catalogued object at that position; therefore this is a previously unknown galaxy. A visual check of the POSS prints revealed what may be an optical counterpart to the HI detection; this, combined with the strength of the HI signal ($> 14\sigma$ in M_{HI}) and its contiguity across several channels confirm the validity of the detection.

The object's systemic (heliocentric) velocity is 242 ± 1.6 km s^{-1} , and its distance, as calculated from its GSR (galactic standard of rest) velocity, is 3.2 Mpc. It has an HI mass of 1.9 ± 0.4 × 10^6 $M_\odot$ and a peak column density of 4.2 ± 0.8 × 10^{20} atm cm^{-2}. Its projected distance from DDO 169 is approximately 3 kpc. Preliminary analysis indicates that a total system mass of greater than 1 × 10^9 is required to bind DDO 169 and this small companion. Since DDO 169 has an estimated total mass of 1.9 × $10^9 M_\odot$, the companion would appear to be gravitationally bound to DDO 169.

The zeroth and first moment maps, as well as the global profile are presented in the following pages. A zeroth moment map showing both DDO 169 and this system is also shown, as is an optical greyscale image with HI contours.

An optical image from the Digitized Sky Survey was obtained and read into AIPS, allowing us to process the image in an effort to ascertain whether there is any optical emission that coincides with the HI we have detected from this small companion galaxy. The optical image was convolved spatially to enhance the contrast and then examined

visually. There does appear to be an area of enhanced optical emission coming from the same location as the companion; indeed, there appears to be faint optical emission stretching from DDO 169 up to the companion. This work is only preliminary but warrants further investigation.

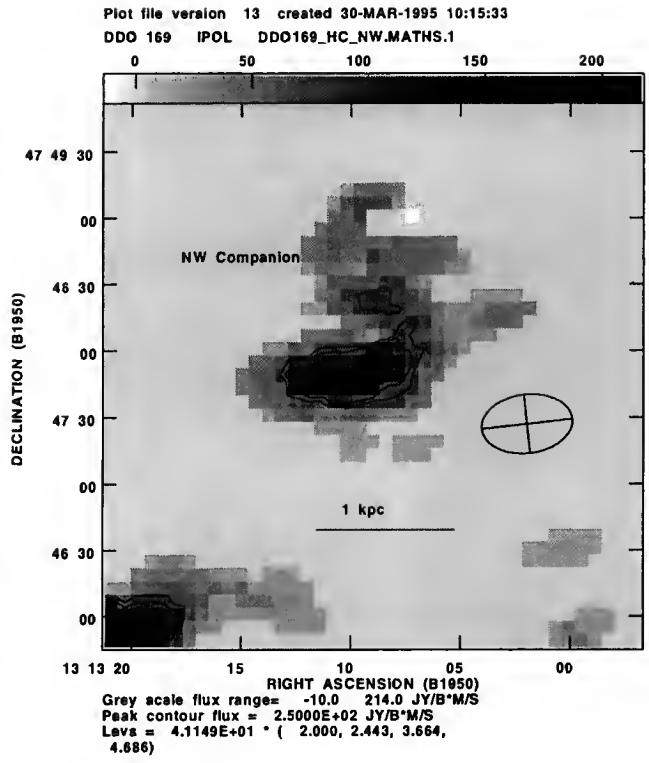

Figure A.1: Integrated HI intensity map of DDO 169 Companion.

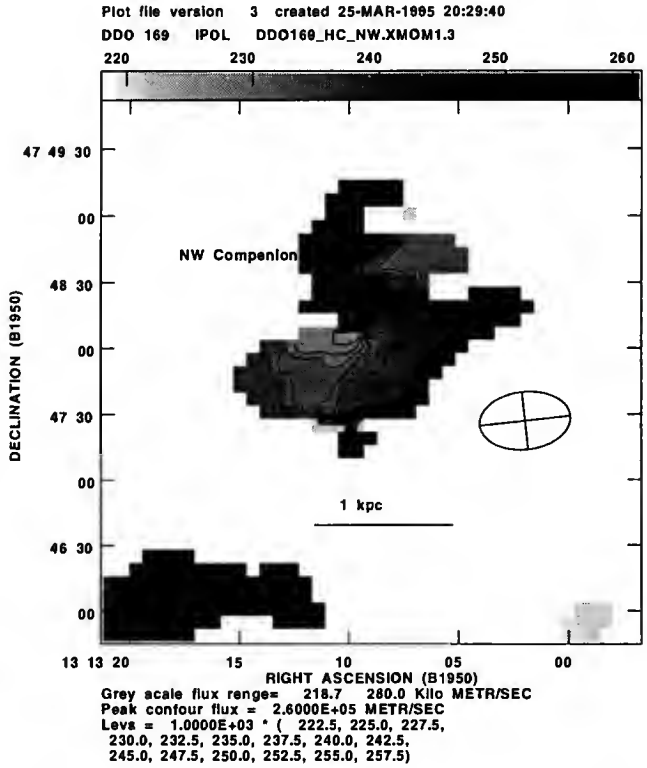

Figure A.2: Velocity field map of DDO 169 Companion.

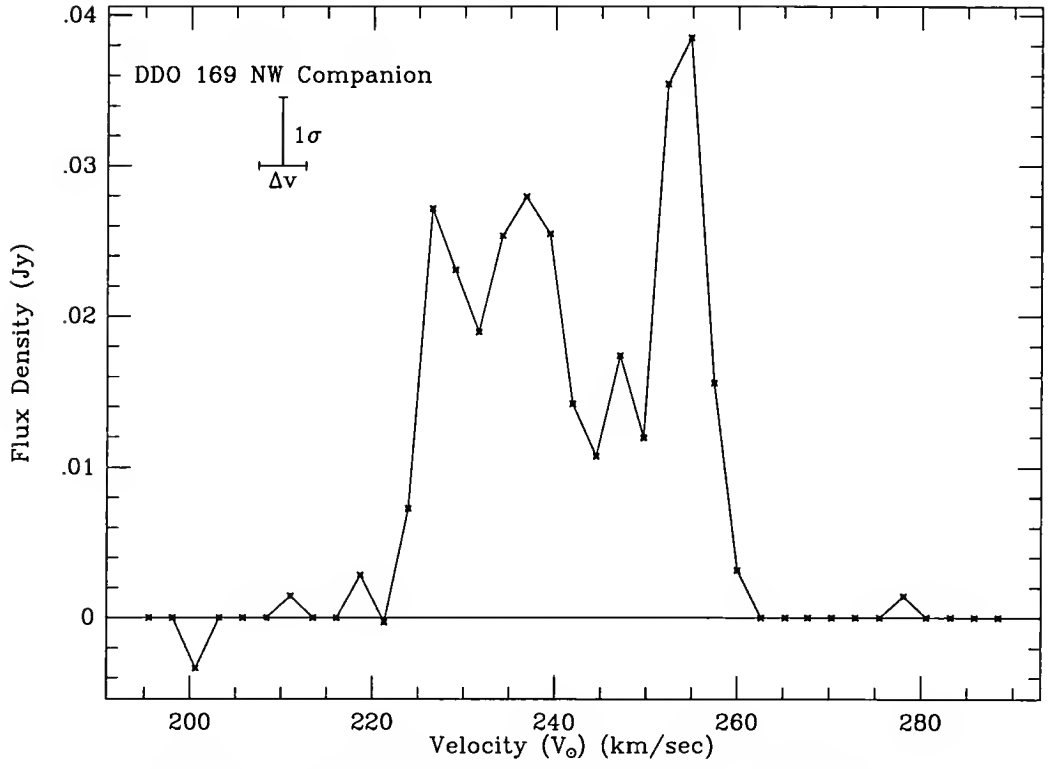

Figure A.3: Global velocity profile of DDO 169 Companion.

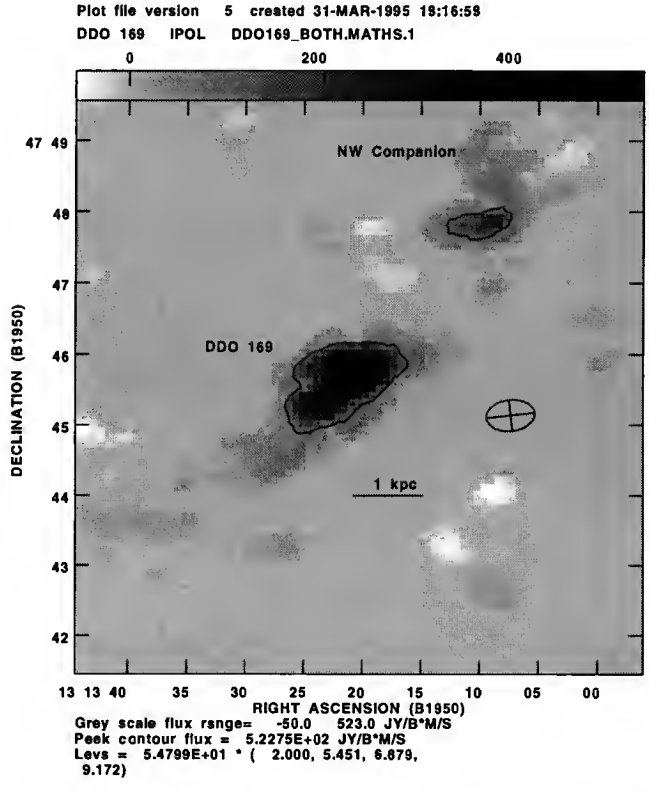

Figure A.4: Integrated HI intensity map of both DDO 169 and its companion.

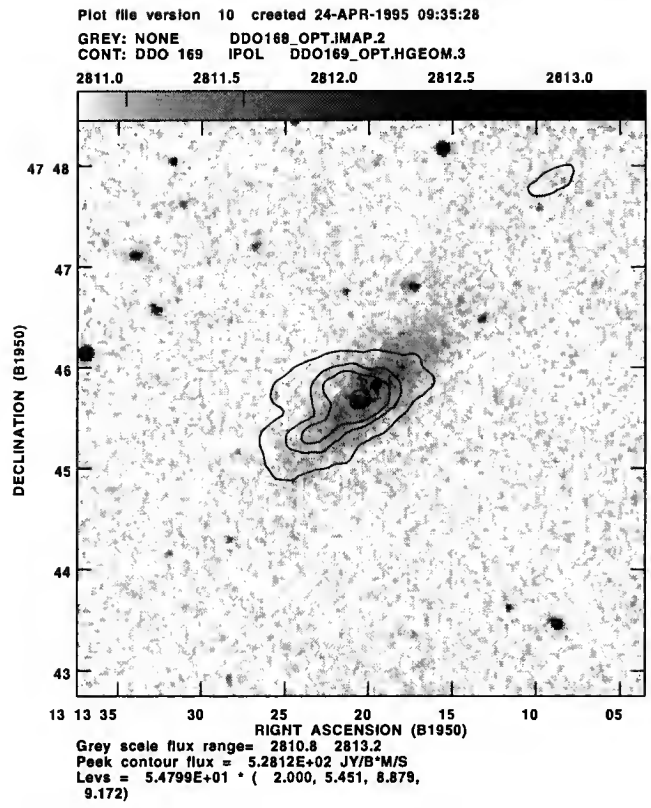

Figure A.5: Optical image with HI contours of both DDO 169 and its companion.

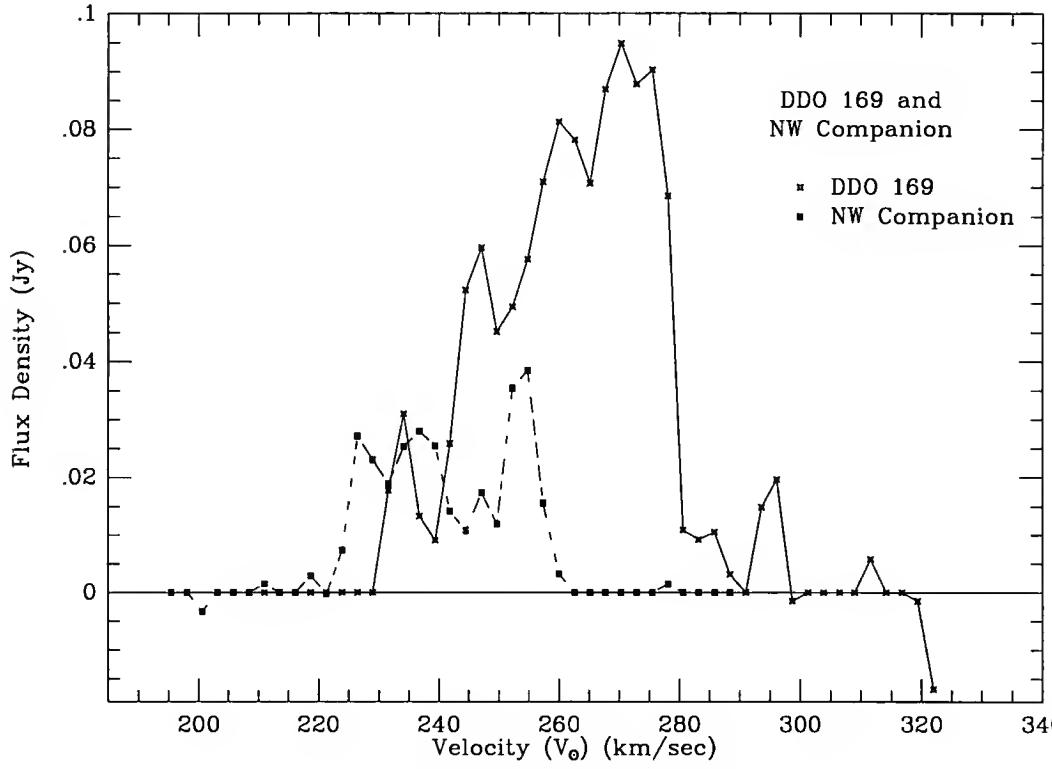

Figure A.6: Combined global velocity profiles of DDO 169 and its companion.

APPENDIX B
VOLUME CALCULATION

The flux sensitivity of the primary beam of the VLA is generally represented by a two-dimensional Gaussian, with the full-width at half-maximum (FWHM) defined as the size of the beam where the power drops to one-half of the maximum. The field-of-view of the VLA is usually defined as that set by the FWHM of the primary beam, and it is this definition that was used to calculate the volumes (and thus the expected number of detectable galaxies) in Chapter 4. The FWHM of the primary beam is 31.6′, which corresponds to a solid angle of 9.6041×10^{-5} steradians (sr), so that the volume of each of our three fields is approximately 5 Mpc, using our minimum and maximum distances of about 2.3 to 53.7 Mpc. The number of detectable galaxies was set by the minimum detectable flux for a given distance within our volume as demonstrated by equation (4–22):

$$M = ks^2 , \tag{B-1}$$

where k represents the minimum detectable intensity as given by the level above the r.m.s. noise of the background and the bandwidth of the observations, and s is the distance.

However, these calculations assumed that constant sensitivity across the FWHM of the beam, so that a mass corresponding to a given distance, as calculated from the above equation, is assumed to be detectable through the entire volume defined by the solid angle as calculated from the FWHM. However, the flux sensitivity of the beam is not constant, it drops off in a Gaussian manner with increasing distance from the center of the beam.

This means that the minimum detectable mass at a given distance is really only detectable at the very center of the field, not across the entire 31.6′ of the (FWHM) field-of-view.

Expressions for the calculation of a volume that includes this dropoff effect have been derived by Dr. Haywood Smith of the University of Florida; the results are presented here. If we let x be the dimensionless distance variable, then $x \equiv \frac{s}{s_0}$, where s_0 is the maximum distance at which a galaxy of mass M is detectable. We then define the minimum and maximum distances for the entire field volume (these are about 2.3 and 53.7 Mpc as set by the bandpass of the observations) as x_1 and x_2. Instead of using the FWHM of the beam, we now use the angle corresponding to the field-of-view of the images actually searched, which is 1.08° (close to the beam-width between first nulls, which is 1.18° for the VLA). We define this angle as θ_F, with a corresponding solid angle ω_F. We now let the dimensionless distance x_F be that at which θ (the angular distance from the center of the field) equals θ_F; this distance is $x_F = \frac{s}{s_0} = \frac{1}{4}$. For distances less than this, the solid angle ω_x is just ω_F. There are then two expressions to calculate the volumes:

$$\begin{aligned} V &= \frac{\omega_F}{3}\left({x_F}^3 - {x_1}^3\right); \quad x_F \geq x_1 \\ &= \frac{\omega_F x_F}{3}\left\{\frac{1}{2\ln 2}\left[\frac{1}{3}\left(\frac{x}{x_F} - 1\right) + \ln xF - \frac{x^3 \ln x}{{x_f}^3}\right]\right\}; \quad x_1 < x \leq 1. \end{aligned} \tag{B-2}$$

The maximum volume surveyed, using this derivation and the BWFN value for the angle, is 17.994 Mpc^3. Although this is considerably larger than that using the FWHM, note the volumes accessible for the lower mass galaxies are smaller, and that it is this end of the luminosity function that is steepest.

Using these values for the volume calculations and Tyson and Scalo's radial distribution function, we find that the expected number of galaxies we should detect in each

field is about 4.9, not 9, with the majority being contributed by systems with total masses in the range of approximately 7.5×10^6 and 5×10^7 solar masses.

Using Poisson statistics, we can estimate the probability of finding n galaxies in a field when the expected value is m:

$$P(n) = \frac{e^{-m} m^n}{n!}. \tag{B-3}$$

We have three fields, with one known galaxy in each (the target galaxy), and another detection in one of these three fields as well. So we have two fields with one galaxy and one field with two galaxies. The probability for this situation is $3P(2) \cdot P(1) \cdot P(1)$. For an expectation value $m = 4.9$, this combined probability is 3.49×10^{-4}, or 0.04% (this assumes no biasing: that the expectation value for each field is the same).

It can be seen here that even with this decreased number of predicted galaxies, our survey results do not support the steeply rising faint end of Tyson and Scalo's luminosity function. If their function was correct, the statistical chances of only detecting a total of four systems is very small, much less than 1%, and so our lack of detections is significant enough to rule out a large population of low-mass, gas-rich galaxies.

REFERENCES

Alimi, J-M. 1994, in *ESO/OHP Workshop on Dwarf Galaxies*, eds. G. Meylan and P. Prugniel (Garching bei München: European Southern Observatory), p. 63.

Arp, H., and O'Connell, R.W. 1975, *Ap. J.*, **197**, 291.

Athanassoula, E. 1994, in *ESO/OHP Workshop on Dwarf Galaxies*, eds. G. Meylan and P. Prugniel (Garching bei München: European Southern Observatory), p. 525.

Binggeli, B. 1986, in *Star-Forming Dwarf Galaxies and Related Objects*, eds. D. Kunth, T.X. Thuan, and J. Tran Thanh Van (Gif sur Yvette: Éditions Frontiéres), p. 53.

Binggeli, B. 1994, in *ESO/OHP Workshop on Dwarf Galaxies*, eds. G. Meylan and P. Prugniel (Garching bei München: European Southern Observatory), p. 13.

Binggeli, B., Sandage, A., and Tammann, G.A. 1988, *Ann. Rev. of Astr. Ap.*, **26**, 509.

Bothun, G.D., Mould, J.R., Caldwell, N., and MacGillivray, H.T. 1986, *A. J.*, **92**, 1007.

Bracewell, R. 1965, *The Fourier Transform and Its Applications* (New York: McGraw-Hill).

Briggs, F.H. 1990, *A. J.*, **100**, 999.

Brinks, E. 1994, NRAO preprint; to be published in *The Cold Universe*, eds. T. Montmerle, C. Lada, and J. Tran Thanh Van (Gif sur Yvette: Éditions Frontiéres).

Christiansen, W.N., and Högbom, J.A. 1985, *Radiotelescopes* (Cambridge: Cambridge University Press).

Clark, B. 1989, in *Synthesis Imaging in Radio Astronomy*, eds. R.A. Perley, F.R. Schwab, and A.H. Bridle (ASP Conference Series Vol. 6), p. 1.

Da Costa, G.S. 1994, in *ESO/OHP Workshop on Dwarf Galaxies*, eds. G. Meylan and P. Prugniel (Garching bei München: European Southern Observatory), p. 221.

Davies, J., and Morgan, I. 1994, in *ESO/OHP Workshop on Dwarf Galaxies*, eds. G. Meylan and P. Prugniel (Garching bei München: European Southern Observatory), p. 19.

Davies, J.I., and Phillipps, S. 1988, *M.N.R.A.S.*, **233**, 553.

Dekel, A., and Silk, J. 1986, *Ap. J.*, **303**, 39.

de Vaucouleurs, G., de Vaucouleurs, A., Corwin Jr., H.G., Buta, R.J., Paturel, G., and Fouqué 1991, *Third Reference Catalogue of Bright Galaxies*, (New York: Springer-Verlag).

Duc, P.-A., and Mirabel, I.F. 1994, *Astr. Ap.*, **289**, 83.

England, M.E. 1986, Ph.D. thesis, University of Florida.

Fisher, J.R., and Tully, R.B. 1981, *Ap. J. Suppl.*, **47**, 139.

Florkowski, D.R. 1980, Ph.D. thesis, University of Florida.

Fomalont, E.B. 1989, in *Synthesis Imaging in Radio Astronomy*, eds. R.A. Perley, F.R. Schwab, and A.H. Bridle (ASP Conference Series Vol. 6), p. 213.

Fomalont, E.B, and Perley, R.A. 1989, in *Synthesis Imaging in Radio Astronomy*, eds. R.A. Perley, F.R. Schwab, and A.H. Bridle (ASP Conference Series Vol. 6), p. 83.

Fomalont, E.B, and Wright, M.C.H. 1974, in *Galactic and Extra-Galactic Radio Astronomy*, eds. G.L. Verschuur and K.I. Kellerman (New York: Springer-Verlag), p. 256.

French, H.B. 1980, *Ap. J.*, **240**, 41.

Gallagher, J.S., and Hunter, D.A. 1984, *Ann. Rev. Astr. Ap.*, **22**, 37.

Gerola, H., and Seiden, P.E. 1978, *Ap. J.*, **223**, 129.

Gerola, H., Seiden, P.E., and Schulman, L.W. 1980, *Ap. J.*, **242**, 517.

Gordon, D., and Gottesman, S.T. 1981, *A. J.*, **86**, 161.

Held, E.V., and Mould, J.R. 1994, in *ESO/OHP Workshop on Dwarf Galaxies*, eds. G. Meylan and P. Prugniel (Garching bei München: European Southern Observatory), p. 201.

Hibbard, J.E., Guhathakurta, P., van Gorkom, J.H., and Schweizer, F. *A. J.*, **107**, 67.

Hjellming, R.M., and Basart, J.P. 1982, in *An Introduction to the NRAO Very Large Array*, ed. R.M. Hjellming (Charlottesville: NRAO), Chapter 2.

Hodge, P. 1971, *Ann. Rev. Astr. Ap.*, **9**, 31.

Hoel, P.G. 1954 *Introduction to Mathematical Statistics* (New York: John Wiley & Sons, Inc.), p. 117.

Hopp, U. 1994, in *ESO/OHP Workshop on Dwarf Galaxies*, eds. G. Meylan and P. Prugniel (Garching bei München: European Southern Observatory), p. 37.

Huchtmeier, W.K., and Richter, O-G. 1989, *HI Observations of Galaxies* (New York: Springer-Verlag).

Hunter, D.A. 1982, *Ap. J.*, **260**, 81.

Hunter, D.A., and Gallagher, J.S. 1986, *P.A.S.P.*, **98**, 5.

Kennicutt, R.C. 1989, *Ap. J.*, **344**, 685.

Kormendy, J. 1985, *Ap. J.*, **295**, 73.

Kormendy, J. 1994, in *ESO/OHP Workshop on Dwarf Galaxies*, eds. G. Meylan and P. Prugniel (Garching bei München: European Southern Observatory), p. 161.

Kunth, D. 1989, in *Evolutionary Phenomena in Galaxies*, eds. J.E. Beckman and B.E.J. Pagel (Cambridge: Cambridge University Press), p. 22.

Lake, G., and Schommer, R.A. 1984, *Ap. J. (Letters)*, **279**, L19.

Lasker, B., Sturch, C.R., McLean, B.J., Russell, J.L., and Jenkner, H. 1990, *A. J.*, **99**, 2019.

Lin, D.N., and Faber, S.M. 1983, *Ap. J. (Letters)*, **266**, L21.

Lo, K.Y., and Sargent, W.LW. 1979, *Ap. J.*, **227**, 756.

Lo, K.Y., Sargent, W.LW., and Young, K. 1993, *A. J.*, **106**, 507.

Marconi, G., Matteucci, F., and Tosi, M. 1994, *M.N.R.A.S.*, **270**, 35.

Mihalas, D., and Binney, J. 1981, *Galactic Astronomy*, (New York: W.H. Freeman and Company).

Mirabel, I.F., Duc, P.-A., and Dottori, H. 1994, in *ESO/OHP Workshop on Dwarf Galaxies*, eds. G. Meylan and P. Prugniel (Garching bei München: European Southern Observatory), p. 371.

Mueller, M.W., and Arnett, W.D. 1976, *Ap. J.*, **210**, 670.

Norton, L., and Lo, K.Y. 1994, in *ESO/OHP Workshop on Dwarf Galaxies*, eds. G. Meylan and P. Prugniel (Garching bei München: European Southern Observatory), p. 291.

Perley, R.A. 1994, *Very Large Array Observational Status Summary*, (Socorro: NRAO).

Puche, D., and Westpfahl, D. 1994, in *ESO/OHP Workshop on Dwarf Galaxies*, eds. G. Meylan and P. Prugniel (Garching bei München: European Southern Observatory), p. 273.

Puche, D., Westpfahl, D., Brinks, E., and Roy, J.-R. 1992, *A.J.*, **103**, 1841.

Pustil'nik, S.A., Ugryumov, A.V., Lipovetsky, V.A., Thuan, T.X., and Salzer, J.J. 1994, in *ESO/OHP Workshop on Dwarf Galaxies*, eds. G. Meylan and P. Prugniel (Garching bei München: European Southern Observatory), p. 133.

Roberts, M.S. 1988, in *New Ideas in Astronomy*, eds. F. Bertola, J.D. Sulentic, and B.F. Madore (Cambridge: Cambridge University Press), p. 65.

Roberts, M.S., and Haynes, M.P. 1994, *Ann. Rev. Astr. Ap.*, **32**, 115.

Rohlfs, K. 1990, *Tools of Radio Astronomy*, (Berlin: Springer-Verlag).

Roukema, B.F. 1994, in *ESO/OHP Workshop on Dwarf Galaxies*, eds. G. Meylan and P. Prugniel (Garching bei München: European Southern Observatory), p. 137.

Salzer, J.J., and Rosenberg, J.L. 1994, in *ESO/OHP Workshop on Dwarf Galaxies*, eds. G. Meylan and P. Prugniel (Garching bei München: European Southern Observatory), p. 129.

Sandage, A., and Binggeli, B. 1984, *A. J.*, **89**, 919.

Sandage, A., Binggeli, B., and Tammann, G.A. 1985, *A. J.*, **90**, 1759.

Sargent, W.L.W., and Lo, K–Y. 1985, in *Star-Forming Dwarf Galaxies and Related Objects*, eds. D. Kunth, T.X. Thuan, and J. Tran Thanh Van (Gif sur Yvette: Éditions Frontiéres), p. 253.

Sargent, W.L.W., and Searle, L. 1970, *Ap. J. (Letters)*, **162**, L155.

Schechter, P. 1976, *Ap. J.*, **203**, 297.

Searle, L., and Sargent, W.L.W. 1972, *Ap. J.*, **173**, 25.

Searle, L., Sargent, W.L.W., and Bagnuolo, W.G. 1973, *Ap. J.*, **179**, 427.

Seiden, P.E., and Gerola, H. 1979, *Ap. J.*, **233**, 56.

Seiden, P.E., Schulman, L.S., and Gerola, H. 1979, *Ap. J.*, **232**, 702.

Skillman, E.D. 1987, in *Star Formation in Galaxies*, ed. C.J. Lonsdale Persson (NASA Conf. Pub. CP-2466), p. 263.

Skillman, E.D., Kennicutt, R.C., and Hodge, P.W. 1989, *Ap. J.*, **347**, 875.

Smecker-Hane, T.A., Stetson, P.B., and Hesser, J.E. 1994, in *ESO/OHP Workshop on Dwarf Galaxies*, eds. G. Meylan and P. Prugniel (Garching bei München: European Southern Observatory), p. 249.

Staveley-Smith, L., Davies, R.D., and Kinman, T.D. 1992, *M.N.R.A.S.*, **258**, 334.

Strom, S. 1980, *Ap. J.*, **237**, 686.

Tammann, G.A. 1994, in *ESO/OHP Workshop on Dwarf Galaxies*, eds. G. Meylan and P. Prugniel (Garching bei München: European Southern Observatory), p. 3.

Thuan, T.X. 1985, *Ap. J.*, **299**, 881.

Thuan, T.X. 1986, in *Nearly Normal Galaxies*, ed. S.M. Faber (Berlin:Springer-Verlag), 67.

Thuan, T.X., and Martin, G.E. 1981, *Ap. J.*, **247**, 823.

Tosi, M. 1994 in *ESO/OHP Workshop on Dwarf Galaxies*, eds. G. Meylan and P. Prugniel (Garching bei München: European Southern Observatory), p. 465.

Tosi, M., Greggio, L., Marconi, G., and Focardi, P. 1991, *A. J.*, **102**, 951.

Tosi, M., Greggio, L., Focardi, P., and Marconi, G. 1992, in *The Stellar Populations of Galaxies*, eds. B. Barbuy and A. Renzini (Dordrecht: Kluwer), p. 207.

Tyson, N.D., and Scalo, J.M. 1988, *Ap. J.*, **329**, 618.

van der Hulst, J.M., Skillman, E.D., Smith, T.R., Bothun, G.D., McGaugh, S.S., and de Blok, W.J. 1993, *A. J.*, **106**, 548.

Weinberg, D.H., Szomoru, A., Guhathakurta, P., and van Gorkom, J.H. 1991, *Ap. J. (Letters)*, **372**, L13.

Westpfahl, D., and Puche, D. 1994, in *ESO/OHP Workshop on Dwarf Galaxies*, eds. G. Meylan and P. Prugniel (Garching bei München: European Southern Observatory), p. 295.

Wirth, A., and Gallagher, J.S. 1983, *Ap. J.*, **282**, 85.

BIOGRAPHICAL SKETCH

Caroline E. Simpson was born March 17, 1961, in Chapel Hill, North Carolina, and moved to Oxford, Ohio, in 1964. In 1967, the family moved to Amherst, Massachusett, where she attended elementary and high school, graduating from Amherst Regional High School in 1979. After working for a year, she attended the University of Massachusetts, obtaining a Bachelor of Science degree in both astronomy and physics in the fall of 1984. In the spring of 1985, she began work with the Hubble Space Telescope Guide Star Catalog Group at Space Telescope Science Institute. Once the initial version of the catalog was completed in 1988, she began graduate studies at the University of Florida, obtaining a Master of Science degree in astronomy in 1991. She was hired by Florida International University in Miami, Florida, and will begin teaching there during the summer of 1995 as a faculty member in in the Physics Department. She expects to receive her Ph.D. in August 1995.

I certify that I have read this study and that in my opinion it conforms to acceptable standards of scholarly presentation and is fully adequate, in scope and quality, as a dissertation for the degree of Doctor of Philosophy.

Stephen T. Gottesman, Chair
Professor of Astronomy

I certify that I have read this study and that in my opinion it conforms to acceptable standards of scholarly presentation and is fully adequate, in scope and quality, as a dissertation for the degree of Doctor of Philosophy.

Humberto Campins
Associate Professor of Astronomy

I certify that I have read this study and that in my opinion it conforms to acceptable standards of scholarly presentation and is fully adequate, in scope and quality, as a dissertation for the degree of Doctor of Philosophy.

Thomas D. Carr
Professor of Astronomy

I certify that I have read this study and that in my opinion it conforms to acceptable standards of scholarly presentation and is fully adequate, in scope and quality, as a dissertation for the degree of Doctor of Philosophy.

Haywood C. Smith
Associate Professor of Astronomy

I certify that I have read this study and that in my opinion it conforms to acceptable standards of scholarly presentation and is fully adequate, in scope and quality, as a dissertation for the degree of Doctor of Philosophy.

E.R. Andrew
Graduate Research Professor of Physics

This dissertation was submitted to the Graduate Faculty of the Department of Astronomy in the College of Liberal Arts and Sciences, and to the Graduate School and was accepted as partial fulfillment of the requirements for the degree of Doctor of Philosophy.

August 1995

Dean, Graduate School

LD
1780
1995
.S612
UNIVERSITY OF FLORIDA
3 1262 08556 9332